

ELASTOMERIC MATERIAL CHEMISTRIES FOR ADDITIVE
MANUFACTURING OF SOFT MACHINES

A Dissertation

Presented to the Faculty of the Graduate School
of Cornell University

In Partial Fulfillment of the Requirements for the Degree of
Doctor of Philosophy

by

Thomas John Wallin

August 2018

© 2018 Thomas John Wallin

ELASTOMERIC MATERIAL CHEMISTRIES FOR ADDITIVE MANUFACTURING OF SOFT MACHINES

Thomas John Wallin, Ph.D.

Cornell University 2018

ABSTRACT

Stereolithography is a rapid, high resolution, and scalable additive manufacturing technique that uses patterned light to build a solid object, layer-by-layer, from a liquid resin of photopolymerizable material. However, the material processing requirements, namely low viscosity and rapid photopolymerization, previously restricted printable materials to highly crosslinked and glassy polymers that exhibit low ultimate strains and prevent technical applications in biomedicine and soft robotics. This dissertation begins by reviewing the existing literature's attempt to additively manufacture soft machines, particularly soft robots. With the problem defined, I then attempt to address the gaps in materials compatibility with stereolithography printing by designing two chemical platforms. First, by incorporating dynamic ionic linkages between anionic nanoparticles and cationic acrylates, we demonstrate tough, elastomeric polyacrylamide-based hydrogels. Such ionic composite hydrogels exhibit fast gelation, remarkable ionic conductivity ($\sigma_{1\text{MHz}} = 1.8 \times 10^{-3} \text{ S m}^{-1}$), and large ultimate elongations ($\gamma_{\text{ult}} > 400\%$) and can be printed into osmotic actuators and soft conductive traces. Second, employing thiol-ene click chemistry of mercaptosiloxanes and vinylsiloxanes enables precise control of the polymer network density and thereby the mechanical properties over orders of magnitude (stiffness, $6 \text{ kPa} < E < 330 \text{ kPa}$; ultimate elongation, $50\% < \gamma_{\text{ult}} < 400\%$). A simple, low cost modification to common commercial desktop printers enables printing of this silicone chemistry into highly resilient soft machines. Fluidic elastomer actuators, when fabricated through this method, can be pressurized with the base liquid resin to impart autonomic self-healing upon puncture in ambient sunlight.

BIOGRAPHICAL SKETCH

Thomas John (T.J.) Wallin was born on May 29th, 1988 in Philadelphia, PA. In 2006, he graduated from La Salle College High School and enrolled in the College of William and Mary in Virginia. There, he obtained a bachelor's degree in physics and Chemistry in May, 2010. During that time, he wrote two undergraduate theses: "Mechanical Properties of Polymer Nanocomposites Based on Functionalized Graphene Sheets" under adviser Prof. Hannes Schniepp and "Preparation and study of a rare ternary insulating magnet" under adviser Prof. Gary Defotis which fulfilled the requirements for high honors in Chemistry. In August 2011, Thomas entered the PhD program at Cornell University in the department of Materials Science and Engineering. In August 2015, he completed his admission to candidacy and received a M.S. in Materials Science and Engineering

ACKNOWLEDGMENTS

I thank my adviser, Prof. Robert Shepherd, for the opportunity to join the Organic Robotics Laboratory in 2014. Since then, his guidance, both intellectually and personally, enabled my success in graduate school. Dr. Shepherd's belief that innovation and creativity can be born from sustained and focused exercises, became a guiding principle for my research. That tenet, combined with a directive to work on compelling problems and the resources to pursue my ideas enabled the enclosed work of this dissertation. I'd also like to acknowledge my two other committee members, Prof. Bonassar, and Prof. Archer for their support and expertise in the topics that comprise my thesis. Additionally, I am grateful for the mentorship I received from Prof. Archer and Prof. Emmanuel Giannelis during my first two years at Cornell.

My colleagues both in the Organic Robotics Laboratory and the department of Material Science and Engineering deserve acknowledgement. The majority of my intellectual growth came from group presentations and informal laboratory conversations in which ideas and knowledge were freely shared. I'd like to specifically thank Dr. Wenyang Pan, Dr. Jeremy Odent, Dr. James Pikul, Dr. Sanlin Robinson, Dr. Bryan Peele, Dr. Chris Larson, Dr. Ben Mac Murray, Ilse van Meerbeek, Shuo Li, Patricia Xu, Cameron Aubin, and Kevin Krumplestadter.

Lastly, I'd like to thank my friends: Anne, Dave, Craig, Nishant, and Rich. Their friendship has not only provided me with support and encouragement necessary to obtain this degree, but is an inexhaustible source of my own personal happiness.

TABLE OF CONTENTS

Chapter 1: 3D Printing of Soft Robotic Systems

1.1 Introduction	1
1.2 Essential Material Properties	3
1.3 Polymers in Soft Robotics	4
1.4 3D printing technologies	9
1.5 Sensing	21
1.6 Integrated devices	26

Chapter 2: Highly Elastic, Transparent, and Conductive 3D-Printed Ionic Composite Hydrogels

2.1 Abstract	43
2.2 Introduction	43
2.3 Results and Discussion	46
2.4 Conclusions	58
2.5 Experimental Section	59
2.6 Supplemental Information	64

Chapter 3: Click Chemistry Stereolithography for Soft Robots the Self-Heal

3.1 Abstract	76
3.2 Introduction	76
3.3 Results	80
3.4 Experimental	85
3.5 Conclusions	87
3.6 Supplemental Information	87

Chapter 4: Conclusions

4.1 Summary of Contributions	102
4.2 Future Work and Outlook	103

Appendix A: 3D Printing Antagonistic Systems of Artificial Muscle Using Projection Stereolithography

A.1 Abstract	107
A.2 Introduction	107
A.3 Methods	108
A.4 Results	112
A.5 Conclusions	117
A.6 Supplemental Information	119

Appendix B: Tough Thiourethane Photopolymers with Tunable Crystallinity for Additive Manufacturing

B.1 Abstract	125
B.2 Introduction	125
B.3 Results	128
B.4 Conclusion	133
B.5 Materials and Methods:	134
B.6 Supplementary Information:	139

Appendix C: Stereolithography for Personalized Left Atrial Appendage Occluder

C.1 Abstract	157
C.2 Introduction	157
C.3 Results	159
C.4 Conclusion	166
C.5 Experimental	167
C.6 Supplemental Information	172

CHAPTER 1

3D PRINTING OF SOFT ROBOTIC SYSTEMS

1.1 Introduction

Soft robotics combines compliant machinery and prime movers to enable continuous movement and equal force distribution. In contrast, canonical “hard” robots use hinges and bolts, assembled drive chains, and other system components to transmit force from a locally-generated source to remote locations.^{1,2} The distributed actuation, complex motion, and compliance make soft robots ideal candidates for applications at the interface of machines and humans. The two primary benefits of soft robotic systems are the safety for both the robot and the human because of a reduced stress concentration achieved through conformal contacts and infinite passive degrees of freedom at low impact forces³, and simple fabrication using additive manufacturing⁴⁻⁸, which allows for the design of sophisticated motion⁴ and chemical manipulation.⁹ Additive manufacturing describes the creation of 3D objects through the consecutive addition of material layers, for example, rotational casting,¹⁰ molding,^{9,11} screen printing,⁵ and 3D printing^{12,13}.

The engineering of the chemical, photonic, mechanical, and electrical actuation and sensing provides the basis of soft robots. However, higher-level embodiments and their application are typically inspired by biology.^{14,15} Although the functional design of hard robots is also guided by physiological principles,^{16,17} the use of soft materials that deform continuously enable soft robots to mimic the structure and function of soft tissues. Therefore, invertebrates, ranging in biological complexity from worms¹⁸ to octopuses¹⁹⁻²¹, often inspire the design of soft robots. The morphing,²² self-healing, and diversity of the musculature and sensory networks²³ of animals have been guiding the technological advances in robots.

Many features of soft robotic systems stem from the ability to process the machinery and motors as complex fluids. For example, *Pneu-Nets* are replica-moulded balloons, made of elastomers that are first poured as liquids into moulds and then

solidified as rubber. The balloons inflate and move according to the patterning profile of an inextensible material that is inserted during the chemical crosslinking of the elastomer.^{4,9,24} In this case, the machinery, motor, and the material are moulded into a monolithic form. Whereas not all soft robotic systems are processed in this manner or with the same degree of multi-functionality, many share similar processing features and abilities.^{6,25,26} Additive manufacturing provides an excellent, systematic tool to directly fabricate soft robots, particularly from elastomeric material, to capture the complexity of animal musculature. The simplicity and versatility of this systematic fabrication approach has led to compelling demonstrations of functional soft robotic systems such as multi-gait locomotion⁴, camouflage and display²⁰, assisting the movement of fingers³, and swimming⁸ (FIG. 1.1).

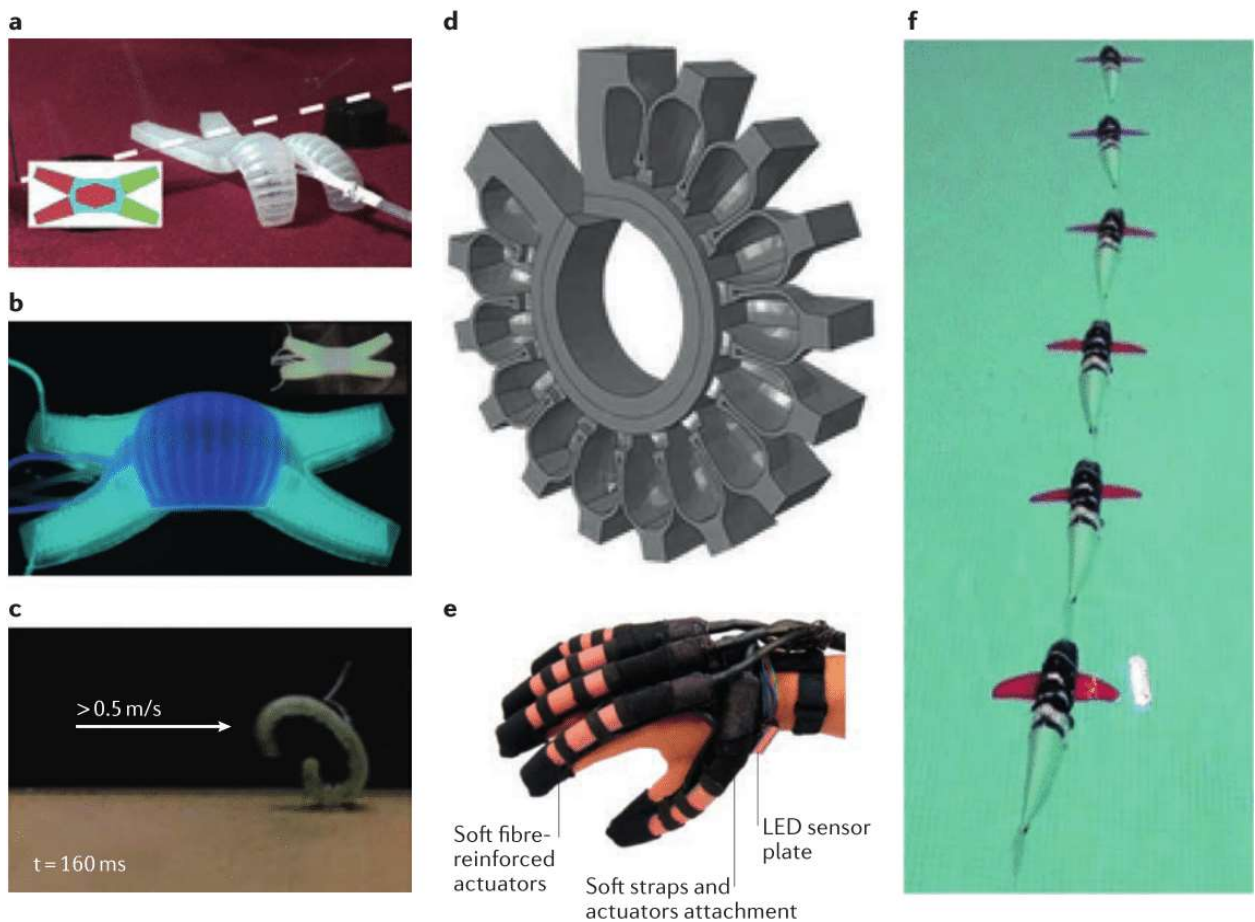


Figure 1.1: Soft Robots via Replica Molding. a) Multigait Soft Robot crawling under an obstacle. (Panel Adapted from Ref. 4) b) Camouflage and display for soft machines. (Panel Adapted Ref. 20) c) GoQBot, a caterpillar inspired rolling robot capable of speeds exceeding 0.5 cm s^{-1} . (Panel Adapted Ref. 40) d) Pneumatic Networks (PneuNets) for soft robots that actuate rapidly. (Ref. 44) e) Soft robotic glove for combined assistance and at-home rehabilitation (Panel Adapted Ref. 3) f) Hydraulic Autonomous Soft Robotic Fish for 3D swimming. (Panel Adapted Ref. 8)

In this Chapter, we survey soft materials and 3D printing technologies for the fabrication of soft robots. Advances in the direct printing of soft actuators and sensors from elastomeric precursors are discussed, and the combination of different elements into autonomous machines is investigated. Finally, we speculate about the future development of the field, and highlight emerging fabrication strategies and applications.

1.2 Essential Material Properties

The functional and safe integration with biological tissue and simple manufacturing procedures are key hallmarks in the majority of publications in the field of soft robots and define the essential material properties. Quantitatively, the stiffness, k , is the ratio of force to deformation of an object. This definition allows certain arrangements of long and thin, but constitutively stiff components, for example, steel wool,²⁷ to be considered soft. Alternatively, the tangent modulus, which measures deformation as a function of stress at a given strain and, therefore, removes any structural contributions to stiffness. Many of the materials used in soft robotics exhibit non-linear stress-strain behaviour which must be accounted for when modelling these systems. However, technical reports often specify the Young's Modulus, E , which is the tangent modulus in the linearly elastic regime, usually taken at very small strains (strain, $\gamma < 2\%$). The mechanical properties of the material should match those of soft tissue to ensure functional engraftment and to prevent damage. Therefore, the Young's Moduli of soft robotic materials encompasses a similar regime to that of soft tissue (generally, $E < 10$ MPa). Intrinsically soft polymers, when 3D printed, fulfil this mechanical requirement of soft robotic systems regardless of device design.

There are numerous other mechanical metrics, beyond softness, that are important for the function of soft robotic systems. Unlike their rigid counterparts that require discrete linkages, soft robots continuously deform along their surface through strain differentials that are programmed through extrinsic (structural) or intrinsic (material) stress or stiffness gradients. The strain tensor of the body controls the local curvature and shape, thus, the ultimate elongation, γ_{ult} , of the material constitutively defines the

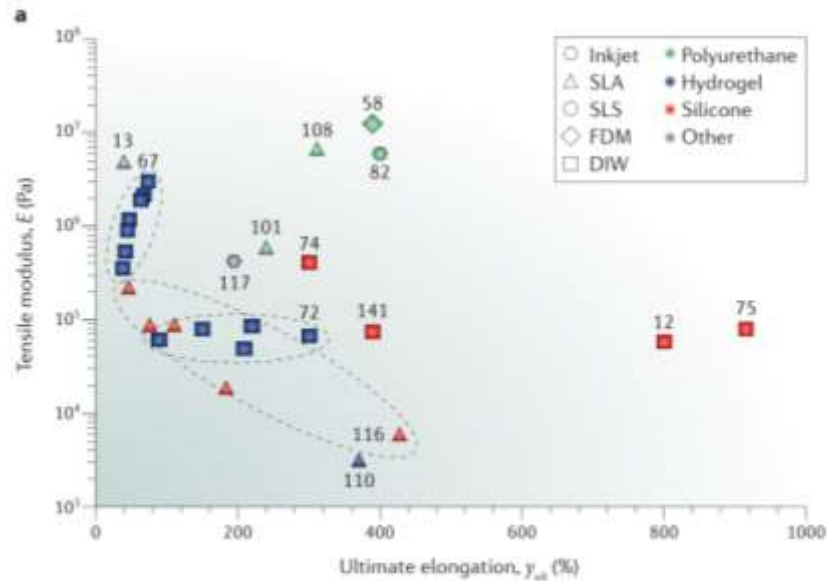
upper bound of the actuation amplitude prior to failure. Common soft robotic materials fail between 40% and 1,000% strain. Toughness, Γ , is the total mechanical energy absorbed by the material prior to rupture, and constitutes another important material property; however, stably functioning soft robotic devices should operate well below these ultimate values (γ_{ult} , Γ) and remain within the elastic regime of the material. A key, but often unreported metric, which is particularly important for soft robotic materials, is the modulus of resilience, U_r . This is the maximum energy that can be entirely elastically recovered during a loading cycle to return the robot to its original, un-deformed state. These intensive material properties (E , γ_{ult} , Γ , and U_r) can be obtained through analysis of the tensile loading and unloading curves.

The material of a specific component of the robotic device should possess an E appropriate for the target application and a maximum, or at least sufficient γ_{ult} , Γ and U_r to enable large, recoverable local strain differentials and to impart resistance to failure and fatigue. Unfortunately, only few soft materials, which fulfil these requirements, can be printed into 3D architectures and even fewer functional materials (e.g. conductive) meet these constraints. Thus, major research efforts seek to address this issue by developing new manufacturing technologies and polymer chemistries.

1.3 Polymers in Soft Robotics

Polymers exhibit a wide range of physical properties, over many orders of magnitude, including those desirable for soft robots ($1\text{kPa} < E < 100\text{ MPa}$) (FIG. 1.2a). The polymer backbone is defined by long, often repeating chains of macromolecules, which govern interchain and intrachain interactions. However, the mechanical behaviour is also heavily dependent on the microstructure; thus, polymers with the same chemical composition can possess disparate mechanical properties. The available microstructures of a polymer are limited by the manufacturing process. Therefore, in the context of 3D printing, the structure-processing-property relationship has to be considered to direct the mechanical performance of the printed part.

The long macromolecules further exhibit viscoelasticity in response to applied forces. The degree of viscous dissipation (that is, the alignment and translation of the polymer) and the stored entropic elastic energy (that is, uncoiling and recoiling of



b Common polyurethane reactions

Urethane formation:



Urea formation:



c Common silicone reactions

Hydrosilylation:



Condensation:



d Common hydrogel reaction

Free radical polymerization:

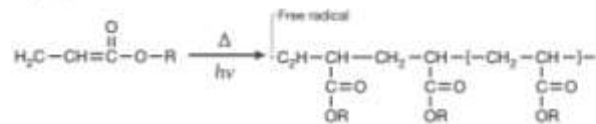


Figure 1.2: Mechanical Properties of Polymeric Materials used in Additively Manufactured Soft Robots and their crosslinking reactions. a) The mechanical behavior of materials are colored by their relevant classification (polyurethane, hydrogel, silicone, or other) and each printing technique (inkjet, stereolithography [SLA], Selective Laser Sintering [SLS], Fused Deposition Modelling [FDM], and Direct Ink Writing [DIW]) corresponds to a given symbol with the respective reference labelled. The dashed line encircles multiple materials from the same publication. b) Reactions of isocyanates with alcohols and amines to form urethane and urea linkages, a common reaction in polyurethane synthesis. c) Common silicone reactions. The hydrosilylation reaction used frequently in platinum (Pt) cured silicones between silicon hydride (SiH) and vinyl (C=C) groups to form a crosslink, and the crosslinking reaction used often in tin-cured (Sn) silicones often involves silicon hydride (SiH) and silanol (SiOH) groups condensing to produce water. d) One common hydrogel polymerization strategy is based on the free radical polymerization of acrylates in response to light (hv) or heat (Δ). This reaction relies on the propagation of a growing radical chain by continued reaction of the unpaired electron (free radical).

polymer chains) depend, among other things, on the polymer microstructure and the

arrangement of the polymer network. Strong crosslinks between the chains, such as covalent bonds, promote elasticity and thus, help to restore the material to its original state after loading. However, the crosslink density is inversely proportional to the uncoiling length, which is the maximal distance at which the polymer segments can unfold within the network prior to permanent deformation. Dynamic, weak interactions and the absence of strong linkages allow for network reconfiguration, which can improve ductility and toughness at the cost of resilience. As the strength of interactions decreases further, the chains begin to slide freely past each other and the polymer becomes a viscous melt.

Materials for soft robotics require a low E with high γ_{ult} , I , and U_r , which can be achieved with polymer microstructures possessing a low crosslink density and a high molecular weight between crosslinks. However, 3D printing of such microstructures is not trivial. For example, polymerizing low viscosity inks often involves precursors with high degrees of functionality that promote gelation at a low degree of conversion, which is necessary for rapid build speeds and print-pattern fidelity.²⁸ However, further polymerization of these multi-armed crosslinkers increases the effective crosslink density, which consequently leads to the stiffening and the embrittlement of the polymer. The target microstructure of such soft, elastomeric materials often exists only in a narrow window of polymerization; therefore, precise control of the printing process is required to account for the idiosyncrasies of the printer, including the geometry of the individual parts and printing direction.

The microstructure and nature of interchain interactions also profoundly impact the processability of the polymer system. Thermoplastic polymers are mainly characterized by macromolecular physical interactions. Heat or solvation can overcome the interaction energy and thus, enable the repeated melting, fusing, and reshaping of the polymer network. By contrast, thermosets are percolated networks of stronger interchain linkages, for example covalent bonds, which prevent large-scale macromolecular rearrangement without causing the degradation of the polymer. The term elastomer, which is often synonymously used with rubber, implies that the material is operating well above its glass transition temperature, T_g , at which

molecular mobility between crosslinks allows for repeated coiling and uncoiling of chains without permanently damaging the network. Elastomers tend to be thermosets; however, thermoplastic elastomers exist that possess significant physical crosslinks which provide for considerable elastic regimes ($\gamma_{\text{elastic}} > 200\%$) prior to plastic deformation.

The 3D printing of polymers involves the transition from a highly-mobile state (the melt, solution or powder state) to a solid network, which is accompanied by a rapid increase in the relative strength of interchain interactions. Unfortunately, it can be difficult to design materials that maintain printability while meeting the mechanical and microstructural requirements. Therefore, although numerous 3D printable polymers exist, for example, polyimides,²⁹ epoxies,³⁰ polycarbonates,³¹ polyesters,³² only three materials have yet been demonstrated to be printable and to possess the correct mechanical properties for applications in soft robotics – polyurethanes, silicones, and hydrogels.

Polyurethanes

Polyurethanes are composed of urethane–urea linkages that result from a condensation reaction between polyol (OH groups) or polyamine (NH groups) and a polyisocyanate (FIG 1.2b).³³ Urethane (R-NH-O-R') and urea (R-NH-O-NH-R') possess a hydrogen bond donor (NH) adjacent to a hydrogen bond acceptor (-O-), resulting in strong hydrogen bonding between the polymer chains, which enables many polyurethanes or ureas to exist as solid polymers at room temperature even without covalent crosslinks, a requirement for thermoplastics. A large library of polymers with hydroxyl or amine functionalities allows for the design of various different chemical backbones for thermoplastic and thermosetting polyurethanes. In fact, multiple oligomeric diol species can be combined in varying amounts to create a single polyurethane with both hard (crystalline) and soft (amorphous) segments to achieve versatile mechanical performance. However, toxicity and flammability concerns remain, which pose not only a problem for applications in soft robots, but

also for printing processes, because it is difficult to use external stimuli to control the nucleophilic reaction of isocyanates at ambient conditions.

Polydimethylsiloxanes

Polydimethylsiloxanes (PDMS), commonly known as silicone rubbers, constitute the most commonly used materials in soft robotic systems. The backbone of PDMS is formed by siloxane (Si-O) linkages, which endow this polymer with extraordinary flexibility owing to the small, divalent oxygen atoms that function as chain extenders between Si atoms, which increases the distance between the side groups of the polymer. This leads to a highly deformable Si-O-Si bond angle of $\sim 143^\circ$ (compared to $\sim 109.5^\circ$ for normal sp^3 -hybridization). Thus, PDMS has enormous chain mobility indicated by a very low glass transition ($T_g \approx -125^\circ\text{C}$) and melting temperature ($T_m \approx -40^\circ\text{C}$).³⁴ Widely used industrially, the different silicone materials possess excellent elasticity and resilience (elastic regimes up to $\gamma \sim 700\%$ strain), chemical inertness, thermal resistance, biocompatibility, dielectric strength, low permeability, and thermal conductivity compared with other polymer systems. Although PDMS exhibits poor solubility in many common solvents,³⁵ the low T_g allows for un-crosslinked PDMS oils ($M_w > 100,000$ Da) to remain fluid at room temperature. A common silicone fabrication technique involves the two-part mixture of liquid siloxanes that react to form a cross-linked network. Typical polymerization pathways include hydrosilylation (SiH with C=C) and condensation (SiOH with SiOH) in the presence of catalysts (FIG 1.2c). These reactions typically occur over the course of a few hours at room temperature.

Hydrogels

Hydrogels are hydrophilic crosslinked polymer networks capable of absorbing or desorbing large amounts of solvent in response to the environmental conditions (T, solvent, pH, etc.). With Young's moduli in the range of biological soft tissue and with the ability to swell in physiological solutions, such as in cell culture media or serum, hydrogels are especially attractive for biomedical applications such as in tissue engineering and as cell culture platforms. However, soft hydrogel networks suffer from weak interactions, which are highly dependent on the volumetric crosslink

density and therefore, the degree of swelling. Hydrogel-based devices often require encapsulation, rehydration or strict control of the ambient environment (temperature, humidity) for stable performance. Alternatively, the incorporation of ionic-covalent entanglements or double networks results in stronger and more ductile hydrogels with toughness comparable to that of silicone rubber. Loading such gels with an electrolytic solvent imparts ionic conductivity, which is particularly useful when creating soft, capacitive sensors and actuators.³⁶

A variety of different hydrophilic acrylates ($\text{CH}_2=\text{CHCOO}^-$) and methacrylates ($\text{CH}_3\text{CH}=\text{CHCOO}^-$) can be used to form hydrogels by a free-radical polymerization reaction (FIG 1.2d). The chemical flexibility and the compatibility with 3D printing systems, which can initiate a free radical polymerization by the use of light or heat, has led to the widespread use of monomeric and oligomeric acrylates in additive manufacturing processes.

1.4 3D printing technologies

Replica Moulding

Early 3D printing technologies were limited to rigid materials, typically made from hard plastics. Additive manufacturing enabled rapid design and fabrication of the first soft robotic components by replica moulding of organic elastomers from 3D printed, hard moulds.^{9,37,38} Commercial elastomers, which are readily processed as liquid mixtures, were poured into these rigid printed moulds and left to cure into shape. Aided by high-throughput design iteration, the accessibility of 3D printers and ease of implementation, replica-moulded devices led to early demonstrations of elastomer-based actuators^{4,39–42} and sensors.⁴³ However, this fabrication strategy limits the geometry of the respective components to the (prismatic) structure of the moulds, whereas sophisticated soft actuators, particularly fluidic elastomer actuators, often require complex internal architectures.^{20,44} It is possible to assemble intricate soft robots from numerous simpler replica-moulded parts, yet this strategy is labour-intensive and difficult for miniaturized devices. Additionally, lamination, that is, the attachment of different replica-moulded layers, often introduces defects that can effect

mechanical integrity, because establishing strong bonds between thermosetting elastomer layers is challenging and remains an active area of research.^{45–47}

Investment casting allows for the fabrication of 3D parts with a single, continuous elastomer shell. This technique is an adaptation of replica moulding, except that the first mould negative is a sacrificial layer, sometimes made of wax, that takes the shape of the fluid chambers in a fluidic elastomer actuator.^{8,48} An elastomer is then cured on top of this layer, which, after removal of the sacrificial material, leads to the formation of a monolithic, hollow device. Advances in material chemistry have also enabled the 3D printing of waxes, gels, and other materials with selective solubility into disposable inner “fugitive moulds” that, upon stimuli, induces dissolution and facilitates high-resolution internal features in elastomeric devices.^{7,49–53} An advantage of investment casting for the fabrication of soft robotic parts is the lack of seams between the elastomer layers, which increases the durability and the maximum achievable pressures, allowing these actuators to exert greater forces prior to rupture than laminated counterparts. Alternatively, porogens or blowing agents embedded within elastomers can be used as templating agents in order to create open-celled foams. Once sealed, such percolated networks of pores reduce the extrinsic stiffness, allow the transport of pressurizing fluid and provide support within complex 3D shapes without the need for pressurized air.^{11,54–56}

Fused deposition modelling

Fused deposition modelling (FDM) is a popular and affordable 3D printing technology, and numerous commercial desktop printers are available. In this direct-writing process, a heated extrusion nozzle melts a filament or wire and deposits the molten material onto a surface, which then fuses into a solid object upon cooling (FIG. 1.3a). The reliance on melting and cooling processes limit the use of FDM to thermoplastic polymers. Although different filament sources have been explored⁵⁷, the most successful FDM material for soft robotics has been the Ninjabflex© family of thermoplastic polyurethanes, which can withstand strains above $\nu_{ult} > 500\%$ with a Young’s modulus $E \sim 10$ MPa.⁵⁸ This material can be printed into high-force

(maximum blocking force, $F_{\max} > 75 \text{ N}$) fluidic elastomer actuators capable of bi-directional motion (FIG. 1.3b).⁵⁹ Thermoplastic polyurethanes have also been used for the 3D printing of flexure hinges for tendon-driven, soft prosthetic fingers.⁶⁰ In this case, the FDM process was programmed to introduce porosity to the material in order to further reduce the effective stiffness to values below or equal to that of the base polyurethane.

The resolution of FDM is restricted by the nozzle diameter, and in the above

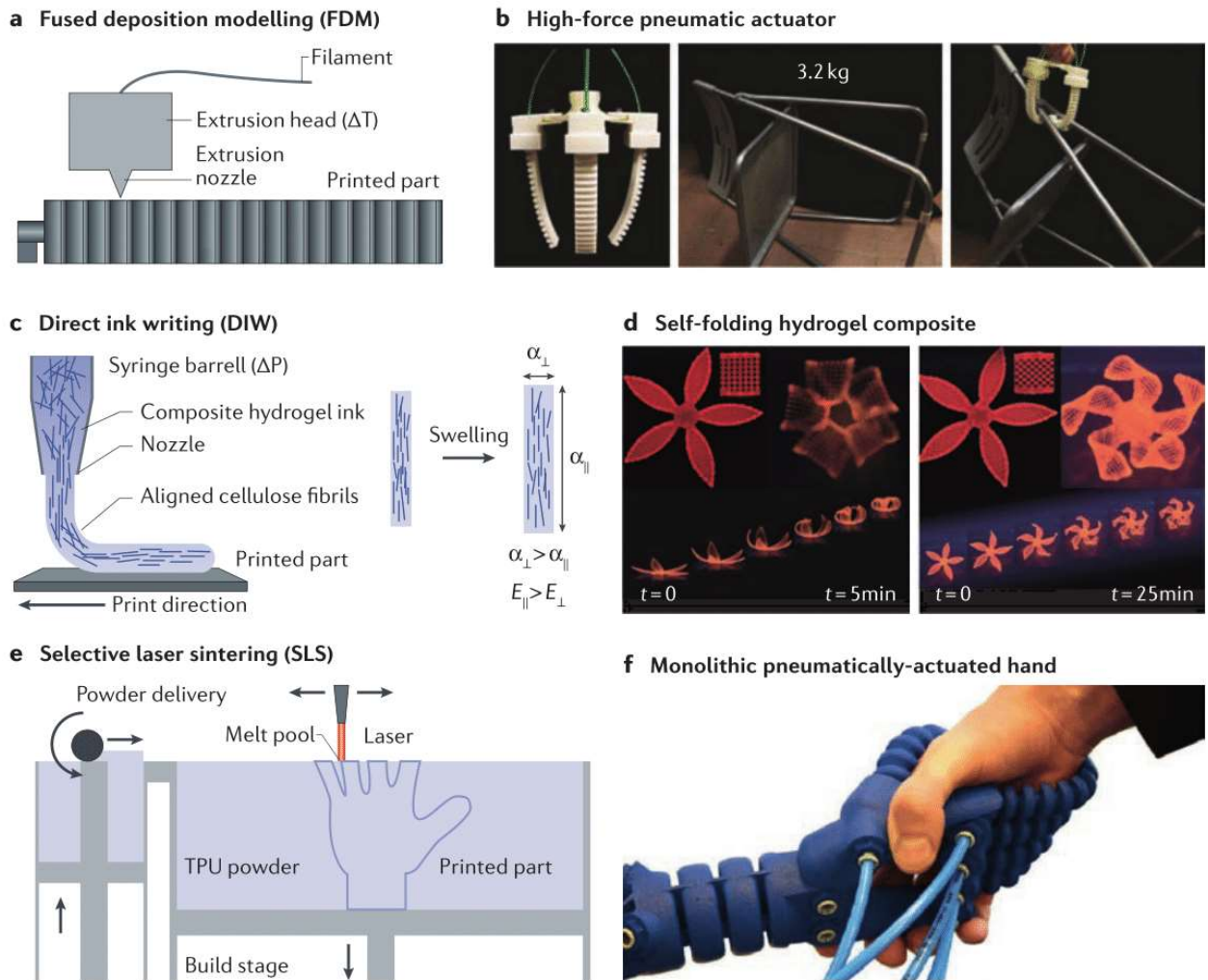


Figure 1.3: Extrusion- and powder-based 3D printing of soft actuators. a) Adapted from *Ref. 59*, Fused deposition modelling (FDM) where a thermoplastic filament is heated (ΔT) by an extrusion head and pushed through an extrusion nozzle to generate b) pneumatic actuators capable of lifting a 3.2 kg chair. c) Direct ink writing (DIW) (modified from *Ref. 70*) of composite hydrogel inks aligns cellulose fibres to obtain a greater modulus ($E_{\parallel} > E_{\perp}$) and thereby constrains swelling ($\alpha_{\parallel} < \alpha_{\perp}$) in the direction parallel to the print direction d) directs osmotic actuation of self-folding flower-like structure. Festo, inc employs e) selective laser sintering (SLS) of thermoplastic powders to create a f) monolithic pneumatically actuated hand capable of safely interfacing with humans. (*Ref. 83*)

examples, nozzle heads of 0.1 mm were used. However, the printing process can introduce heterogeneities, defects or voids. Therefore, for the above fluidic elastomer actuators, the wall thickness should be at least three times the nozzle size to establish a closed, air-tight surface.⁵⁹ Additionally, the temperature needs to be controlled to ensure that the filament fully melts in the nozzle without creating voids, and that a large enough “melt pool” is formed to fuse the layers, but not so large as to prevent a loss of print fidelity prior to vitrification.⁶¹ Build times are proportional to build volumes and inversely proportional to nozzle size and resolution; large, overhanging elements may require post-processing in order to remove sacrificial layers, which prevents the use of FDM for large-scale manufacturing processes. The development of FDM printers with pellet hoppers or multiple nozzles, which are capable of selectively depositing different thermoplastic materials in the same build layer, will pave the way for multi-material printing⁶² and for complex mechanical programming required for advanced robotic devices.

Direct ink writing

Direct ink writing (DIW) relies on fluid-flow-based printing of a viscoelastic ink. A pressure source, for example a plunger, forces a liquid ink of polymeric precursor above the yield stress, allowing it to be selectively deposited through a nozzle (FIG. 1.3c). Once extruded, a sudden stress reduction, phase-change, solvent evaporation polymerization (either continuous or initiated in response to external stimuli) or combination thereof restrains the deposited material into a specific shape. The solidification process competes with gravitational fluid flow, “wetting-out” and self-leveling tendencies of the ink and must be properly balanced to ensure shape retention and interlayer adherence.⁶³ Customized polymeric inks are available, including thermosets and elastomers, with rheologies (for example, shear yield stress and viscosity) compatible with the DIW printing process.⁶³

Post-extrusion heating or photoexposure can thermally or photolytically initiate free radical polymerization in acrylate-based inks to form hydrogels. While DIW has been used for the 3D printing of biocompatible materials with low E for biomedical

applications and tissue engineering,⁶⁴ the soft robotics community has mainly explored the printing of hydrogel systems for osmotic sensors and actuators. So called “4D printing”⁶⁵, where the fourth dimension corresponds to a later shape-change from the printed hydrogel structure, relies on the modulation of the local solvent conditions (for example, the interaction parameter, χ or T) to tune the thermodynamic equilibrium point between a swollen state (the chemical potential for solvation of the polymer chains dominates) and collapsed state (polymer-polymer interactions are more favorable).⁶⁶ The printing of density gradients and different chemistries⁶⁷⁻⁶⁹, or the alignment of high-aspect ratio nanofillers⁷⁰, introduces anisotropy, which, when properly controlled, adds a programmed mechanical response beyond uniform swelling (or collapse) to such devices. This approach can be used to fabricate self-folding microstructures (FIG. 1.3d)⁷⁰ or a hydraulic valve capable of actively regulating fluid flow.⁶⁹

However, the low viscosity of acrylate inks, and often a low crosslink density (and thereby low E) in the printed hydrogel prevents the direct ink printing of overhanging or hollow structures. Thus, the above hydrogel-based objects, which are printed by DIW, are actually “2.5D” or prismatic, and are only later actuated or folded into 3D geometries. Moreover, these simple osmotic devices are of limited use in complex environments, in which subtle changes from multiple stimuli (for example, pH, ionic strength, T, or solvent composition) influence the hydrogel thermodynamics and can greatly alter device performance. Replica moulding of tough hydrogels (with ionic-covalent entanglements or double networks) allows for the construction of elastomeric machines;⁷¹ however, such chemistries possess rheological behaviour and slow polymerization kinetics that are difficult to adapt to DIW. Recent work attempted to extrude a photocurable acrylamide ink with embedded alginate chains, which can then be physically cross-linked to form a second polymer network by immersion in a solution of divalent calcium cations.⁷² Although this material outperforms the homogeneous acrylamide system, the ultimate elongation ($\gamma_{\text{ult}} \leq 300\%$) falls short when compared with similar replica moulded acrylamide-alginate materials ($\gamma_{\text{ult}} \geq 2,000\%$)⁷³; this shortcoming can be attributed to the required ink modifications for

compatibility with DIW, as well as the slow diffusion of calcium ions into the printed acrylamide network.

DIW has also been applied for the manufacturing of fluidic elastomer actuators. Although many silicone elastomers are commercially available as low-viscosity liquid mixtures, the curing process is typically gradual, occurring over a period of a few hours at ambient conditions. Thus, DIW using these commercial formulations suffers from slow polymerization and a corresponding slow increase in viscosity, which leads to material flow after deposition, poor resolution, and long build times. These issues can be addressed by modifying the ink viscosity with thixotropic agents or by increasing the reaction rate through heating, in the case of platinum catalyzed-addition cure,¹² or humidity, for oxime-condensation cure⁷⁴. Although limited in geometric complexity, such fabricated pneumatic actuators are highly resilient and sustained for $n > 30,000$ full actuation cycles (bending angle $\sim 270^\circ$) prior to failure.⁷⁴ Recently, silicone-ethanol emulsions have been printed in order to create foams, which can expand up to 900% in response to resistive heating, which is beyond the liquid-vapour transition of the encapsulated solvent.⁷⁵

Similar to FDM, the resolution of DIW is restricted by the nozzle diameter (up to microns), which is inversely proportional to build speeds. Multi-nozzle arrays that divide a single ink source into multiple streams, offer the possibility to exponentially reduce print times; however, such nozzle heads are relatively large (> 100 microns) and cannot be individually addressed.⁷⁶ Alternatively, multiple nozzles can be used to deposit different inks⁶⁷, leading to multi-material prints, for example, a polyurethane/epoxy-based spider-like soft robot.⁷⁷

Although DIW is amongst the most flexible printing processes in terms of compatible materials, the development of rapidly-solidifying soft material inks that do not deform or collapse is crucial for the printing of complex structures. Therefore, research to minimize fluid flow after deposition and to explore supporting structures through extruding components of the ink into more viscous or immiscible substrates is under way.^{78,79} Kinetically-trapped within the medium, an extruded ink, such as slow-

curing, room-temperature-vulcanizing silicones, can fully polymerize in-situ prior to removal from the bath.⁸⁰

Selective laser sintering

Selective laser sintering (SLS) builds objects from solid grains of powder (FIG. 1.3e). In the case of printing polymers, a better name would perhaps be “selective laser melting”, because at the beginning of the process, a laser is raster-scanning across a bed of powdered material, and once the local temperature rises above the T_m , the small granules melt. Once the irradiation stops, the material cools and fuses together. Then, the next layer of polymer powder is uniformly deposited along the print bed and the process is repeated until the whole structure is built.

Using a combination of reinforcement learning and SLS, pressurized bellows grippers can be assembled into a multi-fingered hand, which is capable of executing gripping, lifting and rotating tasks.⁸¹ SLS can also be applied to print hands that are entirely composed of thermoplastic polyurethane (TPU92A-1, $\gamma_{ult} \sim 400\%$). Such hands contain various customized components, such as bending, rotational, and bidirectional fluidic elastomer actuators, which are attached to a soft, hollow palm that connects fingers and also serves as a sensing air chamber (FIG. 1.3f).^{82,83} Beyond pneumatics, SLS enables the fabrication of porous structures with high compliance, low production costs, and complex designs.⁸⁴ For example, anthropomorphic robots can be printed using stiff polyamide ($E \sim 1.9\text{MPa}$)⁸²; these “anthrobs” contain solid-state hinges and bones with canals for tendon-based actuation as well as ducts for wires of discriminative touch sensors. In SLS, the residual powder can also act as passive physical support for consecutive layers; however, the removal of the powder after the printing process requires external access to hollow chambers through an aperture of at least 10 mm and any internal geometries must be smooth with minimal branching to promote drainage.⁸³ Additionally, SLS can be hindered by a slow assembly time, with one hand requiring over 12.5 hours of printing.⁸³

FDM and SLS have similar constraints regarding material compatibility and printing process. SLS requires a thermoplastic material in the form of a powder with narrow size distribution and homogenous morphology (granulometry) to promote a uniform, dense powder bed.⁸⁵ Moreover, the temperature fields must maintain an appropriately-sized melt pool in order to fully melt and fuse the material without distorting previously-printed geometries. Although the diameter of the laser beam can be less than 1 micron, the resolution in SLS is usually in the range of a few multiples of the powder size (lateral resolution on the order of $\sim 100 \mu\text{m}$ with a wall thickness of 0.8 mm).⁸²

Direct inkjet printing

Direct inkjet printing, which is related to hot-melt printing, inkjet printing on a powder bed or polyjet printing, is a rapid process, in which an entire layer of liquid or molten material is jetted onto a substrate before solidifying (FIG. 1.4a). In a three-step process, small droplets of fluidic ink are formed ($V = 1\text{-}100 \text{ pL}$, $d = 10\text{-}150 \mu\text{m}$) and directly deposited on a substrate, which leads to interactions between neighbouring droplets, followed by vitrification, evaporation, and/or polymerization of the ink, resulting in a solid. Droplets of thermosetting polymers can also contain photopolymers that undergo cross-linking in response to UV light. Finally, the material accumulates through the repeated fabrication of 2D layers.

Moving forward from 2D printing technologies, multiple nozzle heads can jet millions of droplets of different inks within seconds, while maintaining a lateral resolution on the order of $50 \mu\text{m}$.²⁸ Thereby, commercial materials based on methacrylate/acrylate chemistries with distinct mechanical properties can be simultaneously printed to directly fabricate 3D multi-material objects. For example, a robot can be made by leveraging the different E (and T_g) of materials and thereby programming a mechanical response to temperature,⁸⁶⁻⁸⁹ electrical stimuli,⁹⁰ mechanical stimuli,^{90,91} oscillating magnetic fields⁹² or a pressurizing fluid (FIG. 1.4b).^{93,94}

Despite the commercial availability of different materials for inkjet printing, there

is still a lack of compatible inkjet materials suitable for soft robotics. Until now,

mainly the flexible urethane-acrylate *Tango* series of materials ($E \sim 0.7$ MPa, ν_{ult}

~270%),⁹⁵ commercially available from *Stratasys*, has been used for soft robotics

devices. Combining varying amounts of the base ink (TangoPlus FLX930) with a

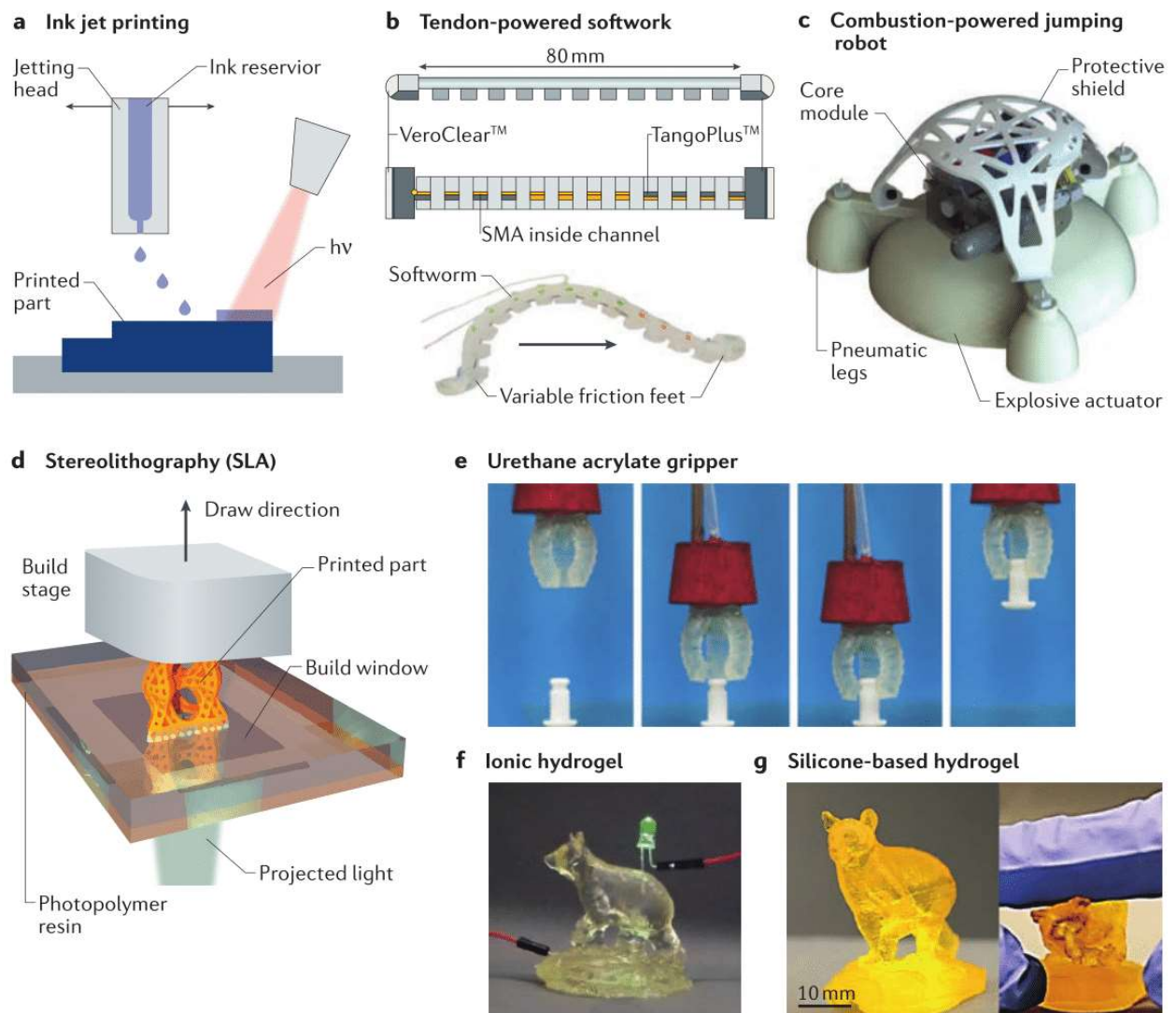


Figure 1.4: Photocurable ink-based 3D printing of soft materials. **a** Inkjet or polyjet printing can deposit millions of independent drops within seconds, which are cured by photoirradiation and used to print multi-material devices like the **b** | tendon-drive “softworm” (*Ref. 90*). This multi-material robot is constructed from stiff Veroclear and flexible TangoPlus inkjet materials with a channel for later embedding of a shape memory alloy (SMA) tendon. Variable friction feet enable worm-like locomotion through repeated actuation of the tendon. **c** | A combustion-powered jumping robot inkjet printed from multiple materials to create mechanical gradients that enable the robot to survive operation without shattering. (*Ref. 96*) **d** | In “bottom-up” Stereolithography (SLA), projected light passes through a transparent build window at the base of a vat containing liquid photopolymer resin. As the resin cures in response to photoexposure, the printed object adheres to a build stage which is pulled out of the vat in the draw direction. SLA enables direct fabrication of soft, monolithic hollow objects for the engineering of a **e** | three armed gripper made of urethane-acrylate capable of lifting small objects (*Ref. 101*) **f** | a conductive ionic hydrogel capable of completing a circuit to power a green LED (*Ref. 110*) and **g** | a soft, silicone based “Touchdown the bear” (left) which is highly deformable upon manipulation (right) (*Ref. 116*)

more rigid commercial ink (VeroWhitePlus) incrementally stiffens the printed parts

spanning a gradient of three orders of magnitude ($1\text{MPa} < E < 1\text{GPa}$).⁹⁶ Inspired by similar mechanical gradients that exist within animal musculoskeletal systems, rigid driving components can be interfaced with soft body parts to minimize stress concentrations and enabling the robot to survive multiple combustion-based jumping cycles without shattering (FIG. 1.4c).

However, other soft robotic applications require even softer, more extensible and more resilient elastomers than the commercially-available inkjet materials. In contrast to DIW, designing custom chemistries for materials suitable for inkjet printing is difficult, and replacing sophisticated printheads can be costly. The physics of droplet formation and deposition require fine control of the processing conditions and the properties of the ink fluid to balance viscous, inertial, and surface-tension forces.^{28,97} For example, highly-viscous inks resist droplet ejection and demand high velocities, which can lead to splashing upon contact with the substrate. The use of inviscid inks does not address this issue, because the dominating surface tension causes droplets to break upon impact. Post-deposition interactions between droplets (for example, wetting or coalescence) further impact the quality of the printed product.⁹⁷

Stereolithography

“Vat polymerization” technologies, broadly referred to as stereolithography (SLA), but includes 2-photon polymerization⁹⁸, micro-stereolithography (μ -SL)⁹⁹, digital mask projection stereolithography¹⁰⁰, digital light processing,¹⁰¹ and continuous liquid interface production,¹⁰² can be used to polymerize objects within a liquid resin. Synthesis in a dense medium provides buoyant forces capable of supporting soft, compliant structures, which is particularly useful for the printing of thin, overhanging structures. Vat polymerization printers exploit the spatial and temporal control of light to selectively photopolymerize a solid object, layer by layer, from a liquid prepolymer (FIG. 1.4d). Depending on the respective technique, different illumination sources are used. Photopolymerization-based resin systems maintain a high resolution, while rapidly fabricating numerous parts in parallel (draw rate $\sim 1\text{m hr}^{-1}$)¹⁰². Moreover, the use of holographic patterning to build entire objects in a single step (deposition

rate $20,000 \text{ mm}^3 \text{ hr}^{-1}$)¹⁰³ reduces the costs and time for large-scale manufacturing. Therefore, SLA provides an efficient and commercially-attractive technique to construct soft robots with micro-scale features and complex geometry,

However, there was a lack of available materials with suitable mechanical properties for soft robot applications (low E , high γ_{ult}) compatible with SLA. The rapid transition from a liquid resin to a solid polymer requires the concentration of solutions of low molecular weight, which enables gelation at low photodosages, but results in dense, highly cross-linked networks and stiff ($E > 10 \text{ MPa}$), brittle ($\gamma_{\text{ult}} < 50\%$) components for rigid structural elements¹⁰⁴. Alternatively, pleated antagonistic actuators with minimal local strains can be fabricated to generate adequate actuation amplitudes.^{13,105} Such monolithic, complex, fluidic elastomer actuators achieve rapid actuation cycle speeds (70 ms), but the low resilience prevents repeated loadings (cycles to failure, $N_{\text{failure}} \sim 12$) even at low strains (25%).¹³

The processing requirements of SLA are amenable to custom elastomeric chemistries so long as certain resin requirements are met. The resin used for SLA must photopolymerize within the same spectrum and intensity as the printer's light source. The polymerization process must further be spatially-controllable and on an acceptable timescale. Moreover, the apparent viscosity of the resin has to be sufficiently low ($\nu_{\text{app}} < 5 \text{ Pa s}$) to allow the recoating of the build area. And lastly, the newly-printed part preferentially adheres to the previous layer and not the interface transmitting the photopattern.¹⁰⁶ This last requirement often poses an important challenge in "bottom-up" systems where the printed part needs to delaminate from a transparent window at the base of a resin vat (FIG. 1.4D). When mechanical shear does not suffice, the creation of a liquid "dead-zone" interface, which can be either chemically-induced¹⁰² (through the diffusion of oxygen in the case of oxygen-inhibited resins) or physically-induced¹⁰⁷ (with a non-reactive "floating layer") prevents unwanted adhesion to the window.

The development of techniques and chemistries for the fabrication of soft and stretchable materials has been an important aspect of SLA research. SLA can be combined with soft lithography to print rigid, thin-walled moulds that can be carefully

backfilled with commercial two-part elastomers. The consequent dissolution in a base removes the brittle SLA mould, leaving just the elastomer.⁴⁹ Alternatively, high-performance, UV-curable polyurethanes, such as Carbon™ EPU and RPU, can be photopolymerized into an acrylate network, which contains unreacted precursors of polyurethane. Thermal treatment of this acrylate “green body” initiates polymerization of a latent, secondary network, which results in a material with large ultimate elongation ($\gamma_{\text{ult}} > 300\%$) but a high Young’s modulus ($E = 7 \text{ MPa}$), exceeding that of many natural tissues.¹⁰⁸

The direct SLA printing of low E , high γ materials for soft robots has been achieved through the use of custom printers that enable both high temperature ($T = 70 \text{ }^\circ\text{C}$) resin vats which simultaneously lowers viscosity and increases the polymerization rate of long-chained acrylate melts into printable regimes.^{101,109} For example, an elastomer, called “5:5”, can be printed into highly-extensible ($\gamma_{\text{ult}} > 200\%$) and soft ($E \sim 0.6 \text{ MPa}$) robotic devices, for example, a three-fingered gripper (FIG. 1.4e).¹⁰¹ The backbone of this material is made of soft (epoxy aliphatic acrylate) and hard (aliphatic urethane diacrylate) segments linked by hydrogen bonds, which endow the material with a large capacity for plastic deformation at the expense of resilience. There is also the possibility to incorporate ionic interactions, such as the electrostatic ones between anionic nanoparticles and cationic ammonium containing polyacrylamide, which improves the gelation kinetics of hydrogel resins (FIG. 1.4f).¹¹⁰ The dynamic physical linkages allow for the formation of a soft, stretchable ($E = 3.5 \text{ kPa}$, $\gamma_{\text{ult}} = 370\%$) and resilient functional material that is ionically conductive (conductivity, $\sigma_{f=1\text{MHz}} = 1.9 \text{ S}\cdot\text{m}^{-1}$) and capable of rapid osmotic actuation (gravimetric swelling ratio, $\Delta w/w \sim 200\%$ within 200 s).

The free radical polymerization of acrylates and the cationic polymerization of epoxies, which provide the basis of many SLA resins, are both based on the propagation reactions of growing chains.^{111,112} Photoreactivity is easily implemented through acrylate functionalities,^{113,114} but such modification can lead to shrinkage, continuous polymerization (for days), and toxicity.¹⁰⁶ Photocatalyzed click chemistries, such as thiol-ene and thiol-isocyanate, are step-wise addition

polymerizations that rapidly proceed to high conversion, which offer an propagation free alternative to acrylate systems.¹¹⁵ Because of absence of a propagating radical in click chemistry, top-down polymerization or a different window substrate is required to enable delamination from the transparent window which transmits the photopattern into the liquid resin. For example, by using a polymethylpentene window, low-viscosity solutions of mercaptosiloxanes and vinylsiloxanes can be printed into PDMS objects of varying network density and mechanical performance ($6 \leq E \leq 225$ kPa, $50 \leq \gamma_{\text{ult}} \leq 430\%$) (FIG. 1.4g).¹¹⁶ This approach takes advantage of the inherent benefits of silicones (for example, chemical inertness, resilience, and low toxicity), and allows for autonomic self-healing through sunlight owing to the lack of oxygen inhibition and the rapid polymerization at low photodosages in click chemistry. For example, fluidic elastomer actuators can be printed to incorporate pockets of unreacted pre-polymer resin, which can be used as pressurizing fluid. In the case of a puncture, the pre-polymer bleeds out of the actuator and undergoes rapid photopolymerization in ambient light, thereby healing the elastomeric membrane and reinstating actuation.

Functionally-graded¹¹⁷ or multi-material^{118,119} printing can be readily accomplished through automated vat or pre-polymer solution exchange, although possible fouling with unreacted resin must be taken into consideration. For example, a polymer exchange approach can be employed to print extensible flowers with methacrylate shape-memory polymers. These flowers bloom when exposed to temperatures above 50 °C.¹¹⁹ Owing to the photocuring kinetics of the methacrylate components, this formulation requires almost 100 times more radiant exposure (radiant exposure, $H_e = 333 \text{ mJ cm}^{-2}$) than conventional acrylate formulations, necessitating long exposure times, and/or light sources capable of large irradiances.

1.5 Sensing

Current soft robots have limited or no sensory capabilities. The implementation of complex functions requires next-generation devices to be able to detect their own deformation state, applied forces, and different environmental conditions. In order to integrate sensing into soft robotic systems without impeding mechanical performance,

the functional components must meet similar material requirements ($E < 10$ MPa, sufficiently high γ_{ult} , Γ , and U_r) as the base elastomer. Multi-material additive manufacturing techniques can be employed to build soft, functional structures with distinct regions of often disparate optical, electrical, and magnetic properties. Moreover, heterogeneities or anisotropies can be introduced by different techniques, such as conformal printing onto arbitrary¹²⁰ or moving surfaces¹²¹, by the use of core-shell printheads¹²², by the alignment of particles in response to shear^{30,70} or other applied external fields.¹²³

Resistive and capacitive sensors

Resistive and capacitive sensors are the most popular choices for measuring strain in soft robots.¹²⁴ A main challenge is the fabrication of soft and stretchable electrodes that maintain conductivity at high strains. Hydrogels can be loaded with an electrolytic solvent (for example, saltwater) to function as ionic resistive sensors, up to a mechanical failure of $\gamma \approx 400\%$.^{36,110} Although hydrogels are popular for the design of stretchable electrodes in soft robotics, there is concern regarding stability. Device encapsulation and the use of AC-driving fields can help to mitigate electrochemical breakdown, ionic migration, and solvent evaporation and therefore improve the lifespan.³⁶

Electrical conductors generally possess lower resistivity than their ionic counterparts. Colloidal inks, made from mixtures of conductive nanofillers and elastomers, can have high electrical conductivity because of nanoparticle percolation; however, the morphology, size, and loading fraction of the colloids has to be precisely controlled to preserve softness and stretchability. For common fillers (for example, carbon nanotubes¹²⁵, carbon black³² and metal nanoparticles¹²⁶), the loading fractions required to maintain electronic connectivity at high strains typically result in a stiff and brittle composite.^{127,128} The patterning of rigid conductive composites into serpentine pathways of resistive sensors minimizes local strains through concentrating stress¹²⁹ and often results in a permanent rearrangement of the conductive network upon deformation, which is reflected by a hysteresis during cyclic loading at moderate

strains.¹³⁰ Additionally, nanoparticles often strongly absorb or scatter UV-visible light and increase the viscosity of the printing inks, restricting their use in inkjet printing and SLA. Alternatively, conductive precursors, like metal salts, can be loaded into elastomeric inks to form an interconnected network of nanoparticles upon galvanic deposition¹³¹ or thermal treatment¹³², leading to composites with high conductivity even at large elongation ($\sigma > 10^3 \text{ S}\cdot\text{cm}$, $\gamma = 250\%$). Such printed resistive sensors can accurately sense temperature and applied pressure over this strain regime.¹³²

Confining mobile liquid-state conductors within a compliant matrix can minimize the aforementioned issues with composites, such as mechanical stiffness or hysteresis. For example, conductive carbon grease can be extruded into a curing silicone reservoir to build a glove with embedded elastomeric strain sensors capable of differentiating five hand gestures (FIG. 1.5a).¹³³ Similarly, DIW of liquid metals at room temperature, for example, eutectic alloys of gallium and indium (EGaIn), into conductive pathways for stretchable antennas and sensors¹³⁴⁻¹³⁶ leads to the creation of a thin, solid oxide shell owing to the ambient oxygen reacting with the gallium. Despite a high modulus, this thin oxide “skin” is extrinsically compliant and ruptures easily under deformation before coalescing and reforming with the now exposed EGaIn liquid.

In general, soft resistive sensors detect gross deformation, because the material needs to considerably strain to elicit useful signal changes.³⁶ Alternatively, adding a dielectric layer between the conductive elastomer electrodes produces a soft analogue to the common capacitor. This compliant device can detect subtle variations in the electrode area, the dielectric thickness, and even changes of the local environment through capacitance measurements.^{137,138} Arrays of such sensors are readily and inexpensively fabricated through lamination^{137,138}, screen printing,¹³⁹ photopatterning and transfer printing,¹⁴⁰ or through multi-material processing,^{121,141,142} often using commercial elastomers (for examples, the elastomer VHB, 3M inc.) as the dielectric. In addition to material (dielectric constant, conductivity) and mechanical considerations (E , γ_{ult} , Γ , and U_r), an appropriate design and manufacturing process has to be identified to achieve the desired layered architecture, while avoiding defects

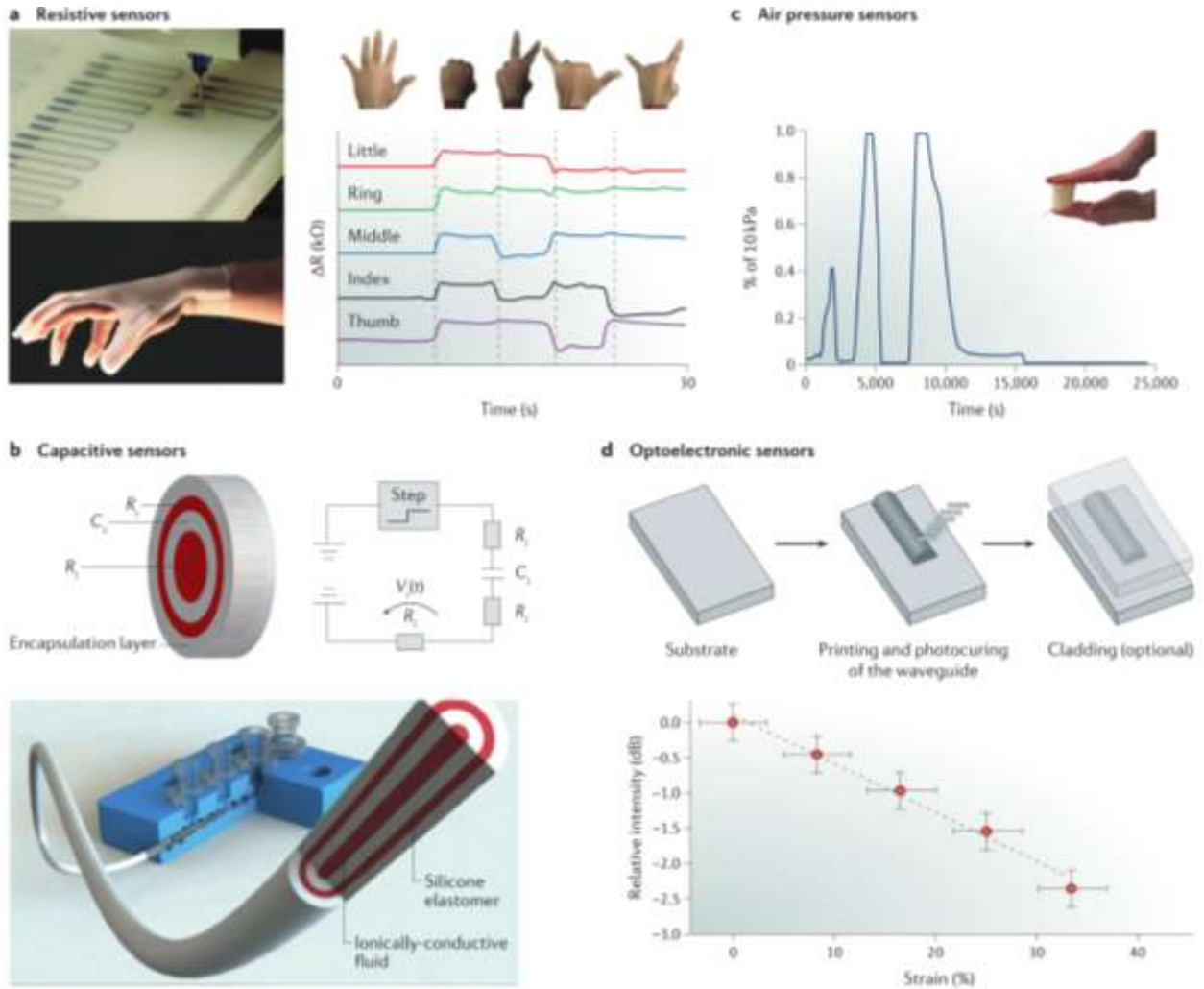


Figure 1.5: 3D printed soft sensors. **a)** Resistive sensors can be fabricated by extruding conductive carbon grease into a viscous silicone pre-polymer matrix. Thereby, a glove can be created with embedded resistive sensors capable of using temporal changes in resistance (ΔR) to distinguish different hand gestures. (Adapted from *Ref. 133*) **b)** Capacitive sensors can be produced by multi-core shell direct ink writing (DIW) of ionically conductive fluid and insulating silicone elastomers, which generates a stretchable fibre with strain-dependent capacitance. (Adapted from *Ref. 143*) **c)** Air pressure sensors can be combined with hollow skins, fabricated by selective laser sintering (SLS), to detect a specific kind of deformation, for example, three compressions shown by changes in internal pressure (y-axis) with time (x-axis). (*Ref. 149*) **d)** Adapted from *Ref. 150*, Inkjet printing of elastomeric waveguides (and optionally cladding) for optoelectronic sensors on to substrates. Optoelectronic sensors infer strain (x-axis) from the relative signal attenuation (y-axis) of the light transmitted by the optical fibre.

that cause dielectric loss and electrical breakdown. Multi-core shell print heads can be

used to concentrically fabricate soft capacitive structures in the form of monolithic “fibres”, which can be stitched or woven into textiles to create wearable and stretchable ($\gamma_{\text{ult}} \sim 250\%$) sensors (FIG. 1.5b).¹⁴³

Magnetic sensors

Magnetic sensors offer numerous benefits over resistive or capacitive sensors, such as the possibility to perform non-contact, remote measurements with minimal hysteresis. Magnetic probes can be sensitized to measure orientation relative to magnetic fields, even beyond fields related to devices; for example, relative to the Earth’s poles. For example, snake-like soft robots can employ magnetic sensors to detect body curvature^{144–146}. In these snake platforms, the strain-limiting layer contains a rigid Hall Effect sensor, which measures the relative orientation of an embedded magnet. As the robot deforms, magnetic fields change the measured Hall voltage. Increasing the number of embedded magnets and Hall sensors allows for the formation of tri-axis tactile sensors that infer contact areas and contact forces with a resolution as high as 2.3×10^{-4} N.^{147,148}

Though demonstrated on rigid polymers, these strategies are likely compatible with 3D printing of elastomers loaded with magnetic nanoparticles. For example, magnetically-assisted SLA fabrication can be employed to selectively align iron oxide platelets in order to generate voxels of controlled magnetization (and mechanical anisotropy); this approach could possibly enable the use of magnetic sensors in proprioception.¹²³ Moreover, the development of printable, soft and stretchable magnetic sensor arrays will certainly lead to interesting applications in soft robotics.

Air pressure sensors

Volumetric sensors, which are analogues of fluidic elastomer actuators, can be realized by inkjet printing¹⁴⁹. For example, chambers plugged with air pressure sensors can be incorporated into hollow thermoplastic polyurethane robot skins in order to infer volume changes by detecting deviations of the internal pressure (FIG. 1.5c). These chambers provide simple building blocks tailored to detect specific types of

deformation (pulling, pushing, bending or twisting); however, complex motions (for example, simultaneous pulling and twisting) cannot be captured by this setup. Clever implementation of multiple sensors and additional signal processing are required to facilitate proprioception derived from scalar volume measurements.

Optoelectronic sensors

Optical sensors are based on stretchable waveguides, in which the internal reflection, and thus, signal attenuation, is dependent on the indices of refraction of the core (n_{core}) and the cladding (n_{cladding}) as well as the path shape and length. Compared with electrical resistive probes, waveguide sensors exhibit low hysteresis and high precision (signal to noise ratio > 50) at appreciable strains ($\gamma = 85\%$). For example, using a moulds, silicone-polyurethane waveguides can be implemented into a soft prosthetic hand to enable the detection of the shape and softness of an object.⁴³ Moreover, soft and stretchable optical fibres can be readily fabricated by printing elastomers with appropriate optical properties; for example, $n_{\text{core}} > n_{\text{cladding}}$ and a high attenuation coefficient allow for meaningful signal-to-noise ratios (10:1). Inkjet printing of photocurable ethylene glycol vinyl ether-2-phenoxyethyl acrylate inks onto PDMS substrates creates free-standing elastomeric waveguide sensors that withstand elongations $\gamma > 30\%$ (FIG 1.5d).¹⁵⁰ Similar to capacitive sensors, the optical fibre and the cladding layer can be simultaneously printed using core-shell DIW.¹²² SLA printing of hydrogels ringlets, which pinch an optical fibre, has also been applied to measure pH by detecting a change of the resonant wavelengths in response to protonation and de-protonation of polyacrylic acid.¹⁵¹

1.6 Integrated devices

Ultimately, the great advantage of using and combining 3D printing technologies is the opportunity to integrate a network of actuators, sensors, controls and power systems into full-autonomous soft robots through a single, on-demand digital fabrication process. Multi-material conformal printing of ionic acrylate and silicone inks onto the surface of fluidic elastomer actuators allows for the integration of soft

actuators and sensors to enable tactile sensing.¹⁴¹ Such a device can locally detect external contact and differentiate it from internal fluidic actuation (FIG. 1.6a). The soft dielectric elastomer sensor can be simultaneously used as an RGB display (hyperelastic light-emitting capacitor) by incorporating electroluminescent inorganic particles into the silicone ink.^{140,152} This approach opens up a route to 3D print a soft and coloured haptic touch-screen.

Hydraulically-actuated robots can be realized by combining actuation with power systems. For example, the simultaneous polyjet printing of non-reactive polyethylene glycol (liquid) and elastomer inks (solid) can be applied to build and mechanically support a bellows actuator with overhanging features and at the same time provide a hydraulic fluid (FIG. 1.6b).⁹⁴ Using this technique, a hexapod robot has been built that only requires the addition of a DC motor for operation. A combination of DIW and replica moulding has enabled the fabrication of an untethered soft robot by incorporating power systems, actuators, and a soft microfluidic chip into a single device (FIG. 1.6c).¹⁵³ In a multi-material embedded 3D printing method, termed “Emb3d printing,” a silicone formulation is cast into a mould to polymerize slowly at room temperature. Prior to this viscous matrix curing, a DIW printhead extrudes pockets of catalyst and connected microfluidic pathways of fuel. After the silicone body cures, a previously implanted microfluidic controller can then direct the transport of hydrogen peroxide where it is catalytically decomposed into hydrogen and oxygen. These gases pressurize the internal channels which can be exploited to selectively operate parts of the printed device. This approach has been applied to engineer a multi-material “Octobot”, which can pneumatically raise its individual tentacles.¹⁵³ A different approach employs the continuous deposition of a material during device operation. For example, a robot with an on-board FDM printer, which deposits polylactic acid, selectively grows and pushes its limbs (FIG. 1.6d).¹⁵⁴ The additional integration of humidity, temperature, chemical, Hall Effect, and touch sensors on the tip of the limb enables tropism and growth in response to an environmental stimulus; thereby, the robot can spatially and temporarily determine material deposition. Applying this technique and inspired by how plant roots make their way through soil,

a soft robot has been developed, which can penetrate soil and climb against gravity to

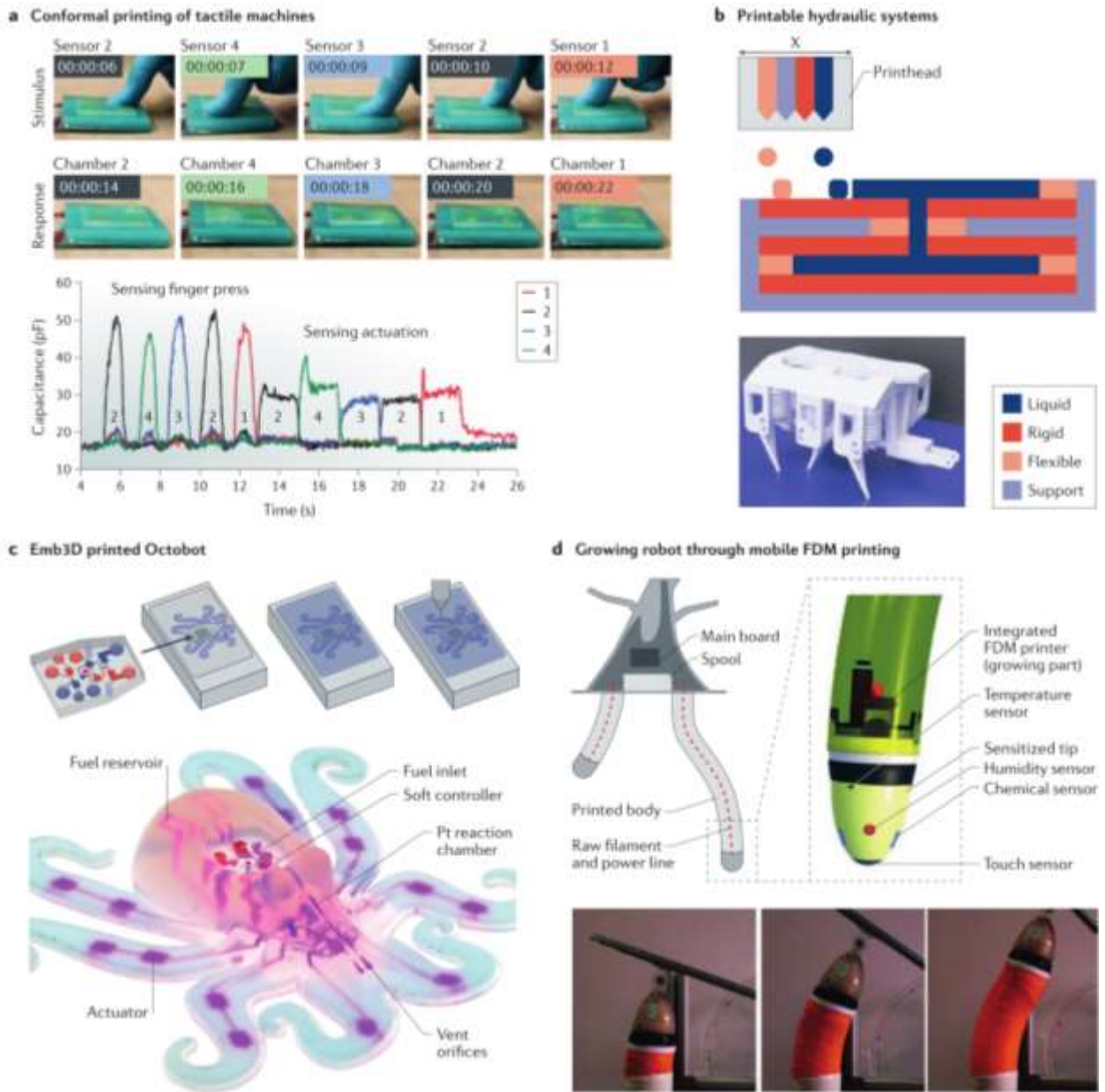


Figure 1.6: Integrated soft robotic systems. a) Conformal direct ink writing (DIW) of silicone and elastomers onto fluidic elastomer actuators can be used to fabricate tactile machines that detect both a time resolved sequence of external presses onto sensors above specific chamber locations (2,4,3,1) and re-played patterns when actuated. (Reproduced from Ref. 141) b) Integrated hydraulic pathways and fluids within a multi-material bellows actuator can be created by inkjet printing of multiple inks (represented by different colors) from the print head. (Reproduced from Ref. 94) c) Adapted from Ref. 153, Multi-material, embedded 3D printing (Emb3D) combines soft lithography and DIW to incorporate catalytic chambers, connected fuel pathways and an attached soft microcontroller within a viscous silicone pre-polymer, curing in a mould. The soft controller allows fuel to flow from reservoirs through inlets and into platinum catalysed reaction chambers where the fuel decomposes into gas. Prior to venting through exposed orifices, these gases pressurize actuators to raise individual tentacles of the “Octobot.” d) Plant-inspired tropic robots use multiple tip sensors and a mobile fused deposition modelling (FDM) printer to sense their surroundings and selectively grow to avoid an obstacle directed by an applied force. (Adapted from Ref. 155)

reach nutrients or an ideal environment. ¹⁵⁵ The field of soft robotics has been and will

continue to be tightly linked to advances in additive manufacturing techniques and materials science. A fully-autonomous soft robot requires a complex assembly of actuators, sensors, controls, and power systems, composed of multiple elastomers, printed at near-micron resolution. Progress in 3D printing technologies will allow for the direct printing of soft robots with indistinguishable functional components; for example, embodied energy wherein portions of the robot skeleton can decompose to release energy on-demand, serving simultaneously as structural elements and power systems. Gradients of printed soft and hard components at the micron scale will, amongst other things, allow robots to operate at resonance for more energy efficient locomotion.

REFERENCES

1. Rus, D. & Tolley, M. T. Design, fabrication and control of soft robots. *Nature* **521**, 467–475 (2015).
2. Trivedi, D., Rahn, C. D., Kier, W. M. & Walker, I. D. Soft robotics: Biological inspiration, state of the art, and future research. *Appl. Bionics Biomech.* **5**, 99–117 (2008).
3. Polygerinos, P., Wang, Z., Galloway, K. C., Wood, R. J. & Walsh, C. J. Soft robotic glove for combined assistance and at-home rehabilitation. *Rob. Auton. Syst.* **73**, 135–143 (2015).
4. Shepherd, R. F. *et al.* Multigait soft robot. *Proc. Natl. Acad. Sci. USA* **108**, 20400–20403 (2011).
5. Rosset, S. & Shea, H. R. Flexible and stretchable electrodes for dielectric elastomer actuators. *Appl. Phys. A* **110**, 281–307 (2012).
6. Palleau, E., Morales, D., Dickey, M. D. & Velev, O. D. Reversible patterning and actuation of hydrogels by electrically assisted ionoprinting. *Nat. Commun.* **4**, 2257 (2013).
7. Schumacher, C. M., Loepfe, M., Fuhrer, R., Grass, R. N. & Stark, W. J. 3D printed lost-wax casted soft silicone monoblocks enable heart-inspired pumping by internal combustion. *RSC Adv.* **4**, 16039 (2014).
8. Katzschmann, R. K., Marchese, A. D. & Rus, D. Hydraulic autonomous soft robotic fish for 3D Swimming. *Intell. Robot. Syst. (IROS), 2011 IEEE/RSJ Int. Conf.* (2014).
9. Ilievski, F., Mazzeo, A. D., Shepherd, R. F., Chen, X. & Whitesides, G. M. Soft robotics for chemists. *Angew. Chem. - Int. Ed.* **50**, 1890–1895 (2011).
10. Zhao H., Li Y., Elsamadisi A., S. R. Scalable manufacturing of high force wearable soft actuators. *Extrem. Mech. Lett.* **3**, 89-104 (2015).
11. Mac Murray, B. C. *et al.* Poroelastic Foams for Simple Fabrication of Complex Soft Robots. *Adv. Mater.* **27**, 6334–6340 (2015).

12. Morrow, J., Hemleben, S. & Menguc, Y. Directly fabricating soft robotic actuators with an open-source 3-D Printer. *IEEE Robot. Autom. Lett.* **2**, 277–281 (2016).
13. Peele, B. N., Wallin, T. J., Zhao, H. & Shepherd, R. F. 3D printing antagonistic systems of artificial muscle using projection stereolithography. *Bioinspir. Biomim.* **10**, 55003 (2015).
14. Kim, S., Laschi, C. & Trimmer, B. Soft robotics: A bioinspired evolution in robotics. *Trends Biotechnol.* **31**, 287–294 (2013).
15. Laschi, C., Mazzolai, B., Mattoli, V., Cianchetti, M. & Dario, P. Design of a biomimetic robotic octopus arm. *Bioinspir. Biomim.* **4**, 15006 (2009).
16. Raibert, M. *BigDog, the rough-terrain quadruped robot*. *IFAC Proceedings Volumes (IFAC-PapersOnline)* **17**, (IFAC, 2008).
17. Grimes, J. & Hurst, J. The design of atrias 1.0 a unique monopod, hopping robot. *15th Int. Conf. Climbing Walk. Robot. Support Technol. Mob. Mach. CLAWAR 2012* 548–554 (2012).
18. Seok, S. *et al.* Meshworm: A peristaltic soft robot with antagonistic nickel titanium coil actuators. *IEEE/ASME Trans. Mechatronics* **18**, 1485–1497 (2013).
19. Laschi, C. *et al.* Soft Robot Arm Inspired by the Octopus. *Adv. Robot.* **26**, 709–727 (2012).
20. Morin, S. *a et al.* Camouflage and display for soft machines. *Science* **337**, 828–32 (2012).
21. Pikul, A. J. H. *et al.* Stretchable surfaces with programmable 3-D texture morphing for synthetic camouflaging skins. *Science* **358**, 210–214 (2017)
22. Norman, M. D., Finn, J. & Tregenza, T. Dynamic mimicry in an Indo-Malayan octopus. *Proc. R. Soc. B Biol. Sci.* **268**, 1755–1758 (2001).
23. Walker, I. D. *et al.* Continuum robot arms inspired by cephalopods. *Proc. SPIE* **5804**, 303 (2005).
24. Onal, C. D. & Rus, D. Autonomous undulatory serpentine locomotion utilizing body dynamics of a fluidic soft robot. *Bioinspir. Biomim.* **8**, 26003 (2013).

25. Keplinger, C., Li, T., Baumgartner, R., Suo, Z. & Bauer, S. Harnessing snap-through instability in soft dielectrics to achieve giant voltage-triggered deformation. *Soft Matter* **8**, 285–288 (2012).
26. Follador, M., Cianchetti, M. & Laschi, C. Development of the functional unit of a completely soft octopus-like robotic arm. *Proc. IEEE RAS EMBS Int. Conf. Biomed. Robot. Biomechatronics* 640–645 (2012).
27. Lessing, J., Morin, S. A., Keplinger, C., Tayi, A. S. & Whitesides, G. M. Stretchable conductive composites based on metal wools for use as electrical vias in soft devices. *Adv. Funct. Mater.* **25**, 1418–1425 (2015).
28. Magdassi, S. in *The Chemistry of Inkjet inks.* (Magdassi, S. ed.) 19-43 (World Scientific Publishing Co. Pte. Ltd., 2010).
29. Guo, Y., Ji, Z., Zhang, Y., Wang, X. & Zhou, F. Solvent-free and photocurable polyimide inks for 3D printing. *J. Mater. Chem. A* **5**, 16307–16314 (2017).
30. Compton, B. G. & Lewis, J. A. 3D-printing of lightweight cellular composites. *Adv. Mater.* **26**, 5930–5935 (2014).
31. Shemelya, C. *et al.* 3D Printed Capacitive Sensors. *2013 Ieee Sensors* 1–4 (2013).
32. Leigh, S. J., Bradley, R. J., Purssell, C. P., Billson, D. R. & Hutchins, D. A. A Simple, Low-Cost Conductive Composite Material for 3D Printing of Electronic Sensors. *PLoS One* **7**, 1–6 (2012).
33. Engels, H. W. *et al.* Polyurethanes: Versatile materials and sustainable problem solvers for today’s challenges. *Angew. Chem. Int. Ed.* **52**, 9422–9441 (2013).
34. Mark, J. E. Overview of Siloxane Polymers. 1–10 (2000).
35. Lee, J. N., Park, C. & Whitesides, G. M. Solvent Compatibility of Poly(dimethylsiloxane)-Based Microfluidic Devices. *Anal. Chem.* **75**, 6544–6554 (2003).
36. Keplinger, C. *et al.* Stretchable, transparent, ionic conductors. *Science* **341**, 984–987 (2013).
37. Marchese, A. D., Katzschmann, R. K. & Rus, D. A Recipe for Soft Fluidic Elastomer Robots. *Soft Robot.* **2**, 7–25 (2015).

38. Cho, K. J. *et al.* Review of manufacturing processes for soft biomimetic robots. *Int. J. Precis. Eng. Manuf.* **10**, 171–181 (2009).
39. Shepherd, R. F., Stokes, A. A., Nunes, R. M. D. & Whitesides, G. M. Soft Machines That are Resistant to Puncture and That Self Seal. *Adv. Mater.* **25**, 6709–6713 (2013).
40. Lin, H.-T., Leisk, G. G. & Trimmer, B. GoQBot: a caterpillar-inspired soft-bodied rolling robot. *Bioinspir. Biomim.* **6**, 26007 (2011).
41. Morin, S. A. *et al.* Using ‘click-e-Bricks’ to Make 3D Elastomeric Structures. *Adv. Mater.* **26**, 5991–5999 (2014).
42. Deimel, R. & Brock, O. A novel type of compliant and underactuated robotic hand for dexterous grasping. *Int. J. Rob. Res.* **35**, 161–185 (2016).
43. Zhao, H., O’Brien, K., Li, S. & Shepherd, R. F. Optoelectronically innervated soft prosthetic hand via stretchable optical waveguides. *Sci. Robot.* **1**, eaai7529 (2016).
44. Mosadegh, B. *et al.* Pneumatic networks for soft robotics that actuate rapidly. *Adv. Funct. Mater.* **24**, 2163–2170 (2014).
45. Wirthl, D. *et al.* Engineering instant tough bonding of hydrogels for soft machines and electronics. *Sci. Adv.* **3**, 1–10 (2017).
46. Yuk, H., Zhang, T., Parada, G. A., Liu, X. & Zhao, X. Skin-inspired hydrogel–elastomer hybrids with robust interfaces and functional microstructures. *Nat. Commun.* **7**, 12028 (2016).
47. Eddings, M. A., Johnson, M. A. & Gale, B. K. Determining the optimal PDMS–PDMS bonding technique for microfluidic devices. *J. Micromechanics Microengineering* **18**, 67001 (2008).
48. Marchese, A. D., Onal, C. D. & Rus, D. Autonomous Soft Robotic Fish Capable of Escape Maneuvers Using Fluidic Elastomer Actuators. *Soft Robot.* **1**, 75–87 (2014).
49. Jiang, Y. & Wang, Q. Highly-stretchable 3D-architected Mechanical Metamaterials. *Sci. Rep.* **6**, 34147 (2016).

50. Loepfe, M., Schumacher, C. M., Burri, C. H. & Stark, W. J. Contrast agent incorporation into silicone enables real-time flow-structure analysis of mammalian vein-inspired soft pumps. *Adv. Funct. Mater.* **25**, 2129–2137 (2015).
51. Loepfe, M., Schumacher, C. M. & Stark, W. J. Design , Performance and Reinforcement of Bearing-Free Soft Silicone Combustion-Driven Pumps. *Ind. Eng. Chem. Res* **53**, 12519–12526 (2014).
52. Therriault, D., Shepherd, R. F., White, S. R. & Lewis, J. a. Fugitive Inks for Direct-Write Assembly of Three-Dimensional Microvascular Networks. *Adv. Mater.* **17**, 395–399 (2005).
53. Valentin, T. M. *et al.* Stereolithographic Printing of Ionically-Crosslinked Alginate Hydrogels for Degradable Biomaterials and Microfluidics. *Lab Chip* **17**, 3474-3488 (2017).
54. Van Meerbeek, I. M. *et al.* Morphing Metal and Elastomer Bicontinuous Foams for Reversible Stiffness, Shape Memory, and Self-Healing Soft Machines. *Adv. Mater.* **28**, 2801–2806 (2016).
55. Argiolas, A. *et al.* Sculpting Soft Machines. *Soft Robot.* **3**, 101–108 (2016).
56. Robertson, M. A. & Paik, J. New soft robots really suck : Vacuum-powered systems empower diverse capabilities. **2**, ean6357 (2017).
57. Yang, W. G. *et al.* Advanced shape memory technology to reshape product design, manufacturing and recycling. *Polymers.* **6**, 2287–2308 (2014).
58. NinjaTek. *NinjaFlex*® 3D Printing Filament: Flexible Polyurethane Material for FDM Printers. (2016). at < <https://ninjatek.com/wp-content/uploads/2016/05/NinjaFlex-TDS.pdf>>
59. Yap, H. K., Ng, H. Y. & Yeow, C.-H. High-Force Soft Printable Pneumatics for Soft Robotic Applications. *Soft Robot.* **3**, 144–158 (2016).
60. Mutlu, R., Alici, G. & Spinks, G. M. 3D printed flexure hinges for soft monolithic prosthetic fingers. *Soft Robot.* **3**, 120–133 (2016).

61. Mohamed, O. A., Masood, S. H. & Bhowmik, J. L. Optimization of fused deposition modeling process parameters: a review of current research and future prospects. *Adv. Manuf.* **3**, 42–53 (2015).
62. Kim, C. J. & Pratt, S. T. Dynamically Controlled Screw-Driven Extrusion. (2016).
63. Lewis, J. A. Direct ink writing of 3D functional materials. *Adv. Funct. Mater.* **16**, 2193–2204 (2006).
64. Barry, R. a. *et al.* Direct-write assembly of 3D hydrogel scaffolds for guided cell growth. *Adv. Mater.* **21**, 2407–2410 (2009).
65. Tibbits, S. 4D printing: Multi-material shape change. *Archit. Des.* **84**, 116–121 (2014).
66. Ebara, M. *et al.* Smart Hydrogels. in *Smart Biomaterials* 9–65 (2014).
67. Bakarich, S. E. *et al.* 3D printing of tough hydrogel composites with spatially varying materials properties. *Addit. Manuf.* **14**, 24–30 (2016).
68. Bakarich, S. E., Gorkin, R. & Spinks, M. Three-Dimensional Printing Fiber Reinforced Hydrogel Composites. (2014).
69. Bakarich, S. E., Gorkin, R., Panhuis, M. in Het & Spinks, G. M. 4D Printing with Mechanically Robust, Thermally Actuating Hydrogels. *Macromol. Rapid Commun.* **36(12)**, 1211-1217 (2015).
70. Sydney Gladman, A., Matsumoto, E. A., Nuzzo, R. G., Mahadevan, L. & Lewis, J. A. Biomimetic 4D printing. *Nat. Mater.* **15**, 413–8 (2016).
71. Yuk, H. *et al.* Hydraulic hydrogel actuators and robots optically and sonically camouflaged in water. *Nat. Commun.* **8**, 14230 (2017).
72. Bakarich, S. E., Panhuis, M. in Het, Beirne, S., Wallace, G. G. & Spinks, G. M. Extrusion printing of ionic–covalent entanglement hydrogels with high toughness. *J. Mater. Chem. B* **1**, 4939 (2013).
73. Sun, J.-Y. *et al.* Highly stretchable and tough hydrogels. *Nature* **489**, 133–6 (2012).

74. Plott, J. & Shih, A. The extrusion-based additive manufacturing of moisture-cured silicone elastomer with minimal void for pneumatic actuators. *Addit. Manuf.* **17**, 1–14 (2017).
75. Miriyev, A., Stack, K. & Lipson, H. Soft material for soft actuators. *Nat. Commun.* **8**, 596 (2017).
76. Truby, R. L. & Lewis, J. A. Printing soft matter in three dimensions. *Nature* **540**, 371–378 (2016).
77. Gul, J. Z., Yang, B.-S., Yang, Y. J., Chang, D. E. & Choi, K. H. In situ UV curable 3D printing of multi-material tri-legged soft bot with spider mimicked multi-step forward dynamic gait. *Smart Mater. Struct.* **25**, 115009 (2016).
78. Hinton, T. J., Hudson, A., Pusch, K., Lee, A. & Feinberg, A. W. 3D Printing PDMS elastomer in a hydrophilic support bath via freeform reversible embedding. *ACS Biomater. Sci. Eng.* **2**, 1781–1786 (2016).
79. Hinton, T. J. *et al.* Three-dimensional printing of complex biological structures by freeform reversible embedding of suspended hydrogels. *Sci. Adv.* **1**, e1500758 (2015).
80. Coward, T., Jindal, S., Waters, M. & Smay, J. 3D printing of facial prostheses. Patent WO107333. (2015).
81. Rost, A. & Schaedle, S. The SLS-generated soft robotic hand - An integrated approach using additive manufacturing and reinforcement learning. *Proc. - 2013 12th Int. Conf. Mach. Learn. Appl. ICMLA 2013* **1**, 215–220 (2013).
82. Materialise. *Laser Sintering Material Properties*. 8-9 (2013). at https://akcelerator-internest.pl/site_media/user-media/datasheets_laser_sintering.pdf
83. Scharff, R. B. N. *et al.* Towards Behavior Design of a 3D-Printed Soft Robotic Hand. in *Soft Robotics: Trends, Applications and Challenges* **17**, 23–29 (2017).
84. Jäntschi, M. *et al.* Anthrob – A Printed Anthropomimetic Robot. *13th IEEE-RAS International Conference on Humanoid Robots (Humanoids)*, Atlanta, GA, 342-347. (2013)
85. Mazzoli, A. Selective laser sintering in biomedical engineering. *Med. Biol. Eng. Comput.* **51**, 245–256 (2013).

86. Yuan, C., Wang, T., Dunn, M. L. & Qi, H. J. 3D Printed Active Origami with Complicated Folding Patterns. *Int. J. of Precis. Eng. and Manuf.-Green Tech.* **4**, 281–289 (2017).
87. Yu, K., Dunn, M. L. & Qi, H. J. Digital manufacture of shape changing components. *Extrem. Mech. Lett.* **4**, 9–17 (2015).
88. Wu, J. *et al.* Multi-shape active composites by 3D printing of digital shape memory polymers. *Sci Rep.* **6**, 31110 (2016).
89. Mao, Y. *et al.* Sequential Self-Folding Structures by 3D Printed Digital Shape Memory Polymers. *Sci. Rep.* **5**, 13616 (2015).
90. Umedachi, T., Vikas, V. & Trimmer, B. A. *Softworms* : the design and control of non-pneumatic, 3D-printed, deformable robots. *Bioinspir. Biomim.* **11**, 25001 (2016).
91. Umedachi, T., Vikas, V. & Trimmer, B. A. Highly deformable 3-D printed soft robot generating inching and crawling locomotions with variable friction legs. *IEEE Int. Conf. Intell. Robot. Syst.* 4590–4595 (2013).
92. Phamduy, P. *et al.* Design and characterization of a miniature free-swimming robotic fish based on multi-material 3D printing. *Int. J. Intell. Robot. Appl.* **1**, 209–223 (2017).
93. Drotman, D., Jadhav, S., Karimi, M., deZonia, P. & Tolley, M. T. 3D printed soft actuators for a legged robot capable of navigating unstructured terrain. *2017 IEEE Int. Conf. Robot. Autom.* 5532–5538 (2017).
94. Maccurdy, R., Katschmann, R., Kim, Y. & Rus, D. Printable hydraulics: A method for fabricating robots by 3D co-printing solids and liquids. *Proc. - IEEE Int. Conf. Robot. Autom.* **2016–June**, 3878–3885 (2016).
95. Stratasys. *PolyJet Materials Data Sheet.* (2015). at <[http://usglobalimages.stratasys.com/Main/Secure/Material Specs MS/PolyJet-Material-Specs/Digital_Materials_Datasheet.pdf?v=635581278098921962](http://usglobalimages.stratasys.com/Main/Secure/Material%20Specs%20MS/PolyJet-Material-Specs/Digital_Materials_Datasheet.pdf?v=635581278098921962)>
96. Bartlett, N. W. *et al.* A 3-D printed, functionalised graded soft robot powered by combustion. *Science* **349**, 161–165 (2015).

97. Derby, B. Inkjet Printing of Functional and Structural Materials: Fluid Property Requirements, Feature Stability, and Resolution. *Annu. Rev. Mater. Res.* **40**, 395–414 (2010).
98. Park, S. H., Yang, D. Y. & Lee, K. S. Two-photon stereolithography for realizing ultraprecise three-dimensional nano/microdevices. *Laser Photonics Rev.* **3**, 1–11 (2009).
99. Beluze, L., Bertsch, A. & Renaud, P. Microstereolithography: a new process to build complex 3D objects. *Proc. Soc. Photo- Opt. Instrum. Eng.* **1**, 808–817 (1999).
100. Yayue Pan, Chi Zhou & Yong Chen. Rapid manufacturing in minutes: The development of a mask projection stereolithography process for high-speed fabrication. *Proc. ASME 2012 Int. Manuf. Sci. Eng. Conf.* 1–10 (2012).
101. Patel, D. K. *et al.* Highly Stretchable and UV Curable Elastomers for Digital Light Processing Based 3D Printing. *Adv. Mater.* **29**. 1606000 (2017).
102. Tumbleston, J. R. *et al.* Continuous liquid interface production of 3D objects. *Science* **347**, 1349-1352 (2015).
103. Shusteff, M. *et al.* One-step volumetric additive manufacturing of complex polymer structures. *Sci. Adv.* **3**, 1–7 (2017).
104. Melchels, F. P. W., Feijen, J. & Grijpma, D. W. A review on stereolithography and its applications in biomedical engineering. *Biomaterials* **31**, 6121–6130 (2010).
105. Kang, H. W., Lee, I. H. & Cho, D. W. Development of a micro-bellows actuator using micro-stereolithography technology. *Microelectron. Eng.* **83**, 1201–1204 (2006).
106. Bartolo, P. J. *Stereolithography: Materials, Processes and Applications.* (2011).
107. Eckel, Z. C. *et al.* Additive manufacturing of polymer-derived ceramics. *Science.* **351**, 58–62 (2016).
108. Carbon3D. *CarbonResin EPU 40.* (2016). Doc #103208 Rev. B (2016). at <<https://www.saberex.com/sbr/wp-content/uploads/103208-b-epu-40-tds.pdf>>

109. Zarek, M. *et al.* 3D Printing of Shape Memory Polymers for Flexible Electronic Devices. *Adv. Mater.* **28**, 4449-4454 (2016).
110. Odent, J. *et al.* Highly Elastic, Transparent, and Conductive 3D-Printed Ionic Composite Hydrogels. *Adv. Func. Mater.* **27**, 1701807 (2017).
111. Pang, T. H. Stereolithography Epoxy Resins SL 5170 and SL 5180: Accuracy, Dimensional Stability, and Mechanical Properties. *Time* 204–224 (1994).
112. Prasad, B. Book Reviews : Stereolithography and Other RP&M Technologies from Rapid Prototyping to Rapid Tooling, Edited by Paul F. Jacobs, Ph.D.; Jointly published by Society of Manufacturing Engineers in cooperation with the Rapid Prototyping Association of SME, De. *Concurr. Eng.* **4**, 199–199 (1996).
113. Velankar, S., Pazos, J. & Cooper, S. L. High-performance UV-curable urethane acrylates via deblocking chemistry. *J. Appl. Polym. Sci.* **62**, 1361–1376 (1996).
114. Sinh, L. H. *et al.* Novel photo-curable polyurethane resin for stereolithography. *RSC Adv.* **6**, 50706–50709 (2016).
115. Hoyle, C. E. & Bowman, C. N. Thiol-ene click chemistry. *Angew. Chem. Int. Ed.* **49**, 1540–1573 (2010).
116. Wallin, T. J. *et al.* Click chemistry stereolithography for soft robots that self-heal. *J. Mater. Chem. B* **5**, 6249-6255 (2017).
117. Chan, V. *et al.* Multi-material bio-fabrication of hydrogel cantilevers and actuators with stereolithography. *Lab Chip* **12**, 88-98 (2012).
118. Choi, J. W., Kim, H. C. & Wicker, R. Multi-material stereolithography. *J. Mater. Process. Technol.* **211**, 318–328 (2011).
119. Ge, Q. *et al.* Multimaterial 4D printing with tailorable shape memory polymers. *Sci. Rep.* **6**, 31110 (2016).
120. Adams, J. J. *et al.* Conformal printing of electrically small antennas on three-dimensional surfaces. *Adv. Mater.* **23**, 1335–1340 (2011).
121. Guo, S. Z., Qiu, K., Meng, F., Park, S. H. & McAlpine, M. C. 3D Printed stretchable tactile sensors. *Adv. Mater.* **29**, 1–8 (2017).

122. Lorang, D. J. *et al.* Photocurable liquid core-fugitive shell printing of optical waveguides. *Adv. Mater.* **23**, 5055–5058 (2011).
123. Kokkinis, D., Schaffner, M. & Studart, A. R. Multimaterial magnetically assisted 3D printing of composite materials. *Nat. Commun.* **6**, 8643 (2015).
124. Li, S., Zhao, H. & Shepherd, R. F. Flexible and stretchable sensors for fluidic elastomer actuated soft robots. *MRS Bull.* **42**, 138–142 (2017).
125. Larson, C., Spjut, J., Knepper, R. & Shepherd, R. OrbTouch: recognizing human touch in deformable interfaces with deep neural networks. (2017). at <<http://https://arxiv.org/abs/1706.02542>>
126. Rosset, S. & Shea, H. R. Flexible and stretchable electrodes for dielectric elastomer actuators. *Appl. Phys. A Mater. Sci. Process.* **110**, 281–307 (2013).
127. Niklaus, M. & Shea, H. R. Electrical conductivity and Young's modulus of flexible nanocomposites made by metal-ion implantation of polydimethylsiloxane: The relationship between nanostructure and macroscopic properties. *Acta Mater.* **59**, 830–840 (2011).
128. Chodák, I., Omastová, M. and Pionteck, Relation between electrical and mechanical properties of conducting polymer composites of. 1903–1906 (2001).
129. Kim, D.-H. *et al.* Epidermal Electronics. *Science* **333**, 838–843 (2011).
130. Sekitani, T. *et al.* A rubberlike stretchable active matrix using elastic conductors. *Science* **321**, 1468–1473 (2008).
131. Kim, H., Sim, K., Thukral, A. & Yu, C. Rubbery electronics and sensors from intrinsically stretchable elastomeric composites of semiconductors and conductors. *Sci. Adv.* **3**, e1701114 (2017).
132. Matsuhisa, N. *et al.* Printable elastic conductors by in situ formation of silver nanoparticles from silver flakes. *Nat. Mater.* **16**, 834–840 (2017).
133. Muth, J. T. *et al.* Embedded 3D printing of strain sensors within highly stretchable elastomers. *Adv. Mater.* **26**, 6307–6312 (2014).
134. Ladd, C., So, J. H., Muth, J. & Dickey, M. D. 3D printing of free standing liquid metal microstructures. *Adv. Mater.* **25**, 5081–5085 (2013).

135. Boley, J. W., White, E. L., Chiu, G. T. C. & Kramer, R. K. Direct writing of gallium-indium alloy for stretchable electronics. *Adv. Funct. Mater.* **24**, 3501–3507 (2014).
136. Tabatabai, A., Fassler, A., Usiak, C. & Majidi, C. Liquid-phase gallium-indium alloy electronics with microcontact printing. *Langmuir* **29**, 6194–6200 (2013).
137. Sarwar, M. S. *et al.* Bend, stretch, and touch: Locating a finger on an actively deformed transparent sensor array. *Sci. Adv.* **3**, e1602200 (2017).
138. Mannsfeld, S. C. B. *et al.* Highly sensitive flexible pressure sensors with microstructured rubber dielectric layers. *Nat. Mater.* **9**, 859–864 (2010).
139. White, E. L., Yuen, M. C., Case, J. C. & Kramer, R. K. Low-cost, facile, and scalable manufacturing of capacitive sensors for soft Systems. *Adv. Mater. Technol.* **2**, 1700072 (2017).
140. Li, S., Peele, B. N., Larson, C. M., Zhao, H. & Shepherd, R. F. A Stretchable Multicolor Display and Touch Interface Using Photopatterning and Transfer Printing. *Adv. Mater.* **28**, 9770–9775 (2016).
141. Robinson, S. S. *et al.* Integrated soft sensors and elastomeric actuators for tactile machines with kinesthetic sense. *Extrem. Mech. Lett.* **5**, 47–53 (2015).
142. Rossiter, J., Walters, P. & Stoimenov, B. Printing 3D dielectric elastomer actuators for soft robotics. *Proc. SPIE* **7287**, 1–10 (2009).
143. Frutiger, A. *et al.* Capacitive soft strain sensors via multicore-shell fiber printing. *Adv. Mater.* **27**, 2440–2446 (2015).
144. Luo, M. *et al.* Slithering towards autonomy: a self-contained soft robotic snake platform with integrated curvature sensing. *Bioinspir. Biomim.* **10**, 55001 (2015).
145. Ozel, S. *et al.* A composite soft bending actuation module with integrated curvature sensing. *Proc. IEEE Int. Conf. Robot. Autom.* **2016–June**, 4963–4968 (2016).
146. Tao, W. *et al.* Bioinspired design and fabrication principles of reliable fluidic soft actuation modules. *2015 IEEE Int. Conf. Robot. Biomimetics, IEEE-ROBIO 2015* 2169–2174 (2015).

147. Wang, H. *et al.* A Low-cost Soft Tactile Sensing Array Using 3D Hall Sensors. *Procedia Eng.* **168**, 650–653 (2016).
148. Wang, H. *et al.* Design methodology for magnetic field-based soft tri-axis tactile sensors. *Sensors (Switzerland)* **16**, (2016).
149. Slyper, R. & Hodgins, J. Prototyping robot appearance, movement, and interactions using flexible 3D printing and air pressure sensors. *Proc. - IEEE Int. Work. Robot Hum. Interact. Commun.* 6–11 (2012).
150. Samusjew, A. *et al.* Inkjet printing of soft, stretchable optical waveguides through the photopolymerization of high-profile linear patterns. *ACS Appl. Mater. Interfaces* **9**, 4941–4947 (2017).
151. Yin, M. J. *et al.* Rapid 3D patterning of poly(acrylic acid) ionic hydrogel for miniature pH sensors. *Adv. Mater.* **28**, 1394–1399 (2016).
152. Shepherd, R. Highly stretchable electroluminescent skin for optical signaling and tactile sensing. *Science* **351**, 1071–1074 (2016).
153. Wehner, M. *et al.* An integrated design and fabrication strategy for entirely soft, autonomous robots. *Nature* **536**, 451–455 (2016).
154. Sadeghi, A., Tonazzini, A., Popova, L. & Mazzolai, B. A novel growing device inspired by plant root soil penetration behaviors. *PLoS ONE* **9**, e90139 (2014).
155. Sadeghi, A., Mondini, A. & Mazzolai, B. Toward self-growing soft robots inspired by plant roots and based on additive manufacturing technologies. *Soft Robot.* **4**, 211-223 (2017).

Portions of this chapter are re-used from Nature Reviews Materials.

CHAPTER 2

HIGHLY ELASTIC, TRANSPARENT, AND, CONDUCTIVE 3D-PRINTED IONIC COMPOSITE HYDROGELS

2.1 Abstract

Despite extensive progress to engineer hydrogels for a broad range of technologies, practical applications have remained elusive due to their, until recently, poor mechanical properties and lack of fabrication approaches, which constrain active structures to simple geometries. We herein demonstrate a family of ionic composite hydrogels with excellent mechanical properties that can be rapidly 3D-printed at high resolution using commercial stereolithography technology. The new materials design leverages the dynamic and reversible nature of ionic interactions present in the system with the reinforcement ability of nanoparticles. The composite hydrogels combine within a single platform tunable stiffness, toughness, extensibility, and resiliency behavior not reported previously in other engineered hydrogels. In addition to their excellent mechanical performance, the ionic composites exhibit fast gelling under near-UV exposure, remarkable conductivity, and fast osmotically-driven actuation. The design of such ionic composites, which combine a range of tunable properties and can be readily 3D-printed into complex architectures provides opportunities for a variety of practical applications such as artificial tissue, soft actuators, compliant conductors and sensors for soft robotics.

2.2 Introduction

Hydrogels are three-dimensional polymeric networks swellable in water. They hold exceptional promise in a wide array of areas including soft robotics, drug delivery, and regenerative medicine^[1]. Despite recent advances, their poor mechanical performance (especially their brittleness) severely limited the scope of practical applications^[2]. Recent successes in toughening hydrogels included dual crosslinked hydrogels and nanoparticle composites^[3]. Good mechanical performance has been shown due to the

range of bonding strength present in double-networks: strong covalent bonds, which serve as permanent crosslinks and preserve the integrity of the material, and weak electrostatic interactions, which behave as dynamic and sacrificial bonds to dissipate energy^[4]. Inspired by the double-network concept, Sun *et al.*^[5] designed hydrogels consisting of two interpenetrating (ionically and covalently) crosslinked networks, which can sustain large deformations and blunt crack growth after localized damage. In addition, composite hydrogels were introduced to generate not only structural diversity but also multi-functional and stimuli-responsive properties^[6].

Composite hydrogels with nanoparticles hold great promise for providing superior functionality and making them ideal for smart materials^[3c]. For instance, Appel *et al.*^[7] developed self-assembled hydrogels with shear-thinning and self-healing properties based on rationally engineered polymer-nanoparticle reversible interactions. Embedding various conducting components into aqueous gels imparts electrical conductivity, thus offering an array of features that facilitate charge transport^[8]. As a result, conducting hydrogels are potential candidates for a broad range of applications from energy storage devices to bioelectronics and implantable electrodes^[9]. Furthermore, hydrogels swollen with electrolytes have been used in some cases as stretchable ionic conductors in dielectric actuators and soft stress-sensors^[10].

Despite this remarkable progress and with mechanical properties comparable to biological tissues, applications of such engineered hydrogels are still limited in terms of accessible chemistry and the methods available for fabrication, with the former putting constraints on formulation and the latter restricting the active structures to simple geometries^[11]. Importantly, and unlike many natural tissues, the reported double network hydrogels lack resilience and show hysteresis upon repeated loadings^[5a]. Additionally, conventional hydrogel chemistries exhibit slow diffusive swelling rates, *i.e.* many objects with cm scale dimensions require days to reach full actuation^[12]. Biological systems, however, rely on complex, hierarchical networks that take advantage of high surface to volume ratios for efficient mass transport to supply cells with oxygen and nutrients. To fully exploit engineered hydrogels we must,

therefore, be able to rapidly fabricate complex structures with high resolution features^[13].

Among additive manufacturing technologies, stereolithography (SLA) offers reduced complexity, scalability, and rapid fabrication speeds^[13b, 14]. Based on spatially controlled layer-by-layer solidification of a liquid resin by photo-polymerization, SLA affords high quality surface finish, dimensional accuracy, and a growing library of compatible materials that enable the fabrication of large-scale 3D objects^[14-15]. Acrylated monomers are frequently used in SLA formulations due to their facile photo-initiated free radical polymerization, as well as high solubility in many common solvents. For example, Tumbleston *et al.*^[16] recently used acrylate photo-chemistry in Continuous Liquid Interface Production (CLIP), a modified version of SLA that can print ~10 cm scale objects in minutes instead of hours. Most stereolithography formulations are based on chain-growth polymerization from concentrated solutions of low molecular weight species that typically form dense, brittle networks^[15b].

In this manuscript, we describe a new highly stretchable (up to 425 %), tough (up to 53.5 kJ·m⁻³), and resilient (up to 97 % strain energy recovered at 100 % strain) ionically conductive (up to 2.9 S·m⁻¹ at $f = 1$ MHz) hydrogel that can be rapidly 3D-printed at high resolution using an aqueous riboflavin-triethanolamine photo-chemistry. The new materials design leverages the dynamic and reversible nature of ionic interactions between ammonium-containing polyacrylamide hydrogels and surface-modified sulfonated silica nanoparticles. The hybrid nature allows for their properties to be readily engineered by varying the amount of nanoparticles (from 0 to 10 wt%) and ammonium groups (from 0 to 50 mol%). The synthesized composite hydrogels exhibit tunable stiffness, toughness, extensibility, and resiliency not reported previously. In addition to their exceptional mechanical properties, the ionic hydrogels exhibit fast photo-polymerization (which allows for rapid 3D printing), high ionic conductivity, and fast actuation using solvent swelling. Hydrogels that are, simultaneously, tough and resilient are an important development. Fabrication of such hydrogels via additive manufacturing into complex geometries with high-resolution

features represents another milestone, which, in our opinion paves the way for their use in advanced engineering applications including soft robotics.

2.3 Results and Discussion

Design of 3D-printed ionic composite hydrogels

In order to permit fast fabrication speeds and high-resolution features, stereolithography (SLA) resins must rapidly photo-polymerize to form solid structures from a low viscosity pre-polymer solution. Acrylamide, commonly used in conjunction with small amounts of *N,N'*-methylenebisacrylamide crosslinker to form hydrogels for electrophoresis, is a model acrylate system and a logical building block in several formulations. Riboflavin, an aqueous type II photo-initiator, and triethanolamine, a co-initiator, enables free radical photo-polymerization of the acrylate groups in acrylamide (AA), [2-(Acryloyloxy)ethyl]trimethylammonium chloride (AETA), and *N,N'*-methylenebisacrylamide (MBA) crosslinker with near-UV SLA systems. The key to our formulation is the addition of ionic, sulfonate modified silica nanoparticles ($\text{SiO}_2\text{-SO}_3^-\text{Na}^+$) to the pre-polymer acrylate solution. The sulfonate groups on the nanoparticles interact electrostatically with the quaternary ammonium groups ($\text{R-N}(\text{CH}_3)_3^+\text{Cl}^-$) on the polymer network and endow the system with dynamic, reversible interactions, in addition to the mechanical reinforcement afforded by the presence of the nanoparticles. Figure 2.1a is a schematic illustration where the nanoparticles are distributed so that they maximize the Coulombic interactions between the cationic ammonium side groups along the hydrogel backbone with the anionic sulfonate groups on the nanoparticles.

We used an EmberTM (Autodesk, Inc.) digital mask projection stereolithography printer to fabricate devices using our photo-polymerizable nanoparticle suspensions. This printer employs a bottom-up process, where the photo-pattern is projected through a transparent, oxygen permeable window at the base of a vat of liquid resin (Figure 2.1b); the printer uses a 405 nm LED projector, which is absorbed by the Riboflavin initiator. In between photo-exposures, the build stage shears the printed object off the window prior to the object moving up one-layer height. Using this

technique, we printed a series of complex 3D hydrogel structures including the Eiffel Tower (Figure 2.1c).

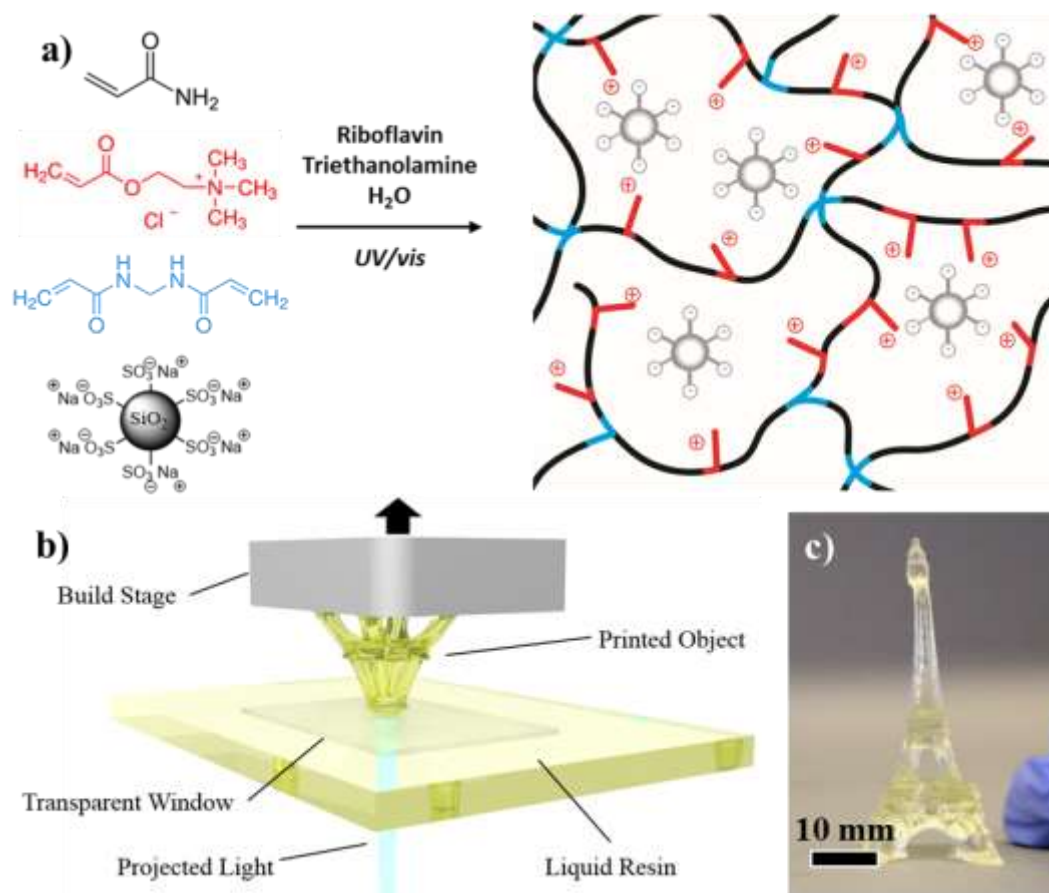


Figure 2.1: a) Chemistry of ionic composite hydrogels via photo-polymerization of AA and AETA in the presence of sulfonate modified SiO₂ (18 nm) using riboflavin:triethanolamine photo-initiator and MBA crosslinker; b) Fast bottom-up fabrication of high resolutions features from the chemistry above using stereolithography;c) 3D printed Eiffel Tower

Photo-polymerization and fast gelling

Photo-rheology is a useful tool in the determination of a resin's SLA compatibility by permitting in-situ monitoring of the photo-polymerization as a function of light illumination. Steady state oscillatory shear experiments at conditions similar to those experienced in the printing process demonstrate that all of the investigated blends initially exhibit sufficiently low viscosities ($\eta_{initial} < 5 \text{ Pa}\cdot\text{s}$), which enable rapid recoating of the build layer (see Table 2.1). Under illumination, the viscosity rapidly increases over many orders of magnitude as the liquid begins to gel (Figure 2.2a). The

loss modulus (G'') is initially greater than storage modulus (G') for all compositions and the liquid-like viscous behavior of the pre-polymer dominates. As the photopolymerization proceeds beyond the gel point, G' becomes greater than G'' , *i.e.* the material becomes more solid-like and the elastic response dominates (Figure 2.2b). We estimated the gel point from our rheological data as the point where the storage modulus crosses above the loss modulus.

Neat AA displays slow polymerization kinetics as the crossover point occurs at both small moduli values ($G' \sim 0.6$ Pa) and at longer near-UV exposures ($t = 12$ s of $E_e = 7.6$ mW·cm⁻², $\lambda = 400$ -500 nm light). On the other hand, pure AETA polymerizes much faster, with a crossover occurring at $G' \sim 2.6$ Pa after just 7 s under illumination. When combined, the new formulation exhibits an intermediate behavior consistent with their statistical copolymerization (*i.e.* crossover at $G' = G'' \sim 4.6$ Pa and $t = 11$ s with 25 mol% AETA). Further, adding sulfonated SiO₂ nanoparticles leads to a faster, more pronounced ($G' \gg G''$) gelation (*i.e.* crossover at $G' = G'' \sim 6.5$ Pa and $t = 9$ s with 3 wt% SiO₂) due to the creation of physical entanglements within the composite hydrogel, consistent with previously reported work by Carlsson *et al.*^[17] (see Figure 2.2 and Figure 2.6 for all compositions). It is worth noting that AA:silica-based composites seem to require double the photo-exposure than the AETA-modified ones to reach similar moduli independently of the silica content. Based on these results, an illumination energy density of $w_e = 1,672$ mJ·cm⁻² and $3,374$ mJ·cm⁻² (*i.e.* double) respectively for AA-based and AETA-modified hydrogels were applied to ensure similar crosslinking density throughout the study and compare their properties.

Table 1.1: Summary of Ionic Composite Hydrogels Performances.

Composition*	T_g (°C)	η_{initial} (Pa·s)	t_{G'=G''} (s)	t_{η = 1000 Pa.s} (s)	E (Pa)	ε_{ult} (%)	TT (kJ·m⁻³)	σ_{1 MHz} (S·m⁻¹)
AA	186	0.078	11	160	820 ± 90	258 ± 48	1.8 ± 0.9	3.2 10 ⁻³
AA + 25 mol% AETA	111	0.066	11	68	2450 ± 390	325 ± 51	9.2 ± 1.2	1.8
AA + 25 mol% AETA + 1 % SiO ₂	-	0.060	10	59	2930 ± 360	342 ± 80	12.1 ± 4.9	-
AA + 25 mol% AETA + 3 % SiO ₂	-	0.075	9.5	57	3150 ± 260	370 ± 37	13.4 ± 2.8	1.9
AA + 25 mol% AETA + 5 % SiO ₂	-	0.064	6	38	8300 ± 310	320 ± 24	26.7 ± 3.7	-
AA + 25 mol% AETA + 10 % SiO ₂	-	0.087	4	30	21260 ± 430	255 ± 24	42.0 ± 7.0	-
AETA	60	0.027	7	126	6540 ± 40	160 ± 37	5.7 ± 2.4	1.8

* See Table 2.2 for all compositions.

T_g: glass transition temperature ; η: complex viscosity ; t: illumination time ; E: Young's modulus ; ε_{ult}: strain at break ; TT: tensile toughness ; σ: conductivity.

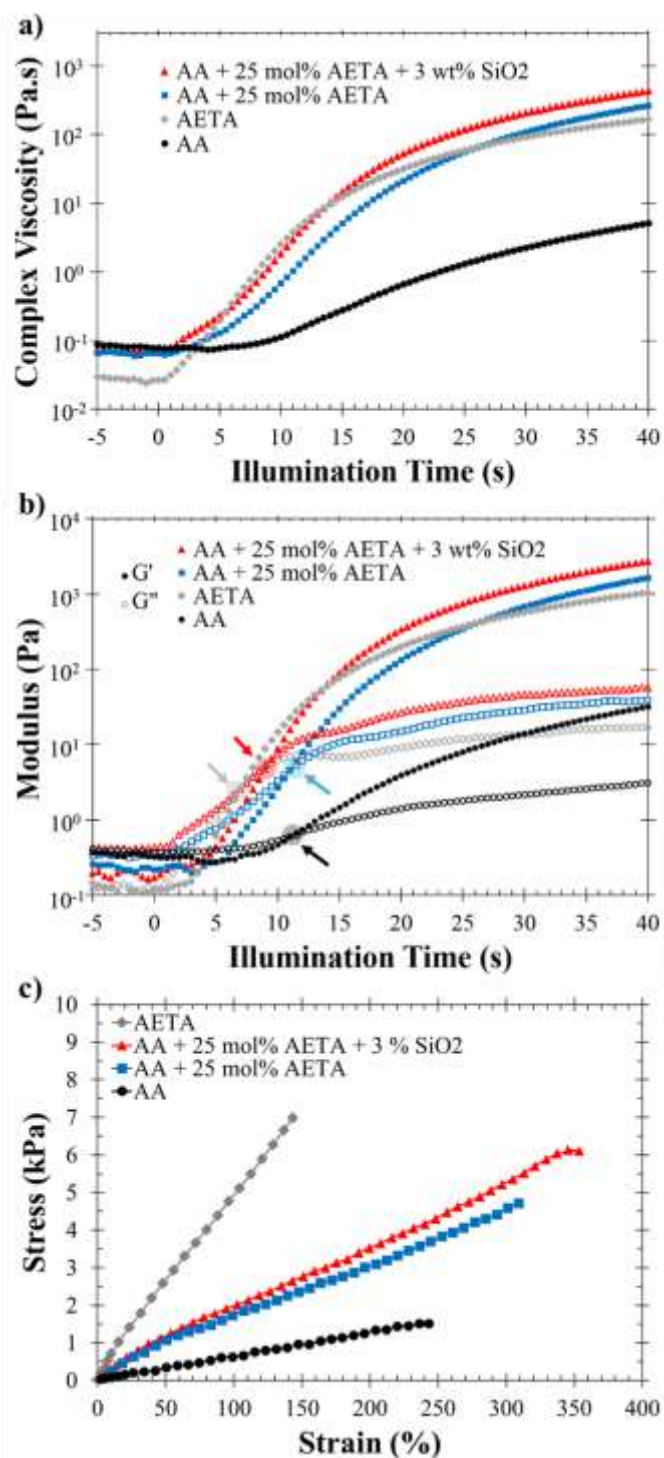


Figure 2.2: Complex viscosity η^* (a) and storage G' and loss G'' modulus (b) with illumination time during photo-polymerization of neat AA, neat AETA and the composite hydrogels (i.e. AA + 25 mol% AETA) containing 0 wt% and 3 wt% of sulfonated SiO₂; c) Typical stress-strain curves of neat AA, neat AETA and the composite hydrogels (i.e. AA + 25 mol% AETA) containing 0 wt% and 3 wt% of sulfonated SiO₂.

Tunable mechanical properties

The new ionic composite hydrogels combine simultaneous improvements in modulus, toughness, and strain at break compared to neat AA and AETA (Table 1 and Table S1 for all compositions). Consistent with conventional composites, the significant increase in tensile modulus, E (from 820 Pa up to 114,500 Pa), measured using a Zwick-Roell Z1010 at a strain rate, $= 10 \text{ mm min}^{-1}$, in AA-based composites (*i.e.* in the absence of ionic interactions) is accompanied by a decrease in ultimate strain, ε_{ult} (from 258 % down to 69 %), upon the addition of silica nanoparticles (Figure 2.7). In contrast, the ionic interactions between the AETA-modified hydrogels and the sulfonated silica lead to composite hydrogels with an improved stiffness (from 820 Pa to 21,260 Pa), toughness (from 1.8 kJ/m³ to 53.5 kJ/m³) and strain to failure (from 258 % to 425 %) profile (Figure 2.2c and Figure 2.7).

Combining AA and AETA within a single formulation leads to an intermediate glass transition temperature (T_g) consistent with the Flory-Fox equation of a statistically random copolymer (see Table 2.1). Thus, one expects the copolymer to show intermediate mechanical performance. As the amount of sulfonated SiO₂ increases, it simultaneously stiffens and toughens the resulting composite hydrogels regardless of the hydrogel composition (Figure 2.7). This result is surprising as increases in modulus are typically accompanied by a decrease in elongation and toughness. The strain at break seems to reach a maximum, $\varepsilon_{ult} \sim 370 \pm 37 \%$ for 25 mol% AETA and $425 \pm 45 \%$ for 50 mol% AETA, at 3 wt% of SiO₂ (Figure 2.7). We attribute the increasing ultimate elongation to the dynamic nature of the ionic interactions between the polymer matrix and the nanoparticles^[18] along with the mobility of the nanoparticles under applied stress^[19], which add an extra mechanism to absorb energy. In addition, the ionic interactions assist with the nanoparticle dispersion to form a well-dispersed composite hydrogel (see Figure 2.8). The latter feature is significant, as challenges with nanoparticle dispersion in the polymer matrix have been a significant obstacle and have limited nanocomposites from reaching their potential.

Elasticity, resilience, and environmental stability

Due to the reversible nature of the ammonium-sulfonate interactions, the new ionic composite hydrogels can recover their initial state after experiencing extensive deformation. We envision the ionic interactions serving as dynamic crosslinks, *i.e.* breaking and reforming so that damage in the network can heal and improve the elongation to failure and, ultimately, the toughness. We observe this property as a linear elastic response upon the time dependent removal of the applied stress. To directly measure the resiliency of the dynamic ionic crosslinks, we performed tensile tests using several loading and unloading cycles (Figure 2.3a).

Neat AA fatigues rapidly during the cyclic tensile test, *i.e.* recovering only $\varepsilon \sim 50\%$ strain after the first loading and fails during the second cycle (Figure 2.9). Similarly, adding solely (cationic) ammonium or (anionic) sulfonate groups (*i.e.* systems void of any cross-ionic interactions) do not lead to any significant fatigue resistance (Figure 2.9). In contrast, the presence of ionic interactions in our composite hydrogels leads to high restitution, recovering 97 % of strain energy from $\varepsilon = 0$ to 100 %, up to 100 loading cycles (Figure 2.3a and video 2.1). To demonstrate the excellent resilience of this composite, we printed a macro-scale 3D “Eiffel Tower” structure and repeatedly stressed it to large deformation (see Figure 2.3c-d-e and Video 2.2).

The ionic motif present in the system not only provides great resilience but creates a hygroscopic matrix via osmoregulation that minimizes evaporative water losses^[20]. As a result, we observed some water loss during the initial cycles of mechanical testing, yet, after a while the system stabilizes, and the residual water shows little evaporation (Figure 2.3a and Figure 2.10). Note that we made no attempt to control room humidity or using any encapsulation strategies of the printed structures. This evaporative stability increases the likelihood that printed parts using these composites could be used in practical devices.

We performed additional relaxation tests to probe the nature of ionic detachment and reattachment between the polymer backbone and surrounding nanoparticles. We stressed the samples to $\varepsilon = 100\%$ strain and held them for increasing periods of time before unloading (Figure 2.3b). In the short time frames ($t < 100$ s), the material behaves elastically, with little hysteresis over the loading and unloading cycle. For

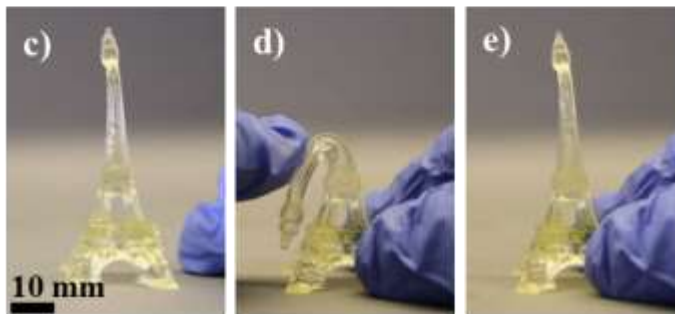
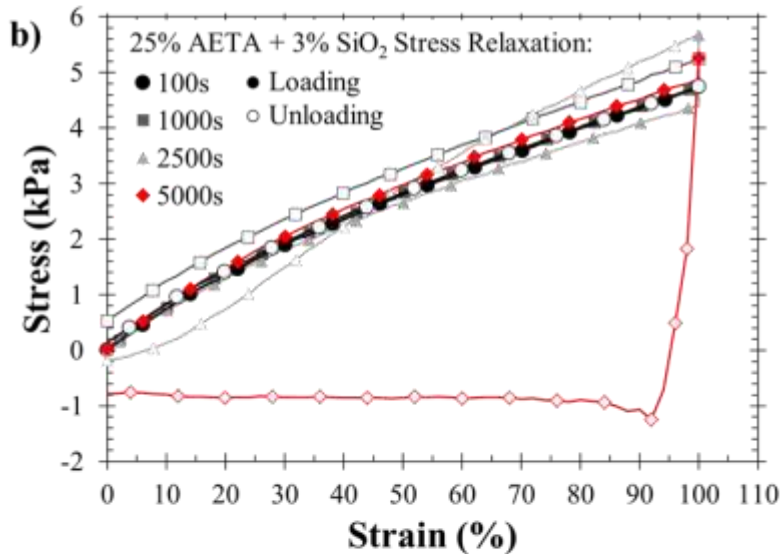
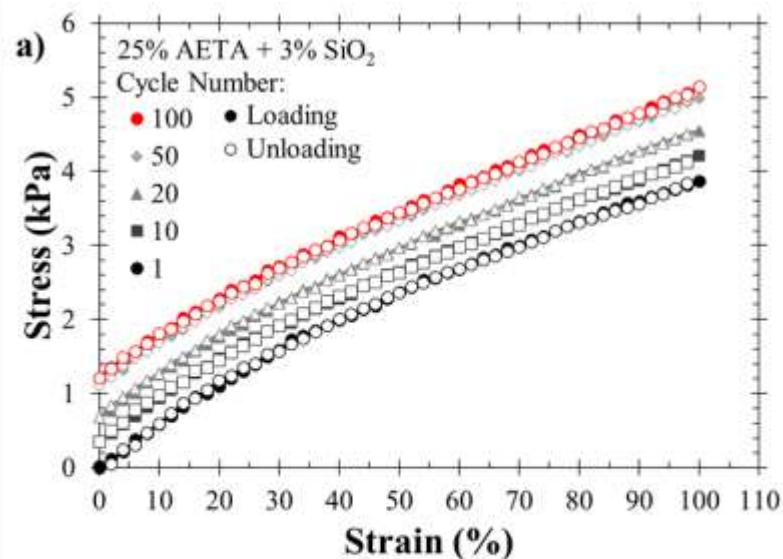


Figure 2.3: **a)** Cyclic test (i.e. 1, 10, 20, 50 and 100 loading-unloading cycles to 100 % strain) of the ionic composite hydrogels (i.e. AA + 25 mol% AETA + 3 wt% SiO₂); **b)** Relaxation tests (i.e. loading-unloading to 100 % strain with a static hold of 100s, 1000s, 2500s and 5000s) probing the dynamic nature of ionic interactions present in the system; **c)** Demonstration of resilience on a printed Eiffel tower in which the repeatable extensive deformation (**d**) is recovered (**e**).

intermediate time scales ($t \sim 1,000$ s), slight evaporative water loss shrinks the

polymer network and causes residual stresses; the as-measured stress increases during the static hold but the material still exhibits linear elasticity during unloading. At longer relaxation periods (*i.e.* 2,500 s and 5,000 s), the gels initially experience similar increases in stress due to evaporative water loss, but eventually the ionic network breaks and reforms to accommodate the applied deformation (see Figure 2.3b). Specifically, nanoparticle-polymer reconfiguration plays an important role after relaxation times of 2,500 s or greater, *i.e.* the partially reconstructed network exhibits lower stress values during unloading due to the breaking and reattaching process. These findings are consistent with theoretical and experimental observations in dual ionic-covalent cross-linked hydrogels^[18b]; however, we observe much longer time-scales required for complete relaxation for our system (compare to $\tau_r \sim 5,000$ s vs. $\tau_r \sim 20$ s for the system of poly (vinyl alcohol) crosslinked by borate ions^[18b]). These enhanced relaxation times are likely due to that the nanoparticle and polymer chains carry multiple ionic groups (*c.a.* 1 mmol·g⁻¹ of nanoparticle and 2.5 mmol·g⁻¹ of copolymer) so numerous dynamic bonds must break and reform to enable nanoparticle and chain mobility. The two orders of magnitude increase in τ_r further increases the opportunity for using this class of hydrogel in engineering applications.

Transparent and conductive

Printed structures from our formulations are virtually optically transparent, with a transmission coefficient of *c.a.* 0.98 cm⁻¹ from 500-750 nm (see Figure 2.11). The printed “Touchdown the Bear” object has better than 100 μ m feature resolution in X-Y-Z dimensions while still being transparent and responding to external loads elastically (see Video 2.3). Note that the ionic AETA monomer and silica nanoparticles are added in solution with their counterions, Cl⁻ and Na⁺, respectively. These ions are incorporated in the hydrogel and the mobility of these electrolytes endows the printed structures with high ionic conductivity (Figure 4a and Table 2.1). Using alternating electric fields, we were able to use this ionic transport to drive electronic devices in a manner consistent with work by Keplinger *et. al*^[10b].

Limitations in hydrogel fabrication methods, however, have restricted the use of such conductive hydrogels to demonstrations with 2D planar structures^[10a, 10b, 10d].

Figure 2.4b-c demonstrates that our printed “Touchdown the Bear” can act as a truly 3-dimensional stretchable ionic conductor (see Video 2.3). We used this bear to complete a circuit and drive a green LED using an alternating electric field ($f = 1 \text{ Hz}$ to 10^6 Hz) as low as $V = 50 \text{ mV}$ across the device. To the best of our knowledge, no other reported SLA material combines the high strain to failure (ϵ_{ult} up to 425 %) and high conductivity (σ up to $2.9 \text{ S}\cdot\text{m}^{-1}$ at $f = 1 \text{ MHz}$) for the ionic composite hydrogels reported here.

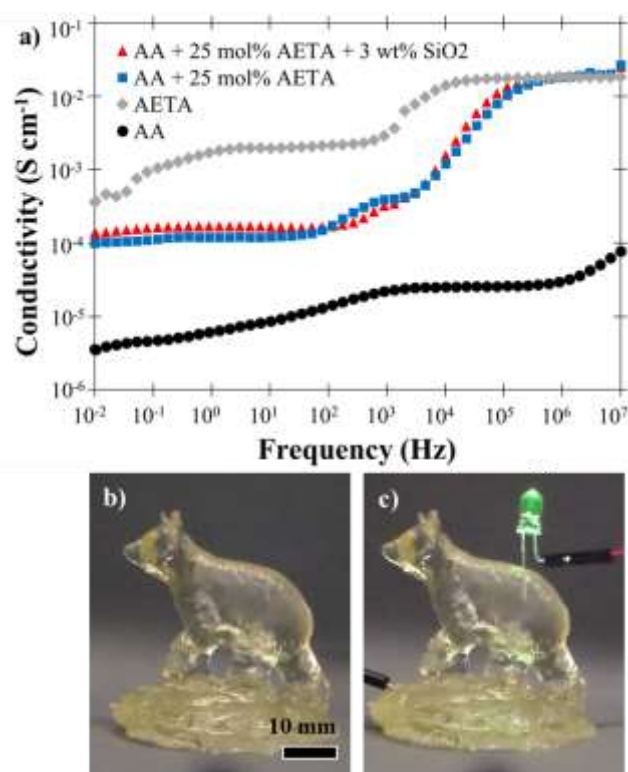


Figure 2.4: **a)** Conductivity as a function of AC frequency for the as-printed composite hydrogels; **b)** 3D printed transparent and conductive ionic composite hydrogels (*i.e.* AA + 25 mol% AETA + 3 wt% SiO₂) of Touchdown the Bear shown driving a green LED when subjected to a square wave (5V, 100 Hz) potential across the object **(c)**.

Swelling and actuation

Hydrogel networks possess the ability to absorb or expel water based on the thermodynamics of the interactions between the polymer and the solvent^[21]. Osmotically driven actuation can generate substantial forces ($\sim 20 \text{ N}$) while only consuming modest amounts of power ($\sim 1 \text{ mW}$)^[22]. Despite these advantages, mass

transport requirements limit swelling rates in conventional hydrogels. Super-porous hydrogels that fare better in diffusion-limited processes suffer from poor mechanical properties^[12].

We used our ability to photo-pattern 3D structures to print osmotic actuators that are porous for rapid mass transport, yet with defined internal and external structure for mechanical integrity. We quantified the rate of osmotic actuation for our printed devices using simple gravimetric analysis, where we define the swelling ratio, S , on a mass basis compared to the originally fabricated part as follows:

$$S = \frac{\text{mass}_{\text{swollen}}}{\text{mass}_{\text{as-printed}}} \quad (1)$$

Based on hydrogels of similar geometries and comparable exposure times, the introduction of AETA into the AA-based network improves both the rate and amount of water uptake compared to neat AA (Figure 2.5a). Indeed, the ionic ammonium-containing AETA monomers require a greater number of water molecules for solvation than their non-ionic AA counterparts. This increase in hydrophilicity corresponds to a larger driving force for swelling and allows the gels to absorb a greater amount of “bound” and “semi-bound” water^[23]. The addition of SiO₂ nanoparticles reduces the swellability in the neat and copolymer networks. This behavior likely results from the stiffer elastic moduli, which requires less strain for the elastic potential energy of the network to balance the chemical potential of the solvent in the hydrogel.

To further enhance the swelling of our composite hydrogels, we relied on mechanical design of the printed devices. Bound and semi-bound water absorption is diffusion limited; in foundational work on spherical polyacrylamide hydrogels, Tanaka *et al.*^[21] developed a relationship relating the characteristic swelling time, τ_{swell} , to the gel radius, a , and diffusion coefficient of the network, D as follow:

$$\tau_{\text{swell}} = \frac{a^2}{D} \quad (2)$$

Reported hydrogel devices with fast actuation capabilities^[24] (*i.e.* $t \sim 25$ minutes to achieve $S \sim 33$ % swelling) possess dimensions on the order of millimeters or less to reduce the characteristic length, a .

Using 3D printing, we can choose which portions of our structure to actuate fast or slow by controlling the feature resolution. To that end, we 3D-printed high surface to volume ratio (S:V) structures for rapid osmotic actuation. Printing such geometries allowed us to achieve greater water flux through the solvent-hydrogel boundary without constraining the overall size of the device. To demonstrate our control over diffusive swelling, we designed cubic lattices with the same total volumes ($V = 2.808 \text{ cm}^3$) but different number of struts and strut sizes. We then printed the corresponding structures using the same material and illumination per layer in order to yield gels with similar network diffusion coefficients. Using AA + 25 mol% AETA + 3 wt% SiO₂, we printed structures with increasing S:V ratios (Figure 2.5b). With a S:V ratio of $\sim 2.5 \text{ mm}^{-1}$, we were able to rapidly absorb over 60 % of their as-printed weight within 100 s. This amount is nearly six times greater than the swelling exhibited by a similar cubic solid we printed with approximately one sixth the S:V, *i.e.* 0.43 mm^{-1} (Figure 2.5c).

The higher S:V structures continue to reach larger swelling ratios at larger time scales (see also Figure 2.11). Figure 2.5d depicts a cubic lattice with a swelling ratio of $S \sim 4.2$ (at $t = 2,600 \text{ s}$) next to the as-printed structure ($S = 1.0$; $t = 0 \text{ s}$). Thus, not only can we fabricate tough, resilient elastomeric structures using the ionic composite hydrogels, but the μm scale 3D resolution permits large, high surface area architectures, which display rapid swelling. To demonstrate function, Supplemental Video 2.4 and Figure 2.13 show a simple example of a centimeter scaled multi-armed gripper swelling from an initially flat and open state to curved and enclosed within minutes (Figure 2.5e-f). This osmotic actuation reverses, when the hydrogel composite is placed in an unfavorable solvent, *e.g.* ethanol, as shown in Supplemental Video 2.5.

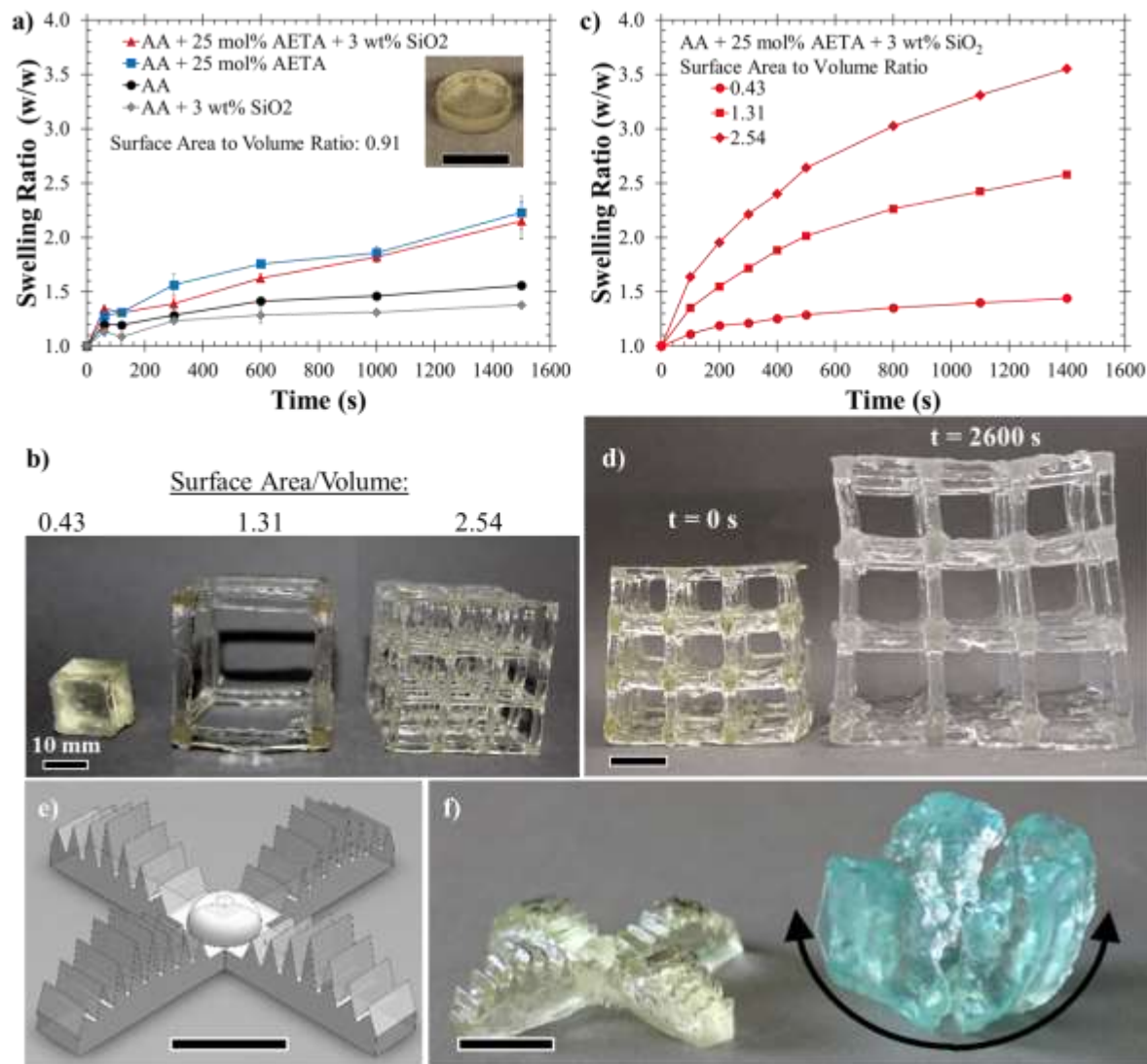


Figure 2.5: **a)** Swelling performance of photo-cured hydrogels with a surface to volume ratio of 0.91 mm⁻¹ showing an increased swellability with the addition of hydrophilic AETA comonomer; **b)** Printed ionic composite hydrogels (*i.e.* AA + 25 mol% AETA + 3 wt% SiO₂) of different surface area to volume ratios and their corresponding swelling ratio (**c**); **d)** A printed high surface area to volume ratio (2.54 mm⁻¹) lattice before and after water absorption for 2600 s; A multi-armed gripper, as designed (**e**), and printed to swell from initially flat and open to curved and enclosed within 10 minutes in dyed blue water (**f**).

2.4 Conclusions

This paper reports the high resolution, stereolithography 3-D printing of new, highly elastic and tough composite hydrogels with high resilience. The key to our formulation is the addition of anionically charged sulfonated silica nanoparticles to the cationic ammonium-containing pre-polymer acrylate solution, which endows the

system with dynamic, reversible ionic interactions and allows rapid fabrication of macro-scale 3D objects at an approximate draw rate of 3 cm·hr⁻¹. The composite hydrogels combine tunable stiffness, toughness, extensibility, and resiliency not reported elsewhere. When fabricated, the composites are optically transparent, recover from repeatable extensive deformation, and act as truly 3-dimensional compliant ionic conductors. Additionally, designing high surface to volume ratio structures from this chemistry permits fast diffusive swelling for practical implantation of large osmotically-driven actuators.

Such advancements expand the application space for hydrogels in soft electronics and sensors, tissue engineering, biomedical devices, and soft robotics. Primarily, the combination of tough structures that can repeatedly withstand extensive loadings without damage is required for base level function in high-performance devices such as actuators. As a compliant conductor (ϵ_{ult} up to 425 %, σ up to 2.9 S·m⁻¹ at $f = 1$ MHz), the rapid fabrication of active 3D structures of complex geometries offers promise for use in the sensing and control of autonomous soft robots. Our work is a platform for designing other 3D-printed composite hydrogels beyond silica; the addition of other types of nanoparticles would add additional optical, electrical, or magnetic functionality to the as-printed devices.

2.5 Experimental Section

Materials

Acrylamide (AA, 99 %, Aldrich), [2-(Acryloyloxy)ethyl]trimethylammonium chloride (AETA, 80 % wt in H₂O, Aldrich), *N,N'*-methylenebisacrylamide (MBA, 99 %, Aldrich), riboflavin (98 %, Neta Scientific), triethanolamine (> 99 %, Neta Scientific), hydroquinone (99 %, Aldrich), Ludox HS 30 colloidal silica (mean diameter 18 nm, Aldrich), 3-(trihydroxysilyl)-1-propane sulfonic acid (SIT, 40 wt%, Gelest), sodium hydroxide solution (1 M, Aldrich) and dialysis tubing (Spectra/Por RC Biotech Membrane, 15K MWCO, 16 mm flat width) were purchased as indicated and used without further purification.

Sulfonate functionalization of nanosilica: According to a previous reported^[25], Ludox HS 30 colloidal silica (3 g) was diluted in a flask with deionized water (22 ml).

In another flask, 3-(trihydroxysilyl)-1-propane sulfonic acid (4 g) was diluted with deionized water (20 ml). The colloidal silica suspension was slowly added to the SIT suspension, while stirring vigorously. To the mixture, a solution of sodium hydroxide (1 M) was added dropwise until a pH of about 5 was reached. The entire solution was then heated to $T = 70$ °C and stirred vigorously for 24h. After that, the suspension was cooled to room temperature and placed into dialysis tubing and dialyzed against deionized water for 3 days while changing the water twice a day. A suspension of sulfonated nanosilica at 12 wt% was prepared with deionized water for further use. Dynamic Light Scattering and Thermal Gravimetric Analysis suggest a particle size of $d \approx 17 \pm 5$ nm and an organic content of $R_{organic} \approx 24$ %, respectively. A titration curve for the reaction between the surface-modified sulfonated silica nanoparticles and NaOH 1 M show the equivalence point at $pH \approx 7$ consistent with an average sulfonate concentration of $M_{SO_3Na} \approx 1$ mmol·g⁻¹ (Figure 2.13).

Preparation of ionic composite hydrogels

AA and AETA monomers at different ratios together with 1 mol% of MBA crosslinker were dissolved in a combination of deionized water and sulfonated silica suspension (12 wt%) to reach a final monomers to water ratio of 1:1. The silica content is modulate from 0 to 10 wt% within the resulting ionic composite hydrogels. The final addition of 0.015 mol% of Riboflavin, an aqueous type II photo-initiator, and 1.5 mol% of triethanolamine, a co-initiator, enables free radical photopolymerization of the resulting acrylate groups under near-UV exposure. A full-spectrum light exposure at a measured (Silver Line UV 230-410nm) energy density of $w_e = 3.34$ J·cm⁻² for pure AA-based composites and $w_e = 1.67$ J·cm⁻² for AETA-containing composites makes fabrication of aqueous ionic composite hydrogels feasible in any shape (dog-bones, disks, *etc.*).

Photo-rheology

We characterized the photo-polymerization reaction using a Discovery Hybrid Rheometer HR-3 (TA Instruments) through constant frequency and amplitude ($\omega = 1$ Hz and $\Gamma = 1$ % strain) oscillatory shear rheology during photo-exposure. We used a circular parallel plate (diameter = 20 mm) with a gap of 1 mm. The fixed bottom plate was transparent acrylic connected to an ultra-violet (UV) light-source (Omniculture

Series 1500, Lumen dynamics) and UV filter ($\lambda = 400\text{-}500\text{ nm}$) using a light guide. A radiometer (Silver Line UV 230-410 nm) placed directly on top of this plate recorded irradiance of $E_e = 7.6\text{ mW}\cdot\text{cm}^{-2}$.

3D Printing

For this work, we use an Ember by Autodesk™ desktop 3D printer. Since the Ember uses a LED projector ($\lambda = 405\text{ nm}$) with an irradiance of $E_e \sim 22.5\text{ mW}\cdot\text{cm}^{-2}$ and is controlled by open source software, it is ideal for our custom hydrogel system. Artist Brian Caverly provided a *.obj* file from the 3D-scan of the Touchdown the Bear statue. Autodesk Print Studio™ imported, modified and sliced the design into discrete $100\text{ }\mu\text{m}$ layers. The resulting image stack of photo-patterns and the corresponding actions for the 3D printer were exported to a *.tar.gz* file and loaded on to the Ember. For the ionic composite hydrogels, short layer exposure times ($t = 6\text{ s}$ per $100\text{ }\mu\text{m}$) yielded high resolution objects (as seen on Figures 2.3-4-5). Longer photo-exposures resulted in similar, but stiffer structures consistent with a denser polymer network. $60\text{ }\mu\text{g}$ of hydroquinone were included in the formulation as a radical scavenger to improve the resolution of large-scale prints and pot-life of the resins.

Mechanical tests

Mechanical testing coupons were fabricated by replica-molding from dog-bone shaped molds (width = 4 mm , depth = 1.5 mm and gauge length = 13 mm). Photopolymerization of the different hydrogel compositions occurred after exposure to a $E_e = 83.6\text{ mW}\cdot\text{cm}^{-2}$ UV light (Omnicure Series 1500 Lumen dynamics) for $t = 40\text{ s}$ for pure AA-based composites and $t = 20\text{ s}$ for AETA-containing composites respectively. The mechanical performance of these hydrogels is highly dependent on hydration state, with lower water content corresponding to stiffer and more brittle behavior as the hydrogel networks collapse. Samples were either stored in sealed plastic bags or tested immediately after fabrication to maintain hydration state. However, during mechanical testing the samples were exposed to ambient room conditions which impacted mechanical behavior in longer tests. Using a Zwick-Roell Z1010 universal tensile testing machine (Ulm, Germany), we conducted uniaxial tensile tests at a strain rate of $\dot{\epsilon} = 10\text{ mm}\cdot\text{min}^{-1}$. Samples that slipped or failed due to

grip stresses were disregarded and tests were repeated until each composition was successfully measured at least 5 times. We further measured the fatigue strength and resilience of these ionic composite hydrogels through cyclic tensile tests by repeatedly load and unload to $\varepsilon = 100\%$ strain at a speed of $d\varepsilon/dt = 10\text{ mm}\cdot\text{min}^{-1}$ (See Supplemental Video 2.1). For the first cycle, the strain energies as calculated from the area under the stress-strain curves for loading and unloading were $2.301\text{ kJ}\cdot\text{m}^{-3}$ and $2.223\text{ kJ}\cdot\text{m}^{-3}$, respectively. Using our printed Eiffel Tower, we demonstrate the remarkable fatigue strength of our ionic design by repeatedly bending the upper part of the printed structure (see Supplemental Video 2.2). To determine the effects of the ionic ammonium-sulfonate interactions, we conducted stress relaxation measurements. Samples were pulled to 100% strain at a rate of $10\text{ mm}\cdot\text{min}^{-1}$ and held for a predetermined interval while continuously measuring stress. After this static hold, the crosshead returned to the original separation at 0% strain at $10\text{ mm}\cdot\text{min}^{-1}$.

Dielectric conductivity: Ionic conductivity measurements were performed on a Broadband Dielectric Spectrometer from $f = 10^{-2}$ to 10^7 Hz using an ALPHA analyzer supplied by Novocontrol. Samples were placed between two gold-plated electrodes (diameter 20 mm). Conductivity measurements were performed at ambient temperature. Using our printed Touchdown the Bear, we demonstrate the low resistivity of our materials system by connecting the positive terminal of green LED on the top of the printed bear and placing an electrode some centimeters away on the front of the object. The LED lights up when a sinusoidal output (Agilent 33120A Function/Arbitrary Waveform Generator 15 MHz) provides an alternating potential difference at voltages as low as $V = 50\text{ mV}$ and at a large range of frequencies ($f = 10$ to 10^6 Hz) (see Supplemental Video 2.3).

Swelling Ratio Measurements

To observe the difference in swelling ratios between compositions, samples were fabricated by replica-molding $200\text{ }\mu\text{l}$ volumes in cylindrical shaped molds (diameter = 10 mm) yielding a final surface area to volume ratio of approximately $S:V = 0.91\text{ mm}^{-1}$. The photo-polymerization of the different hydrogel compositions matched the intensity and duration of the mechanical testing coupons. Samples were then soaked in deionized water for the specified time, placed on a dry cellulose pad to remove surface

water and then promptly massed. At least 8 samples were averaged for each composition and data point. The swellability as a function of surface area to volume ratio was investigated for the ionic composite hydrogels (*i.e.* AA + 25 mol% AETA + 3 wt% SiO₂). We used Solidworks™ software to design and calculate surface area and volume for the varying lattice structures. Structures were printed as designed with an irradiance of $E_c = 22.5 \text{ mW}\cdot\text{cm}^{-2}$ for $t = 8 \text{ s}$ for each 100 μm layer. These structures again were soaked in deionized water, placed on a dry cellulose pad and immediately weight at different time intervals. We can determine the nature of diffusion of water into hydrogels by fitting the data to the following equation^[23]:

$$F = kt^n \quad (S1)$$

Where F is the fraction uptake of water ($dw\cdot w^{-1}$) at time t , k is a constant that captures the behavior of the macromolecular network and penetrant, and n is the diffusion exponent. Figure 2.12 contains the Power-Law fits of the data and the value diffusion exponents suggest simple Fickian diffusion ($n = 0.5$). Dividing the fitted k -values by the corresponding S:V ratio (*i.e.* $k[S:V]^{-1}$) all yield a value of 0.03, confirming the observation that the swelling rate scales linearly with S:V. As seen in Supplemental Video 2.4, we immersed the gripper in deionized water with small amounts of blue food coloring to improve contrast during imaging. Dye was absorbed in the gripper during this process which explains the slight tint noted in Figure 2.5f. Supplemental Video 2.5 also demonstrates the deswelling under immersion in a non-solvent such as ethanol.

Water Retention

We note that the hydration state of printed hydrogels drastically impacts the measured mechanical properties. We accordingly quantified the rate of water loss in ambient conditions ($T = 22.5 \text{ }^\circ\text{C}$ and 30 % humidity) by measuring the weight loss over time for 8 dog-bone shaped samples. These findings support our observation that the hydration state changes over time. For this reason, all mechanical tests were carried out as close to sample preparation as possible to minimize these effects. Samples were also stored in plastic bags to minimize water losses.

Additional techniques

We conducted Dynamic Light Scattering (DLS) measurements on samples in water (concentration less than 1 wt%) at $T = 25$ °C using a Malvern Zetasizer. Thermal gravimetric analysis (TGA) was performed using a TGA Q500 from TA Instruments at a heating rate of 20 °C/min under nitrogen flow. We performed Differential scanning calorimetry (DSC) using a DSC Q2000 from TA Instruments at heating and cooling rates of 10 °C·min⁻¹ under nitrogen flow (to avoid any thermal history effects the 2nd scan was used). Using Molecular Devices Spectramax Plate Reader, we measured the absorbance of uncured and cured hydrogels in a disposable cuvette over visible wavelengths ($\lambda = 350$ to 750 nm). The consumption of the photo-initiator during curing led to the disappearance of the absorbance peak at $\lambda = 450$ nm. Transmission electron microscopy (TEM) was carried out using a FEI Tecnai T12 Spirit Twin TEM/STEM microscope operated at $V = 120$ kV. The samples were cryo-microtomed at $T = -100$ °C by a Leica UCT microtome.

2.6 Supplemental Information

Table 2.2. Summary of Ionic Composite Hydrogel Performances.

Composition	T_g (°C)	$\eta_{initial}$ (Pa·s)	$t_{G'=G''}$ (s)	$t_{\eta = 1000 \text{ Pa}\cdot\text{s}}$ (s)	E (Pa)	ϵ_{ult} (%)	TT (kJ·m ⁻³)	σ (S)
AA + 1 % SiO ₂	-	0.054	13	136	1160 ± 460	247 ± 38	2.9 ± 0.4	
AA + 3 % SiO ₂	-	0.044	12	118	2860 ± 260	165 ± 44	3.4 ± 0.2	3.
AA + 5 % SiO ₂	-	0.031	11.5	109	6160 ± 370	151 ± 46	5.0 ± 1.6	
AA + 10 % SiO ₂	-	0.135	7	33	114500 ± 6390	69 ± 14	23.9 ± 7.7	
AA,+ 50 mol% AETA	94	0.043	10	64	2580 ± 450	367 ± 53	11.9 ± 3.5	
AA + 50 mol% AETA + 1 % SiO ₂	-	0.089	9.5	56	3140 ± 130	400 ± 59	16.4 ± 3.5	
AA + 50 mol% AETA + 3 % SiO ₂	-	0.064	7	54	5400 ± 310	425 ± 45	28.5 ± 5.7	
AA + 50 mol% AETA + 5 % SiO ₂	-	0.081	4	32	9550 ± 1010	380 ± 54	37.6 ± 7.3	
AA + 50 mol% AETA + 10 % SiO ₂	-	0.115	4	27	19850 ± 840	278 ± 39	53.5 ± 2.6	

T_g : glass transition temperature ; η : complex viscosity ; t: illumination time ; E: Young's modulus ; ϵ_{ult} : strain at break ; TT: tensile toughness ; σ : conductivity.

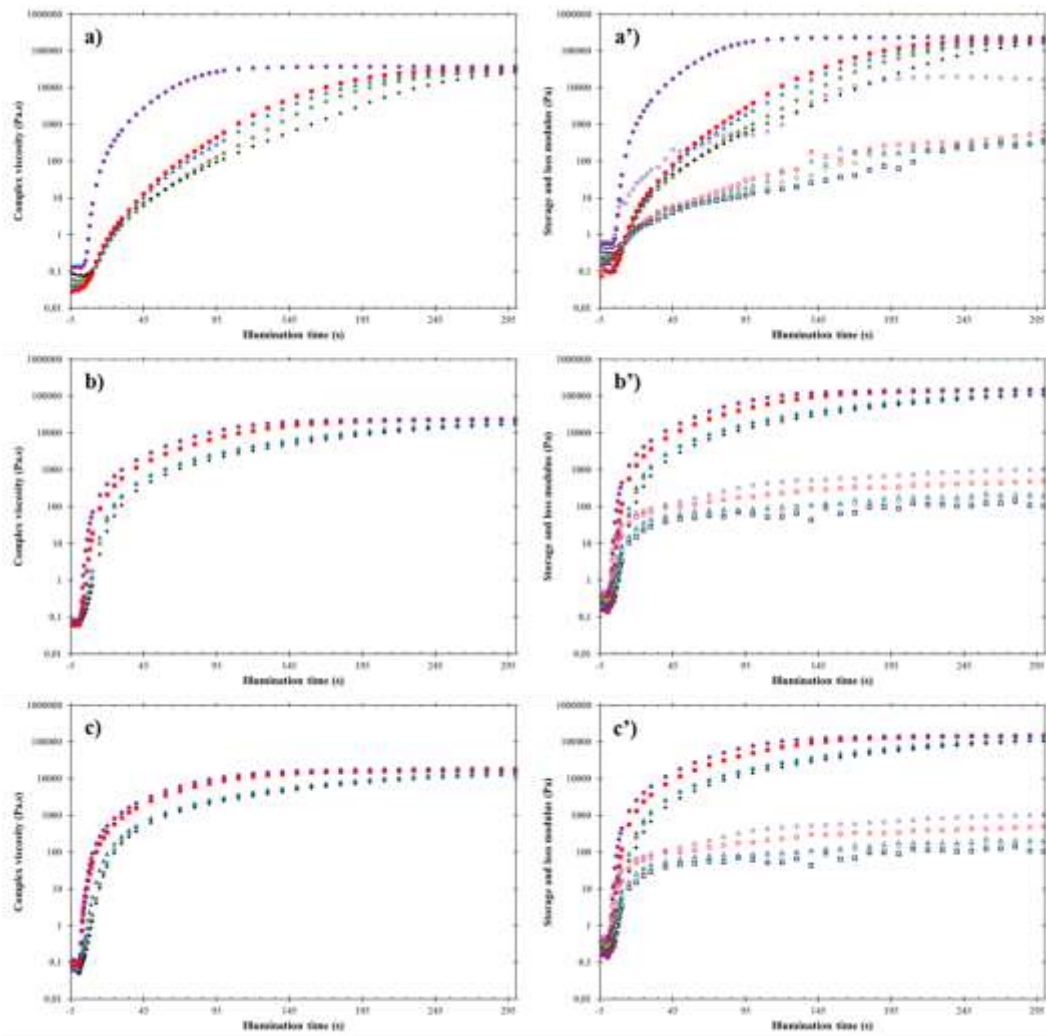


Figure 2.6. Complex viscosity η^* (a, b, c) and storage G' (full dots) and loss G'' (empty dots) modulus (a', b', c') with illumination time during photo-polymerization of AA-based composites (a, a'), AA + 25 mol% AETA-based composites (b, b') and AA + 50 mol% AETA-based composites (c, c'): 0 wt% (black crosses), 1 wt% (green diamonds), 3 wt% (blue triangles), 5 wt% (red squares) and 10 wt% (purple circles) of sulfonated SiO₂.

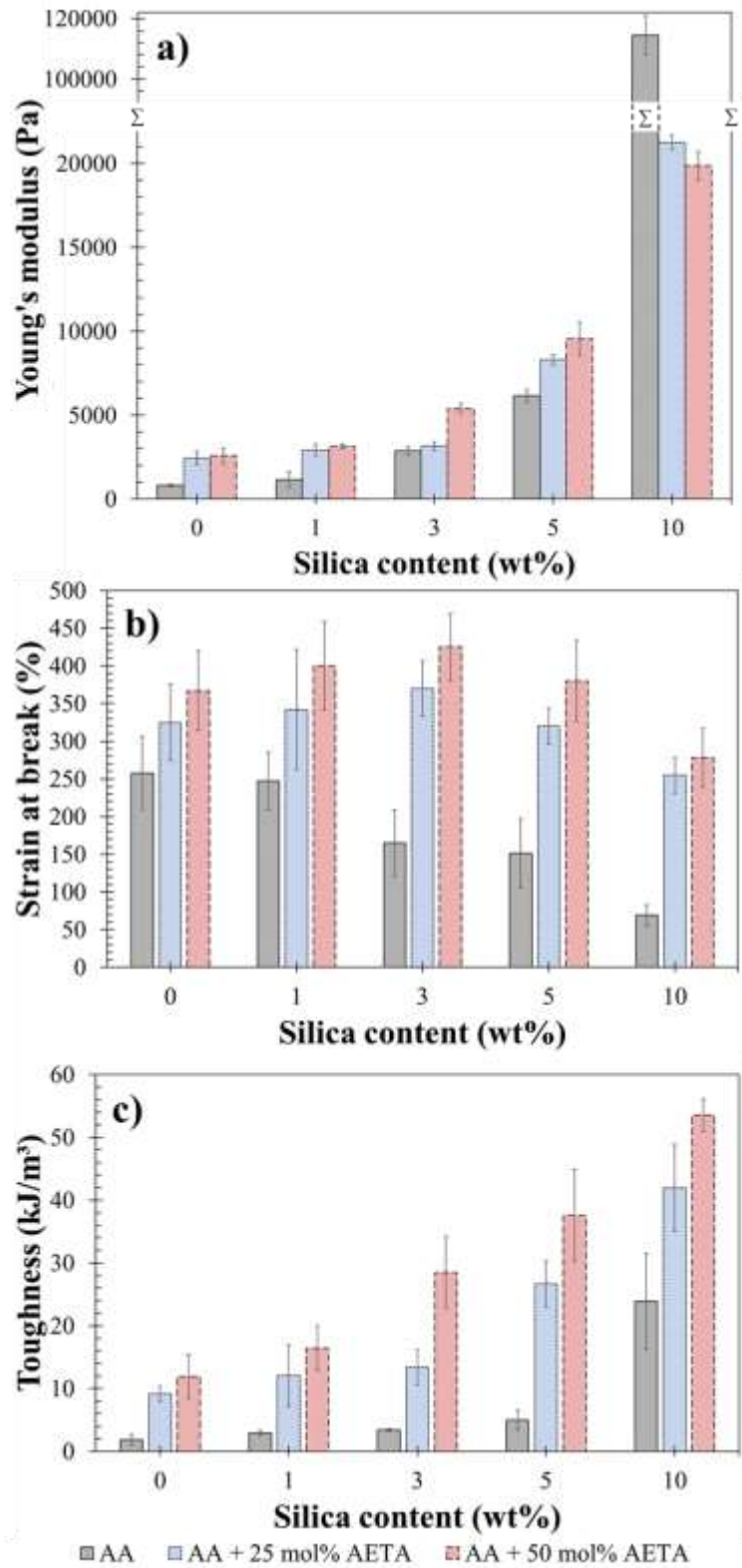


Figure 2.7 Young's modulus (a), strain at break (b), and toughness (c) of AA-based composites (solid grey), AA + 25 mol% AETA-based composites (short dash blue) and AA + 50 mol% AETA-based composites (long dash red) with different sulfonated SiO₂ loading.

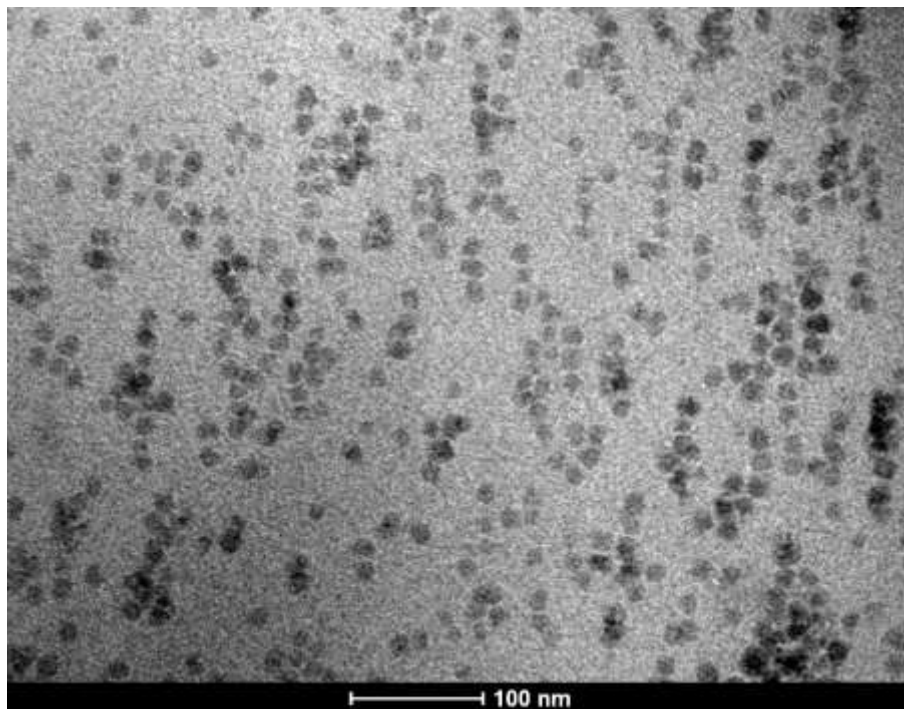


Figure S2.8. TEM micrographs of the ionic composite hydrogels (*i.e.* AA + 25 mol% AETA + 3 wt% SiO₂).

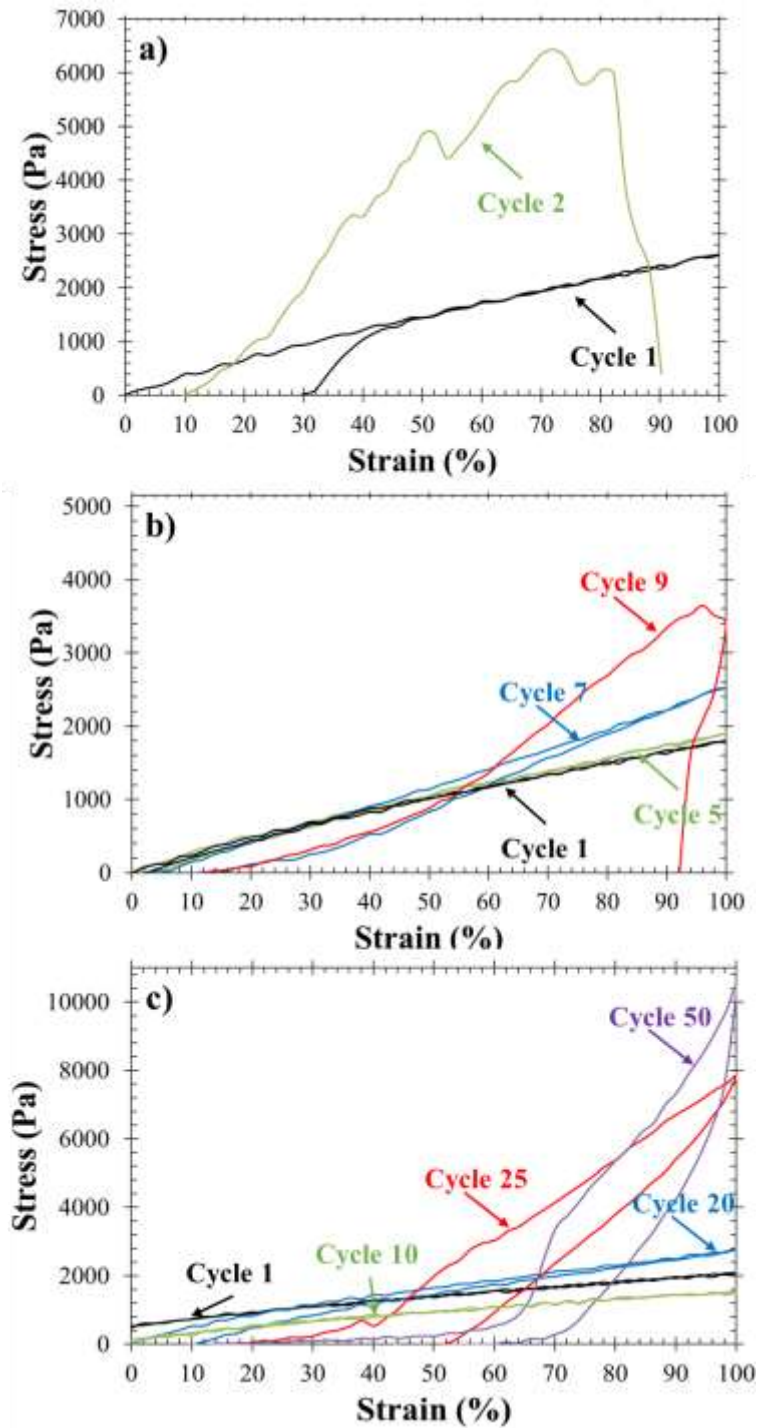


Figure 2.9. Cyclic test of neat AA (a), AA-based composite containing 3 wt% of SiO₂ (b) and the AA + 25 mol% AETA-based hydrogel (c).

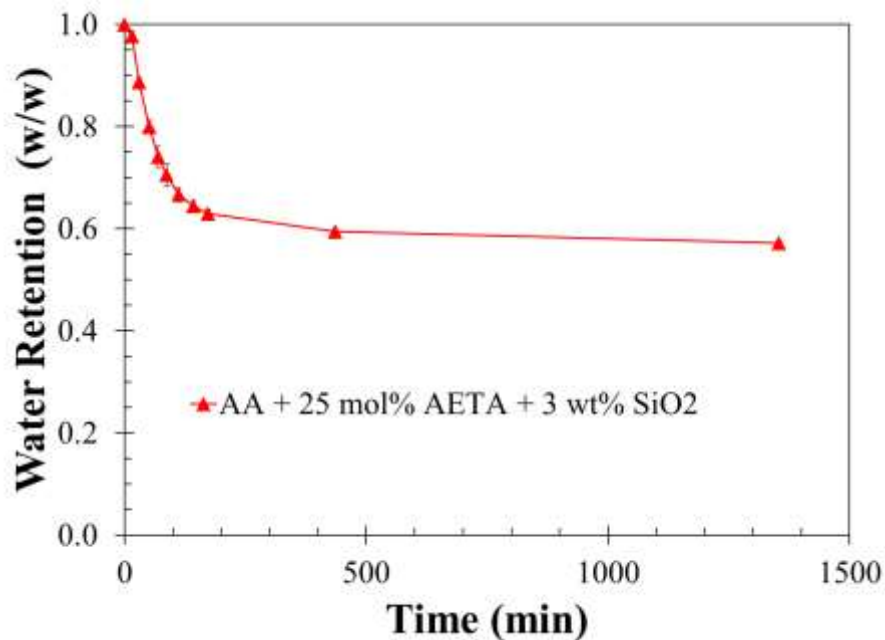


Figure 2.10. Water retention of the as-printed ionic composite hydrogels (*i.e.* AA + 25 mol% AETA + 3 wt% SiO₂) in ambient conditions (T= 22.5 °C, 30 % relative humidity).

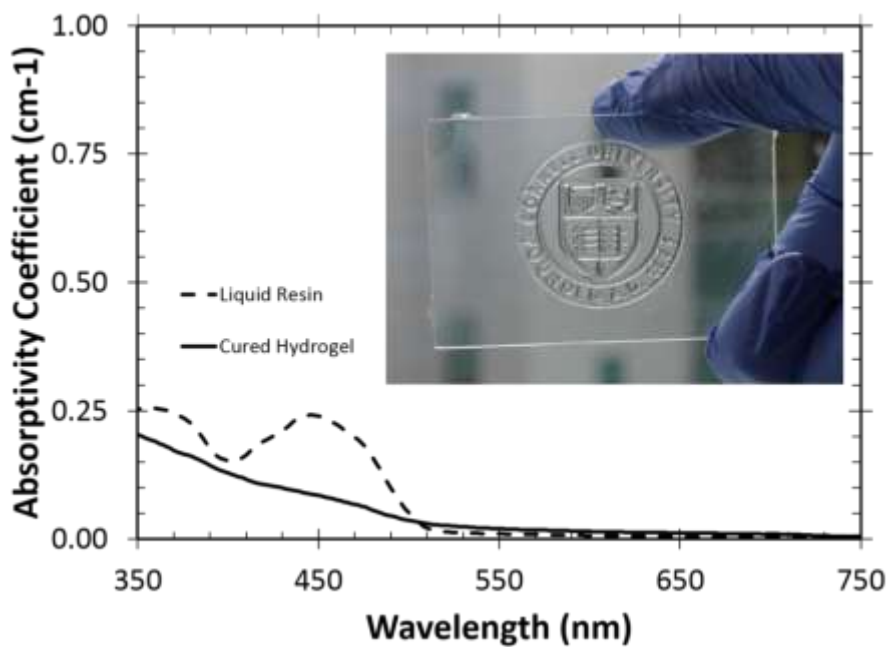


Figure 2.11. Absorptivity coefficient of the ionic composite hydrogels (*i.e.* AA + 25 mol% AETA + 3 wt% SiO₂) (solid line) and the pre-polymer solution (dash line).

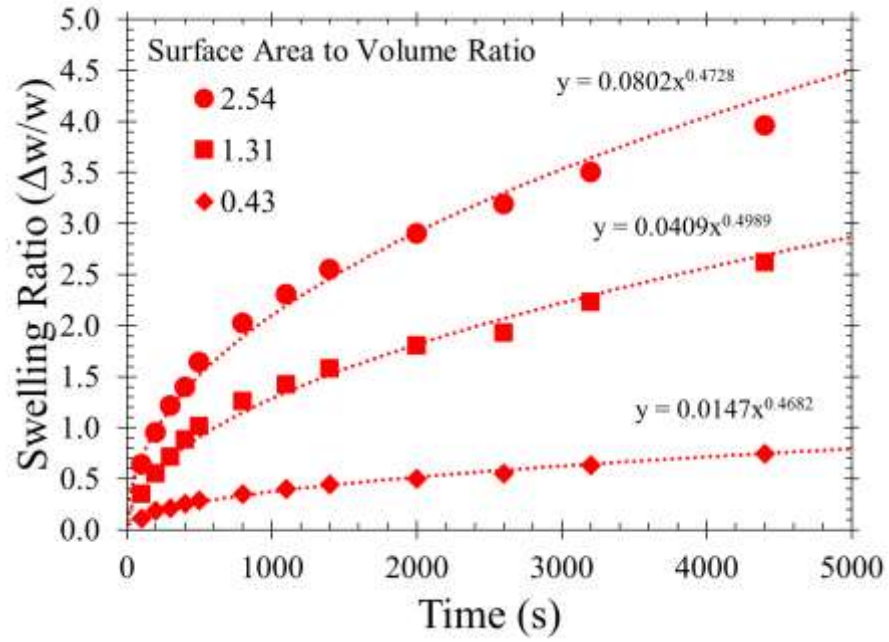


Figure 2.12. Power law fits of the osmotic swelling rate of lattices with different designed S:V ratios.

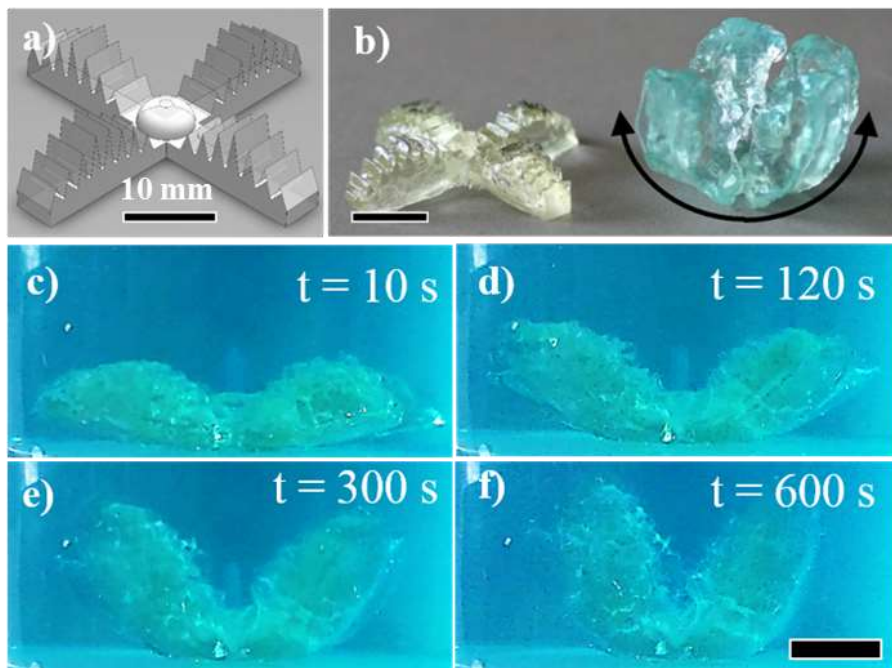


Figure 2.13. Osmotic swelling actuator as designed (a) and printed from our ionic composite hydrogels (*i.e.* AA + 25 mol% AETA + 3 wt% SiO₂) and after soaking in water and blue food dye for a period of 600 s (b); The change in actuation state over ten minutes of soaking (c-d-e-f).

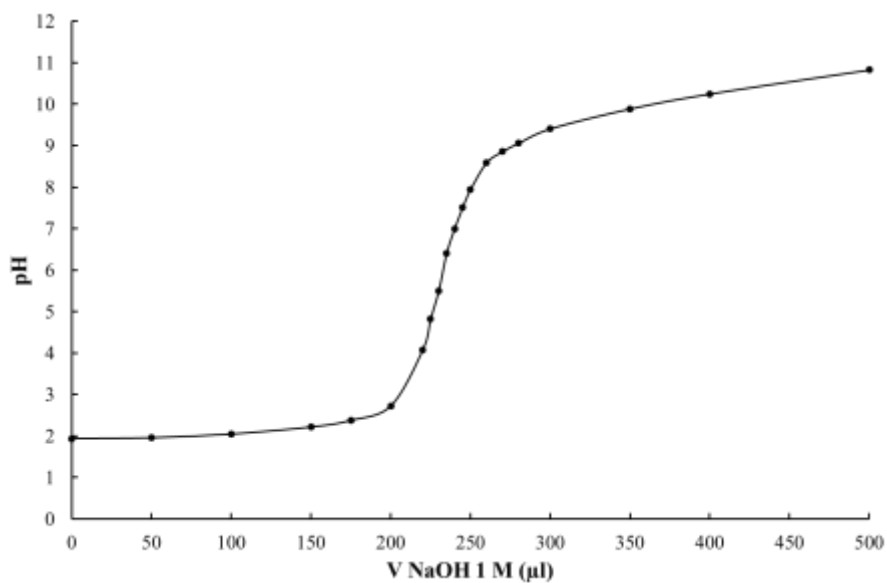


Figure 2.14. Titration curve for the reaction between the surface-modified sulfonated silica nanoparticles (10 ml, 2.4 wt%) and NaOH 1M. The equivalence point of the reaction occurs at $pH \approx 7$ which is consistent with an average sulfonate concentration of $1 \text{ mmol} \cdot \text{g}^{-1}$.

Supplementary Video

Video 2.1 – Demonstration of the recovery of the repeatable extensive deformation by loading-unloading.

Video 2.2 – Demonstration on a printed “Eiffel Tower” of the high resilience and fatigue strength.

Video 2.3 – Demonstration on a printed “Touchdown the Bear” of the elastomeric response and its ionic conductivity.

Video 2.4 – Demonstration on a printed “Actuator Design” of the fast actuation by swelling.

Video 2.5 – Demonstration on a printed “Actuator Design” deswelling from actuated state under immersion in a non-solvent (ethanol).

REFERENCES

- [1] J. Elisseeff, *Nat Mater* **2008**, 7, 271.
- [2] P. Calvert, *Advanced Materials* **2009**, 21, 743.
- [3] a) C. W. Peak, J. J. Wilker, G. Schmidt, *Colloid & Polymer Sci* **2013**, 291, 2031; b) J. P. Gong, *Soft Matter* **2010**, 6, 2583; c) P. Thoniyot, M. J. Tan, A. A. Karim, D. J. Young, X. J. Loh, *Advanced Science* **2015**, 2, 1400010.
- [4] a) Z. Liang, C. Liu, L. Li, P. Xu, G. Luo, M. Ding, Q. Liang, *Scientific Reports* **2016**, 6, 33462; b) H. Yuk, T. Zhang, S. Lin, G. A. Parada, X. Zhao, *Nat Mater* **2016**, 15, 190; c) J. P. Gong, Y. Katsuyama, T. Kurokawa, Y. Osada, *Advanced Materials* **2003**, 15, 1155; d) W. Yang, H. Furukawa, J. P. Gong, *Advanced Materials* **2008**, 20, 4499; e) H. J. Zhang, T. L. Sun, A. K. Zhang, Y. Ikura, T. Nakajima, T. Nonoyama, T. Kurokawa, O. Ito, H. Ishitobi, J. P. Gong, *Advanced Materials* **2016**, 28, 4884; f) Q. Chen, D. Wei, H. Chen, L. Zhu, C. Jiao, G. Liu, L. Huang, J. Yang, L. Wang, J. Zheng, *Macromolecules* **2015**, 48, 8003.
- [5] a) J.-Y. Sun, X. Zhao, W. R. K. Illeperuma, O. Chaudhuri, K. H. Oh, D. J. Mooney, J. J. Vlassak, Z. Suo, *Nature* **2012**, 489, 133; b) T. L. Sun, T. Kurokawa, S. Kuroda, A. B. Ihsan, T. Akasaki, K. Sato, M. A. Haque, T. Nakajima, J. P. Gong, *Nat Mater* **2013**, 12, 932; c) F. Luo, T. L. Sun, T. Nakajima, T. Kurokawa, Y. Zhao, K. Sato, A. B. Ihsan, X. Li, H. Guo, J. P. Gong, *Advanced Materials* **2015**, 27, 2722.
- [6] a) S. Rose, A. PrevotEAU, P. Elzriere, D. Hourdet, A. Marcellan, L. Leibler, *Nature* **2014**, 505, 382; b) D. Zhang, J. Yang, S. Bao, Q. Wu, Q. Wang, *Scientific Reports* **2013**, 3, 1399; c) L. Shi, Y. Han, J. Hilborn, D. Ossipov, *Chem. Commun.* **2016**, 52, 11151; d) K. Haraguchi, T. Takehisa, *Advanced Materials* **2002**, 14, 1120; e) L.-W. Xia, R. Xie, X.-J. Ju, W. Wang, Q. Chen, L.-Y. Chu, *Nature Communications* **2013**, 4, 2226.
- [7] E. A. Appel, M. W. Tibbitt, M. J. Webber, B. A. Mattix, O. Veiseh, R. Langer, *Nature Communications* **2015**, 6, 6295.
- [8] a) K. Lee, S. Cho, S. Heum Park, A. J. Heeger, C.-W. Lee, S.-H. Lee, *Nature* **2006**, 441, 65; b) S. Naficy, J. M. Razal, G. M. Spinks, G. G. Wallace, P. G. Whitten, *Chemistry of Materials* **2012**, 24, 3425; c) Y. Xia, H. Zhu, *Soft Matter* **2011**, 7, 9388; d) Y. Shi, C. Ma, L. Peng, G. Yu, *Advanced Functional Materials* **2015**, 25, 1219.
- [9] a) S. Lin, H. Yuk, T. Zhang, G. A. Parada, H. Koo, C. Yu, X. Zhao, *Advanced Materials* **2016**, 28, 4497; b) A. G. Rylie, B. Sungchul, A. P.-W. Laura, J. M. Penny, *Science and Technology of Advanced Materials* **2010**, 11, 014107.

- [10] a) S. S. Robinson, K. W. O'Brien, H. Zhao, B. N. Peele, C. M. Larson, B. C. Mac Murray, I. M. Van Meerbeek, S. N. Dunham, R. F. Shepherd, *Extreme Mechanics Letters* **2015**, 5, 47; b) C. Keplinger, J.-Y. Sun, C. C. Foo, P. Rothmund, G. M. Whitesides, Z. Suo, *Science* **2013**, 341, 984; c) Y. Lu, W. He, T. Cao, H. Guo, Y. Zhang, Q. Li, Z. Shao, Y. Cui, X. Zhang, *Scientific Reports* **2014**, 4, 5792; d) C. Larson, B. Peele, S. Li, S. Robinson, M. Totaro, L. Beccai, B. Mazzolai, R. Shepherd, *Science* **2016**, 351, 1071.
- [11] a) J. Wei, J. Wang, S. Su, S. Wang, J. Qiu, Z. Zhang, G. Christopher, F. Ning, W. Cong, *RSC Advances* **2015**, 5, 81324; b) K. Pataky, T. Braschler, A. Negro, P. Renaud, M. P. Lutolf, J. Brugger, *Advanced Materials* **2012**, 24, 391.
- [12] R. J. M. Nobuhiko Yui, Kinam Park, *Reflexive Polymers and Hydrogels: Understanding and Designing Fast Responsive Polymeric Systems*, CRC Press.
- [13] a) A. Sydney Gladman, E. A. Matsumoto, R. G. Nuzzo, L. Mahadevan, J. A. Lewis, *Nat Mater* **2016**, 15, 413; b) C. K. Chua, K. F. Leong, *3D printing and Additive Manufacturing: Principles and Applications - fourth edition of rapid prototyping*, World Scientific, **2014**.
- [14] K. V. Wong, A. Hernandez, *ISRN Mechanical Engineering* **2012**, 2012, 10.
- [15] a) J.-W. Choi, H.-C. Kim, R. Wicker, *Journal of Materials Processing Technology* **2011**, 211, 318; b) F. P. W. Melchels, J. Feijen, D. W. Grijpma, *Biomaterials* **2010**, 31, 6121.
- [16] R. F. Shepherd, J. C. Conrad, S. K. Rhodes, D. R. Link, M. Marquez, D. A. Weitz, J. A. Lewis, *Langmuir* **2006**, 22, 8618.
- [17] L. Carlsson, S. Rose, D. Hourdet, A. Marcellan, *Soft Matter* **2010**, 6, 3619.
- [18] a) K. Mayumi, A. Marcellan, G. Ducouret, C. Creton, T. Narita, *ACS Macro Letters* **2013**, 2, 1065; b) R. Long, K. Mayumi, C. Creton, T. Narita, C.-Y. Hui, *Macromolecules* **2014**, 47, 7243.
- [19] a) D. Gersappe, *Physical Review Letters* **2002**, 89, 058301; b) D. Shah, P. Maiti, D. D. Jiang, C. A. Batt, E. P. Giannelis, *Advanced Materials* **2005**, 17, 525.
- [20] Y. Bai, B. Chen, F. Xiang, J. Zhou, H. Wang, Z. Suo, *Applied Physics Letters* **2014**, 105, 151903.
- [21] T. Tanaka, D. J. Fillmore, *The Journal of Chemical Physics* **1979**, 70, 1214.
- [22] E. Sinibaldi, A. Argiolas, G. L. Puleo, B. Mazzolai, *PLOS ONE* **2014**, 9, e102461.

- [23] D. Saraydin, E. Karadağ, O. Guven, *Polym J* **1997**, 29, 631.
- [24] H. Arora, R. Malik, L. Yeghiazarian, C. Cohen, U. Wiesner, *J. Polym. Sci., Part A: Polym. Chem.* **2009**, 47, 5027.
- [25] R. Rodriguez, R. Herrera, L. A. Archer, E. P. Giannelis, *Advanced Materials* **2008**, 20, 4353.

CHAPTER 3

CLICK CHEMISTRY STEREOLITHOGRAPHY FOR SOFT ROBOTS THAT SELF-HEAL

3.1 Abstract

Although soft robotics promises a new generation of robust, versatile machines capable of complex functions and seamless integration with biology, the fabrication of such soft, three dimensional (3D) hierarchical structures remains a significant challenge. Stereolithography (SLA) is an additive manufacturing technique that can rapidly fabricate the complex device architectures required for the next generation of these systems. Current SLA materials and processes are prohibitively expensive, display little elastic deformation at room temperature, or exhibit Young's moduli exceeding most natural tissues, all which limit use in soft robotics. Herein, we report a low-cost build window substrate that enables the rapid fabrication of high resolution ($\sim 50 \mu\text{m}$) silicone (polydimethylsiloxane) based elastomeric devices using an open source SLA printer. Our thiol-ene click chemistry permits photopolymerization using low energy ($H_e < 20 \text{ mJ}\cdot\text{cm}^{-2}$) optical wavelengths ($405 \text{ nm} < \lambda < 1 \text{ mm}$) available on many low-cost SLA machines. This chemistry is easily tuned to achieve storage moduli, $6 < E < 283 \text{ kPa}$ at engineering strains, $\gamma = 0.02$; similarly, a large range of ultimate strains, $0.5 < \gamma_{\text{ult}} < 4$ is achievable through appropriate selection of the two primary chemical constituents (mercaptosiloxane, M.S., and vinylsiloxane, V.S.). Using this chemo-mechanical system, we directly fabricated compliant machines, including an antagonistic pair of fluidic elastomer actuators (a primary component in most soft robots). During printing, we retained unreacted pockets of M.S. and V.S. that permit autonomic self-healing, via sunlight, upon puncture of the elastomeric membranes of the soft actuators.

3.2 Introduction

Advances in material science and manufacturing technologies permit the fabrication of machines comprised entirely of soft components. Such devices deform

continuously about their surface, respond to external loads via mechanical compliance, and can perform complex functions in uncontrolled environments¹⁻³. All of these advantages stem from the use of resilient, highly extensible materials with low elastic moduli ($E \sim 1 \text{ kPa} - 10 \text{ MPa}$) similar to biological tissues⁴. These new capabilities can be readily applied to many fields including robotics, stretchable electronics and biomedicine. Soft machines, however, are highly constrained in their construction due to the current practical limitations of lithography and molding processes⁵.

Shaping polymers from rigid molds is the most common method for manufacturing elastomeric devices because it is easy and compatible with a wide variety of chemistries; this strategy, however, is architecturally limited to prismatic structures restricting the design and function of soft machines^{6,7}. Additional labor intensive fabrication steps can combine such molded objects into useful devices, but 3D printing has the potential to simplify and expedite the manufacturing process for hierarchical builds. Direct Ink Writing (DIW) enables the 3D printing of elastomeric chemistries, but the process must choose between high resolution or expedited print times; even with multiple printheads, forming large and complex geometries at high resolution requires long processing times. Further, overhanging designs require sacrificial supports, and more complex architectures are entirely un-printable^{8,9}.

By comparison, stereolithography (SLA) enables rapid (draw rate $\sim 50 \text{ cm}\cdot\text{hr}^{-1}$)¹⁰, direct fabrication of intricate 3D geometries with micron sized resolution¹¹⁻¹⁴. Fig. 3.1A shows a schematic of a bottom-up SLA printer where patterned light travels through a transparent window onto the base of a vat of liquid photopolymer, curing and adhering it to the build stage or previously printed layer. A horizontal shearing force removes the newly formed solid from the substrate window, the part is then translated up one layer height and the low apparent viscosity liquid resin replenishes the build area prior to next light exposure. A common strategy to permit easy delamination is to create a liquid interface between the build window and the cured photopolymer by using a substrate that releases an oxidant, often molecular oxygen, that can stabilize free radicals and obstruct the polymerization reaction. This requirement constrains SLA chemistries to those that undergo free radical chain-

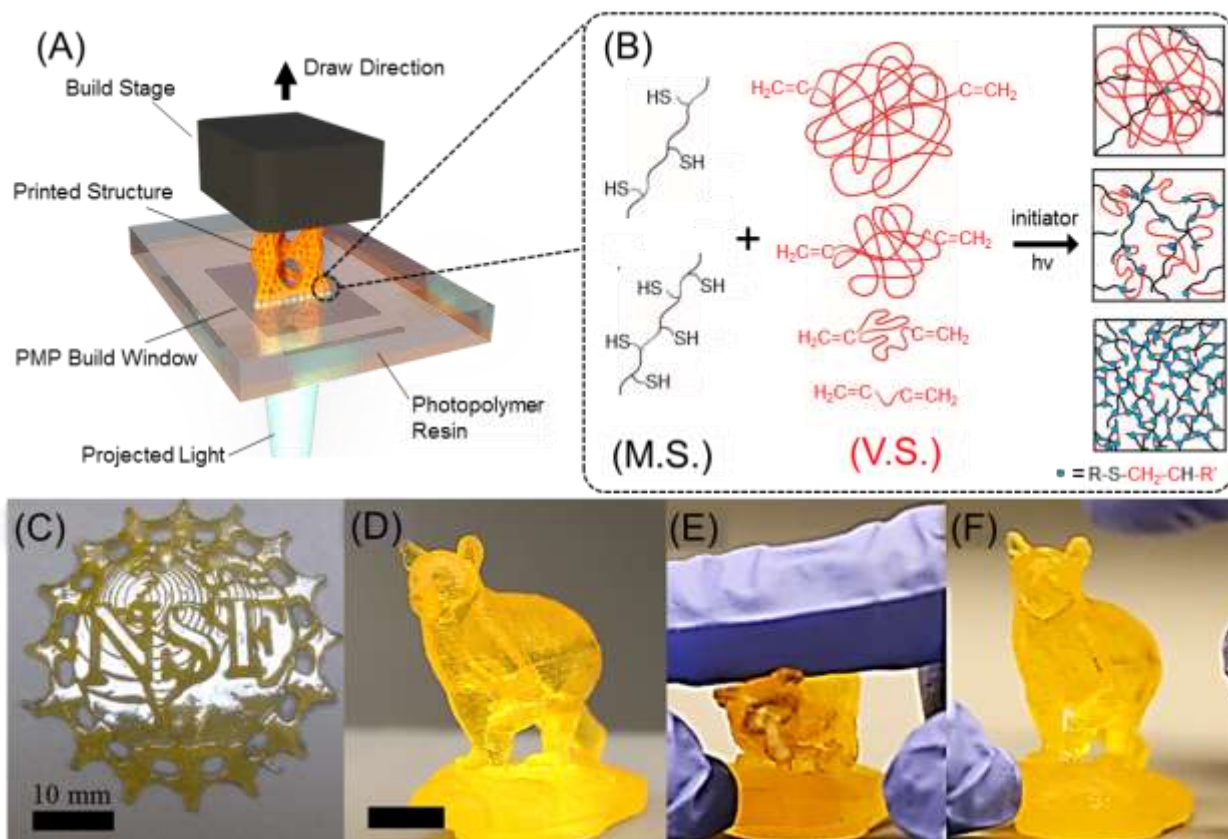


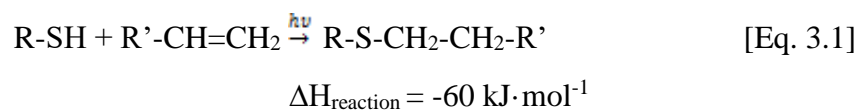
Figure 3.1: An overview of the stereolithography printer, thiol-ene photochemistry and printed demonstrations. (A) A bottom-up SLA printer showing a 3D solid object forming under exposure to patterned light. (B) Photopolymerization reaction schema. Appropriate selection of the M.S. thiol density and molecular weight of V.S. permit tuning of the polymer network. As printed (C) NSF Logo from 2.5%17200 resin, Cornell University's Touchdown the Bear mascot with hollow center from 5%6000 resin (D) before (E) during and (F) after manipulation.

growth polymerization (CGP) upon photoirradiation ultimately limiting the set of available SLA materials. Major efforts in this field are directed towards increasing the library of compatible materials.

Soft machines often necessitate the use of materials with low Young's moduli, high resilience and large ultimate elongations. The SLA processing requirements (i.e., fast, controlled photopolymerization from a low viscosity ($v_{app} < 5 \text{ Pa}\cdot\text{s}$)¹⁵, oxygen-inhibited resin) prevent such soft elastomeric chemistries from being readily accessible for printing¹⁶. To date, the majority of SLA formulations are concentrated solutions of acrylate monomers and crosslinkers that rapidly reach their gel point upon photoexposure, which is necessary for printing; however, the uncontrolled propagation reaction during CGP leads to further chain-growth, ultimately yielding dense, stiff and

brittle networks that display significant shrinkage and incorporate large residual stresses. Only a few works report SLA printed parts with ultimate strains, $\gamma_{ult} > 100\%$. One strategy is to print oligomeric acrylate melts that require large photodosages ($H_e > 150 \text{ mJ cm}^{-2}$) and custom printers that maintain high resin temperatures to reduce resin viscosity and overcome slow polymerization kinetics^{17,18}. The Carbon™ FPU and EPU materials offer large elongations, but only after a post-processing heat treatment polymerizes a latent polyurethane network. The printer required to use these proprietary materials is also prohibitively expensive for most research groups¹⁹. The high elastic moduli ($E > 3 \text{ MPa}$) of these polyurethanes greatly exceeds that of the soft biological systems (i.e., stromal tissue (3 kPa)²⁰, skeletal muscle (12 kPa)²¹ and cartilage (500-900 kPa)²² that soft robots and biomedical devices seek to replicate. Additionally, the most extensible of these materials possesses poor resilience at room temperature owing to the irreversible deformation of soft-segments along their polymer backbone¹⁸. Thus, current acrylated-based SLA materials are impractical for soft machines that require high fatigue strength or cyclic loading (e.g., springs, living hinges and soft robots).

Thiol-ene chemistry, or alkyl hydrothiolation, is a well-known reaction compatible with photo-initiation, resulting in the formation of an alkyl sulfide from a thiol and alkene as shown in Eq. 3.1²³.



This highly exothermic reaction proceeds rapidly and in such a high yield as to be widely regarded as a form of “click-chemistry”²⁴. Photoiniated thiol-ene reactions yield homogenous polymer networks that show reduced shrinkage and exhibit a rapid increase in gel fraction over a small photodosages²⁵. Unlike CGP of acrylates, where undesired propagation reactions can continue for days after gelation,¹⁵ the free radical generated on the alkene is immediately satisfied by a hydrogen abstraction from the thiol. This step-growth polymerization (Fig. 3.1B) and high conversion combine to provide fine control of the resulting photopolymer’s network density, and thereby mechanical properties²⁶.

Without the ability to kinetically stabilize or quench free radicals, click-reactions are incompatible with oxygen-inhibited methods for delamination from window substrates likely explaining the lack of SLA printed elastomers from known thiol-ene chemistries²⁷⁻³⁰. To circumvent this issue, prior work on printing tightly crosslinked pre-ceramics³¹ employed a floating layer of fluorosiloxane lubricant above a polydimethylsiloxane (PDMS) window. The transient nature of this liquid layer limits the printed objects to short build heights (~ 2 cm) and low cross sectional areas. Additionally, the commonly used PDMS window coating absorbs species from the resin which cloud the window over time, reducing light flux and photopatterning resolution. Our work further enables elastomeric thiol-ene material chemistries for SLA by using a new, low surface energy, high transparency poly-4-methylpentene-1 (PMP) build window that allows for easy delamination of printed parts and does not degrade over time.

3.3 Results

Ember™ by Autodesk, a commercial desktop SLA printer, uses light emitting diodes ($\lambda = 405$ nm, $E_e \sim 22.5$ mW·cm⁻²) to project 1280 x 800 pixels on to a build area of 64 x 40 mm. Widely available and inexpensive (< \$1 for a 75 mm x 50 mm x 1 mm sheet), we used PMP to replace the conventional PDMS build window in the printer. PMP is stiff, transparent (>90% transmission at 400nm, > 80% transmission at 325 nm), and oxygen permeable (12,000 cm³ mm m⁻² d⁻¹ MPa⁻¹ at 25 °C)³². A linear, isotactic polymer with a low surface tension (24 mN m⁻¹), PMP is a great release substrate with low separating forces from a variety of materials, including siloxanes. Additionally, PMP's excellent chemical resistance and low swelling in common solvents prevents performance degradation in the build window over long periods. These windows do not change appreciatively in their surface energy, as measured using goniometry (Fig. 3.6), over 100s of hours of use.

Our resins use a blend of poly-(mercaptopropyl)methylsiloxane-co-dimethylsiloxane (M.S.: $M_w \sim 6,000-8,000$) and bifunctional vinyl terminated PDMS (V.S.). PDMS, a class of silicones, is a widely used elastomeric material owing to its excellent mechanical properties, chemical inertness, low toxicity, and resistance to

thermal degradation. Functional groups, including vinyl and mercaptan, can be added along the polymeric backbone to impart desired chemical reactivity to the PDMS materials platform. We further narrowed the polymer compositions by considering the rheology of the liquid resin and the mechanical properties of the polymerized elastomer: high molecular weight PDMS ($M_w > 50,000$) is too viscous for fast printing and low molecular weight PDMS yields highly crosslinked and brittle elastomers³¹. We control the photopolymerized network structure by selecting the relative density of pendant thiol groups on the M.S. (2-3 mole% and 4-6 mole%) and varying the length of the backbone of the V.S. ($M_w \sim 200, 800, 6000, 17200, 42000$) as shown in Fig. 3.1B. To promote thiol-ene conversion, we maintain a 1:1 thiol to vinyl stoichiometry in our materials system (table 3.1). By convention, we refer to our resins by the molar fraction of thiol groups followed by the molecular weight of the vinyl PDMS (e.g. 2.5%17200 is a blend of 2-3% M.S. in V.S. with a molecular weight of 17,200). The addition of a small amount of photoinitiator (diphenyl (2,4,6-trimethylbenzoyl) phosphine oxide [TPO]) and absorptive species (Sudan I) permits high resolution ($\sim 50 \mu\text{m}$ in plane, Fig. 3.7) fabrication via SLA from these resins as exemplified by Fig. 3.1C-1F.

Photopolymerization

Characterization of the photopolymerization helped inform the print parameters (i.e., time of exposure per layer) for each resin. Fig. 3.2A and Fig. 3.2B highlight three representative blends that have the flow properties compatible with our SLA system and yield tough silicone elastomers. Prior to exposure, these blends exhibit low apparent viscosities ($v_{app} < 5 \text{ Pa}\cdot\text{s}$) sufficient to evenly recoating the build layer¹⁵. As expected with thiol-ene click reactions, we note a rapid gelation as inferred by the crossover in the storage, G' , and loss moduli, G'' , measured using oscillatory rheology (frequency, $\omega = 1 \text{ Hz}$ and amplitude, $\Gamma = 1\%$ strain). Compared to photopolymerized acrylate based elastomer resins^{18,33}, gelation happens within our chemistry at much lower photodosages ($H_e \sim 10 \text{ mJ cm}^{-2}$) enabling more rapid build speeds ($\sim 3 \text{ cm/hr}$) with the light sources used in commercial printers. We report data for all ten blends in Fig. 3.8 and table 3.1. The evolution of storage and loss moduli in all resins plateau immediately after gelation, consistent with click reactions that rapidly reach

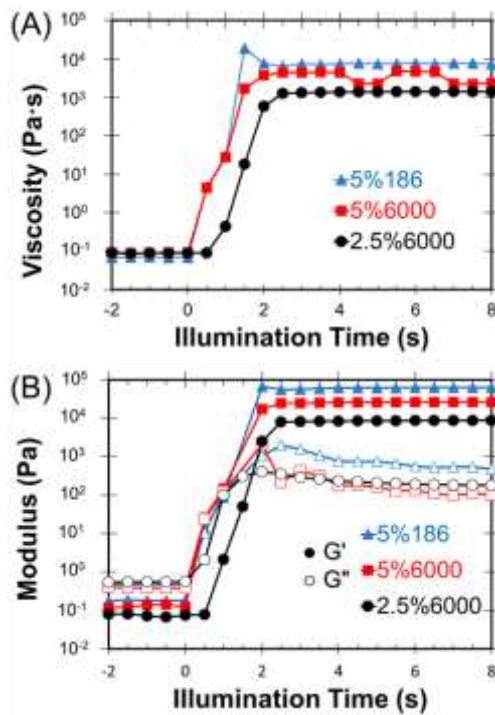


Figure 3.2: Photopolymerization behavior of select resins. The time-evolution of the resin's complex viscosity (A) and storage and loss moduli (B) under photoexposure ($E_c = 10 \text{ mW}\cdot\text{cm}^{-2}$, $\lambda = 400\text{-}500 \text{ nm}$).

completion. The different magnitudes of moduli highlight the wide range of possible mechanical properties.

Controllable Mechanical Properties

We investigated the range of mechanical performance by conducting tensile tests of our SLA materials in accordance with ASTM D638. Dogbone test coupons were formed via photopolymerization of the resins in a mold to rapidly iterate through samples. Our mechanical tests reveal a wide range of possible elastic moduli ($6 < E < 287 \text{ kPa}$), ultimate stresses ($13 < \sigma_{\text{ult}} < 129 \text{ kPa}$) and ultimate elongations ($0.45 < \gamma_{\text{ult}} < 4$) within this materials chemistry. Table 3.3 contains more detailed mechanical data for all blends. Fig. 3.3A depicts representative tensile data for these blends; for further discussion, we focus on the 5% 186, 5%6000, 2.5%6000 resins which demonstrate the wide range of elastic moduli and ultimate elongations possible in this material system.

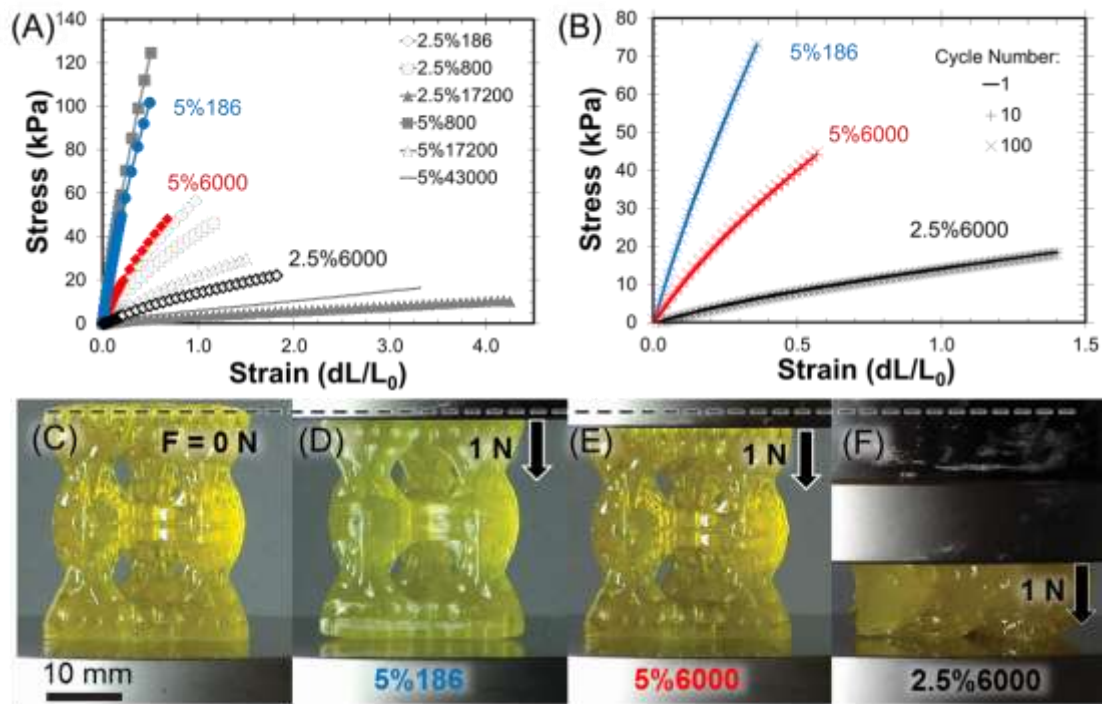


Fig. 3.3: Mechanical Behavior of the photopolymerized resins. (A) Representative data of tensile tests to failure for all blends. (B) Cyclic tensile tests to 75% of the ultimate elongation. Printed Kagome Tower structures under different compressive loads: (C) 5%6000 material at $F=0$ N; (D) 5%186 at $F=1$ N; (E) 5%6000 at $F=1$ N; (F) 2.5%6000 at $F=1$ N.

In addition, to tunable elastic moduli and ultimate elongations, these SLA demonstrate excellent resilience; this property is required for any useful soft machine that will undergo more than a few actuation cycles. Our photopolymerized siloxane systems show great fatigue resistance with little hysteresis at 75% of the achievable ultimate strain (i.e., $0.75 \cdot \gamma_{ult}$) over at least 100 cycles (Video 3.2 and Fig. 3.3B). Fig. 3.3C shows towers made from Kagome lattices that are extremely difficult to fabricate at these scales with traditional molding techniques³⁴. Fig. 3.3D-F and Video 3.3 show structures made from 5%186, 5%6000 and 2.5%6000 blends, respectively, undergoing different amounts of deformation and buckling in response to a 1N compressive load. The high strain and resilience, coupled with low elastic modulus of these materials are similar to biological tissues and ideal for manufacturing soft robots.

Printing Soft Machines

Fluidic Elastomer Actuators (FEAs) are examples of soft machines that bend when internal channels are pressurized by a fluid and expand³. 3D printing has been used to

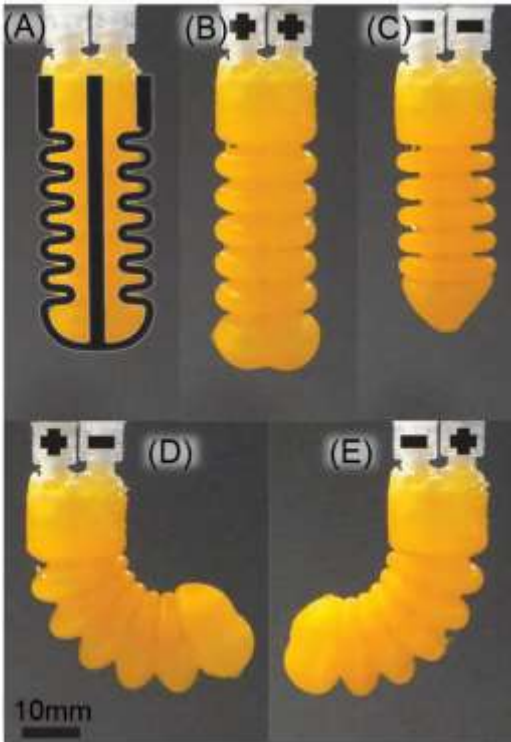


Figure 3.4: **A monolithic device as printed from the 5%6000 resin with a pair of antagonistic FEAs with: (A) both chambers deflated; (B) both chambers inflated; (C) both chambers evacuated; (D) and (E) one chamber inflated and the other evacuated.**

print FEAs with great success; ^{9,14,35-38} however, the ability to rapidly and directly print whole actuators out of highly resilient and extensible materials has not been demonstrated. FEAs deform continuously about their surface which can enable a variety of locomotive gaits^{35,39-42} and the manipulation of delicate objects of arbitrary shape ². With our 5%6000 blend, we directly printed monolithic, synthetic antagonistic muscles ¹⁴ containing a pair of FEAs (Fig. 3.4A). By pressurizing or evacuating the chambers individually, we demonstrate elongation (Fig. 3.4B), contraction (Fig. 3.4C), and bidirectional actuation over $>180^\circ$ (Fig. 3.4D and Fig. 3.4E). The inflation of one actuator drives the deflation of the other, resulting in rapid cycle speed ~ 250 ms as shown in Video 3.4. By inflating and deflating the individual actuators from 0 to 14 kPa alternatively, this device cycled $\sim 50\%$ of the maximum actuation amplitude over 5,000 times.

Autonomic Self-Healing via Sunlight

FEAs, like balloons, fail when a hole or tear in the body of the actuator prevents the creation of a pressure differential between a fluidic channel and the environment. Our material system permits rapid autonomic self-healing via sunlight induced photopolymerization that recovers actuation capability from such punctures. Fig. 3.5A shows an antagonistic FEA hydraulically pressurized with unreacted low-viscosity prepolymer resin. We embedded this resin during the printing process by simply polymerizing the structure around the prepolymer, this technique is similar to that for embedding inert hydraulic fluid in polyjet printing⁴³. To demonstrate the self-healing efficacy, we pierced the actuator using a scalpel (Fig. 3.5B) and the actuating

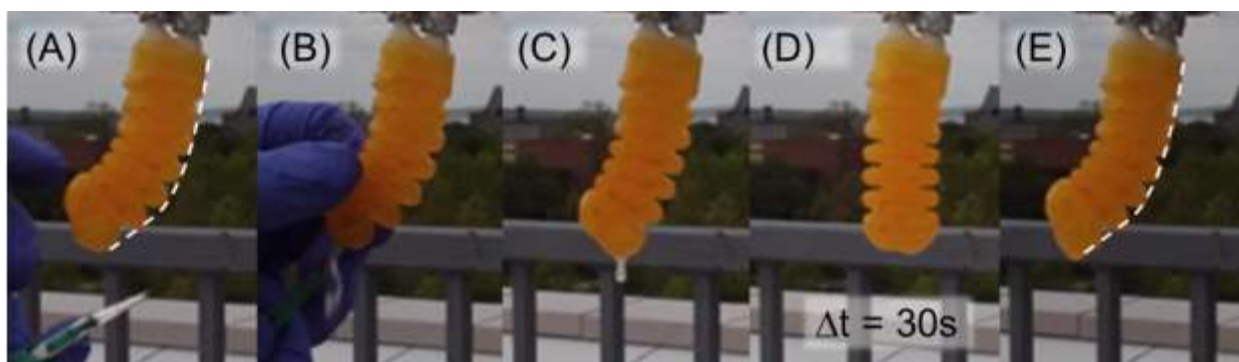


Figure 3.5: Synthetic antagonistic muscle actuator printed from the 2.5%186 resin: (a) pressurized with low-viscosity prepolymer resin; **(b)** pierced by a scalpel; **(c)** pressurized fluid draining; **(d)** autonomic self-healing via ambient sunlight in the relaxed state for 30 seconds **(e)** returning to its original actuated state (dashed line) with re-pressurization.

fluid escaped as the pressure equilibrated with atmosphere (Fig. 3.5C). Unlike acrylate resins, which are oxygen-inhibited and require large photodosages to cure, photorheology (Fig. 3.2) shows that our thiol-ene resins polymerize in the presence of oxygen at low, optical photodosages ($H_e < 20 \text{ mJ}\cdot\text{cm}^{-2}$, $\lambda = 400\text{-}500\text{nm}$). Thus, ambient sunlight ($\sim 15000 \text{ cd}\cdot\text{m}^2$ as measured by Screen Luminance Meter M208) rapidly provides the newly exposed thiol-ene fluid with sufficient spectrum and illumination to polymerize and re-seal the torn actuator within 30 s (Fig. 3.5D). The punctured FEA rapidly healed, allowing re-pressurization and return of the device to its original actuated state as shown in Fig 3.5E. The entire sequence is shown in real time in Video 3.5.

3.4 Experimental

Materials

Vinyl terminated polydimethylsiloxanes (V.S.) with varying molecular weights (Mw): 186, 800, 6000, 17200 and 43000 were added to their stoichiometric equivalent quantities of [2-3% (mercaptopropyl)methylsiloxane]-dimethylsiloxane (M.S.) and [4-6% (mercaptopropyl)methylsiloxane]-dimethylsiloxane (M.S.) copolymer in 1:1 ratios as shown in Table 3.1. All the siloxanes were procured from Gelest, Inc. To these mixtures diphenyl (2,4,6-trimethylbenzoyl) phosphine oxide dissolved in toluene (10 mg/100 μ L) was added to obtain 1% (w/w) of photoinitiator to polymer. The polymer solutions were then mixed in a planetary mixer (Thinky-ARM 310) for 30 s.

Photorheology

A photorheometer (DHR3, TA instruments) coupled with a light-source (Omniscure Series 1500, Lumen dynamics) and filter ($\lambda = 400$ -500 nm) with a constant frequency and amplitude ($\omega = 1$ Hz, $\Gamma = 1\%$ strain) oscillatory shear mode was used to determine the cure behavior of the resin: evolution of apparent viscosity and the complex moduli. A parallel plate (diameter = 20 mm) geometry was used with a gap size of 1 mm. The power density at the sample was measured to be $9 \text{ mW}\cdot\text{cm}^{-2}$ using a Silver Line UV Radiometer (230-410 nm). Data for each sample was collected in triplicate and with the average reported.

Mechanical Tests

Resins were poured into dog-bone shaped coupons (width = 4 mm, depth = 1.5 mm and gage length = 13 mm) and cured with $80 \text{ mW}\cdot\text{cm}^{-2}$ projected light (Omniscure Series 1500; Lumen dynamics) for 60 s to ensure complete exposure. Uniaxial tensile tests were carried out for each type of resin using a universal testing machine (Zwick/Roell Z1010, Testing systems) at a cross-head movement rate of 10 mm min^{-1} according to ASTM D638 standard. Strain values were calculated by comparing the change in crosshead displacement to the original gage length. Samples that slipped or fractured as a result of grip stresses were discarded and data was collected until at least seven specimens were successfully tested to failure. Elongation at break, engineering elastic modulus ($0.005 < \gamma < 0.02$), ultimate stress and toughness were evaluated for all the resin systems from the stress-strain curves as reported in Table 3.3. Cyclic tensile tests were also conducted to understand the fatigue strength of this materials

system. Dog-bone specimens were made from the 5%186, 5%6000, and 2.5%6000 resins were subjected to load-unload cycles at a rate of 10% L_0 min⁻¹. The specimens were stretched to ~75% of their ultimate elongations (36%, 56.25% and 138.75% respectively) and then unloaded to 0% strain for each cycle.

3.5 Conclusions

We report the use of thiol-ene photochemistry enabled by a PMP build window for the stereolithography of siloxane elastomers possessing a wide range of mechanical properties. This versatile platform offers the ability to obtain multiple polymer network densities without substantially decreasing the photopolymerization rate or increasing the viscosity beyond SLA limitations. The ability to rapidly fabricate highly extensible silicones with stiffnesses similar to natural, organic tissues in complex 3D architectures offers new technological applications, particularly in the field of soft robotics. To prove this feature, we have demonstrated directly printed, long life cycle antagonistic actuator pairs. We further capitalize on the rapid polymerization of our thiol-ene based formulations at ambient conditions by using our low-viscosity resin as the pressurizing fluid enabling autonomic self-healing in sunlight after rupture in our 3D printed FEAs.

The reported blends are simple stoichiometric equivalents of thiol and vinyl bearing PDMS polymers, but there is potential to increase functionality by modifying the chains to contain an excess of thiol/vinyl groups or even other chemical groups for improved biocompatibility or molecular recognition. Small loading fractions of filler particles (e.g., iron-oxide nanoparticles) might also introduce improved mechanical properties or new optical, electrical or magnetic properties into the printed siloxanes. Additionally, the inexpensive PMP window should enable 3D printed thiol-ene chemistries to be extended to other polymeric back-bones as well as other carbon-carbon double bond groups beyond vinyl, including acrylates.

3.6 Supplemental Information

Video 3.1: Touchdown the Bear Being Manipulated

https://www.dropbox.com/s/ayj23pmdfyqf53o/MovieS1_TouchdownTheBearManipulated.MOV?dl=0

Video 3.2: Cyclic Tensile Test

https://www.dropbox.com/s/riop545a8bmj06t/MovieS2_CyclicTensileTest.mp4?dl=0

Video 3.3: Kagome Tower Compression

https://www.dropbox.com/s/ojmo20fqm6m451q/MovieS3_KagomeTowerCompression.mp4?dl=0

Video 3.4: Fluidic Elastomer Actuators at 2 psi

https://www.dropbox.com/s/zyhsa6bn9lygoap/MovieS4_FEAs_2psi.mp4?dl=0

Video 3.5: Autonomic Self-Healing of FEA

https://www.dropbox.com/s/7w4k99kfshi98a0/MovieS5_Autonomic_SelfHealing.mp4?dl=0

Resiliency of the PMP Windows

Qualitatively, we have been able to successfully use the same build window in the printer for 100s of hours, likely due to PMP's low surface tension, low swellability in common solvents, and chemical inertness. As we believe the primary mechanism for its success as a build window is low surface energy to promote delamination, we quantified the change in surface energy over time using goniometry, or contact angle measurements. We first performed these tests on a clean, unused sheet of PMP and then on a build window that has spent 100s of hours in use in our printers. Using 15 μL drops of water, we measured (VGA Optima Contact Angle) the contact angle of the pristine PMP window to be $98.15 \pm 7.38^\circ$ compared to $95.95 \pm 4.57^\circ$ for the used build window. Fig. 3.6 shows two representative droplets. The similar wettability of these two surfaces suggests that there is little fouling of the surface, and therefore little change in the surface energetics over this duration of use.”

Printed Resolution

The resolution of a stereolithography resin is highly dependent on the printer used and parameters chosen. The Autodesk Ember printer project 1280 x 800 pixels on to a build area of 64 x 40 mm which yields a nominal x and y resolution of ~ 50 microns. The photoirradiation dosage, absorptivity of the resin and build stage translations combine to determine the z-axis resolution. For the printed synthetic muscle device shown in Fig. 3.4 of the main text, we used 5%6000 resin containing 1 mg mL^{-1} of Sudan I, with a desired layer height of 100 microns and photoirradiation dosage of $w_e = 90 \text{ mJ cm}^{-2}$. In Fig. 3.5, the 2.5%186 resin was utilized as the base material (with 1 mg mL^{-1} Sudan I) and pressurizing fluid. Fig. 3.7 shows the surface of that monolithic device as measured 3D laser scanning microscope (Keyence VK-X260). Following

the build direction (z-axis), the blue line displays a wave with an amplitude of $\sim 50 \mu\text{m}$ and a period of roughly $175 \mu\text{m}$. The amplitude corresponds to the x and y resolution demonstrating that the 5%6000 resin reaches the nominal resolution of the projected pixel size. We infer z-axis resolution from the period which is well above the build stage translations of 100 microns in between printing steps. While some photopolymerization beyond the desired layer height might improve adhesion between adjacent layers, increasing the resin's absorptivity, or decreasing the photoirradiation could enable greater z-axis resolution.

Photo Differential Scanning Calorimetry

Differential scanning calorimetry (DSCQ1000, TA instruments) was conducted under exposure to light. The sample and reference pans were left uncovered inside a modified cell with a dual light guide adapter. The cell was aligned such that the reference and sample pans received identical light intensity from the light source (Omnicure Series 1500, Lumen dynamics). As in the photorheology experiments, a filter was used ($\lambda = 400\text{-}500\text{nm}$) and the power density was measured to be $E_e \sim 10 \text{mW}\cdot\text{cm}^{-2}$. Samples were equilibrated at $30 \text{ }^\circ\text{C}$ for 2 minutes prior to exposure for 3 additional minutes with a flow rate of 50mL min^{-1} . All data was analyzed in TA Quantitative Analysis software. Normalized heat flow curves (mW mol SH^{-1} vs time), as shown in Fig. 3.9, were integrated over the exposure using a horizontal sigmoidal baseline and scaled relative to enthalpy of polymerization for thiol-ene reactions ($60 \text{kJ}\cdot\text{mol}^{-1}$) to obtain the total conversion. For the 2.5%186 and 5%186 resins, the molecular mobility of the shorter V.S. species leads to a slightly faster conversion rate for the first second of polymerization; however, the low molecular weight ultimately limits the final conversion to $\sim 82\%$ likely due to a reduced probability that the chain is long enough for both vinyl end groups to reach thiol counterparts on other polymers. When the V.S. molecular weight increases, a higher conversion (i.e., 96% conversion for 2.5%6000) becomes obtainable.

3D Printing

Files for the Kagome Tower, NSF Logo, and Stanford Bunny were obtained freely on the internet. A .obj file of Touchdown the Bear statue was obtained from artist Brian Caverly and modified using Meshmixer™ software. All other files were created

using Solidworks™ software. Using Autodesk Print Studio™, each design was imported, modified, sliced into discrete photopatterns, and converted to a .tar.gz format. The exposure times used varied from 1-5 s depending on the resin composition and layer height. To reduce jamming, the separation slide velocity was set to 2 rpm. Autodesk Ember 3D printer was used to print all objects shown. We mixed Sudan I with toluene in the ratio of 1 mg mL⁻¹ and added this absorptive species to the resins before printing to limit cure depth to the layer height and improve z-axis resolution. Fig. 3.10 shows that the printed photopolymer blend is optically translucent, but without the addition of Sudan I, the orange absorptive species, z-axis resolution is poor and layer heights are clearly visible.

Fluidic Elastomer Actuator:

Fig. 3.11 shows a schematic of the monolithic synthetic muscle device composed of a pair of antagonistic fluidic elastomer actuators. Two three-way solenoid valves (Parker model 912-000001-031) connected each actuation chamber to both the ambient atmosphere and a pressurized air source at ~ 14 kPa. Inlet connections to the 3D printed objects were sealed by Sil-Poxy™ (Smooth-On, Inc.) silicone adhesive to prevent leakage. Using an Arduino Uno to control each valve, the antagonistic pair of inflation chambers were alternatively pressurized for 250 ms and then depressurized (via venting to the atmosphere) for 250 ms. With this cycling frequency, the actuator achieved steady-state actuation rapidly, with little deviation from the periodic displacement after the initial 1-2 cycles. This stable periodic actuation lasted for >5,000 inflation cycles with no noticeable decay. Periods of greater than 250 ms similarly achieved bidirectional actuation, but at cycle durations of 100 ms or lower no coherent motion was detected.

Table 3.1: The composition of resins that yield a 1:1 stoichiometry between thiol and vinyl groups

M.S. (MWT: 4000-6000)		V.S.	
Thiol Mole %	Amount added (g)	Molecular Weight	Amount added (g)
2-3%	970	186	30
2-3%	884	500	116
2-3%	502	6000	498
2-3%	260	17600	740
4-6%	942	186	58
4-6%	794	500	206
4-6%	338	6000	662
4-6%	152	17600	848
4-6%	66	43000	934

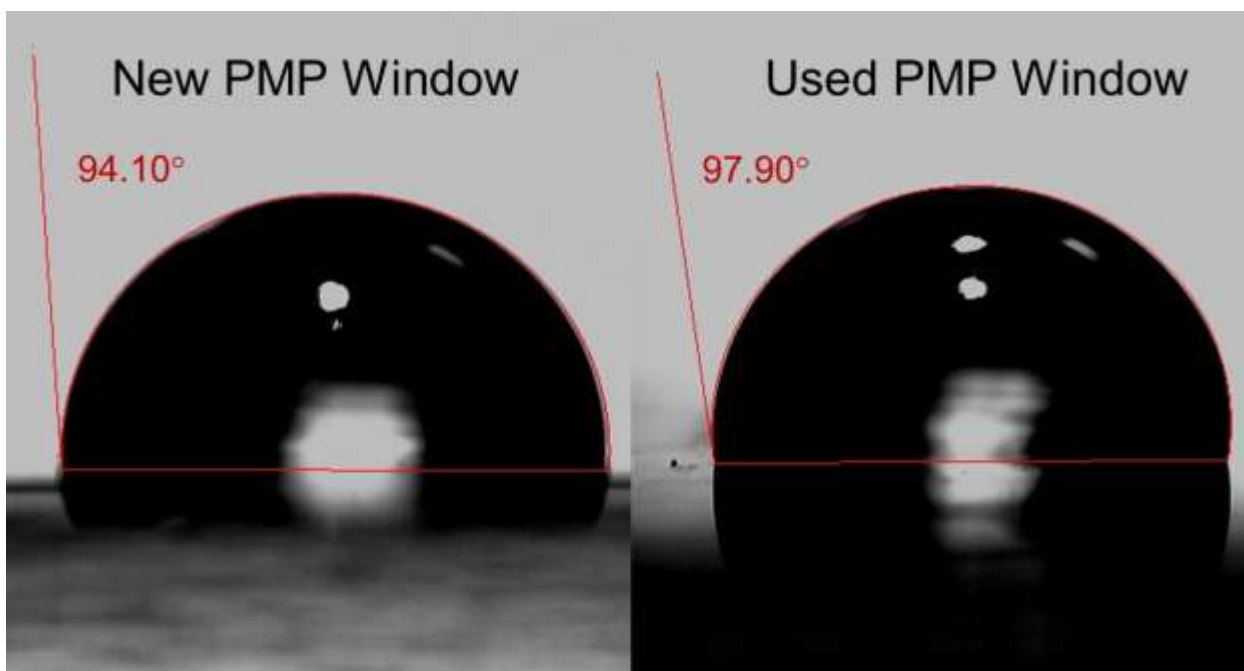


Fig. 3.6: The contact angle between water and PMP Windows before and after 100s of hours of use in the printer.

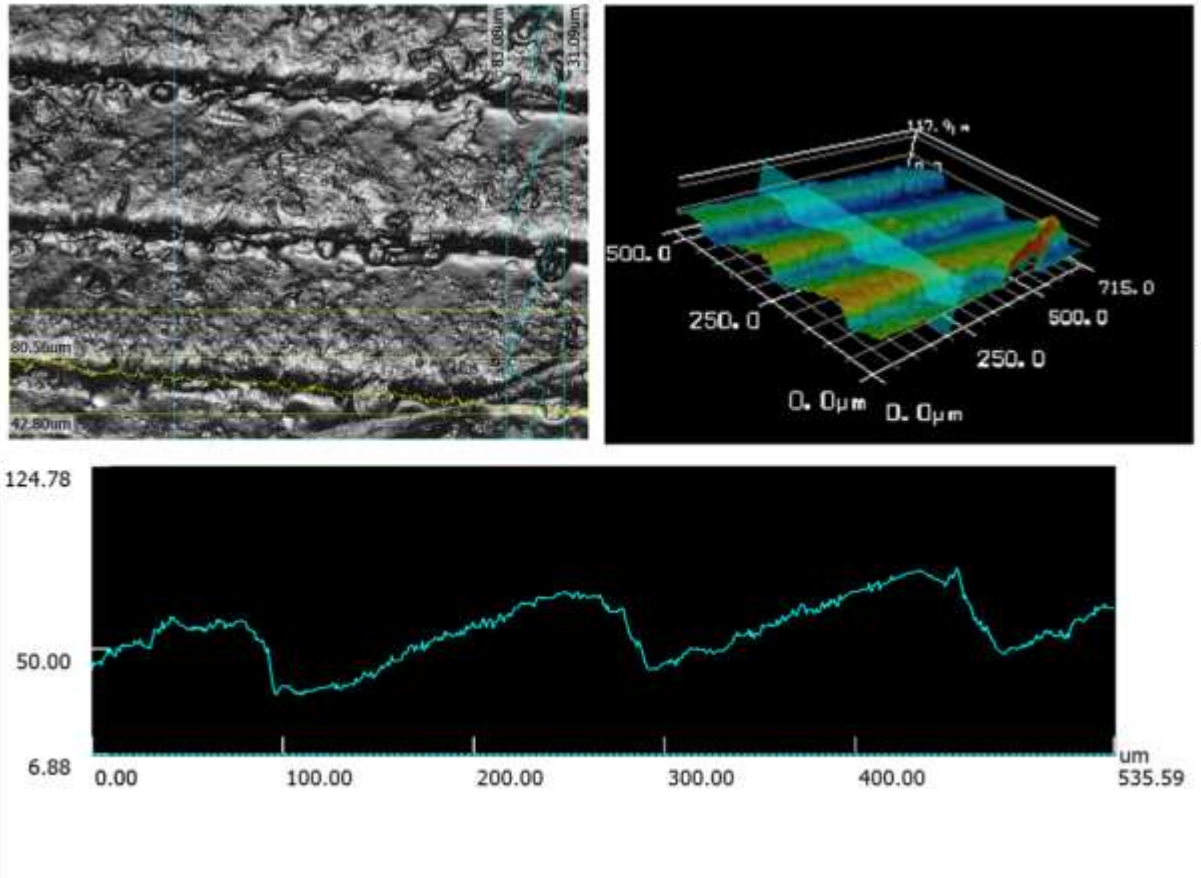


Fig. 3.7: 3D Laser Confocal Microscopy of Monolithic Device of Antagonistic FEAs. The blue line is parallel to build direction (z-axis).

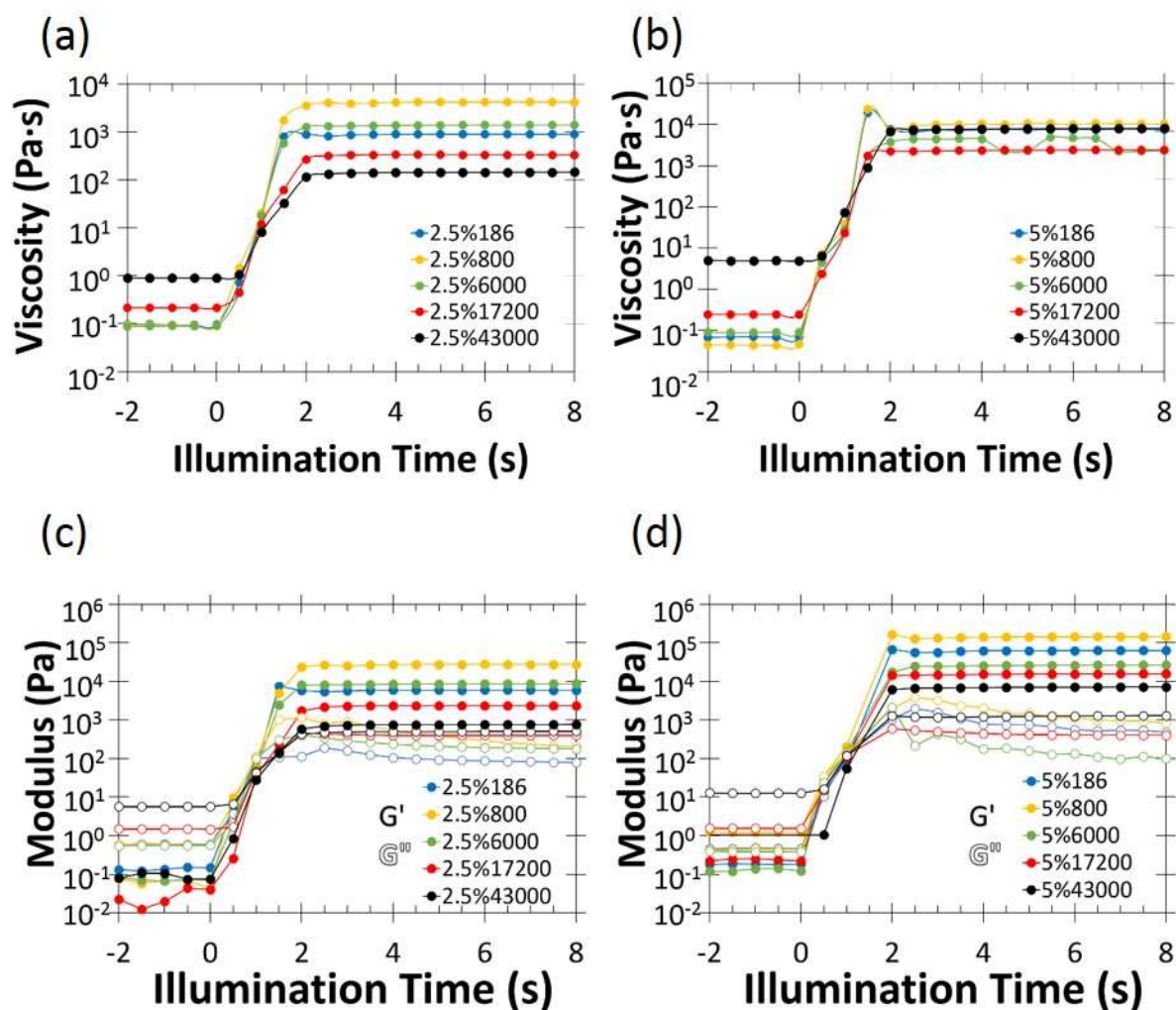


Fig. 3.8: Photopolymerization behavior for all resins. The time-evolution of the complex viscosity for resins based on (a) 2.5% and (b) 5% poly-mercaptopropylmethylsiloxane-co-dimethylsiloxane. The time evolution in the storage and loss moduli under photoexposure for (c) 2.5% and (d) 5% poly-mercaptopropylmethylsiloxane-co-dimethylsiloxane

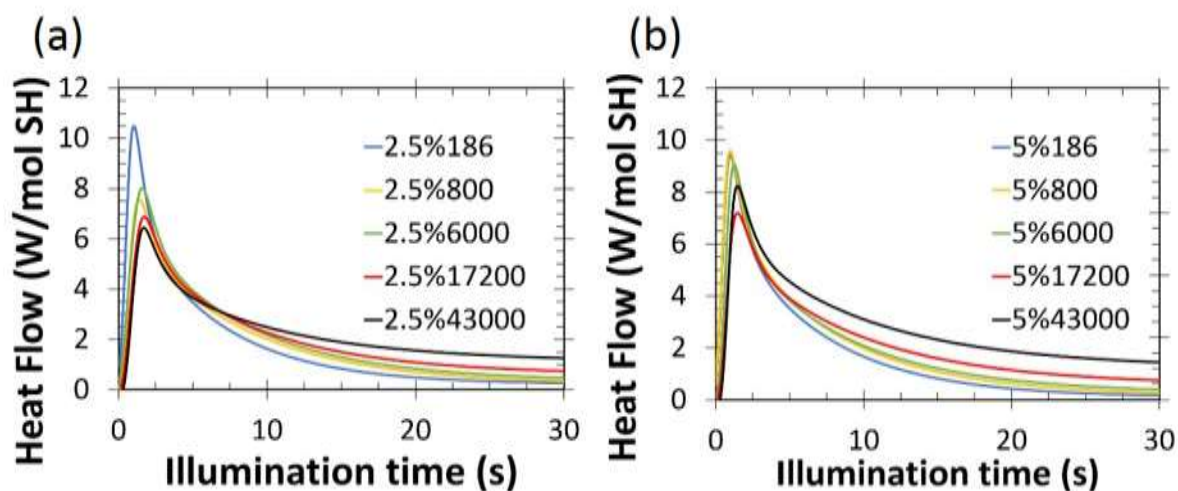


Fig. 3.9: Normalized heat flow vs. illumination time for the blends based on (a) 2.5% and (b) 5% poly-mercaptopropylmethylsiloxane-co-dimethylsiloxane

Table 3.2: Summarized photocure behavior for all blends.

Sample Name	t_{cure} (s)	$\eta_{t=0}$ (Pa.s)	G'_{final} (Pa)	G''_{final} (Pa)	Thiol Conversion (%)
2.5% 186	<1.5	0.089	5600	62	81.8
2.5% 800	<1.5	0.088	24880	72	85.8
2.5% 6000	<1.5	0.089	8620	165	96.8
2.5% 17200	<1.5	0.237	2310	410	83.0
2.5% 43000*	<2.0	0.896	790	536	76.8
5% 186	<1.0	0.057	31610	226	83.9
5% 800	<1.0	0.044	62870	580	96.1
5% 6000	<1.0	0.066	26890	91	91.8
5% 17200	<1.5	0.247	14850	42	87.7
5% 43000	<1.5	1.884	7430	1380	79.3

The time to cure (t_{cure}) is measured by the crossover in storage and loss moduli. The unreacted viscosity $\eta_{t=0}$ was measured for 20 s prior to photoexposure. G'_{final} and G''_{final} are the stable values measured after 60 s of exposure. Similarly, Thiol conversion was calculated from the total enthalpy of polymerization after 60 s of exposure.

Table 3.3: Complete mechanical data for all blends

Sample Name	Modulus E (kPa)	Ultimate Elongation γ_{ult} (%)	Ultimate Stress σ_{ult} (kPa)	Ultimate Toughness ($J m^{-3}$)
2.5% 186	83 ± 11	110 ± 34	64 ± 12	26 ± 12
2.5% 800	56 ± 5	111 ± 22	45 ± 8	21 ± 7
2.5% 6000	19 ± 19	185 ± 29	23 ± 4	16 ± 2
2.5% 17200	6 ± 1	427 ± 49	13 ± 3	20 ± 10
2.5% 43000*	*	*	*	*
5% 186	223 ± 19	48 ± 13	88 ± 19	32 ± 28
5% 800	287 ± 24	54 ± 13	129 ± 20	38 ± 16
5% 6000	85 ± 17	76 ± 15	50 ± 12	20 ± 8
5% 17200	32 ± 6	151 ± 8	31 ± 7	26 ± 8
5% 43000	9 ± 1	348 ± 32	18 ± 4	37 ± 11

*Sample 2.5%43000 was too soft to manipulate and so no measure mechanical properties were measured.

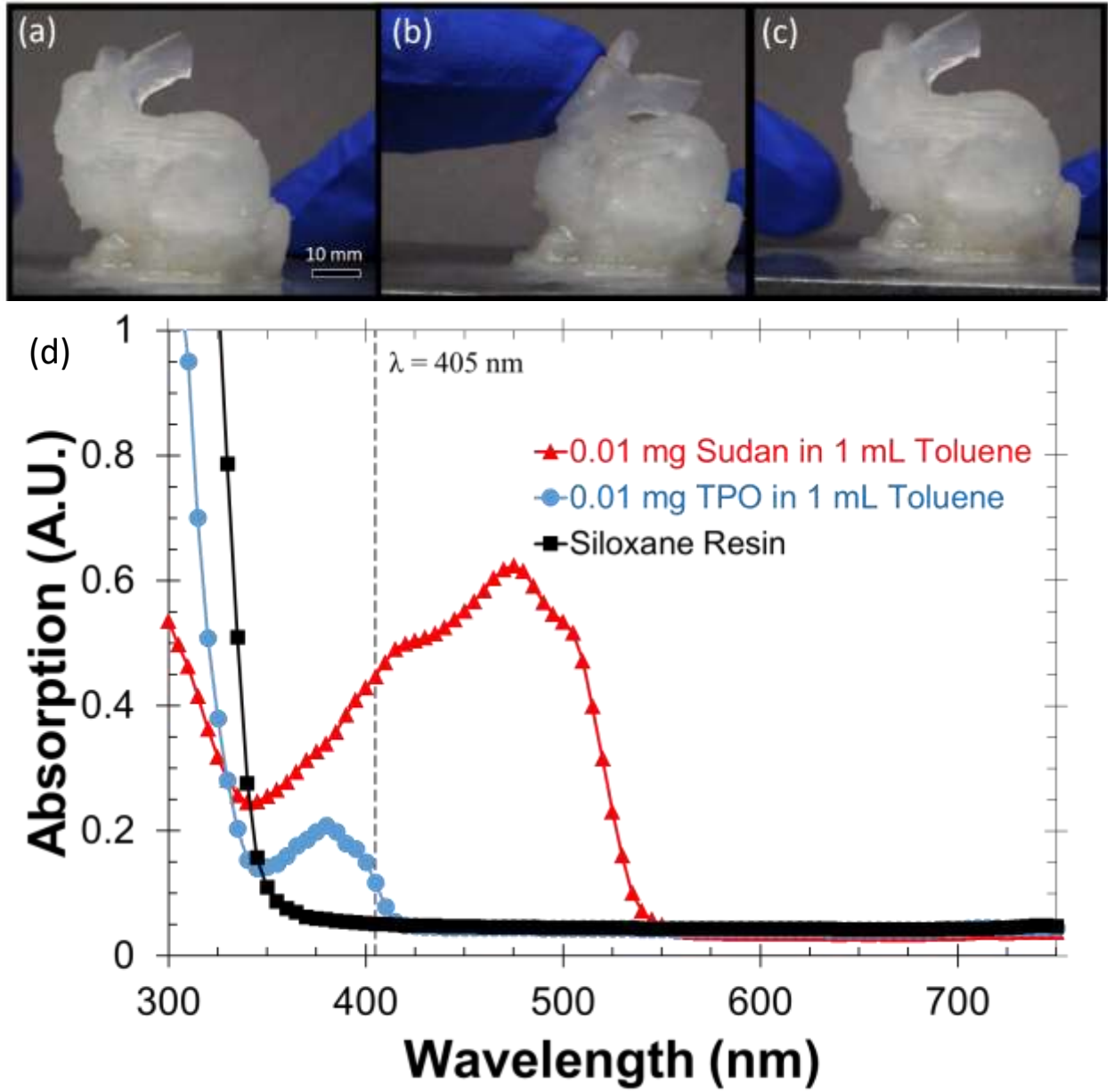


Fig. 3.10: A Stanford bunny model printed from 2.5%6000 material without incorporation of an absorptive species. This complaint structure is shown (a) before, (b) during, and (c) after manipulation and (d) the absorption of the individual components of our resin system

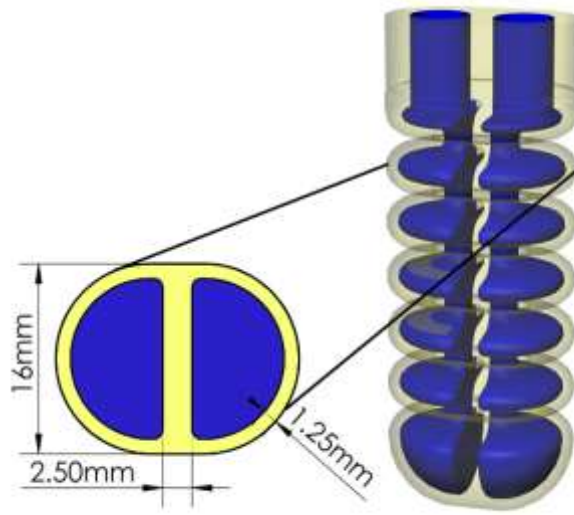


Fig. 3.11: Schematic of Synthetic Antagonist Muscle Device. Fluidic channels are colored blue, printed siloxane colored yellow

REFERENCES

1. Majidi, C. Soft Robotics: A Perspective—Current Trends and Prospects for the Future. *Soft Robot.* **1**, 5–11 (2014).
2. Ilievski, F., Mazzeo, A. D., Shepherd, R. F., Chen, X. & Whitesides, G. M. Soft robotics for chemists. *Angew. Chemie - Int. Ed.* **50**, 1890–1895 (2011).
3. Marchese, A. D., Katzschmann, R. K. & Rus, D. A Recipe for Soft Fluidic Elastomer Robots. *Soft Robot.* **2**, 7–25 (2015).
4. Vogel, S. *Comparative Biomechanics: Life's Physical World*. (Princeton University Press, 2003).
5. Shepherd, R., Correll, N., Petersen, K. & Tolley, M. Advanced Engineering Materials Soft robotics : Review of Fluid-Driven Intrinsically Soft Devices ; manufacturing , sensing , control , and Applications in Human-Robot Interaction. *Adv. Eng. Mater.* **(In Press)**, (2017).
6. Rolland, J. P. *et al.* Solvent-Resistant Photocurable ‘ Liquid Teflon ’ for Microfluidic Device Fabrication. 2322–2323 (2004).
7. Rogers, J. a. & Nuzzo, R. G. Recent progress in soft lithography. *Mater. Today* **8**, 50–56 (2005).
8. Morrow, J., Hemleben, S. & Menguc, Y. Directly Fabricating Soft Robotic Actuators With an Open-Source 3-D Printer. *IEEE Robot. Autom. Lett.* **2**, 277–281 (2016).
9. Yap, H. K., Ng, H. Y. & Yeow, C.-H. High-Force Soft Printable Pneumatics for Soft Robotic Applications. *Soft Robot.* **3**, 144–158 (2016).
10. Tumbleston, J. R. *et al.* Continuous liquid interface production of 3D objects. *Science (80-.)*. 1–7 (2015). doi:10.1126/science.aaa2397
11. Yayue Pan, Chi Zhou & Yong Chen. Rapid manufacturing in minutes: The development of a mask projection stereolithography process for high-speed fabrication. *Proc. ASME 2012 Int. Manuf. Sci. Eng. Conf.* 1–10 (2012). doi:10.1115/MSEC2012-7232
12. Sun, C., Fang, N., Wu, D. M. & Zhang, X. Projection micro-stereolithography using digital micro-mirror dynamic mask. *Sensors Actuators A Phys.* **121**, 113–

- 120 (2005).
13. Choi, J. W. *et al.* Fabrication of 3D biocompatible/biodegradable micro-scaffolds using dynamic mask projection microstereolithography. *J. Mater. Process. Technol.* **209**, 5494–5503 (2009).
 14. Peele, B. N., Wallin, T. J., Zhao, H. & Shepherd, R. F. 3D printing antagonistic systems of artificial muscle using projection stereolithography. *Bioinspir. Biomim.* **10**, 55003 (2015).
 15. Bartolo, P. J. *Stereolithography: Materials, Processes and Applications.* (2011). doi:10.1007/978-0-387-92904-0
 16. Melchels, F. P. W., Feijen, J. & Grijpma, D. W. A review on stereolithography and its applications in biomedical engineering. *Biomaterials* **31**, 6121–6130 (2010).
 17. Ge, Q. *et al.* Multimaterial 4D Printing with Tailorable Shape Memory Polymers. 1–11 (2016). doi:10.1038/srep31110
 18. Patel, D. K. *et al.* Highly Stretchable and UV Curable Elastomers for Digital Light Processing Based 3D Printing. *Adv. Mater.* 1606000 (2017). doi:10.1002/adma.201606000
 19. Stevenson, K. Tallying up the Carbon M1's Total Cost of Ownership. (2016). Available at: <http://www.fabbaloo.com/blog/2016/4/6/tallying-up-the-carbons-total-cost-of-ownership>. (Accessed: 1st January 2017)
 20. Cox, T. R. & Erler, J. T. Remodeling and homeostasis of the extracellular matrix : implications for fibrotic diseases and cancer. **178**, 165–178 (2011).
 21. Butcher, D. T., Alliston, T. & Weaver, V. M. A tense situation : forcing tumour progression. *Nat. Rev. Cancer* **9**, 108–122 (2009).
 22. Athanasiou, K. A., Rosenwasser, M. P., Buckwalter, A., Malinin, S. T. I. & Mow, V. C. Interspecies Comparisons of In Situ Intrinsic Mechanical Properties of Distal Femoral Cartilage. *J. Orthop Res* **9**, 330–340 (1991).
 23. Ravve, A. *Light-Associated Reactions of Synthetic Polymers.* (Springer Science, 2006).
 24. Kolb, H. C., Finn, M. G. & Sharpless, K. B. Click chemistry: Diveverse

- chemical function from a few good reactions.pdf. *Angew. Chemie - Int. Ed.* **40**, 2004–2021 (2001).
25. Hoyle, C. E. & Bowman, C. N. Thiol-ene click chemistry. *Angew. Chemie - Int. Ed.* **49**, 1540–1573 (2010).
 26. Zhang, J. L., Srivastava, R. S. & Misra, R. D. K. Core-shell magnetite nanoparticles surface encapsulated with smart stimuli-responsive polymer: Synthesis, characterization, and LCST of viable drug-targeting delivery system. *Langmuir* **23**, 6342–6351 (2007).
 27. Campos, L. M. *et al.* Applications of photocurable PMMS thiol-ene stamps in soft lithography. *Chem. Mater.* **21**, 5319–5326 (2009).
 28. Carlborg, C. F., Haraldsson, T., Oberg, K., Malkoch, M. & van der Wijngaart, W. Beyond PDMS: off-stoichiometry thiol-ene (OSTE) based soft lithography for rapid prototyping of microfluidic devices. *Lab Chip* **11**, 3136–3147 (2011).
 29. Nguyen, K. D. Q., Megone, W. V, Kong, D. & Gautrot, J. E. Ultrafast diffusion-controlled thiol-ene based crosslinking of silicone elastomers with tailored mechanical properties for biomedical applications. *Polym. Chem.* **7**, 5281–5293 (2016).
 30. Goswami, K., Skov, A. L. & Daugaard, A. E. UV-cured, platinum-free, soft poly(dimethylsiloxane) networks. *Chem. - A Eur. J.* **20**, 9230–9233 (2014).
 31. Eckel, Z. C. *et al.* Additive manufacturing of polymer-derived ceramics. *Science (80-.).* **351**, 58–62 (2016).
 32. *TPX Polymethylpentene.* (2011).
 33. Baudis, S. *et al.* Elastomeric degradable biomaterials by for vascular tissue engineering. *Biomed. Mater.* **6**, (2011).
 34. Jiang, Y. & Wang, Q. Highly-stretchable 3D-architected Mechanical Metamaterials. *Sci. Rep.* **6**, 34147 (2016).
 35. Marchese, A. D., Onal, C. D. & Rus, D. Autonomous Soft Robotic Fish Capable of Escape Maneuvers Using Fluidic Elastomer Actuators. *Soft Robot.* **1**, 75–87 (2014).
 36. Bartlett, N. W. *et al.* A 3-D printed, functionalised graded soft robot powered by

- combustion. *Science* (80-.). **349**, 161–165 (2015).
37. Wehner, M. *et al.* An integrated design and fabrication strategy for entirely soft, autonomous robots. *Nature* **536**, 451–455 (2016).
 38. Schumacher, C. M., Loepfe, M., Fuhrer, R., Grass, R. N. & Stark, W. J. 3D printed lost-wax casted soft silicone monoblocks enable heart-inspired pumping by internal combustion. *RSC Adv.* **4**, 16039 (2014).
 39. Onal, C. D. & Rus, D. Autonomous undulatory serpentine locomotion utilizing body dynamics of a fluidic soft robot. *Bioinspir. Biomim.* **8**, 26003 (2013).
 40. Seok, S. *et al.* Meshworm: A peristaltic soft robot with antagonistic nickel titanium coil actuators. *IEEE/ASME Trans. Mechatronics* **18**, 1485–1497 (2013).
 41. Katzschmann, R. K., Marchese, A. D. & Rus, D. Hydraulic Autonomous Soft Robotic Fish for 3D Swimming. *Intell. Robot. Syst. (IROS), 2011 IEEE/RSJ Int. Conf.* (2014).
 42. Shepherd, R. F. *et al.* Multigait soft robot. *Proc. Natl. Acad. Sci.* **108**, 20400–20403 (2011).
 43. Maccurdy, R., Katzschmann, R., Kim, Y. & Rus, D. Printable hydraulics: A method for fabricating robots by 3D co-printing solids and liquids. *Proc. - IEEE Int. Conf. Robot. Autom.* **2016–June**, 3878–3885 (2016).

CHAPTER 4

CONCLUSIONS

4.1 Summary of Contributions

This work reports recent advances in materials chemistry and manufacturing that enable the direct manufacture of soft, elastomeric machines. The main contributions are highlighted below.

Additive manufacturing, in particular the subset of “3D Printing” technologies, propels the emerging field of soft robotics. Chapter 1 reviews the state of this field while highlighting a major trade-off—conventional manufacture via replica molding permits the use of engineering materials but restricts the design space while 3D printing enables complex architectures but only with limited available elastomeric chemistries.

While the varying 3D printing techniques possess their own limitations, stereolithography offers the best combination of chemical flexibility, design complexity, and deposition rates for custom elastomeric materials. Even with comparatively brittle and stiff materials, directly 3D printing antagonistic systems of artificial muscle using projection stereolithography (Appendix A) enable devices with higher degrees of freedom and rapid cycle speeds ($t_{cycle} \sim 70$ ms).

As shown in Chapter 2, the incorporation of dynamic ionic linkages between anionic nanoparticles and cationic acrylate-based photopolymers maintains excellent printability, i.e. low viscosity and rapid gelation, and mechanical performance in printed devices. These ionic groups serve a dual purpose, the breaking and formation of bonds not only dissipates strain energy, but ions within the printed body also conduct charge under alternating electric fields. While modulating the relative ratio of chemical components tunes the material performance, one exemplary ionic composite material simultaneously possessed low tensile modulus ($E \sim 5.4$ kPa), high ultimate strain ($\gamma_{ult} \sim 425\%$) and high ionic conductivity ($\sigma_{f=1MHz} = 2.9$ S cm⁻¹).

Silicone, or polydimethylsiloxane (PDMS), remains an ideal material for many soft devices. However, most silicone inks for 3D printing fail to realize the same ultimate

elongation as their room temperature vulcanizing (RTV) counterparts. The material chemistry reported in Chapter 3 utilizes thiol-ene click reactions to permit the fabrication of soft, highly extensible ($8 \text{ kPa} < E < 300 \text{ kPa}$, $50\% < \gamma_{ult} < 425\%$) silicone devices from mercaptosiloxane and vinylsiloxane precursor. The benefits inherent to this photochemistry also enable autonomic healing of fluidic elastomer actuators after rupture.

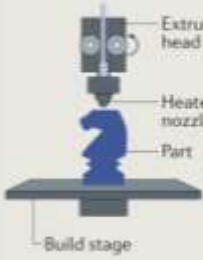
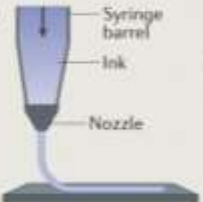
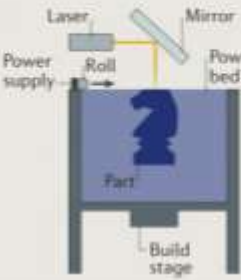
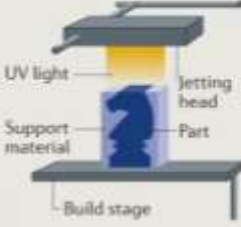
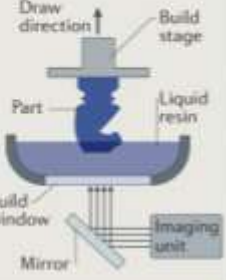
4.2 Future Work and Outlook

In the short term, numerous straightforward pathways exist to expand upon this work and improve the disclosed material chemistries. For example, extending the “ionic composite motif” of Chapter 2 to other acrylate monomers and nanoparticles should enable the printing of tough, functional hydrogels with a wide range of solubility parameters. Here, the different available side groups alter the thermodynamics of swelling, changing the available stimuli for osmotic actuators and chemical sensors. In Chapter 3, I demonstrate a series of silicone resins possessing sufficient moduli, resiliency, and ultimate elongations for soft robotic applications. However, these materials are far less tough than their common room temperature vulcanizing counterparts. In such conventional materials, the addition of particles (usually fumed silica) provide for physical entanglements that improve mechanical performance. However, these improvements correspond to high volumetric loading fractions, typically around 30%, which coincide with dramatic increases in the effective viscosity of the suspension. Such strategies are incompatible with common stereolithography printing. Future work could exploit the thixotropic nature of the polymeric precursors by increasing the shear imposed upon the resin and relax this viscosity requirement ($\eta < 5 \text{ Pa}\cdot\text{s}$) of SLA printing. From a materials perspective, alternative toughening mechanisms like increasing polymer crystallinity (Appendix B), forming interpenetrating double networks, or the post-printing precipitation of nanoparticles from unreacted precursors are viable strategies moving forward.

Looking beyond this dissertation and at the fabrication of soft devices holistically, the best fabrication strategy may include a combination of manufacturing technologies, however, currently-available 3D printing technologies still face various

limitations in terms of resolution, speed, material compatibility and scale-up (Table 4.1). Printing processes based on the melting of solids, such as SLS and FDM, are restricted to the use of thermoplastic materials, which are unlikely to meet the advanced material demands for highly resilient functional components. In contrast, liquid ink-based techniques allow for the chemical modification of the material; for example, in DIW, the only constraint is that the material has to solidify after flowing through the nozzle. Moreover, DIW can be used for multi-material printing. However, the trade-off between speed and resolution (nozzle size) prevents the use of DIW for large-scale manufacturing. Inkjets enable rapid, multi-material printing, but there is currently no elastomer available that exceeds 200% strain and the requirements of jetting (e.g. low viscosity) makes the incorporation of functional fillers difficult; additionally, the processing parameters must be finely tuned to achieve uniform and controlled deposition.

Table 4.2: Summary of 3D Printing Strategies and their Capabilities

Fused deposition modelling (FDM)	Direct ink writing (DIW)	Selective laser sintering (SLS)	Ink jetting	Stereolithography (SLA)
				
Approximate deposition rate				
$10^3 \text{ mm}^3 \text{ h}^{-1}$ Inversely proportional to resolution ²⁰⁸	$10^3 \text{ mm}^3 \text{ h}^{-1}$ Inversely proportional to resolution ²⁰⁸	$10^3 \text{ mm}^3 \text{ h}^{-1,209}$	$5 \times 10^3 \text{ mm}^3 \text{ h}^{-1,210}$	$10^3 \text{ mm}^3 \text{ h}^{-1}$ Slower rates for microsystems ^{211,212}
Approximate resolution				
$100 \mu\text{m}^{208}$	$1\text{--}100 \mu\text{m}^{208}$	$100 \mu\text{m}^{210}$	$50 \mu\text{m}^{210}$	$1 \mu\text{m}$ (microsystems) ^{211,212} $50 \mu\text{m}$ (projection-based) ²¹³
Starting material requirements				
Thermoplastic (filament)	Flowable (ink) that solidifies	Thermoplastic (powder)	Low viscosity ink $\nu_{\text{vis}} < 0.25 \text{ Pa}\cdot\text{s}^{214}$	Low viscosity ink $\nu_{\text{vis}} < 5 \text{ Pa}\cdot\text{s}^{215}$ photopolymerizable

In practice, the minimum device feature size is often many multiples of the nominal resolutions reported in Table 4.1 due to incorporated defects and poor layer adhesion. Moreover, high resolution is not necessarily equivalent to complexity; it is challenging to apply DIW and inkjet printing for the direct printing of complex architectures, including voids, without also incorporating sacrificial supports and additional production steps. Printing in a buoyant media, for example in a powder bed (SLS) or in liquid resin (SLA), provides such a passive support to fabricate overhanging features, but “vents” need to be added in order to remove any unreacted precursor. SLA addresses many of these issues in terms of speed, resolution, and design complexity, but still faces challenges in terms of rapid multi-material printing (even automated vat replacement strategies are slow). The use of phase separation or orthogonal photopolymerization chemistries could enable multi-material SLA from single resin systems. Such improvements in material chemistries will certainly make this process a powerful tool for the direct printing of sophisticated soft robots.

The technical capabilities of soft robots can be improved by increasing the printing resolution, which enables a higher density of actuators and sensors. Additional actuators provide for greater adaptability through higher active degrees of freedom,

and an array of imprecise sensors can extract robust information about the deformation of a soft body, if used in conjunction with machine learning algorithms.¹²⁵ Improvements in the resolution of 3D printing should occur in concert with new materials compatible with these techniques. Inks that exploit the thermodynamically driven self-assembly of block copolymers can potentially generate ordered structures in a wide range of morphologies with sub-micron scale, potentially breaking the Rayleigh criterion diffraction limit (resolution $> \lambda/2$) for 3D printed structures from photopolymers. However, successfully maintaining these assemblies during printing will likely require a deep understanding of the thermodynamics, kinetics, phase space, and morphological transitions of the polymer system.

APPENDIX A

3D PRINTING ANTAGONISTIC SYSTEMS OF ARTIFICIAL MUSCLE USING PROJECTION STEREOLITHOGRAPHY

A.1 Abstract

The detailed mechanical design of a digital mask projection stereolithography system is described for the 3D printing of soft actuators. A commercially available, photopolymerizable elastomeric material is identified and characterized in its liquid and solid form using rheological and tensile testing. Its capabilities for use in directly printing high degree of freedom (DOF), soft actuators is assessed. An outcome is the ~40% strain to failure of the printed elastomer structures. Using the resulting material properties, numerical simulations of pleated actuator architectures are analyzed to reduce stress concentration and increase actuation amplitudes. Antagonistic pairs of pleated actuators are then fabricated and tested for four-DOF, tentacle-like motion. These antagonistic pairs are shown to sweep through their full range of motion (~180°) with a period of less than 70ms.

A.2 Introduction

Elastomeric soft robotic systems, that possess a range of advantages over rigid machines, have become viable due to advances in materials, fabrication techniques and simulation tools¹. Foundational work² already demonstrates that these systems deform their shape continuously and manipulate delicate objects using their intrinsic compliance. By mimicking the properties of biological organisms, deformable materials such as fluids, gels, and elastomers change the way machines interact with their environment. Inspired by nature, previously reported soft robots imitate an octopus squeezing through tiny crevices or an earthworm navigating uneven terrain³. Furthermore, this materials platform maintains the benefits of low-cost, processability, and biocompatibility common to many classes of polymers.

Despite recent advances in pneumatically actuated elastomeric systems, current fabrication techniques limit the ability to create architectures of arbitrary complexity. In theory, the ability of elastomeric materials to deform continuously permits such soft robotic systems to move and bend anywhere along their surface. In order to access the higher degrees of freedom (DOF) enabled by these materials, the fabrication of intricate device architectures and configurations must be feasible. Soft lithography and lost wax casting may generate complex internal structures,⁴⁻⁷ but these processes tend to be labor intensive and limit the design space to forms which are readily moldable. A recent investigation into rotomolding⁸ reliably produces monolithic soft actuators, but the creation of arbitrary internal geometries using this technique is impossible.

A long standing goal in the robotics community are manipulators that mimic the 3-Dimensional arrangement of helical, longitudinal, and circumferential muscle in an octopus tentacle⁹ for high DOF manipulators. The only likely method for achieving this goal is the bottom up assembly of actuators using 3D printing; by enabling this technology to print elastomeric material (key to *intrinsically* soft robots, ISRs), the design space for soft robots will be greatly increased. Moreover, the capacity to fabricate actuators directly from CAD files allows for rapid iteration between prototype designs. Presently, many different 3D printing technologies are capable of using elastomeric materials (e.g., direct-write assembly, inkjet and stereolithography).¹⁰⁻¹⁶ To our knowledge, however, a simple and reliable solution for 3D printing high DOF actuators has not been reported. In this note, we report a detailed material and mechanical description of a low-cost, reliable, and simple method for 3D printing elastomeric pneumatic actuators.

A.3 Methods

We chose to use an automated, layer-by-layer stereolithography technique as it is not susceptible to alignment issues common to single nozzle extrusion machines, can print at high resolutions quickly, and does not require an additional support material. For this project, we developed a low-cost (<\$1,500) system for Digital Mask Projection Stereolithography (DMP-SL)¹⁷⁻²¹ that utilizes a digital mirror device (DMD) to illuminate and photopolymers an entire layer at once. For our setup we used

an HD projector (Acer P1500) without modification, to provide high intensity visible light. When focused to our build area of 40.0 by 71.1 mm², we achieve a nominal resolution of 37 μm in the XY (horizontal) plane.

Figure A.1a depicts a schematic of our fabrication process and figure A.1b (see supplemental Video A.1) shows a picture of an actuator being printed. We selected a “bottom-up” process which allows an image from the projector to pass through the bottom of a transparent build tray onto a photopolymerizable resin vat. As described by *Pan et al.*,²⁰ there are numerous advantages to using a bottom-up system: (i) the vat can be shorter than the part being printed, requiring less resin material; (ii) precisely controlling the distance between the build platform and the transparent substrate permits small layer heights (e.g. 50 μm or less); (iii) isolation of the curing photopolymer layer from the atmosphere minimizes oxygen inhibition enabling rapid polymerization.

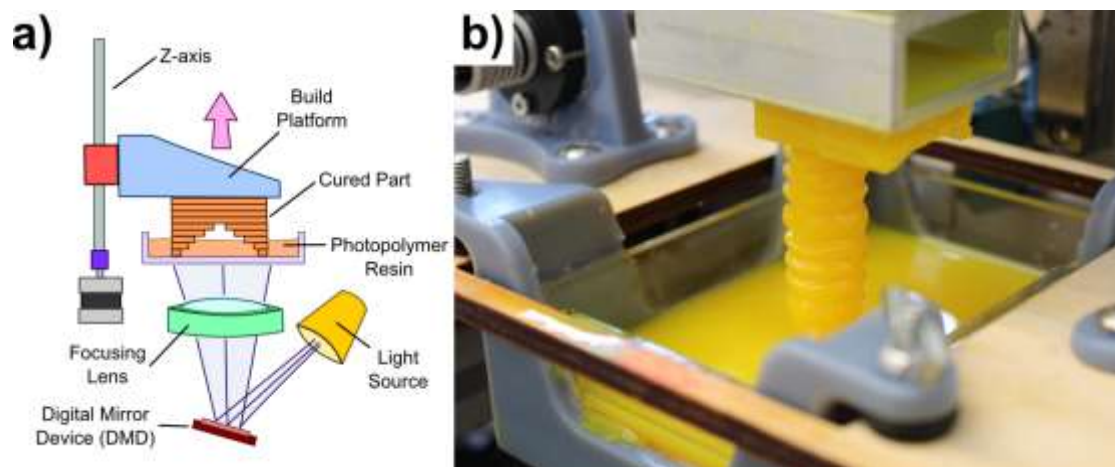


Figure A1.1: (a) Schematic of the bottom-up Digital Mask Projection Stereolithography (DMP-SL) process (b) Soft pneumatic actuator being printed using elastomeric precursor (EP)

Our system uses a resin vat constructed from borosilicate glass with a thin layer of Sylgard 184 (PDMS) adhered to the bottom surface; this layer serves as a polymerization inhibitor²² that prevents sticking of the cured resin to the substrate. To begin the printing process, we position a filled vat of suitable photopolymer and an aluminum build platform one layer height, $d = 50 \mu\text{m}$, above the PDMS layer. The projector then directs light on to the desired areas for selective polymerization. Upon curing, the build platform repositions along the Z-axis for the next layer and the

process is repeated until all layers are cured. Our printer also uses an X-axis to translate the vat horizontally between layers; work by *Pan et al*²¹ indicates that the shearing force required to release the part with a sliding motion is less than the force required to separate the part by simply pulling vertically.

We use *Creation Workshop* by Envision Labs to control our printer: we upload 3D design files in the STL file format and the software slices the design into individual layers, generating a g-code which coordinates the motion of each axis with the projector's illumination image for each layer. G-code is transmitted to an Arduino Uno Rev3 loaded with the open source *Grbl* firmware, a high performance g-code parser that converts the desired trajectories of the g-code into discrete pulses to control each stepper motor.²³ The adjustment of any one of numerous control parameters, such as illumination time, axis motion and velocity, and layer height, could improve the printing performance for a specific material.

Currently, only a limited number of elastomeric materials exists for use with a visible light DMP-SL printer. In this paper, we focus on a commercially available Elastomeric Precursor (EP; Spot-E resin, Spot-A Materials, Inc.). This material is designed and marketed for applications needing soft and resilient materials. During this printing process, the material is controllably cured from and translated within its own uncured liquid state. Therefore, the rheological properties of the system are critical to obtaining a successful print. To understand these properties, we used a controlled stress rheometer (DHR3, TA Instruments; 25 mm parallel plate geometry) to determine the shear rate dependence on viscosity. In this measurement, the top plate is constantly rotated at increasing shear rates from 0.01 to 1,000 s⁻¹ while the rheometer measures the applied torque and calculates the apparent viscosity.

Typically, soft pneumatic actuators fabricated using elastomeric materials, such as the EcoFlexTM family of silicones (Smooth-On, Inc.), undergo elastic strains greater than 600%²⁴. In order to gage the suitability of the EP resin system for use in pneumatic actuators and biomedical applications, we measured critical mechanical properties needed for actuators that must elastically deform under normal use. Specifically, we measure the strain to failure, toughness (work to fracture), strength

(maximum stress that the material withstands) and elastic modulus (at 2% strain). We performed tensile tests using a Zwick/Roell Z010 testing system in accordance with ASTM D638, the standard test method for tensile properties of plastics. We designed testing coupons with a gage length of 7.62 mm, a thickness of 4.00 mm, and a width of 3.18 mm as shown in figure A.2a. Samples were fabricated with a layer height of 50 μm and an illumination time of 1.25 s for each layer. The first five layers were treated to an illumination time of 7.0 s in order to assure adequate adhesion to the aluminum build substrate; we aligned our samples with the layer lines parallel to the width of the coupon. After fabrication, we cleaned the uncured resin from the samples by washing them in isopropanol before leaving them to dry overnight. We measured the dimensions of each sample immediately before tensile testing to failure at a strain rate of 10 mm min⁻¹.

As the life-cycle of an elastomeric actuator depends on the fatigue behavior of the material, we performed cyclic loading. For each cycle, we strain the sample at 10 mm min⁻¹ until it reaches 125% of its original, unstretched length. After reaching 25% strain, we gradually unload the applied tensile force to zero. For each sample, we record the number of cycles to fracture (see supplemental figure A.7). Though the number of cycles and ultimate strains are much lower than those reported for silicones,²⁴ the ability to prototype actuator designs quickly is useful.

Typical Newtonian fluids do not exhibit shear rate dependence in their viscosity. As shown in figure A.2c, the uncured EP resin displays non-Newtonian behavior at shear rates below $\sim 60 \text{ s}^{-1}$. In this regime, the material exhibits a decreasing apparent viscosity with an increasing shear rates, or shear-thinning behavior. These fluids usually contain long polymeric chains that form random coils under low shear. As the shear rate increases, these chains uncoil, aligning with the flow fields, thus reducing the viscosity.

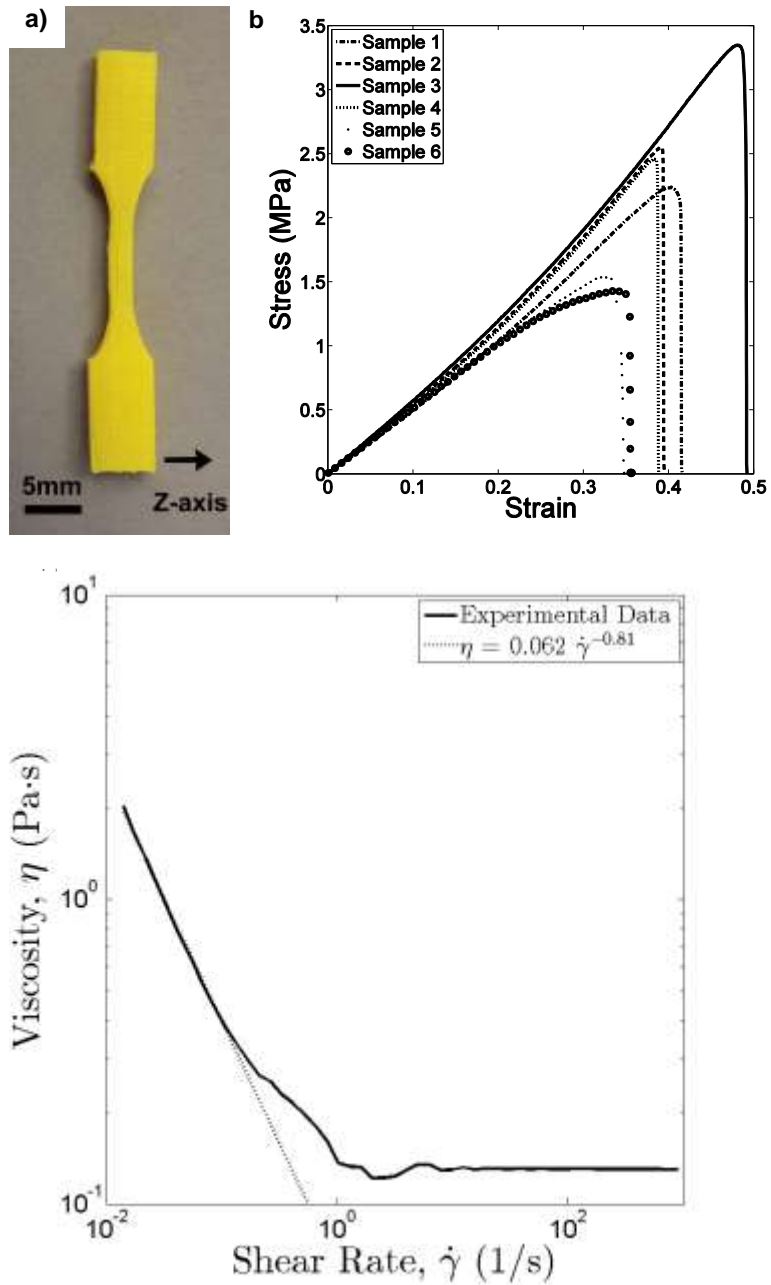


Figure B: (a) An EP tensile testing coupon as printed (b) Stress-strain curves for six EP tensile testing coupons (c) Rheological results for the uncured EP resin demonstrating shear-thinning and a fitted data for a power-law fluid as described by the Ostwald-de Waale relationship for $n=0.19$

A.4 Results

The Ostwald-de Waale (equation A.1) relationship describes the shear stress (τ) for generalized power-law fluids in terms of a flow consistency index (K), a shear rate ($\dot{\gamma}$) and a flow behavior index (n).

$$\tau = K \dot{\gamma}^n \quad [\text{equation 1}]$$

Since shear stress is proportional to the product of viscosity and shear rate, equation 1 is more conveniently rewritten in terms of apparent viscosity (η).

$$\eta = K \dot{\gamma}^{n-1} \quad [\text{equation 2}]$$

By fitting the rheology data to equation A.2, we obtain a value of $n = 0.19$. A flow behavior index less than unity is consistent with shear-thinning behavior.

During each step of the fabrication process, the fluid experiences a maximum shear rate of approximately 0.33 Hz that results from the build platform being translated approximately 5 mm in the z direction at a speed of 100 mm min⁻¹. At this shear rate, the fluid remains in the shear thinning regime with an apparent viscosity $\eta=0.23$ Pa·s. Upon cessation of shear, the viscosity then increases towards a zero shear viscosity of $\eta=2.02$ Pa·s, this increase might be important for high resolution printing and should be considered when designing materials for DMP-SL.

The results of the tensile tests are shown in figure A.2b. We found that this material exhibits a linear stress-strain relationship consistent with elastic behavior. The average elastic modulus over the initial proportional regime is $E = 5.20 \pm 0.30$ MPa. We found an average ultimate strength, $\sigma_{ult} = 2.26 \pm 0.71$ MPa and the samples sustained an ultimate elongation, $\gamma_{ult} = 1.40 \pm 0.05$. As calculated by the area under the stress-strain curve, the results indicate an average toughness, $F = 4.6 \pm 1.8$ kJ m⁻³. Fatigue tests demonstrate that the elastomer typically fails after 9 ± 3 cycles (figure A.7, although one sample was able to undergo greater than 50 cycles without failure).

In order to test the viability of the DMP-SL process to directly fabricate soft robots, we designed a single-channeled actuator using *Solidworks*TM (DASSAULT Systems). As the EP resin lacks the ultimate strains of the silicones and polyurethanes typically used to fabricate such devices²⁴, we incorporated a pleated architecture to allow large overall deformations without high local strains²⁵. As shown in figure A.3a, our design uses a flat inextensible layer opposite the pleated structure to direct actuation. Surface stress concentrations develop at areas of small radii of curvature. We developed an FEA model of our actuator using *ANSYS Mechanical*TM that imposes a fixed boundary condition on the cylindrical base and applies a uniform pressure on the internal

surfaces. We then simulated different device geometries with the same overall length and wall thickness but different number of pleats (from zero to eight). Results show (figure A.2) that actuation curvature increases with pleat frequency, but local stress reaches its minimum value at a pleat number of four. We chose a total of six pleats as a compromise between minimizing stress concentrations and maximizing actuation amplitude. The 3D model imported into ANSYS as well as the boundary conditions are shown in figure A.3a. To simplify the simulation, we assumed the material as isotropically elastic with an elastic modulus, $E = 6 \text{ MPa}$ and Poisson's ratio as 0.495. A grid size of 1 mm was sufficient to demonstrate convergent results. We varied the applied pressure from $\Delta P = 34$ to 69 kPa (5 to 10 psi) and simulated the maximum stress and strain on the surface of the actuator (figure A.3). For an internal pressure, $\Delta P = 34 \text{ kPa}$ (5 psi), the resulting deformation and equivalent stress fields are shown in figure A.3b,c. The actuator bends to one side with a maximum equivalent stress of 0.68 MPa, well below the EP's measured ultimate strength of 2.26 MPa, suggesting the actuator's ability to operate under these conditions.

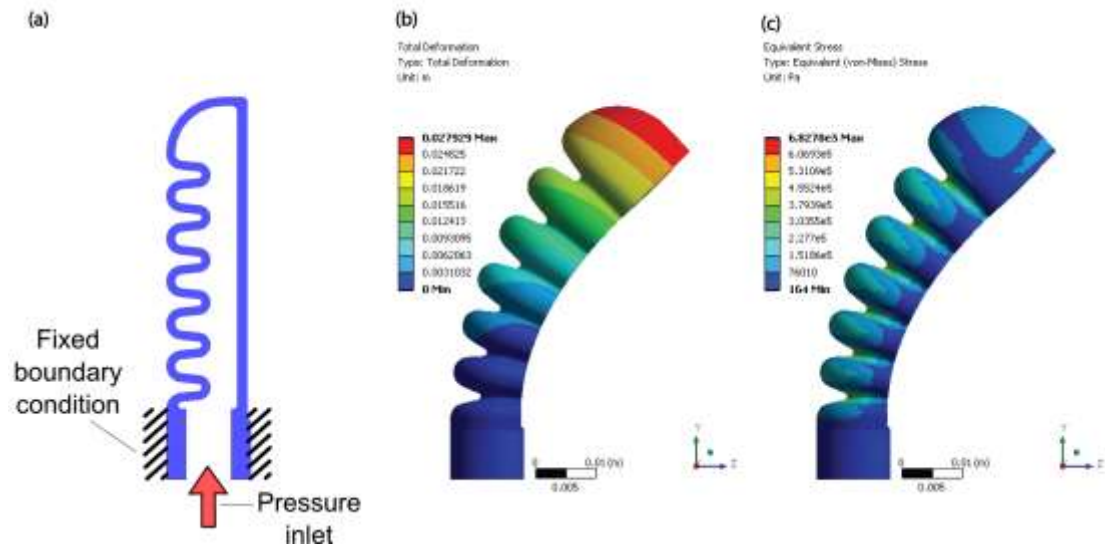


Figure A1.3: (a) As designed actuator with pleated structures with the resulting deformation (b) and equivalent stress fields (c) when pressurized to 5 psi.

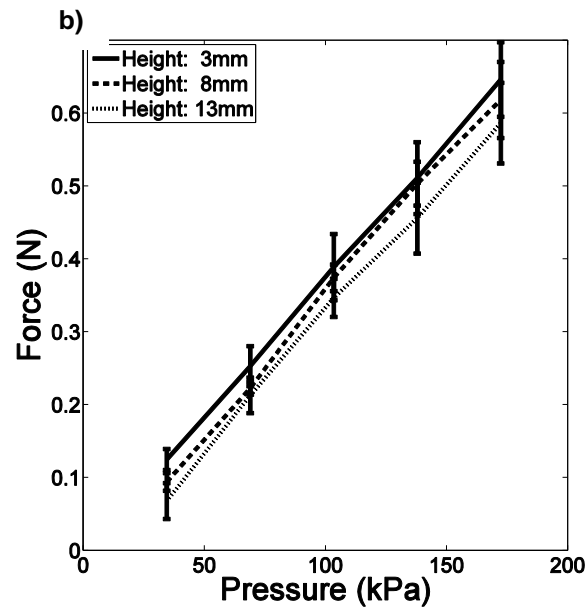
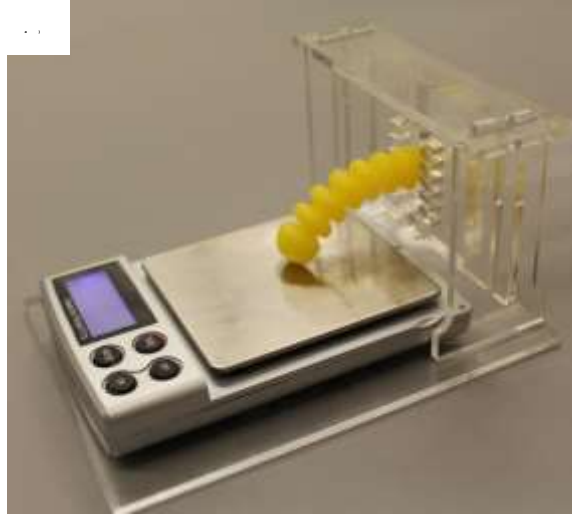


Figure A1.4: (a) Test setup used to measure the force output of actuators with varying stroke length. (b) Average force output of six sample actuators with varying pressure and height above the digital scale used to measure force.

In order to characterize the force output of the actuator, we constructed the test setup shown in Figure A.4a. We then measured the force exerted by the actuator using a digital scale (American Weigh Scales SM-501). Using preset slots in the laser-cut test rig, we adjusted the mounting height above the scale in order to vary the stroke of the actuator. For each actuator, we recorded the generated force as height was varied from 3 to 13 mm and pressure, ΔP , was varied from 34.5 to 172 kPa (5 to 25 psi). Figure A.4b shows the average force generated by six samples of the single-channel

actuator design shown in figure A.3a. The force output of the actuator increases linearly with increasing pressure, as we expected from the tensile testing data. At the highest tested input pressure, $\Delta P = 172$ kPa (25 psi), and an elevation of 3 mm above the load cell, we found the force exerted by the actuators to be $F = 0.65 \pm 0.05$ N. During the testing process, samples often began to leak after a few cycles, consistent with our cyclic loading tests (figure A.7). We patched leaks by applying small drops of EP resin and polymerizing under a UV lamp (Omnicure Series 1500).

In addition to the single-channel actuators, we also designed and tested increasingly sophisticated geometries towards our goal of synthetically mimicking complex 3D musculatures like those of an octopus. One of these architectures incorporates an antagonistic pair of independent chambers as pictured in figure A.5a. We achieve a large range of motion by cycling the pressure between the two chambers (Figures A.5 b,c; Video A.3). By decreasing the wall thickness, the cycle time can be reduced to less than 70 ms (Video A.4), comparable to high speed contraction in animal muscle²⁶.

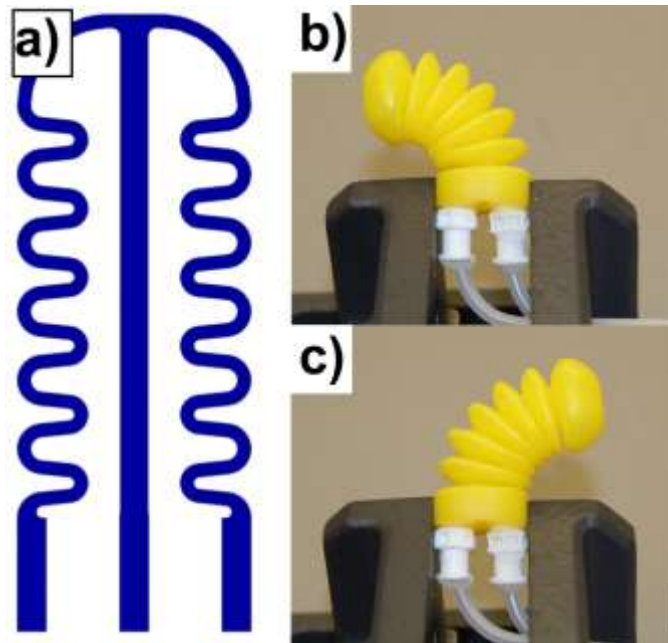


Figure A.5: (a) Cross-section of antagonistic actuator design. (b) Right chamber pressurized to $\Delta P = 103$ kPa (15 psi). (c) Left chamber pressurized to $\Delta P = 103$ kPa (15 psi).

Architectures with higher degrees of freedom, allow us to more closely approximate the continuous motion of living systems. Antagonistic pairs like those

described above can serve as fundamental building blocks for building arbitrarily complex soft machines. Figure A.6a shows an actuator with two antagonistic pairs (four independent chambers) that has been printed as a monolithic structure, including the pneumatic routing system that feeds each chamber. Because the bending axes of the antagonistic pairs are offset by 90°, this device is able to move beyond a 2D plane in order to perform complex 3D motions. (Figure A.6b-d; Video A.5).

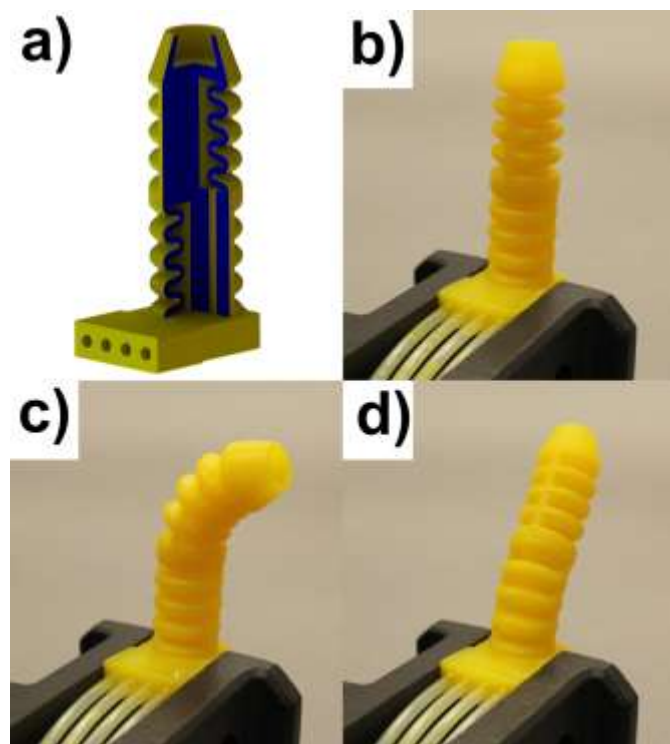


Figure A.6: (a) CAD model of actuator with four independently actuated pressure chambers. (b) Printed actuator in non-pressurized state. (c) Left, top chamber pressurized to $\Delta P = 138$ kPa (20 psi). (d) Front, bottom chamber pressurized to $\Delta P = 138$ kPa (20 psi).

A.5 Conclusions

We successfully employed DMP-SL to make multi-degree of freedom soft actuators with complex internal architectures, using a commercially available visible-light photocurable elastomeric precursor. Despite the relatively low ultimate strain ($\epsilon_{ult} \sim 1.40$) of the cured EP resin, we successfully fabricated devices with large actuation amplitudes. We have developed the antagonistic actuator pairs that mimic the function (but not mechanism) of musculature in animals, and have comparable actuation times to living muscle. Combinations of these pairs can be used to create actuation systems of arbitrary complexity that can be printed in a single process as a

monolithic structure. Due the high level of design sophistication available and the material compliance comparable to some biological tissue,²⁷ the DMP-SL is uniquely suitable for developing soft machines that mimic and interact with biological systems.

Many of the material limitations of the EP system can be overcome through design of tough, photocurable elastomer chemistries. There is an extensive library of suitable monomer candidates bearing vinyl groups compatible with free radical polymerization (e.g. acrylic acid). Additionally, a wide array of photo-initiators systems that absorb at a visible wavelengths are thoroughly established. So, while future work needs to ascertain the correct stoichiometry of chemical constituents to optimize cure kinetics, resin rheology, and resulting mechanical properties, a multitude of potential combinations of synthetic systems exist that may offer mechanical properties even better suited for this class of actuators. Based on the demonstration reported here and the possibilities for improved materials, this nascent printing process for soft actuators is a promising route to sophisticated, biomimetic systems.

A.6 Supplemental Information

Videos:

- Video A.1: Pleated pneumatic actuator being 3D printed using digital mask projection stereolithography (DMP-SL)
- Video A.2: FEA simulation of pressurized single-channeled pleated pneumatic actuator.
- Video A.3: Antagonistic pair of 3D printed pneumatic actuators performing sweep through full range of motion
- Video A.4: Rapid movements (period <70ms) from thin-walled antagonistic pair of 3D printed pneumatic actuators
- Video A.5: 3D printed pneumatic actuator with four independent pressure chambers printed as monolithic structure

Plots:

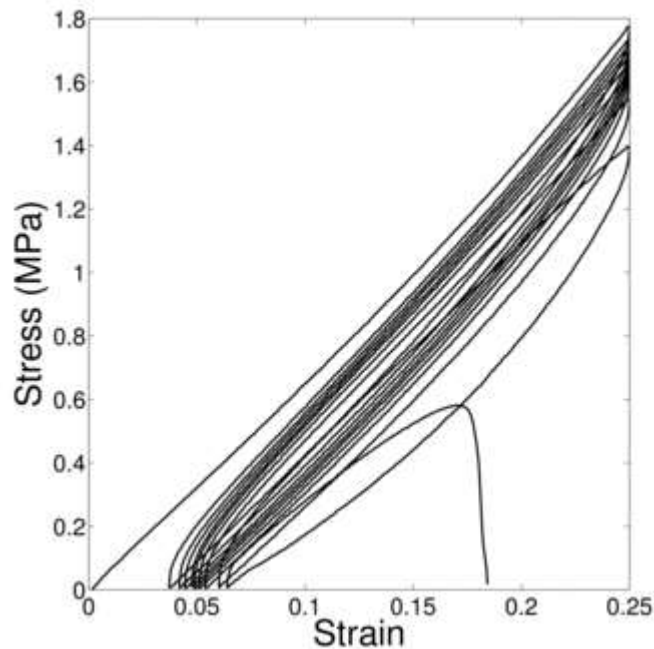


Figure A.7: Representative cyclic loading data for 3D printed test coupon

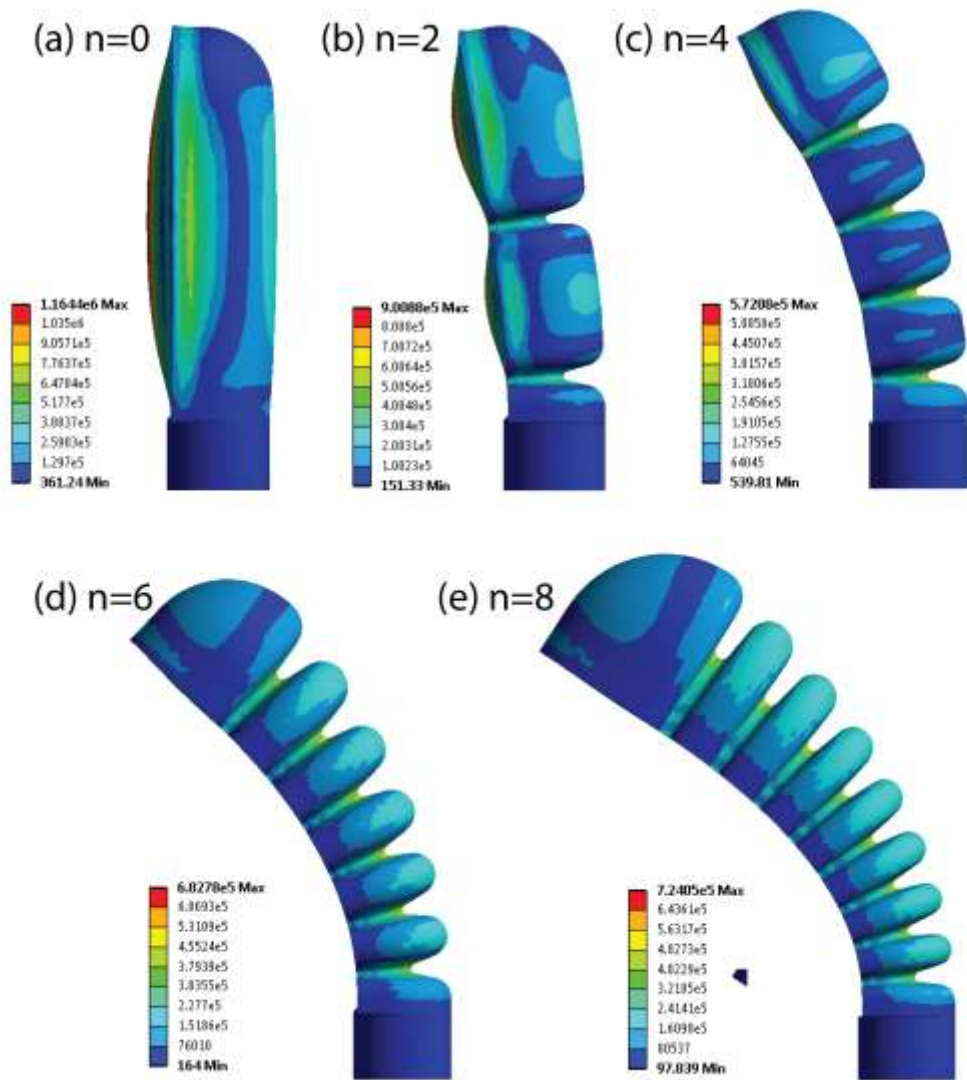


Figure A1.8: Results of FEA study to determine the relationship between number of pleats and stress concentration on the pleated actuator

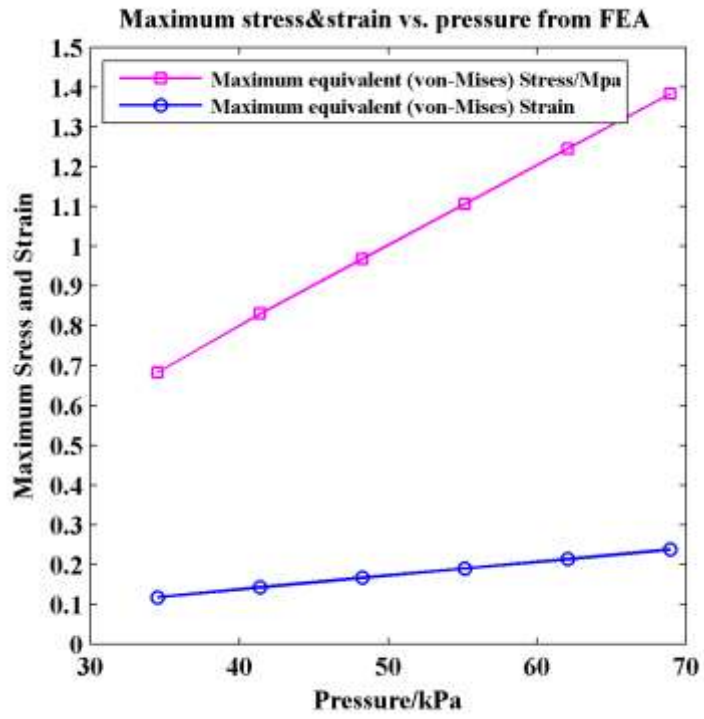


Figure A.9: Results of FEA study to determine the maximum stress and strain for pleated pneumatic actuators as pressure is varied

REFERENCES

1. Trimmer, B. A Journal of Soft Robotics: Why Now? *Soft Robot.* **1**, 1–4 (2014).
2. Shepherd, R. F. *et al.* Multigait soft robot. *Proc. Natl. Acad. Sci.* **108**, 20400–20403 (2011).
3. Majidi, C. Soft Robotics: A Perspective—Current Trends and Prospects for the Future. *Soft Robot.* **1**, 5–11 (2014).
4. Rogers, J. a. & Nuzzo, R. G. Recent progress in soft lithography. *Mater. Today* **8**, 50–56 (2005).
5. Xia, Y. & Whitesides, G. M. Soft Lithography. *Annu. Rev. Mater. Sci.* **28**, 153–184 (1998).
6. Katzschmann, R. K., Marchese, A. D. & Rus, D. Hydraulic Autonomous Soft Robotic Fish for 3D Swimming. *Intell. Robot. Syst. (IROS), 2011 IEEE/RSJ Int. Conf.* (2014).
7. Loepfe, M., Schumacher, C. M. & Stark, W. J. Design , Performance and Reinforcement of Bearing-Free Soft Silicone Combustion-Driven Pumps. (2014).
8. Zhao, H., Robinson, S. & Shepherd, A. R. Innovative Manufacturing for Soft Actuators : Rotational casting and 3D Printing. 1120296
9. Trivedi, D., Rahn, C. D., Kier, W. M. & Walker, I. D. Soft robotics: Biological inspiration, state of the art, and future research. *Appl. Bionics Biomech.* **5**, 99–117 (2008).
10. Chan, V. *et al.* Multi-material bio-fabrication of hydrogel cantilevers and actuators with stereolithography. *Lab Chip* **12**, 88 (2012).

11. Rossiter, J., Walters, P. & Stoimenov, B. Printing 3D dielectric elastomer actuators for soft robotics. **7287**, 1–10 (2009).
12. Kamamichi, N., Maeba, T., Yamakita, M. & Muka, T. Fabrication of bucky gel actuator/sensor devices based on printing method. *2008 IEEE/RSJ Int. Conf. Intell. Robot. Syst. IROS* 582–587 (2008). doi:10.1109/IROS.2008.4651100
13. Hockaday, L. a *et al.* Rapid 3D printing of anatomically accurate and mechanically heterogeneous aortic valve hydrogel scaffolds. *Biofabrication* **4**, 035005 (2012).
14. P., W. Digital fabrication of smart structures and mechanisms-creative applications in art and design. *Int. Conf. Digit. Print. Technol. Digit. Fabr. 2011* **27**, 185–188 (2011).
15. Hung, K. C., Tseng, C. S. & Hsu, S. H. Synthesis and 3D printing of biodegradable polyurethane elastomer by a water-based process for cartilage tissue engineering applications. *Adv. Healthc. Mater.* 1578–1587 (2014). doi:10.1002/adhm.201400018
16. Barry, R. a. *et al.* Direct-write assembly of 3D hydrogel scaffolds for guided cell growth. *Adv. Mater.* **21**, 2407–2410 (2009).
17. Lee, H. & Fang, N. X. Micro 3D printing using a digital projector and its application in the study of soft materials mechanics. *J. Vis. Exp.* e4457 (2012). doi:10.3791/4457
18. Sun, C., Fang, N., Wu, D. M. & Zhang, X. Projection micro-stereolithography using digital micro-mirror dynamic mask. *Sensors Actuators A Phys.* **121**, 113–120 (2005).

19. Choi, J. W. *et al.* Fabrication of 3D biocompatible/biodegradable micro-scaffolds using dynamic mask projection microstereolithography. *J. Mater. Process. Technol.* **209**, 5494–5503 (2009).
20. Yayue Pan, Chi Zhou & Yong Chen. Rapid manufacturing in minutes: The development of a mask projection stereolithography process for high-speed fabrication. *Proc. ASME 2012 Int. Manuf. Sci. Eng. Conf.* 1–10 (2012). doi:10.1115/MSEC2012-7232
21. Pan, Y., Zhou, C. & Chen, Y. A Fast Mask Projection Stereolithography Process for Fabricating Digital Models in Minutes. *J. Manuf. Sci. Eng.* **134**, 051011 (2012).
22. Shepherd, R. F. *et al.* Stop-flow lithography of colloidal, glass, and silicon microcomponents. *Adv. Mater.* **20**, 4734–4739 (2008).
23. Skogsrud S., J. S. Github: Grbl. (2013). at <<https://github.com/grbl/grbl>>
24. Mosadegh, B. *et al.* Pneumatic networks for soft robotics that actuate rapidly. *Adv. Funct. Mater.* **24**, 2163–2170 (2014).
25. Shepherd, R. F., Stokes, A. A., Nunes, R. M. D. & Whitesides, G. M. Soft Machines That are Resistant to Puncture and That Self Seal. 6709–6713 (2013). doi:10.1002/adma.201303175
26. McNeill, A. *Principles of Animal Locomotion*. 384 (Princeton University Press, 2013).
27. Vogel S. *Comparative biomechanics: life's physical world*. 294 2nd ed. Princeton, NJ: Princeton University Press; 2013.

APPENDIX B

TOUGH THIOURETHANE PHOTOPOLYMERS WITH TUNABLE CRYSTALLINITY FOR ADDITIVE MANUFACTURING

B.1 Abstract

Acrylic photopolymers currently used for additive manufacturing have sub-standard mechanical and thermal performance in comparison to common engineering materials such as polyamide, polypropylene, and EPDM rubber. We demonstrate that thiol-isocyanate chemistry can produce 3D printed, semi-crystalline, photocured parts with properties similar to these commercial engineering materials. Photopolymerization is completed within seconds using a photolabile base to cure the multi-monomer resin under 365 to 405 nm light. The mechanical and thermal properties are controlled by varying the structure of the polymer backbone to enhance or suppress crystallinity. The resultant materials increase toughness by 10× and heat deflection temperatures by 2× in comparison to commercially available acrylic photopolymers, placing performance in-line with engineering grade polymers. Tough, thermally resistant 3D printed parts are produced on multiple photopolymer-based 3D printing platforms.

B.2 Introduction

Photopolymers are light-cured plastics that have applications across a wide variety of industries including coatings, medical adhesives, biomaterials, photoresists, inks, and more recently additive manufacturing.^{1,2} Additive manufacturing is a rapidly growing field with uses in industries ranging from medicine to consumer goods.³ Photopolymer-based systems such as stereolithographic addition (SLA), continuous digital light processing (DLP), and UV inkjetting are known for fast printing speeds, isotropic mechanical properties, and high detail and surface finish. However, the acrylic chemistries that these systems rely on to function have difficulty producing functional parts with simultaneously high toughness and heat deflection temperatures.⁴⁻¹⁰ This is contrary to the tough, thermally resilient polymers frequently

used in industries such as aerospace, automotive, and apparel. As a result, photopolymer systems have seen only limited adoption for producing end-use parts, with most applications being related to prototyping.¹¹

Industrially relevant polymers such as polyamide, polypropylene, and rubbers gain their superior toughness and heat deflection behavior by virtue of their strong inter-chain interactions and high strain capacity. Semi-crystalline polymers in particular have long been known for their toughness and ductility in comparison to amorphous materials, due to mechanisms such as crystal plasticity, where strain energy is dissipated through the destruction of polymer spherulites. In some materials, chain realignment and stabilization results in necking, which manifests as high ductility and toughness.^{12,13} The acrylic resins used in photopolymer 3D printing systems are typically amorphous and do not crystallize. When these materials are stressed, micro-cracks easily expand to the critical fracture size, resulting in brittle behavior.^{3,4,6,7} In addition, the radical propagation mechanism by which acrylates polymerize makes it difficult to develop useful acrylic 3D printing resins with low degrees of crosslinking without encountering excessive brittleness and warping.^{14,15} Incorporation of multifunctional acrylate species promote rapid print speeds, but the resulting increase in crosslink density limits the maximum elongation. There is a distinct need to develop photopolymers with chain structures that promote chain interactions such as crystallinity and hydrogen bonding while allowing lower degrees of crosslinking. We demonstrate that the base-catalyzed, step-growth photopolymerization of thiol-isocyanate resins can be used to produce rapidly curing 3D-printable materials with controllable crystallinity and low crosslink density. The resins are compatible with contemporary printing techniques; allowing structures such as a chess rook with an internal staircase and a gyroid cube to be printed via SLA or fine-featured parts via UV inkjetting (Fig B.1A,B).¹⁶ The resultant materials are tough, with high stiffness and strain capacity allowing them to take high loads with minimal permanent deformation (Fig. B.1C). These materials retain their performance at temperature, up to the onset of the crystal melting point (Fig. B.1D).

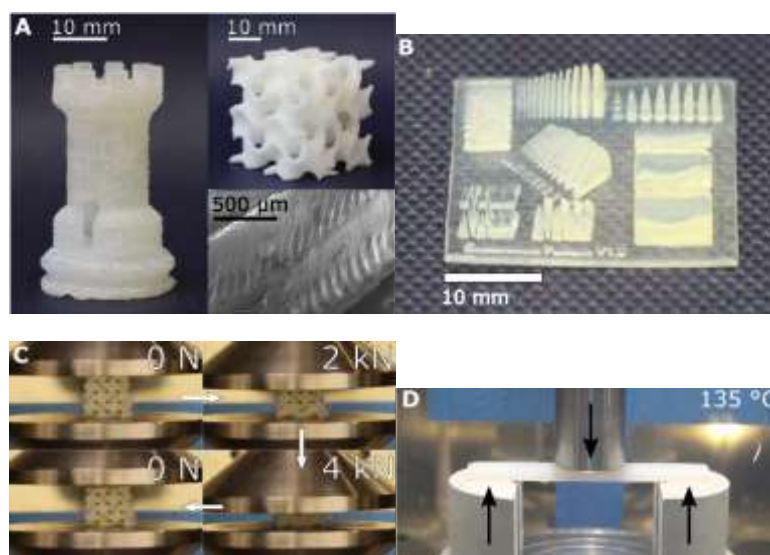


Figure B.1: Thiol-isocyanate photopolymer resins can be used to 3D print tough, thermally resilient thiourethane parts using traditional top-down SLA printing techniques.

(A) A thiourethane rook with an internal staircase and gyroid cube printed via stereolithographic addition (SLA) at 100 μm layer heights. (B) A demonstration piece showing fine features achievable using UV inkjet printing techniques. (C) A 35 mm \times 35 mm \times 35 mm gyroid cube is compressed to 4 kN and returns to its original shape with minimal plastic deformation after unloading. (D) Thiol-isocyanate photopolymer resins enable tough 3D printed parts which retain their structural integrity at heightened temperatures.

Thiol-isocyanate coupling allows for a heightened level of structural control in comparison to acrylics. In acrylic polymerization, a single acrylate moiety only extends the growing polymer chain by one C-C bond. As a result, the carbon-only backbone of an acrylate chain is pre-determined, allowing only the ability to tune side-chain chemistry or adjust crosslinking chains via, for example, higher viscosity multi-functional oligomers.¹⁷ Today, approaches to overcome this issue include 3D printing acrylic scaffolds which can be subsequently infused with monomer and oligomer combinations, such as epoxies or polyurethanes, to yield final parts with sufficient thermomechanical properties.^{1,3,6} Thiourethane polymerizations require at least two thiol or isocyanate functional groups on each monomer or oligomer to extend the polymer chain due to the underlying step-growth reaction mechanism. As a result, the linkage connecting the two or more functional groups of a monomer is integrated into the main chain of the polymer.¹⁸ This has two implications; there is direct control over the structure of the main chain by choice of the di-functional monomer, and this main chain structure control is independent of the degree of crosslinking.

B.3 Results

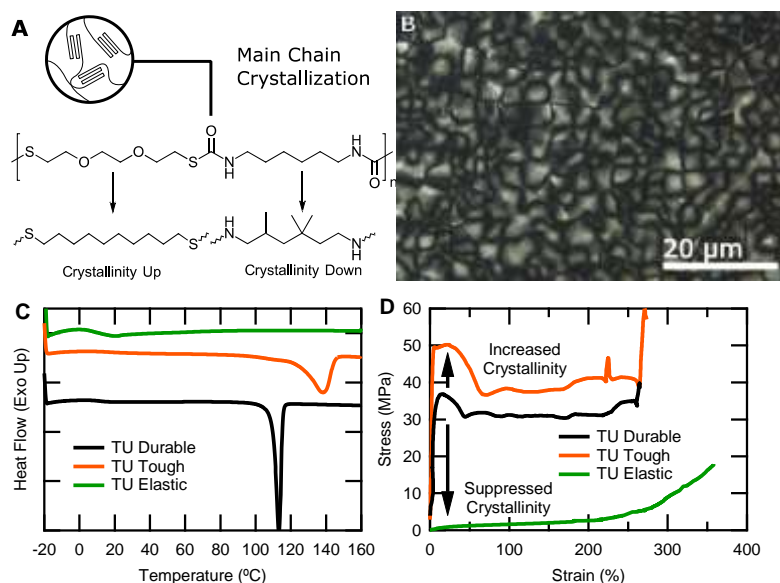


Figure B.2: Mechanical performance is controlled by modulating crystallinity (A) Polymer crystal behavior may be altered by adjusting the resin composition. Monomers capable of more efficient crystal packing will enhance crystallinity, while those with disordered side groups suppress crystal formation. (B) An optical micrograph showing the spherulitic microstructure of the *TU Durable* resin. Typical spherulites are between 5 and 10 μm in size. (C) Differential scanning calorimetry confirms the effects of resin formulation on crystal behavior. The base material has a melt centered near 110 °C. The DDT-containing polymer has an up-shifted melt endotherm centered at 140 °C, while the TMHDI-containing material is amorphous and has no crystal melt. The glass transition temperature for all three resins is near 11 °C. (D) Tensile behavior is a function of crystallinity. Increased crystallinity corresponds to increased yield stress, failure stress, and toughness. Eliminating crystallinity produces an elastomer.

These characteristics were used to rationally design low crosslink density thiol-isocyanate thermoset resins intended to crystallize upon curing into thiourethanes (Fig. B.2A, Table B.1). The base material, *TU Durable*, contains 2,2'-(ethylenedioxy)diethanethiol (EDDT) and hexamethylene diisocyanate (HDI) with a small amount of tris(6-isocyanatohexyl)isocyanurate (HDI-T) as a trifunctional crosslinking molecule (Fig. B.5A,B,C). The linear backbone and extensive hydrogen bonding promote compact arrangement of its main chain crystals resulting in 23.6% crystallinity by XRD (Fig. B.6, Table B.3). Crystallinity is controlled by substituting other di-functional thiol or isocyanate monomers. Addition of 1,10-decanedithiol (DDT) increases the crystallinity to 55.0% by allowing more efficient crystal packing compared to the ether-containing EDDT molecule (Fig. B.5D, Fig. B.7, Table B.4).

This degree of crystallinity is similar to that of polypropylene and polyamide-6, which have crystal fractions in the range of 50-70% depending on processing.¹⁹ Conversely, crystallinity is suppressed when substituting trimethylhexamethylene diisocyanate (TMHDI), which inhibits packing due to pendant methyl groups on the main chain and creates a fully amorphous material (Fig. B.5E, Fig. B.7, Table B.5). The spherulitic structure of the semi-crystalline polymers is visible under polarized light microscopy (Fig. B.2B). Typical spherulites are on the order of 5-10 μm in size. The changes in crystallinity due to monomer formulation are seen via differential scanning calorimetry (Fig. B.2C). The *TU Durable* melting endotherm has a peak near 110 °C. The *TU Tough* resin, which replaces 55 mol% of EDDT for DDT to increase the crystallinity, has a melt endotherm centered at 140 °C. The *TU Elastic* polymer is amorphous due to the addition of TMHDI, showing no melt endotherm. All three materials exhibit a glass transition temperature at approximately 11 °C. In the semi-crystalline variants this produces a microstructure similar to polypropylene, with rigid spherulites separated by amorphous regions of elastic material. This in effect creates a rubber-toughened polymer, the degree of which is controlled via the crystal fraction.

Uniaxial tensile testing illustrates the changes in mechanical performance as a function of crystallinity (Fig B.2D, Table B.6). *TU Durable* is a flexible material with a yield stress of 36.3 ± 1.7 MPa, straining beyond the yield point at a near constant 30 MPa while plastically deforming. Increasing crystallinity results in a corresponding increase in yield point and plastic deformation stress, with *TU Tough* yielding at 49.8 ± 0.9 MPa and maintaining approximately 40 MPa stress until failure. Eliminating crystallinity turns the material into an elastomer. *TU Elastic* has no yield point, showing typical rubbery behavior until failure at $353\% \pm 27\%$ strain. Notably, the semi-crystalline thiourethanes exhibit necking when strained beyond the yield point. This phenomenon, indicative of ductility and toughness, is common to engineering-grade thermoplastics but is generally not observed in photo-cured materials compatible with additive techniques.

To 3D print the thiol-isocyanate photopolymer resins, it was first necessary to synthesize a photo-catalyst which allows the resin to remain stable in the dark, but

rapidly induces polymerization upon irradiation with a commonly used source such as 365, 385, or 405 nm light. Previous attempts at synthesizing adequate photolabile bases have had poor resin stability, slow polymerization rates, or operated only at sub-300 nm wavelengths.^{18,20-25} One class of materials, quaternary ammonium salts, have shown promise as photo-bases due to their modularity. The chromophore, tertiary amine, and counter-anion may be designed and implemented independently with relative ease.^{26,27} By utilizing a thioxanthone chromophore, the amidine 1,5-diazabicyclo[4.3.0]non-5-ene (DBN), and a tetraphenylborate counter-anion we were able to synthesize the photolabile base 5-(2'-(methyl)thioxanthone)-1,5-diazabicyclo[4.3.0]non-5-ene tetraphenylborate (Fig. B.9,10). This molecule remains pH neutral in solution but cleaves under the 365 to 405 nm source commonly used in 3D printing systems, releasing DBN (Fig. B.3A, B.11). This base catalyzes thiol-isocyanate coupling via proton abstraction from a thiol. The thiolate anion then attacks the electron-withdrawn carbon in the isocyanate group. A proton is removed from the DBN or another nearby thiol to complete the formation of a thiourethane bond (Fig. B.3B,B.12).¹⁸ The high basicity (pKa ~ 13.5) of the released DBN molecule allows photopolymerization to occur rapidly using minimal amounts of photo-catalyst and low degrees of crosslinking, as required by highly extensible thermosetting polymers. Photo-rheometry confirms this finding with resin viscosities increasing sharply at UV doses on the order of 50 mJ cm⁻², 30 times lower than previously reported photo-catalyzed thiourethane couplings and similar to that of acrylic photopolymer resins.²⁸ (Fig. B.3C). This rapid gelation at low crosslinking density is surprising; Flory-Stockmayer theory (Supplemental Information) suggests that these materials must reach ~97% NCO conversion before gelation. Further characterization of the photopolymerization by photo-DSC yields large, narrow exotherms consistent with a rapid and highly exothermic reaction (Fig B.3D). The resins possess similar total enthalpies of reaction ($\Delta H_{rxn} \sim -70$ kJ mol⁻¹) that exceeds those of acrylic ($\Delta H_{rxn} \sim -20$ kJ mol⁻¹) and even thiol-ene ($\Delta H_{rxn} \sim -60$ kJ mol⁻¹) based formulations (Fig B.3E).⁽²⁹⁾ *In situ* tracking of the photopolymerization via FTIR confirms that the thermodynamically favorable thiourethane couplings reach near-complete conversion

following a dose of 70 mJ cm^{-2} , in agreement with results gained from photorheometry and photo-DSC (Fig B.3F). The excellent photopolymerization kinetics, in combination with the sensitivity to longer wavelengths of light, enables 3D printing on conventional systems.

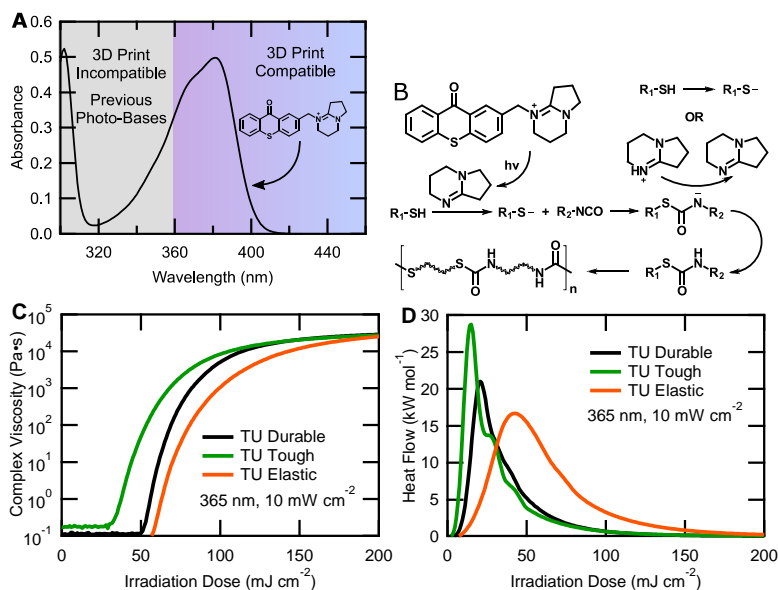


Figure B.3: Photolatent bases rapidly cure thiol-isocyanates upon exposure to light, enabling 3D printing of tough, resilient thiourethanes. (A) Photolatent superbases are synthesized which release 1,5-diazabicyclo[4.3.0]non-5-ene (pKa 13.5) upon photo-induced cleavage, catalyzing thiol-isocyanate coupling via proton abstraction from a thiol. (B) The photo-catalyst is sensitive to light up to 410 nm, allowing use in commercial photopolymer 3D printing systems. (C) Photo-rheometry demonstrates that thiol-isocyanate resins initiate gelation at irradiation doses between 35 and 55 mJ cm^{-2} . (D) Photo-DSC shows that reaction kinetics are dependent on the choice of monomer; reaction rate increases with the use of DDT and decreases when TMHDI is used. (E) The reaction enthalpies are similar for the three thiourethane formulations, converging to values near $70 \text{ kJ mol NCO}^{-1}$. (F) Real-time Fourier transform infrared spectroscopy of a representative thiol-isocyanate resin with 0.1 wt/wt% QAS-MTX shows near-complete conversion of isocyanates after receiving 70 mJ cm^{-2} of 365 nm irradiation.

The thiourethane photopolymers demonstrate improved thermomechanical performance compared to typical polyacrylate photopolymers, and exhibit performance comparable to engineering plastics (Fig. B.4A,B,C). Failure strain is much higher in the thiourethane parts than in a comparable acrylic, due to the ability to decrease crosslink density while preserving printability. Tensile strength is also above that of the acrylic materials despite the thiourethanes' flexibility. The tensile performance is on par with engineering plastics such as polyamide, polypropylene, and EPDM rubber. *TU Tough* shows tensile behavior between neat PA-6 and PA-12,

which have respective yield stresses of 58.4 ± 0.7 MPa and 27.1 ± 0.5 MPa and failure strains of $269\% \pm 19\%$ and $494\% \pm 42\%$. *TU Durable* behaves similarly to polypropylene, which yields at 32 MPa and plastically deforms at 17 MPa until failure at 450%.(19) *TU Elastic* initially behaves much like EPDM rubber but has a rapid increase in stress after reaching $\sim 200\%$ strain, whereas EPDM has a more gradual increase in stress until failure at $573\% \pm 44\%$ elongation.

The similarity in tensile behavior to the engineering materials is reflected in the toughness, taken as the integrated area underneath a stress-strain curve (Fig.B.4D,E,F). The tough, durable, and elastic thiourethane photopolymers have respective tensile toughness of 119.5 ± 14.6 MJ m⁻³, 90.4 ± 10.6 MJ m⁻³, and 15.5 ± 3.5 MJ m⁻³. This represents an order of magnitude improvement over the acrylic counterparts in all cases, which have respective toughness of approximately 9.9 MJ m⁻³, 17.5 MJ m⁻³, and 1.0 MJ m⁻³.⁷⁻⁹ Toughness is now on the same order of magnitude as polyamide, polypropylene, and EPDM rubber.

Heat deflection is also an important metric for industrially relevant materials. Typical tough and durable acrylic photopolymers gain their flexibility by incorporating chemical species that reduce the glass transition temperature. While this improves the mechanical performance, it comes at the cost of reduced heat deflection temperatures. Example heat deflection temperatures of tough and durable acrylic photopolymers are 63 °C and 43 °C.⁷⁻⁹ Because the mechanical performance of the thiourethane photopolymers are not linked to their glass transition, their mechanical strength is largely preserved up to the crystal melting point of the material. These temperatures are also in-line with polyamide and polypropylene, whose heat deflection temperatures are also linked to their crystalline melt. *TU Tough* has a deflection point at 136.1 ± 1.8 °C, between PA-6 (165 °C) and PA-12 (115 °C), whereas *TU Durable* has a deflection point at 104.4 ± 3.5 °C, approximately that of polypropylene at 107 °C.(19)

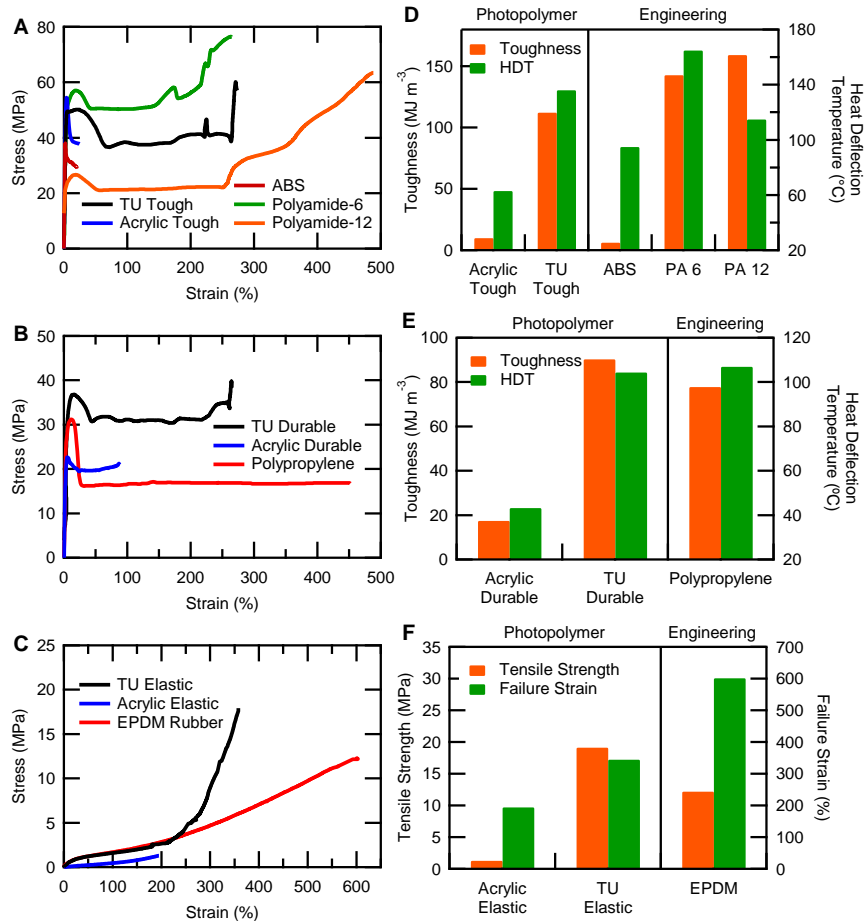


Figure B.4: Semi-crystalline thiourethanes are tougher and more thermally resilient than conventional 3D printing photopolymers (A,B,C) Comparative stress-strain curves of *TU Tough*, *TU Durable*, and *TU Elastic* versus acrylics used in commercially available printing systems and comparable (non-3D printed) engineering polymers. The thiourethane photopolymers have higher elongation and tensile strength than the acrylic materials, with behavior similar to polyamide, polypropylene, and EPDM rubber. **(D,E,F)** The thiourethane materials show an order of magnitude improvement in toughness for the tough, durable, and elastic formulations. The semi-crystalline thiourethanes have heat deflection temperatures over twice that of comparable acrylics, with values similar to polyamide and polypropylene.

B.4 Conclusion

All three of these engineering materials, polyamide, polypropylene, and EPDM rubber, have been difficult at best to process in a 3D printing environment. Polyamides have been made compatible with laser sintering and filament extrusion techniques, but come at high cost and substantially reduced mechanical performance compared to molded parts.³⁰ Despite their advantages in speed and part quality, photopolymer systems especially have had difficulty producing materials with both thermal and mechanical performance comparable to engineering plastics. This has largely been due

to reluctance to move away from the acrylate-based chemistries that have been in use since the inception of stereolithography. This work demonstrates that alternative chemistries may be used to create printable photopolymers with 10x the toughness and 2x the heat deflection temperature in comparison to traditional acrylics. Combined with their compatibility with both SLA and UV inkjetting, these materials give 3D printing systems the material performance needed for use in demanding markets such as automotive, apparel, and aerospace. The wide range of available thiol and isocyanate monomers additionally keeps the door open to other novel photo-curable formulations with unique application-driven properties. Thiourethane resins cured via photo-latent bases have the potential to expand additive manufacturing into spaces that require high performance, end-use parts.

B.5 Materials and Methods:

Materials

2-iodobenzoic acid, 4-methylbenzenethiol, copper iodide, 1,5-diazabicyclo[4.3.0]non-5-ene, sodium tetraphenylborate, and N-methylmorpholine were purchased from Sigma Aldrich (St. Louis, MO). Potassium hydroxide, hydrochloric acid, sulfuric acid, N-bromosuccinimide, anhydrous dichloromethane, and methanol were purchased from Fisher Scientific (Waltham, MA). Fomblin M03 was purchased from Engineered Custom Lubricants (Aurora, IL). 2,2'-(ethylenedioxy)diethanethiol (EDDT), 1,10-decanedithiol (DDT), hexamethylene diisocyanate (HDT), and trimethylhexamethylene diisocyanate (TMHDI) were purchased from TCI America (Portland, OR). Polyamide-6, polyamide-12, polypropylene, and ethylene propylene diene monomer rubber sheets were purchased from McMaster-Carr (Elmhurst, IL). All materials were used as received without further purification.

Photo-catalyst (QAS-MTX) synthesis

2-iodobenzoic acid (3.5 g), 4-methylbenzenethiol (1.75 g), potassium hydroxide (3.96 g), and copper iodide (0.27 g) were dissolved with water (mL) in a round-bottom flask. The solution was refluxed for 12 hours, then acidified using 10% hydrochloric

acid solution. A white precipitate formed upon acidification, which was filtered and confirmed to be 2-[(4-methylphenyl)thio]-benzoic acid via ^1H NMR (4.05 g, 84% yield).

2-[(4-methylphenyl)thio]-benzoic acid (4.05 g) was dissolved in concentrated sulfuric acid (20 mL) and heated to 110 °C for 4 hours while stirring. The solution was pipetted into water (200 mL) in an ice bath while stirring. A yellow precipitate formed immediately, which was filtered and washed with 10% sodium bicarbonate solution (100 mL). The remaining product was confirmed to be 2-(methyl)thioxanthone via ^1H NMR (3.45 g, 92% yield).

2-(methyl)thioxanthone (1.00 g) was added to a dry round-bottom flask with N-bromosuccinimide (0.79 g) in benzene (10 mL). The solution stirred at room temperature under nitrogen and halogen illumination for 6 hours. The solution was washed with water (20 mL) to remove succinimide byproduct, then the benzene was removed by rotary evaporation. The remaining solid was found to be 2-(bromomethyl)thioxanthone via ^1H NMR (1.15 g, 85% yield).

2-(bromomethyl)thioxanthone (2.00 g) was added to a dry nitrogen-purged round-bottom flask and dissolved in anhydrous dichloromethane (150 mL). 1,5-Diazabicyclo[4.3.0]non-5-ene (0.82 g) was dissolved in anhydrous dichloromethane (5 mL) and added dropwise to the flask while stirring. The reaction progressed for 2 hours before extracting the product with water (300 mL). The water was removed by rotary evaporation and the remaining product dissolved into methanol (300 mL). Sodium tetraphenylborate (2.24 g) was dissolved in methanol (20 mL) and added dropwise to the bromide salt solution while stirring. A thick white precipitate formed immediately, which was isolated by vacuum filtration. The solid was dried under desiccation and confirmed to be 5-(2'-(methyl)thioxanthone)-1,5-diazabicyclo[4.3.0]non-5-ene tetraphenylborate by ^1H NMR (3.42 g, 78% yield).

Sample Preparation

Bulk samples were made by mixing the requisite amounts of thiol and isocyanate monomers in a vial with 0.25 wt/wt% of QAS-MTX in a Flacktek DAC 400

speedmixer until homogenous. The solution was pipetted between two glass slides separated by a 500 μm polypropylene spacer. The slide was placed in a UVP CL-1000L ultraviolet crosslinker and cured under 365 nm irradiation for at least 30 minutes. Cured films were annealed at 85 $^{\circ}\text{C}$ for at least 12 hours prior to testing.

Stereolithographic 3D Printing

Stereolithographic addition (SLA) 3D printing was performed on a custom top-down system. It utilizes a DLP projector (Keynote Photonics LC4500-UV) fitted with a 385 nm UV LED. It was positioned above the build vat on a motorized vertical drive to maintain focus and ensure consistent irradiation at 10 mW cm^{-2} to the resin surface. The build plate was fixed in the build vat, which was filled to the build plate with a perfluorinated polyether (PFPE) oil (Fomblin M03). The thiol-isocyanate print resin was poured into the vat, sitting on the surface of the PFPE. The resin height was adjusted by pumping additional PFPE into or out of the vat using a syringe pump (New Era Pump Systems NE-1000L) fitted with two 140 mL syringes using a custom Arduino-based controller (Adaptive3D Technologies).

Parts were printed using 100 μm layer heights and 3-5 seconds of UV exposure per layer depending on the material used. Supports were manually added to the printed model as needed to ensure consistent part geometry. All parts were printed without any inclination relative to the build platform.

Printed parts were removed from the build vat and washed with ethyl acetate to clean any unreacted resin. The *TU Durable* and *TU Elastic* parts were then post-cured at 125 $^{\circ}\text{C}$ for one hour before annealing at 85 $^{\circ}\text{C}$ for at least 12 hours. *TU Tough* parts were heated to 180 $^{\circ}\text{C}$ for one hour prior to annealing.

UV Inkjet Printing

UV inkjet printing was performed on the MultiFab 3D printing platform developed by the Computational Fabrication Group at the Massachusetts Institute of Technology. This system operates by scanning a piezoelectric printhead across the build platform. The printhead selectively deposits material while scanning and is followed by a 365 nm LED unit irradiating the surface at 8 W cm^{-2} , which cures the deposited material

immediately after deposition. This process is repeated until the build is completed and the part may be removed from the build platform. The selected part demonstrated in this work was printed with approximately 20 μm layer heights and no support material.

Differential Scanning Calorimetry

Differential scanning calorimetry (DSC) was performed on a Mettler Toledo DSC1/700 with an auto-loading robot. Samples approximately 5 mg in mass were placed into 40 μL aluminum crucibles and inserted into the machine at 50 $^{\circ}\text{C}$ before cooling to -20 $^{\circ}\text{C}$. The sample was then cycled between -20 $^{\circ}\text{C}$ and 160 $^{\circ}\text{C}$ three times. Tests were performed under constant nitrogen flow at 40 mL min^{-1} with heating rates of 10 $^{\circ}\text{C min}^{-1}$. All samples were tested in triplicate.

Uniaxial Tensile Testing

Uniaxial tensile testing (UTM) was performed on a Lloyd LR5k Plus fitted with a 500 N load cell and Laserscan 200 extensometer. Dog bones were cut from cast or printed sheets using a certified ASTM D638-V cutting die and were tested according to the standard. Each sample was tested at least five times.

Heat Deflection Testing

Heat deflection testing specimens were cast in a machined aluminum mold and milled to ASTM D648-16 specifications. Testing was performed by Element Materials Technology (Warren, MI) according to the ASTM D648-16 standard. All samples were tested in triplicate.

Fourier-Transform Infrared Spectroscopy

Fourier-transform infrared spectroscopy (FTIR) was performed on a Shimadzu IRAffinity-1 with an attenuated total reflection attachment. Real-time recordings were performed by placing a drop of stoichiometrically balanced EDDT-HDI mixture with 0.1 wt% of the photo-catalyst onto the ATR crystal. A 365 nm UV LED was positioned above the crystal to provide even irradiation at 10 mW cm^{-2} . Scanning was initiated with a 1 second capture rate for 10 seconds to establish a baseline prior to the UV source being turned on for the remainder of the test. The percent isocyanate

conversion was taken by the height of the isocyanate peak between 2275-2250 cm^{-1} relative to the baseline reading.

Photo-Rheometry

Photo-rheometry was performed on a TA Instruments DHR-3 with a UV Light Guide Accessory. The UV source was an Excelitas Omnicure S2000 outputting filtered 365 nm light to the rheometer plates at an intensity of 10.0 mW cm^{-2} . Resin for *TU Tough*, *TU Durable*, or *TU Elastic* with 0.1 wt/wt% of photo-catalyst was pipetted between the plates at room temperature. The oscillatory measurement at constant amplitude ($\Gamma = 1\%$) and frequency ($\omega = 5$ Hz) was initiated to establish a baseline viscosity reading prior to the UV source being turned on. The light source remained on until the conclusion of the test. All samples were tested in triplicate.

Photo-Differential Scanning Calorimetry

Photo differential scanning calorimetry (photo-DSC) was performed on a TA Instruments Q2000 modulated DSC with a photo-curing attachment. Samples weighing approximately 5 mg were placed into an uncapped aluminum cell and inserted next to an identical uncapped reference cell in the machine. After equilibration at 30 °C, waveguides coupled to a UV source (Omnicure S2000) illuminated the sample and reference with approximately 10 mW cm^{-2} of 365 nm filtered light. All samples were tested in triplicate.

Polarized Light Microscopy

Polarized light microscopy was performed on an Olympus BX43 microscope under a cross-polarizing filter. The microscope was fitted with an Olympus DP27 camera system and images were acquired using the Olympus cellSens software suite.

Scanning Electron Microscopy

Scanning electron microscopy was performed on cold-fractured specimens using a Zeiss Supra 40. Specimens were coated with 3 nm of gold-titanium using a Hummer VI sputter deposition system prior to imaging. Images were taken at 5.00 kV using a 30.00 μm aperture.

X-Ray Diffraction

XRD data was collected by a coupled Theta-2Theta scan on a PANalytical X'Pert Pro MRD 6-axis diffractometer equipped with a Copper X-ray tube and parallel-beam optics. Samples were polymer films approximately 500 μm thick on top of a glass substrate. Correction was performed by subtracting sample background before fitting was used to assign amorphous or crystalline character to the peaks. Once all peaks were fitted, percent crystallinity was calculated by dividing the crystalline peak area by the total peak area.

B.6 Supplementary Information:

Bulk vs. Printed Properties

The mechanical performance of the thiourethane polymers varies between the bulk materials and those which are 3D printed. Data indicates that there is no discernable chemical difference between printed parts and the bulk material, but rather that the layer-wise printing process is the primary cause of reduced performance. FTIR of bulk vs. printed pieces show no differences beyond what might be attributed to noise (Fig. B.13). DSC results further support that the bulk and printed polymers are chemically identical, showing the same glass transition temperature and crystal melt endotherms of *TU Durable* (Fig. B.14). Differences between bulk and printed parts are only apparent in mechanical testing, where the yield stress shows a tendency to decrease as the layering effect is increased (Fig. B.15, Table B.5). The bulk *TU Durable* material yields near 36.3 ± 1.7 MPa and strains at approximately 30 MPa until failure at $254 \pm 35\%$ strain. X-axis dog bones show a slightly decreased yield of 31.8 ± 1.0 MPa. The yield stress continues to decrease in the Y and Z-axis dog bones, with respective yield stresses of 25.7 ± 2.1 MPa and 22.2 ± 0.8 MPa. However, it is important to note that the failure strains remain similar for the bulk and both printed orientations, in the 240% to 280% range. As a result, the toughness of the printed *TU Durable* material remains quite high even in the Z-axis, at 53.5 ± 10.5 MJ m^{-3} . While this represents a 40% decrease in toughness compared to the bulk material, it remains over twice as large as the comparable acrylic photopolymer. The amorphous *TU Elastic* shows no

significant degree of anisotropy, with failure stresses and strains in the range of 19 MPa and 350% for the bulk material and 3D printed parts in the Y and Z testing orientation (Fig. B.16). X-axis samples are the exception, with decreased tensile stress of 9.5 ± 2.3 MPa while retaining high failure strains of $363 \pm 39\%$. The authors are confident that printed performance will only increase as refinements to the printing system and parameters are made in future studies.

Flory Stockmayer Theory

The gelation of step-wise addition polymerizations can be theoretically modeled with Flory Stockmayer Theory.(31) If we neglect to include intramolecular interactions and assume an equal reactivity among functional groups regardless of oligomer backbone, then gelation occurs when the polymer forms a completely percolated network. The resins contain bifunctional (f=2) thiol species and a combination of bifunctional (f=2) and crosslinking trifunctional (f=3) isocyanates. With this construction in mind, the critical isocyanate conversion for gelation can be described as Equation B.1.

$$p_{NCO} > \sqrt{\frac{\left(\frac{1}{f-1}\right)}{r \left[\left(\frac{1}{f-1}\right) + \rho - \rho \left(\frac{1}{f-1}\right)\right]}} \quad \text{(Equation B.1)}$$

Where p_{NCO} is the conversion of isocyanate groups, r is the total molar ratio of thiol and isocyanate groups (1 in the case of our resins), f is the functionality of our branched unit, HDI-T (f=3), and ρ is the molar ratio of isocyanates in the branched unit to total isocyanate groups in the resin. As shown in Table B.1, all three materials possess the same molar ratio of HDI-T to total isocyanate content (6%) and therefore the same critical conversion for gelation:

$$p_{NCO,critical} = 0.97$$

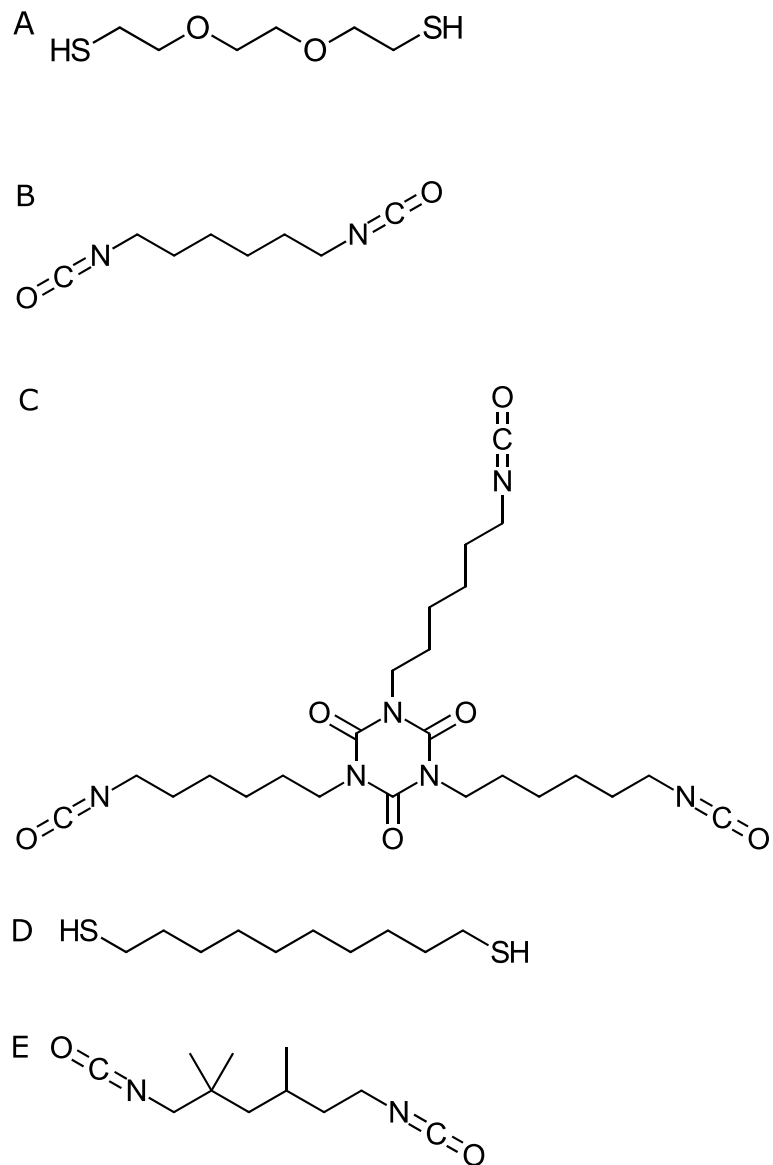


Figure B.5: Chemical structures of thiol and isocyanate monomers used to formulate resins

The base resin, *TU Durable*, is composed of the di-functional thiol monomer (A) 2,2'-(ethylenedioxy)diethanethiol (EDDT), the di-functional isocyanate monomer (B) hexamethylene diisocyanate, and the tri-functional isocyanate monomer (C) tris(6-isocyanatohexyl)isocyanurate. The *TU Tough* and *TU Elastic* resins were made by replacing some amount of di-functional thiol or isocyanate monomers with (D) 1,10-decanedithiol or (E) trimethylhexamethylene diisocyanate, respectively.

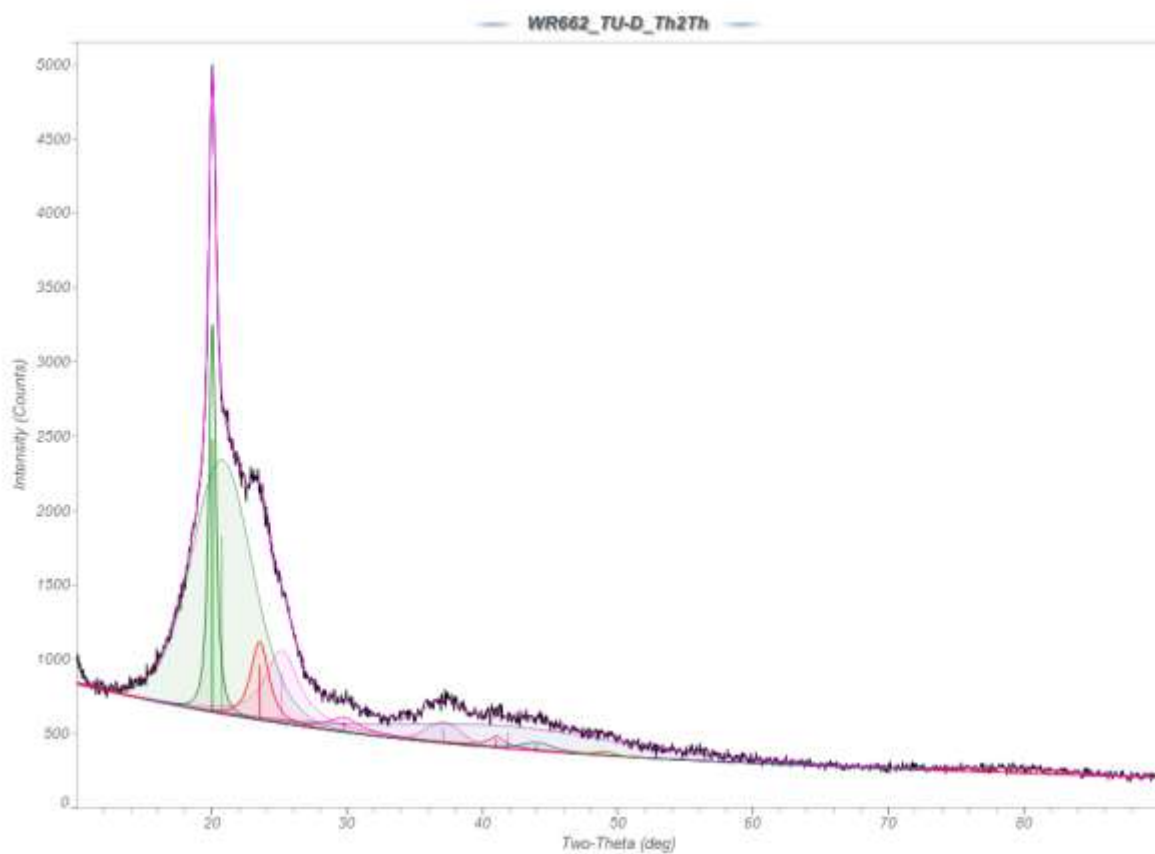


Fig. B.6. X-ray diffraction profile fitting for *TU Durable*. XRD analysis of *TU Durable* shows two major diffraction peaks at 20.02° and 23.53° with smaller subsequent crystalline peaks between 29.76° and 48.97° . This results in a calculated crystallinity of 23.6%.

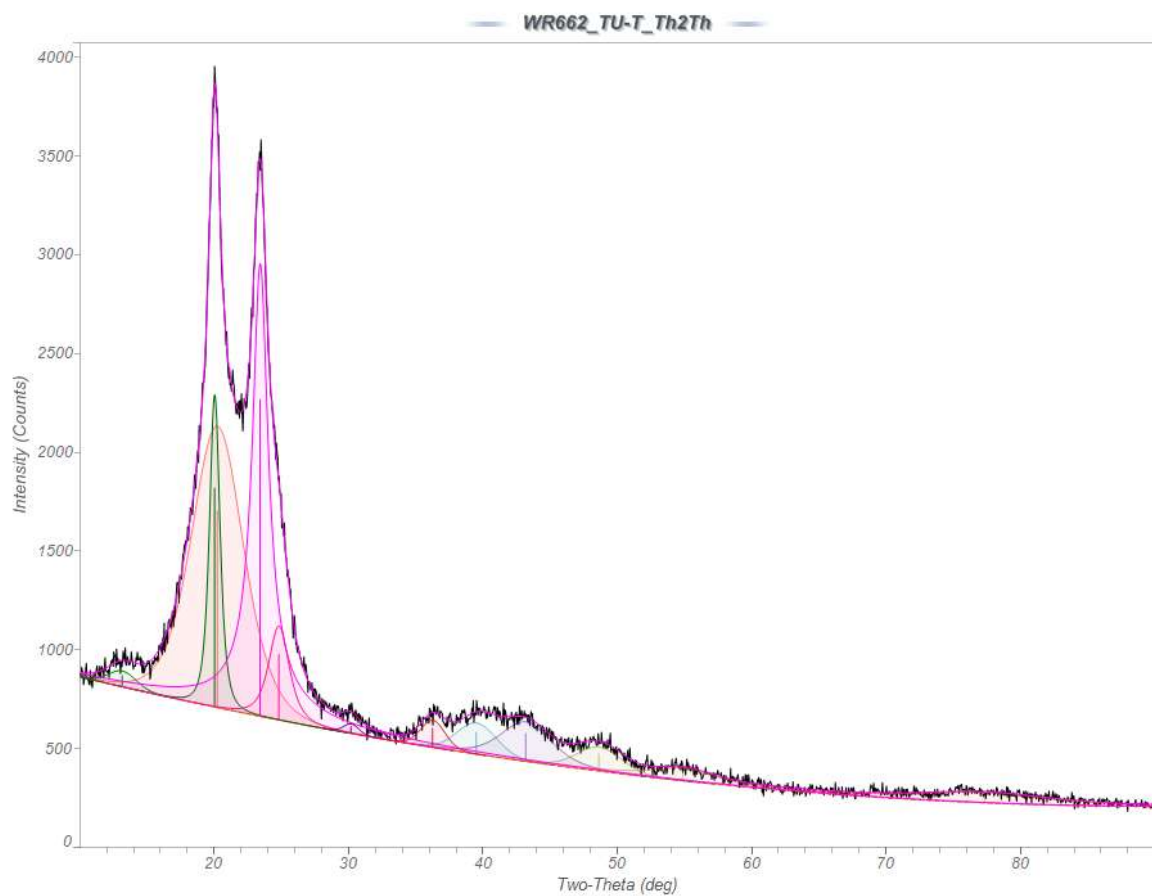


Fig. B.7: X-ray diffraction profile fitting for *TU Tough*. XRD analysis of *TU Tough* shows two major diffraction peaks at 20.02° and 23.41° with smaller subsequent crystalline peaks between 30.18° and 54.86° . This results in a calculated crystallinity of 55.0%.

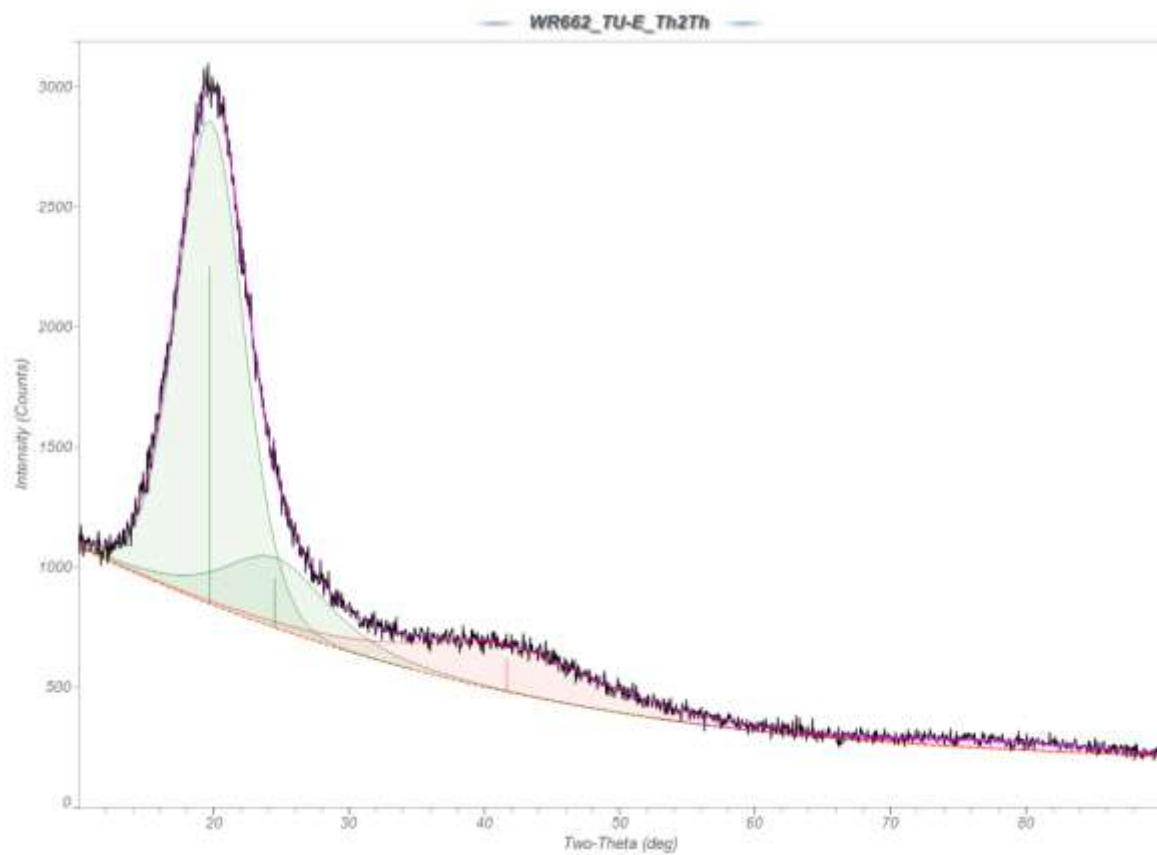


Fig. B.8: X-ray diffraction profile fitting for *TU Elastic*. XRD analysis of *TU Elastic* is a non-crystalline material, showing only amorphous diffraction peaks at angles ranging from 19.70° to 78.44°.

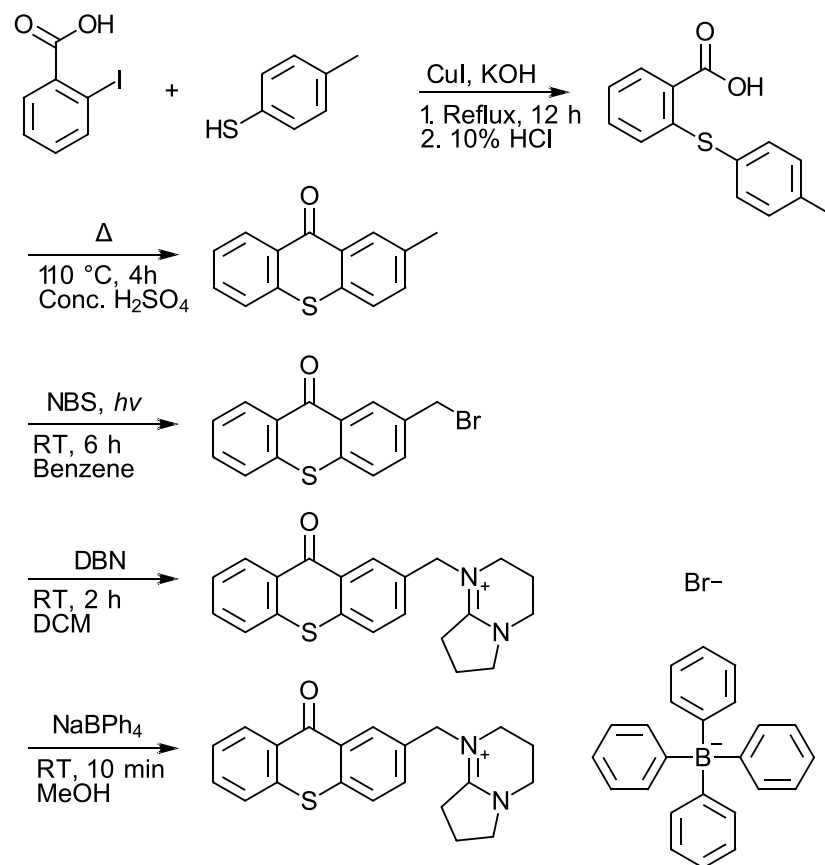


Fig. B.9: Photo-catalyst synthetic procedure. The photolabile superbase 5-(2'-(methyl)thioxanthone)-1,5-diazabicyclo[4.3.0]non-5-ene tetraphenylborate is synthesized via a four-step reactive procedure using commercially available reagents. The reaction takes place under mild conditions and can be done in large batches with relative ease.

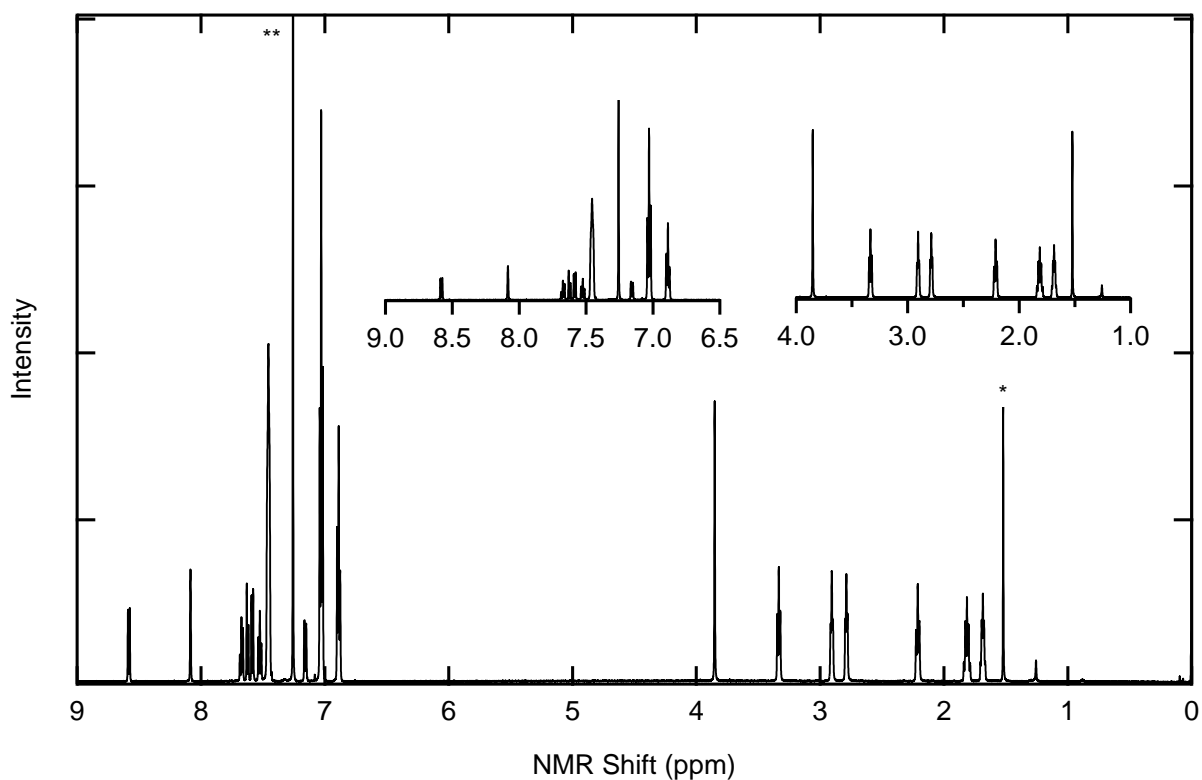


Fig. B.10: ^1H NMR spectrum of the photo-catalyst. Proton NMR in CDCl_3 confirms the structure of the photolabile superbases. Highly shielded protons from the thioxanthone moiety are present between 8.6 and 7.5 ppm. Protons from the tetraphenylborate anion are located between 7.5 and 6.8 ppm. Protons from the methyl group bridging the thioxanthone and ammonium are located at 3.8 ppm. Protons from the 1,5-diazabicyclo[4.3.0]non-5-ene are located between 3.4 and 1.1 ppm. *Water
**Solvent

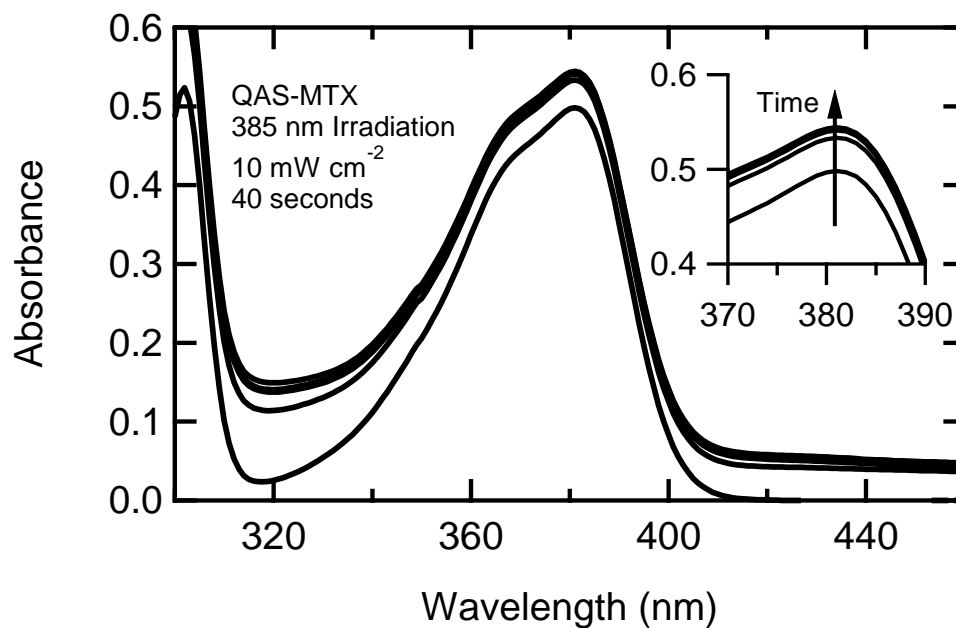


Fig. B.11: UV-visible absorption spectrum of the photo-catalyst. UV-vis spectra show an ultraviolet absorption peak between 320 and 410 nm, peaking at 380 nm. Spectral changes are seen upon irradiation with 385 nm light over the course of 40 seconds, with the peak height increasing as the material undergoes photolysis.

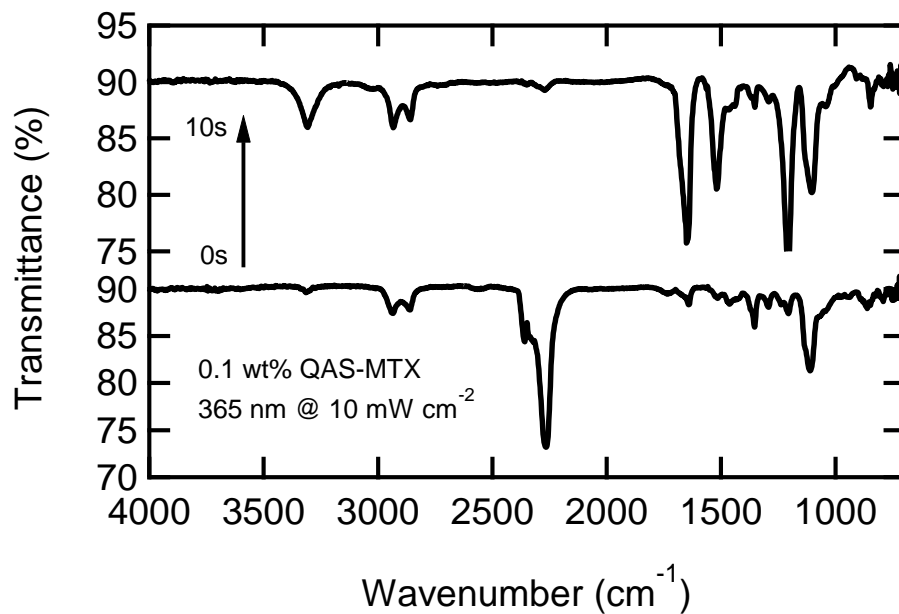


Fig. B.12: FTIR spectra of thiol-isocyanate resin before and after UV curing. FTIR shows the difference in spectra of thiol-isocyanate resin before and after 10 seconds of 365 nm UV irradiation at 10 mW cm⁻². The characteristic isocyanate peak between 2275 cm⁻¹ and 2250 cm⁻¹ disappears, followed by the appearance of the secondary amine peak at 3325 cm⁻¹ and fingerprint peaks for the thiourethane bond at 1600 cm⁻¹, 1500 cm⁻¹, and 1200 cm⁻¹.

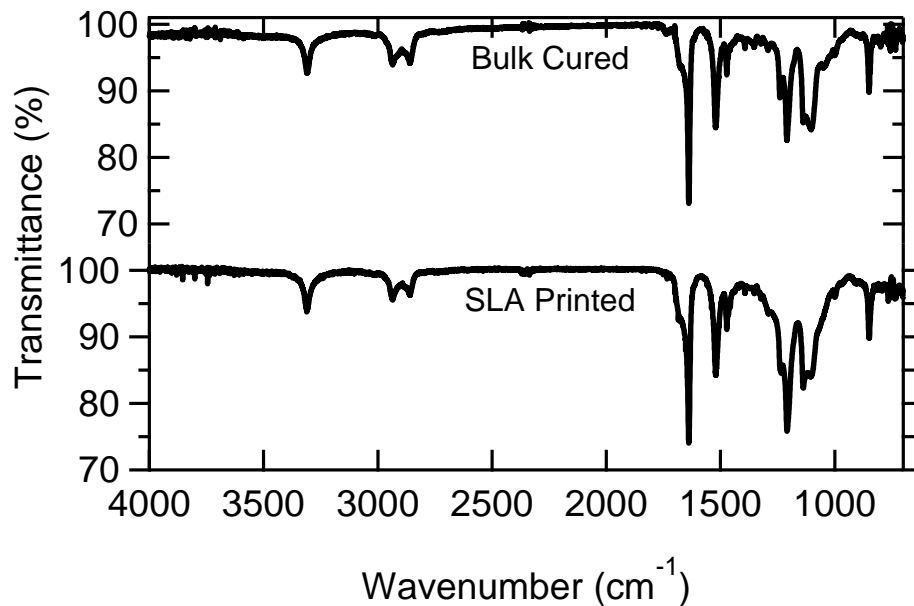


Fig. B.13: FTIR spectra of thiol-isocyanate resins in the bulk and as-printed. FTIR spectra of bulk and printed thiol-isocyanate resins show little difference in the location and intensity of the peaks. Both the bulk and printed materials have no apparent isocyanate peak at 2250 cm⁻¹ and show the characteristic thiourethane peaks near 3325 cm⁻¹, 1600 cm⁻¹, 1500 cm⁻¹, and 1200 cm⁻¹.

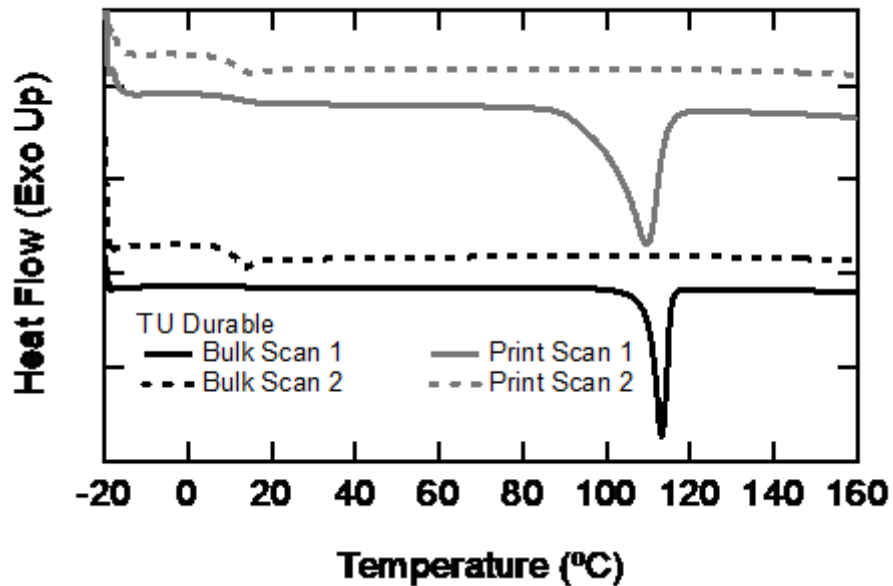


Fig. B.14: Differential scanning calorimetry of bulk and printed thiol-isocyanate resins. Differential scanning calorimetry of bulk and printed *TU Durable* resins show near-identical glass transition temperatures and similar crystal melt behavior. The *TU Durable* resin has a glass transition temperature near 11 °C with a crystal melt endotherm present near 110 °C.

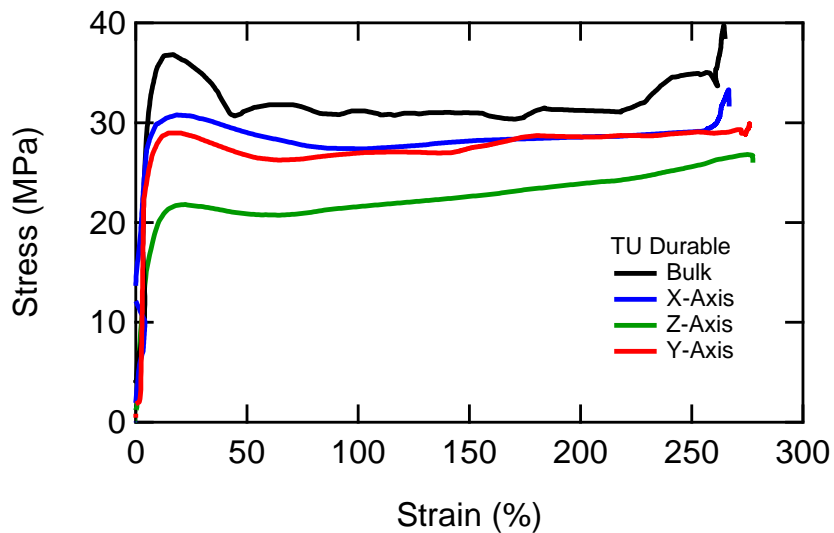


Fig. B.15: Tensile performance of bulk and printed *TU Durable* resin. Uniaxial tensile testing of *TU Durable* resin in the bulk versus printed samples in the X, Y, and Z orientations show the effects of printing on the mechanical performance of the material. The printed polymer has performance similar, but not identical to, the bulk when stressed with the printed layers. When stressed perpendicular to the printed layers performance degrades, indicating that the layering technique used when printing has detrimental effects on the mechanical performance in the semi-crystalline material.

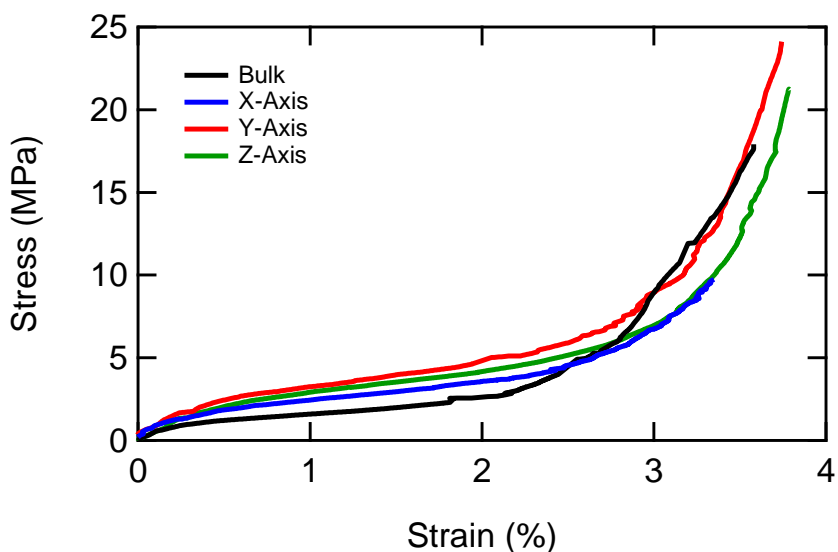


Fig. B.16: Tensile performance of bulk and printed *TU Elastic* resin Uniaxial tensile testing of *TU Elastic* resin in the bulk versus printed samples in the X, Y, and Z orientations show the effects of printing on the mechanical performance of the material. Performance is largely the same across the samples, with failure strains near 350%. Failure stresses are close to 20 MPa with the exception of the X-oriented samples, which tended to fail at lower stresses.

Table B.1: Thiol-isocyanate molar ratios for photopolymer formulations

Sample	EDDT (% SH)	DDT (% SH)	HDI (% NCO)	HDI-T (% NCO)	TMHDI (% NCO)
TU Durable	100	0	94	6	0
TU Tough	55	45	94	6	0
TU Elastic	100	0	44	6	50

Table B.2. X-ray diffraction profile fitting results for *TU Durable*

#	Angle(°)	d(nm)	Height	Area(α 1)	Area(α 1)%	FWHM(°)
1	20.0238	0.4431	1834.9	1506.7	21.4	0.615
2	20.7280	0.4282	1195.1	7024.7	100.0	5.296
3	23.5264	0.3778	368.5	768.3	10.9	1.602
4	25.1602	0.3537	344.2	1551.6	22.1	3.014
5	29.7594	0.3000	70.9	391.3	5.6	2.781
6	37.1031	0.2421	99.0	324.3	4.6	3.064
7	40.9964	0.2200	56.6	248.9	3.5	1.458
8	44.0091	0.2056	41.1	181.2	2.6	2.905
9	41.8796	0.2155	107.4	2397.3	34.1	20.000
10	48.9747	0.1858	20.8	39.6	0.6	1.774
11	79.4734	0.1205	21.4	215.9	3.1	9.473

*amorphous peaks in yellow

Table B.3. X-ray diffraction profile fitting results for *TU Tough*

#	Angle(°)	d(nm)	Height	Area(α 1)	Area(α 1)%	FWHM(°)
1	13.1522	0.6726	55.6	143.7	2.8	2.419
2	20.0195	0.4432	1106.6	1261.1	24.7	0.910
3	20.2229	0.4388	995.2	5112.1	100.0	4.522
4	23.4052	0.3798	1603.3	4303.8	84.2	1.485
5	24.8028	0.3587	332.6	741.6	14.5	1.796
6	30.1754	0.2959	33.9	48.3	0.9	1.331
7	36.2479	0.2476	96.0	220.6	4.3	2.119
8	39.4967	0.2280	110.8	407.7	8.0	3.445
9	43.1751	0.2094	140.5	715.5	14.0	4.430
10	48.6237	0.1871	85.5	359.6	7.0	3.914
11	54.8595	0.1672	45.8	383.3	7.5	5.639
12	77.3318	0.1233	38.3	558.8	10.9	11.900

*amorphous peaks in yellow

Table B.4. X-ray diffraction profile fitting results for *TU Elastic*

#	Angle(°)	d(nm)	Height	Area(α 1)	Area(α 1)%	FWHM(°)
1	19.7010	0.4503	1401.9	8894.1	100.0	5.815
2	24.5244	0.3627	203.7	2157.8	24.3	8.992
3	41.6663	0.2166	136.6	2671.0	30.0	15.899
4	78.4419	0.1218	23.5	387.4	4.4	16.128

*amorphous peaks in yellow

Table B.5. Mechanical properties in tension of thiol-isocyanate photopolymers

Sample	Axis	Yield Stress (MPa)	Tensile Strength (MPa)	Failure Strain (%)	Toughness (MJ m⁻³)
TU Durable	Bulk	36.29 ± 1.71	46.40 ± 7.79	254.08 ± 35.26	90.35 ± 10.64
	X	31.82 ± 0.97	32.57 ± 6.23	253.92 ± 59.82	71.28 ± 15.80
	Y	25.70 ± 2.05	30.91 ± 4.69	236.41 ± 34.80	62.43 ± 12.59
	Z	22.17 ± 0.80	26.23 ± 2.96	239.00 ± 40.02	53.46 ± 10.51
TU Tough	Bulk	49.84 ± 0.93	55.27 ± 9.48	290.32 ± 20.83	119.55 ± 14.64
TU Elastic	Bulk	-	19.59 ± 5.30	352.76 ± 27.05	15.46 ± 3.54
	X	-	9.53 ± 2.25	362.71 ± 39.50	14.33 ± 2.08
	Y	-	21.81 ± 8.08	358.91 ± 35.92	19.64 ± 5.43
	Z	-	18.74 ± 9.84	355.69 ± 29.73	17.21 ± 5.98

REFERENCES

1. J. V. Crivello, E. Reichmanis, Photopolymer Materials and Processes for Advanced Technologies. *Chemistry of Materials* **26**, 533-548 (2014).
2. B. Baroli, Photopolymerization of biomaterials: issues and potentialities in drug delivery, tissue engineering, and cell encapsulation applications. *Journal of Chemical Technology & Biotechnology* **81**, 491-499 (2006).
3. I. Gibson, D. W. Rosen, B. Stucker, *Additive manufacturing technologies*. (Springer, 2010), vol. 238.
4. H. Lipson, M. Kurman, *Fabricated: The new world of 3D printing*. (John Wiley & Sons, 2013).
5. S. Ltd., "Digital Materials Data Sheet," (2015).
6. P. J. Bártolo, *Stereolithography: materials, processes and applications*. (Springer Science & Business Media, 2011).
7. Stratasys Ltd., "PolyJet Materials Data Sheet," (2016).
8. Formlabs Inc., "FLTOTL03 Materials Properties Datasheet," (2016).
9. Formlabs Inc., "FLDUCL01 Material Properties Datasheet," (2017).
10. J. R. Tumbleston *et al.*, Continuous liquid interface production of 3D objects. *Science* **347**, 1349-1352 (2015).
11. T. Wohlers, *Wohlers report 2016*. (Wohlers Associates, Inc, 2016).
12. A. Galeski, Strength and toughness of crystalline polymer systems. *Progress in Polymer Science* **28**, 1643-1699 (2003).
13. A. Argon, R. Cohen, Toughenability of polymers. *Polymer* **44**, 6013-6032 (2003).
14. W. K. Neo, M. B. Chan-Park, A New Model and Measurement Technique for Dynamic Shrinkage during Photopolymerization of Multi-Acrylates. *Macromolecular rapid communications* **26**, 1008-1013 (2005).
15. J. W. Stansbury *et al.*, Conversion-dependent shrinkage stress and strain in dental resins and composites. *Dental Materials* **21**, 56-67 (2005).

16. P. F. Jacobs, *Rapid prototyping & manufacturing: fundamentals of stereolithography*. (Society of Manufacturing Engineers, 1992).
17. K. D. Belfield, J. V. Crivello, *Photoinitiated polymerization*. (ACS Publications, 2003).
18. C. E. Hoyle, A. B. Lowe, C. N. Bowman, Thiol-click chemistry: a multifaceted toolbox for small molecule and polymer synthesis. *Chemical Society Reviews* **39**, 1355-1387 (2010).
19. J. E. Mark, *Polymer data handbook*. (Oxford University Press, 2009).
20. J. Shin, H. Matsushima, C. M. Comer, C. N. Bowman, C. E. Hoyle, Thiol–Isocyanate–Ene Ternary Networks by Sequential and Simultaneous Thiol Click Reactions. *Chemistry of Materials* **22**, 2616-2625 (2010).
21. S. Katogi, M. Yusa, Photobase generation from amineimide derivatives and their use for curing an epoxide/thiol system. *Journal of Polymer Science Part A: Polymer Chemistry* **40**, 4045-4052 (2002).
22. M. Sangermano, A. Vitale, K. Dietliker, Photolabile amines producing a strong base as photocatalyst for the in-situ preparation of organic–inorganic hybrid coatings. *Polymer* **55**, 1628-1635 (2014).
23. J.-X. Li, L. Liu, A.-H. Liu, Study on synthesis and photoactivity of N-substituted diazabicyclononane derivatives with different substituents. *International Journal of Adhesion and Adhesives* **57**, 118-124 (2015).
24. K. Suyama, M. Shirai, Photobase generators: Recent progress and application trend in polymer systems. *Progress in Polymer Science* **34**, 194-209 (2009).
25. H. Salmi, X. Allonas, C. Ley, Polythiourethane networks catalyzed by photobase generators. *Progress in Organic Coatings* **100**, 81-85 (2016).
26. A. Sarker, D. Neckers, Tetraorganylborate salts as convenient precursors for photogeneration of tertiary amines. *Journal of the Chemical Society, Perkin Transactions 2*, 2315-2322 (1998).
27. A. M. Sarker, Y. Kaneko, D. Neckers, Synthesis of tetraorganylborate salts: photogeneration of tertiary amines. *Chemistry of materials* **13**, 3949-3953 (2001).

28. J. Shin, J. Lee, H. M. Jeong, Properties of polythiourethanes prepared by thiol–isocyanate click reaction. *Journal of Applied Polymer Science*, 46070-n/a.
29. A. Ravve, *Light-associated reactions of synthetic polymers*. (Springer, 2006).
30. Stratasys Inc., "FDM Nylon 12 Material Specification Sheet," (2017).
31. W. H. Stockmayer, Theory of molecular size distribution and gel formation in branched polymers II. General cross linking. *The Journal of Chemical Physics* **12**, 125-131 (1944).

APPENDIX C

STEREOLITHOGRAPHY FOR PERSONALIZED LEFT ATRIAL APPENDAGE OCCLUDER

C.1 Abstract

Mass-produced medical implants typically come in several standard geometries and sizes that often fail to address the various patient morphologies encountered, particularly when a patient's anatomy is in a diseased state. With advancements in high resolution imaging, segmentation software, and rapid prototyping,¹⁻⁴ the development of patient-specific implants has become more accessible to the medical community. To date, personalized implants have been fabricated for a variety of medical needs such as airway disorders,⁵ mitral valve insufficiencies,^{6,7} craniomaxillofacial defects,^{8,9} and orthopedic replacements.¹⁰⁻¹² Due to manufacturing and chemistry limitations, most of these custom implants require fabrication from high elastic modulus ($E > 1$ GPa) materials that are mechanically dissimilar to the soft tissues of the human body ($E < 1$ MPa).¹³ Such rigid devices fail to conform to neighboring anatomical structures, concentrate stress, and can perforate tissues.¹⁴ Here we present stereolithography (SLA) of elastomeric polyurethane (EPU) as a fast (~ 3 cm hr⁻¹ draw-rate), low-cost (\$0.25 mL⁻¹ of material), and scalable 3D printing process for fabricating patient-specific (P-S) medical implants. As a demonstration, we have fabricated patient-specific left atrial appendage (LAA) occluders (Fig. C.1a) for those at high risk of blood clot formation due to atrial fibrillation (AF).

C.2 Introduction

Patients with AF have nearly a five times greater risk of stroke due to cardiac emboli,¹⁵ with greater than 50% of these emboli originating in the LAA, possibly due to the low flow velocities of blood within the complex structure.¹⁶ Blood-thinners are currently the first line of therapy to prevent stroke in high-risk patients. These drugs, however, are only effective in a narrow therapeutic window, require frequent and ongoing monitoring, increase the risk of internal bleeding, and can negatively interact

with the individual's physiology or other drugs.¹⁷ Therefore, surgical removal or mechanical occlusion of the LAA is the recommended alternative for stroke prophylaxis.¹⁸⁻²⁰ Unfortunately, conventional surgical resection of the appendage not only hinders the contractile function of the remaining left atrial tissue²¹ but can also result in incomplete closure (~36% of cases) and commensurate risk of stroke.^{22,23} These risks lead many practitioners to avoid recommending surgical interventions that remove or remodel the LAA. As an alternative, mechanical LAA occlusion devices that employ a self-expanding metal alloy (nitinol) cage are now available in a set number of sizes. These occluders deploy into a round dome that caps the ostium of the appendage.¹⁸⁻²⁰ Implantation of these rigid devices requires physically anchoring them using hooks that concentrate mechanical stress and can cause tears in the thin-walled tissue of the LAA. Additionally, due to the high variability of LAA morphology—standardized, off-the-shelf occluder geometries often fail to completely block an ostium from residual blood flow.^{14,24,25}

Recently our labs demonstrated the efficacy of patient-specific, soft, hollow LAA occluders²⁶ implanted in a canine model to address the issues of incomplete occlusion, perforation of LAA tissue, and device anchoring. Construction with elastomers is key to this advancement—the highly compliant endovascular devices are selectively inflated to fully conform to the complex LAA morphology at low volumes, which minimizes stress and damage to the surrounding tissues. Though fabricated via rapid prototyping (i.e., replica molding, lamination, and dip-coating), the workflow for constructing personalized occluders remains laborious and time-consuming; we required at least three days to fabricate the patient-specific designs. Additionally, this manufacturing strategy is incompatible with potentially un-moldable morphologies and requires a lamination step that introduces a seam, (reducing the mechanical integrity) creating non-uniform wall thicknesses. Herein, we demonstrate a rapid approach where we perform segmentation of the LAA from computed tomography (CT) scans, create a computer aided design (CAD), and 3D print the custom geometry to realize a monolithic, thin-walled elastomeric LAA occluder (Fig. C.1). This process requires only ~12 hours.

Though various 3D printing technologies (e.g., Direct Ink Writing, Fused Deposition Modeling, Selective Laser Sintering)^{7,27-29} have been used in medicine, we chose to use stereolithography (SLA). Based on layer-by-layer solidification of a liquid resin in response to photopatterned light (Fig. C.5), SLA enables direct fabrication of complex, hollow elastomeric architectures with feature sizes on the order of 100 μm .^{2,30,31} Additionally, by projecting multiple images onto the same build stage, we can rapidly ($t_{\text{print}} \sim 1.5$ hr) manufacture in a single print (i) multiple design variations for the same patient (i.e. iterate design complexity; Fig. C.6a), (ii) multiple occluders for different patients (Fig. C.6b, C.7), and (iii) multiple copies of one design for one patient (i.e. scale up manufacturing; Fig. C.1c).

C.3 Results

Design of patient-specific occluders for 3D printing

Non-invasive, human cardiac CT scans guide the design of patient-specific (P-S) occluders, a method thoroughly described previously by Robinson et al. (Fig. C.1b).²⁶ Briefly, we used open-source software (ITK-Snap, University of Pennsylvania) to perform semi-automatic image segmentation on the left heart blood volume from human CT scans. We used Next, an additional image processing software (Geomagic Wrap, 3D Systems) isolates the LAA, smoothes the surface and shells the object for 3D printing a hollow structure with a wall thickness of 300 μm . To prepare the design for direct printing, we used SOLIDWORKS (Dassault Systems) to (i) add a valve to the ostial surface of the occluder, and (ii) insert drainage holes to reduce vacuum forces that occur during SLA printing of hollow structures (Fig. C.1b).

Fabrication of patient-specific occluders

We used a high-resolution, projection-based SLA printer (M1, Carbon, Inc.) and a commercial elastomeric polyurethane (EPU, Carbon) resin to directly print custom LAA occluder designs (Fig. C.1c). With a 141 mm x 79 mm build stage, 10 - 15 occluders can be printed at once, greatly increasing the fabrication speed over previous methods. After printing, the base material is not fully polymerized and the “*green*

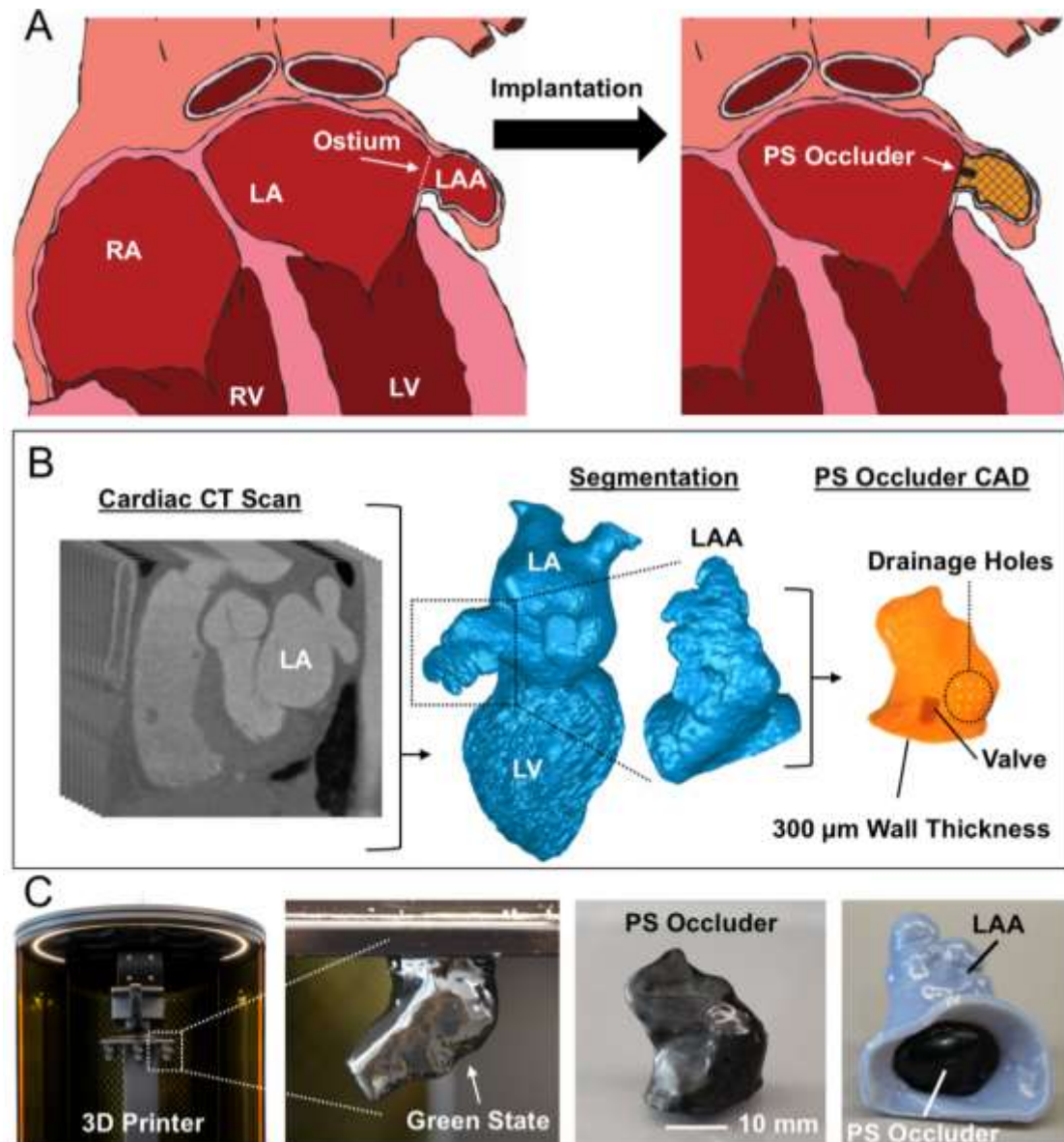


Figure 1| Direct 3D printing of patient-specific (PS) left atrial appendage (LAA) occluder. (a) Schematic of heart with right atrium (RA), right ventricle (RV), left atrium (LA), and left ventricle (LV) labeled. The ostium is the opening between the LA and LAA. A P-S occluder is implanted into the LAA and conforms to the surrounding tissue. **(b)** CT Segmentation of left heart blood volume, isolation of LAA, CAD design of P-S hollow occluder with 300 μm wall thickness, 3 mm diameter valve, and drainage holes for venting during printing. **(c)** 3D printing of P-S occluder. The freshly printed part as a delicate *green body*. Final printed P-S occluder after cleaning and full cure. P-S occluder implanted into 3D printed LAA.

bodies” are fragile and covered in liquid resin (Fig. C.1c). We used isopropyl alcohol to gently clean resin off both the external and internal surfaces. The drainage holes that allowed for venting of the hollow prints aid in the removal of encapsulated,

unreacted resin inside the occluders. Applying a thin layer of fresh resin over these holes, followed by exposure under a UV light source (ECE 5000, Dymax Inc.) sealed the green body. A post-processing thermal treatment (120°C for 8 hr) fully cures the EPU material to obtain the full elastomeric properties (Fig. C.1c, C.2a). Lastly, we injected silicone pre-polymer (Ecoflex 00-30, Smooth-On) into the cavity of the valve where it interlocks and cures with printed crossbars to create a self-sealing valve (Fig. C.2a).

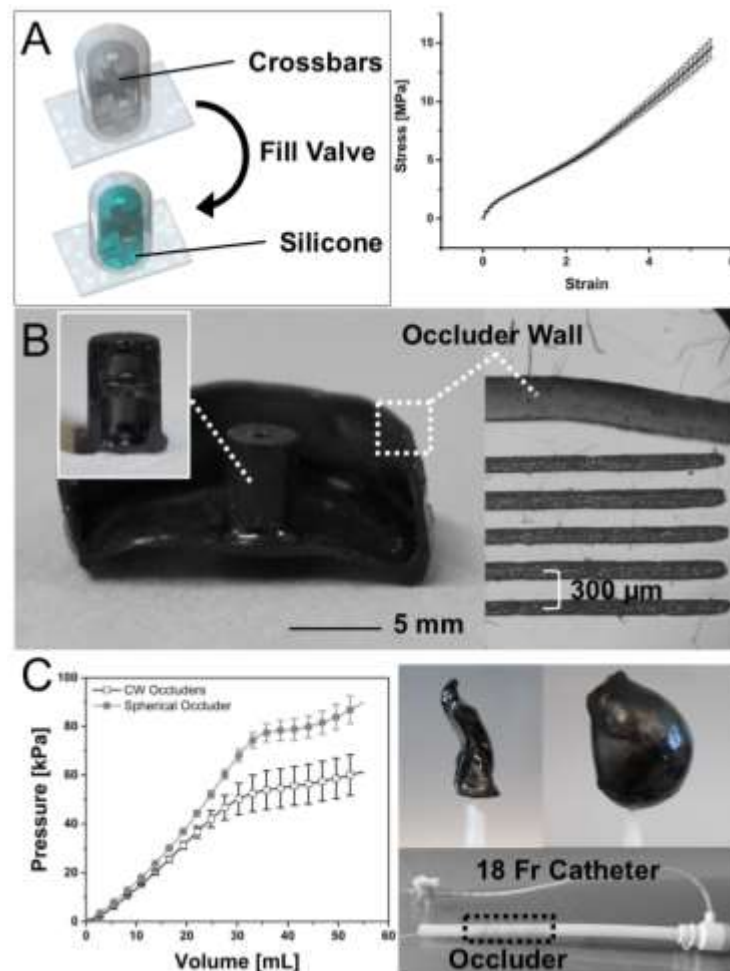


Figure 2| Features of 3D printed, patient-specific occluders. (a) Schematic of printed valve before and after filling with silicone. The printed crossbars (black) lock the added silicone (blue) in position so no covalent bonding is necessary (left). The uniaxial tensile behavior of elastomeric polyurethane (EPU; $n = 11$, mean \pm s.d.). (b) Cross-section of occluder with cross-section of valve inset. Right, optical microscope image of cross section of occluder wall next to reticle for measuring wall thickness, $t \sim 318.6 \pm 49 \mu\text{m}$ ($n = 9$, mean \pm s.d. from 3 occluders). (c) Comparison of P-S and spherical occluders pressure-volume behavior (left, $n = 7$, mean \pm s.d.). Right top, image of P-S occluder evacuated and inflated to very large volumes using air ($\Delta P > 50 \text{ kPa}$) Right bottom, potential delivery method, P-S occluder within an 18 Fr catheter (outlined by dotted line).

By iterating this process with a representative geometry (e.g., Chicken Wing) obtained from a CT scan, we empirically determined the minimum wall thickness ($t = 318.6 \pm 49 \mu\text{m}$) compatible with our printing process (Fig. C.2b). Replica molding pathways for similar elastomeric occlusion devices could only achieve thickness with large dimensional variance, $t = 500 \pm 125 \mu\text{m}$. The final printed occluder, when compressed, fits into an 18 Fr Catheter ($d = 6 \text{ mm}$) for surgical intervention (Fig. C.2c).

Our material choice also imparts important mechanical performance to the printed devices. Compared to other available SLA materials, EPU is an excellent candidate owing to its large ultimate strains ($\gamma_{\text{ult}} > 300\%$; Fig. C.2a) and high tear strength ($T_{\text{tear}} = 23 \pm 3 \text{ kN m}^{-1}$). Combined, these properties lead to a robust, highly deformable device even when dimensions are miniaturized. Despite having a 40% thinner wall, these occluders operate safely at pressures and volumes ($\Delta P > 60 \text{ kPa}$, $\Delta V > 50 \text{ mL}$; Fig. C.2c, C.8) that exceed the corresponding failure regimes of their replica molded silicone counterparts ($\Delta P_{\text{burst}} \sim 30 \text{ kPa}$, $\Delta V_{\text{burst}} \sim 40 \text{ mL}$).²⁶

Stable anchoring and resistance to embolism

Another concern with implanted occluders is the possibility of device embolization into the left atrium. To probe the long-term viability of our printed geometries, we conducted *in vitro* pull-out tests at different device inflation volumes, $V_{\text{inflation}} = (V_{\text{injected}}/V_{\text{rest}})*100\%$ (Fig. C.3a). We 3D printed a custom attachment for the bottom grip of our tensile tester (Zwick & Roell, z010) that replicates the Chicken Wing LAA anatomy (Fig. C.3b, C.9). We implanted either a patient-specific or spherical occluder ($r_{\text{rest}} = 8.75 \text{ mm}$) into this synthetic LAA. After implantation, we applied an increasing tensile force on the ostial surface of the occluder until ejection of the device from the simulated appendage (Fig. C.3b, C.9). We report the maximum force during separation as a function of inflation volume (Fig. C.3a, Table C.1). These forces dramatically exceed those required to dislodge the Watchman® and Amulet® occlusion devices ($F_{\text{pull-out}} \sim 3.5 \text{ N}$), which make use of nitinol hooks to pierce the tissue for anchoring. For the P-S morphology, we estimated a minimum occlusion volume of $V_{\text{inflation}} \sim 200\%$ (Fig. C.10) that corresponds to a pull-out force of

approximately $F_{pull-out} \sim 14.9 \pm 1.47$ N. Increasing the volume of both the P-S and spherical occluders logically increases the

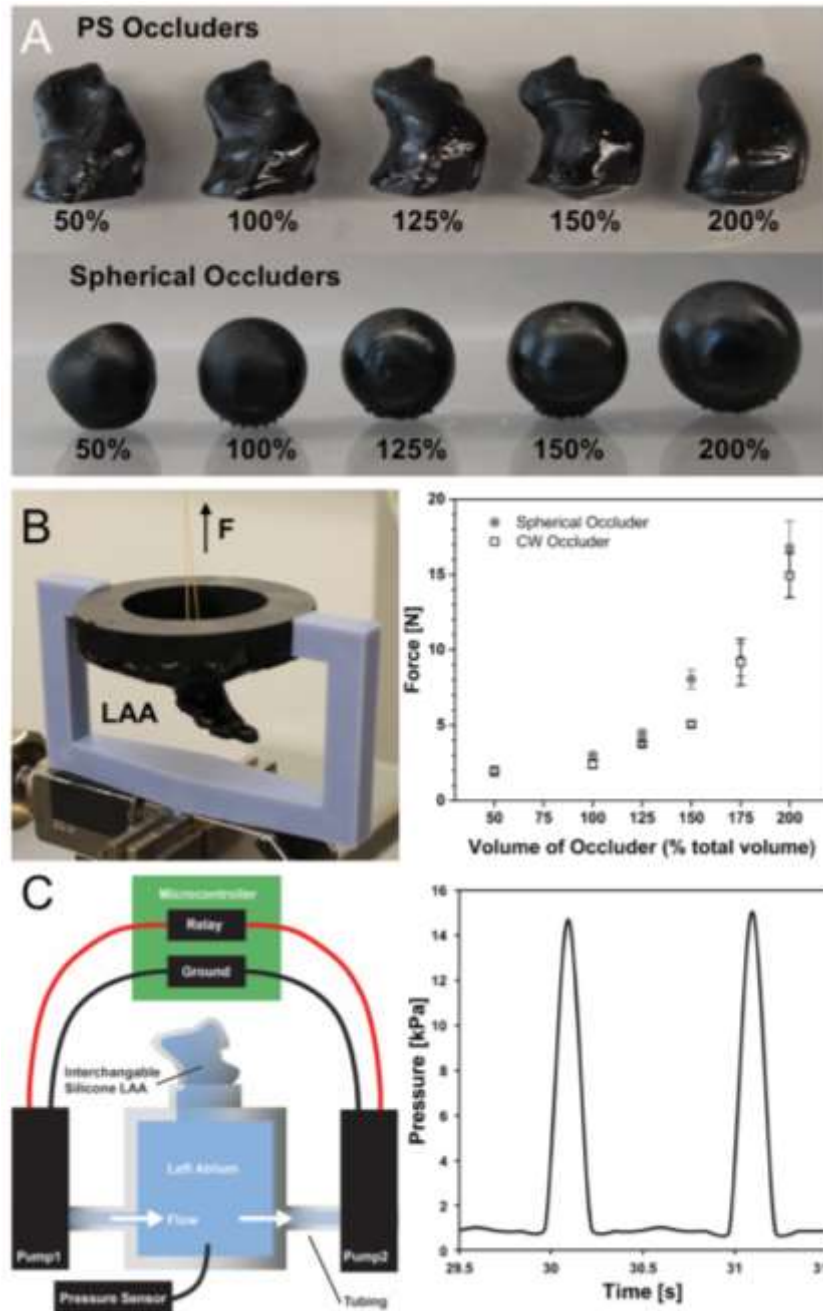


Figure 3| Pull-out and embolism performance of patient-specific (PS) vs spherical occluders. (a) P-S and spherical occluders filled with Ecoflex 00-30 up to $V_{inflation} \sim 200\%$. (b) 3D printed pull-out test jig attached to Zwick tensile tester (left). Force needed to pull occluder out of LAA when inflated by increasing amounts ($n = 5$, mean \pm s.d.). (c) Schematic of embolism test set-up. P-S or spherical occluder was implanted into the silicone LAA for 48 hours to see if occluder would embolize (left). Physiological pressure drops $\Delta P \sim 15$ kPa and frequencies ($f \sim 1$ Hz) were maintained throughout the 48 hours.

pull-out forces, but likely impinges upon the adjacent anatomy. In particular, the spherical samples with large inflation volumes ($V_{inflation} > 150\%$) visibly deformed the simulated LAA, which is consistent with our observations that non-P-S geometries have the potential to strain and damage both the LAA and neighboring tissues while attempting to fully occlude the ostium.

Whereas the pull-out measurements were made on a static appendage, the *in vivo* atrial environment is dynamic. The oscillating pressures within the heart, coupled with the expansion and contraction of the atria may contribute to device embolism at forces less than the previously measured thresholds. Here, we simulated the LAA anatomy using a silicone phantom attached to an idealized left atrium flow loop (Fig. C.3c, C.11). After implanting our printed device, we controlled the operation of two pumps at pulsatile flow ($f \sim 1$ Hz) and pressure regimes ($\Delta P \sim 15$ kPA) that approximated the systolic and diastolic behavior of the left heart ($\Delta P \sim 16$ kPA; Fig. C.3c).³² Table C.1 notes any embolism event or damage to the LAA phantom during subsequent continuous operation for 48 hours. We found that both P-S and spherical occluders embolized when they were underinflated, $V_{inflation} \sim 50\%$ (Fig. C.12). We also observed that over-inflation ($V_{inflation} > 200\%$) of spherical occluders tore the silicone LAA within the first 24 hours (Fig. S9).

Table C.1| Embolism and pull-out test results for occluders of various inflation volumes.
($n = 5$, mean \pm s.d.)

$V_{inflation}$	50%	100%	125%	150%	200%
<i>Embolism Test Results</i>					
<i>P-S</i>	Embolized	Stable	Stable	Stable	Stable
<i>Spherical</i>	Embolized	Stable	Stable	Stable	Tore LAA
<i>Pull-out Test Results [N]</i>					
<i>P-S</i>	2.0 \pm 0.22	2.4 \pm 0.27	3.8 \pm 0.14	5.0 \pm 0.19	14.9 \pm 1.47
<i>Spherical</i>	1.9 \pm 0.22	3.0 \pm 0.17	4.4 \pm 0.30	8.0 \pm 0.64	16.8 \pm 1.78

Hemodynamic flow analysis of atrial-facing geometry

Currently available mechanical closure devices are round in shape, while the ostium of most LAAs are elliptical. This mismatch in geometry causes large crevices

to form on either side of implanted occluders; these cavities can lead to residual flow of blood into the LAA and to clots forming on or around the device. To ensure stable anchoring and to mitigate residual flow, these round devices are typically oversized by 8-20%.³³ While this practice helps eliminate blood flowing into the appendage, it does not diminish—and may worsen—the severity of the crevices between the occluder and the atrial wall. The ability of our printed LAA to change volume in a “balloon-like” manner is a key differentiator compared to existing LAA occluders and allows them to conform to the LAA anatomy. The atrial-facing geometry of our occluders was designed from the CT scans to exactly match the existing anatomy.

We used computational flow dynamics (CFD) to analyze the atrial-facing geometry of patient-specific and spherical occluders (Fig. C.4). We used SolidWorks™ to assemble either a P-S or spherical occluder into the appendage of a Chicken Wing LAA morphology. After creating a solid body and mesh we then performed the flow analysis. We overlaid the contour results from the wall shear stress of both the P-S and spherical geometries over their left heart models (Fig. C.4b-c). Our observations indicate that the regions along the edges of the spherical occluder had very low wall shear stress regimes (Fig. 4c), which prior studies have correlated with clot formation.³⁴ These areas of low wall shear stress were not as pronounced in the P-S design (Fig. 4b), likely due to better conformal matching the internal atrial wall.

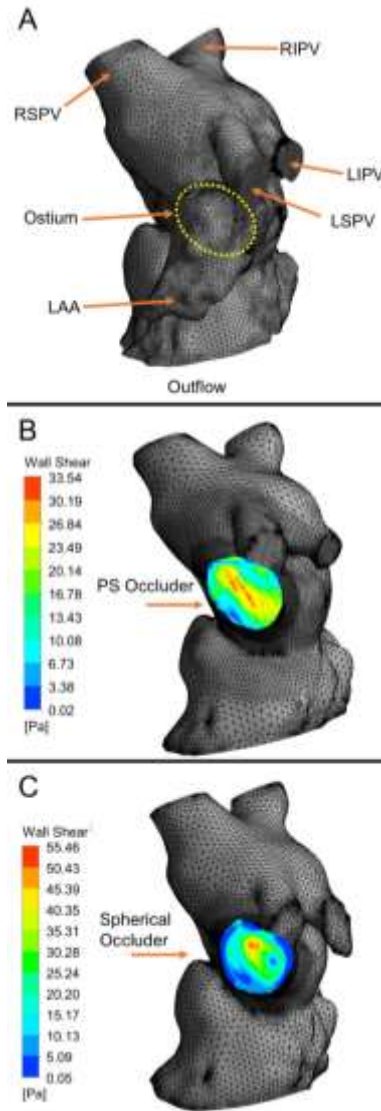


Figure 4| Computational hemodynamics of the atrium facing wall of a PS or spherical occluder. (a) Fluid domains discretization with 441,162 tetrahedron elements. Right superior pulmonary vein (RSPV), right inferior pulmonary vein (RIPV), left superior pulmonary vein (LSPV), and left inferior pulmonary vein (LIPV) are the inflow regions. The ostium is not visible from this surface view, but its position on the interior surface has been outlined using a yellow dotted line. The Chicken Wing morphology LAA has also been highlighted. The outflow region is the left ventricle, it has been cropped out. (b) Model of left heart with patient-specific (PS) occluder within the LAA, it has 472,741 tetrahedron elements. The wall shear stress contour of the atrial wall of the occluder has been overlaid on the model. (c) Model of left heart with spherical occluder within the LAA, it has 408,667 tetrahedron elements. The wall shear stress contour of the atrial wall of the occluder has been overlaid on the model. Note the areas of dark blue on the outer edges. These are located where crevices have formed between the occluder and the atrial wall.

C.4 Conclusion

Although medical 3D printing is most commonly used for education and surgical planning,^{29,35-37} we have demonstrated the fabrication of patient-specific medical

devices as another promising application. We developed a strategy for rapidly producing a left atrial appendage occluder designed specifically for an individual patient suffering from atrial fibrillation. These occluders are printed using elastomeric polyurethane and function balloons that can conform to a patient's anatomy once inflated. While previous manufacturing strategies are too laborious for practical implementation²⁶ our 3D printing technique allows for fabrication of 10-15 patient-specific occluders in under 12 hours for less than \$0.50 per device. These hollow occluders possess thin walls ($t \sim 318.6 \pm 49 \mu\text{m}$) that enable surgical implantation, as well as robust mechanical properties ($\Delta P_{burst} > 60 \text{ kPa}$, $\Delta V_{burst} > 50 \text{ mL}$). In addition to this example, our method could be more broadly applied to other areas of medicine, where soft materials and patient-specificity are needed (e.g. stents, valves, prosthetics).

In brief, using CT segmentation²⁶ we obtained patient-specific volumetric renderings that are compatible with SLA printing using elastomeric material. Post printing, we added a self-sealing silicone valve to enable rapid inflation and deflation of these thin-walled elastomeric balloons. We demonstrated the stable anchoring of these occluders within a simulated appendage by measuring the pull-out force, and testing the long-term implantation of the occluder. We found that the pull-out force needed to dislodge a fully inflated P-S occluder was $F_{pull-out} \sim 14.9 \pm 1.47 \text{ N}$, and that only underinflated occluders ($V_{inflation} \sim 50\%$) were not stable over long periods of time in bench-top studies. Using CFD, we concluded that spherical occluder geometries have much lower shear regions which would likely cause more clots. These low shear regions are not observed in the P-S device. Though we did not investigate hemocompatibility of our base EPU material, prior work demonstrates a straightforward process to sterilize and impart hemocompatibility onto their surface²⁶. Future work should include long term durability testing in order to assess efficacy of these occluders *in vivo*, where biological interactions can be unpredictable.

C.5 Experimental

Uniaxial tensile tests

We performed tensile tests according to ISO 37 on a Zwick Roell z010 instrument. All tests were conducted at room temperatures using a 10 kN load cell and a strain rate of 200 mm min⁻¹. The data were averaged across common strain range and plotted with standard deviation ($n = 11$). We chose to skip every 35 points to make data more visible.

Thickness variation

We sampled three specimens from three different occluders, for a total of nine samples. We used a razor blade to slice portions of the printed occluder along a variety of planes. We then used an optical microscope (Zeiss) to image these samples against a reticle of known dimensions (Fig. C.2b, right). This reticle was fabricated by etching lines with set dimensions into acrylic using a laser cutter (Epilog Zing 50W, Epilog Laser). The images were processed using ImageJ by measuring each specimen in three positions. We calculated the mean and standard deviation using Microsoft Excel (Excel for Mac, Version 15.32, 2017).

Pressure – volume tests

All Pressure-Volume data in this manuscript was collected using custom LabVIEW™ code (Code can be made available upon request, National Instruments). The code controlled the input volume through a programmable syringe pump (NE-1000, New Era Pump Systems Inc.) and recorded the output pressure data from a pressure transducer (0-100 PSI, TDH30-CG-0100-03-D004, Transducers direct). These tests were performed on fourteen occluders (7 patient-specific, 7 spherical geometries). Each sample was inflated and deflated five times. To remove the initial inelastic effects in the stress-strain behavior of the base polymer, we only used the fifth recording to determine the mean and standard deviation between the samples (Fig. C.2c).

Pull-Out Tests

To characterize the pull-out force required to remove our devices from the LAA, we designed and 3D-printed a custom testing set-up which could be attached to a Zwick Roell z010 tensile tester (Fig.C. 3b). We used elastomeric polyurethane (M1 Carbon, EPU) to fabricate an anatomically correct synthetic LAA and secured this to one end of a rigid adapter (Objet30 Scholar Stratasys, Veroblue) which connects to the

load cell of the tensile tester. We then inflated six P-S occluders (with a Chicken Wing morphology that corresponded to the LAA in the testing rig) and six spherical occluders to six different volumes ($V_{inflation} \sim 50\%$ to 200%). We backfilled the occluders with an RTV-silicone pre-polymer (Ecoflex 00-30, Smooth-on) blended with 10 wt% silicone thinner (Smooth-on) which allowed for easier injection. After the silicone fully cured, we threaded a loop of Kevlar through the ostial surface of the occluder (Fig. C.9). We properly positioned and oriented the occluder within the simulated LAA and secured the Kevlar string to the moving head of the tensile tester. Next, we pulled the occluder back out of the LAA at a rate of 25 mm min^{-1} while recording the tensile force ($n = 5$). We report the maximum tensile force applied to the occluder during this pull-out test.

Embolism Tests

A custom benchtop flow-loop determined if the P-S or spherical occluders would embolize during the first 48 hours of implantation (Fig. C3c, C.11). This setup was modified from one described in our previous publication.²⁶ Briefly, we attached a sealed, 3D printed idealized left atrium to two pumps (ZKWP03A, FORTRIC), a patient-specific silicone LAA, and a pressure transducer (0-15 PSI, TDH30-CG-0015-03-D004, Transducers direct; Fig. C.11). A relay switch alternatively operates these pumps at physiological rates ($f \sim 1$ Hz). An external reservoir feeds and collects water from these pumps. By placing this reservoir at a height ~ 15 inches below the flow loop, we produced a pressure of $\Delta P \sim 15$ kPa inside of the chamber. We then implanted our occluder into the simulated LAA and took pressure readings at 0, 24, and 48 hours to ensure we maintained the desired physiological pressure range.

Occlusion tests

A P-S occluder was attached to a programmable syringe pump (NE-1000, New Era Pump Systems Inc.) via plastic tubing before being correctly oriented inside of a 3D printed, anatomically correct LAA (M1 Carbon, EPU; Fig. C.10). We used an additional syringe and 3-way valve to remove the air inside of the occluder. We then infused water into the empty occluder using the syringe pump at a rate of 1 mL min^{-1} . We used a custom LabVIEW™ code to control and record the input volume. While the occluder was being inflated, we continuously poured water into the LAA. A small hole in the distal tip of the LAA allowed the water to flow around the occluder and out of the LAA in a steady stream. As the occluder inflated and conformed to the walls of the LAA, the volume of water flowing out of the LAA decreased. When water ceased flowing out of the LAA, the occluder was determined to have fully occluded the vessel, and the volume of infused liquid was recorded ($n=10$). We then compared this volume to the known internal volume of the P-S occluders to determine the occlusion volume.

Computational Flow Dynamics

The geometry of the left atrium (with extension of approximately 20 mm downstream of the mitral annulus) was reconstructed from segmentations of CT cardiac images. The spherical and P-S occluders were positioned inside the LAA. The

fluid domain was then defined as the remaining volume inside of the atrium in either the spherical or P-S occluder models. Mass blood flows of the pulmonary veins (Fig. C.14) as measured previously³⁸ were prescribed as the inlet boundary conditions. The flow profile was defined parallel to the pulmonary veins walls to minimize the influence of inlet curvature on inflow streamline. The cross-section of the ventricle (outflow) was defined as an opening at zero-gauge pressure. The fluid domains of spherical and P-S occluders were discretized by 408,667 and 472,741 tetrahedral elements respectively (Fig.C.4). Increasing the number of the tetrahedral mesh elements resulted in a less than 5% variation in maximum wall shear stress (WSS) on the occluders walls, proving mesh independence. The blood flow was simulated in Ansys Fluent (Version 18.0) using a shear stress transport k-w model for a diastolic phase of 650 ms. Blood was modelled as Newtonian fluid with a density of 1050 kg m⁻³ and a dynamic viscosity of 3.5 x 10⁻³ kg m⁻¹ s⁻¹. The atrium and vascular walls were assumed rigid, and no-slip boundary conditions were applied at the walls. The mitral valve was not included in either case to simplify the model.

Statistical analyses

Sample size, mean, and standard deviation are reported for all data sets. No statistical methods were used to pre-determine the sample-sizes for the characterization of the performance of the occluders. All statistical analyses were performed in Origin® (Academic Version, 2016) and Microsoft Excel (Excel for Mac, Version 15.32, 2017).

Code availability

The LabVIEW™ and Arduino Uno™ codes that were used in this study can be made available upon request to the corresponding author.

Data availability

The authors declare that all data supporting the findings of this study are available within the paper and its Supplementary Information.

Image acquisition

All photographs in the manuscript were taken with a Canon (EOS Rebel T3i).

Image processing

Except where explicitly stated (i.e. where we state that we changed the contrast), photographs were only cropped and positioned in figures using Adobe® Illustrator® (CS6, Version 16.0.3), Adobe® Photoshop® (CS6, Version 12.0), and PowerPoint

(Microsoft Office). SolidWorks® (Education Edition, 2016) renderings were performed using PhotoView 360® Add-In feature. Geomagic Wrap® (Version 2015) renderings were taken using the Snapshot feature. Schematics were created using Adobe® Illustrator®. All arrows, dotted lines, and text were added to images in Adobe® Photoshop® or PowerPoint. All plots were created in Origin® (Academic Version, 2016).

C.6 Supplemental Information

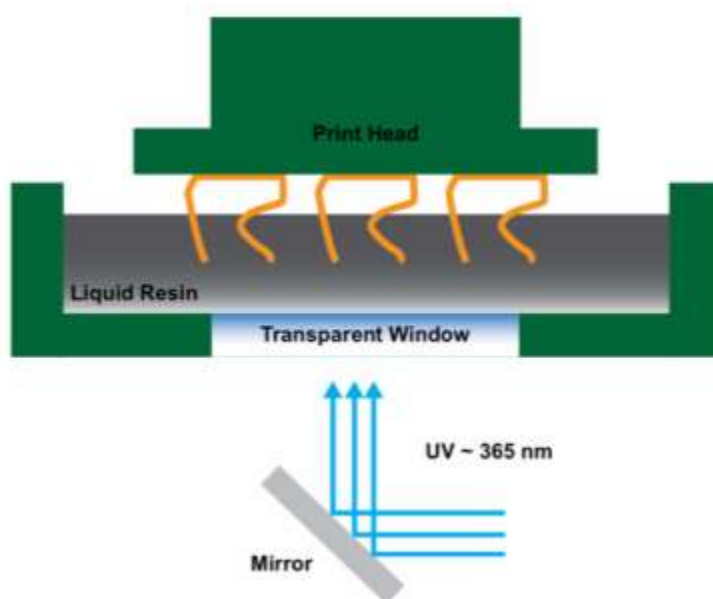


Figure C.5| Schematic of stereolithography printing process. Printed parts are cured layer by layer after exposure to UV light. Printed parts are pulled out of the liquid resin.

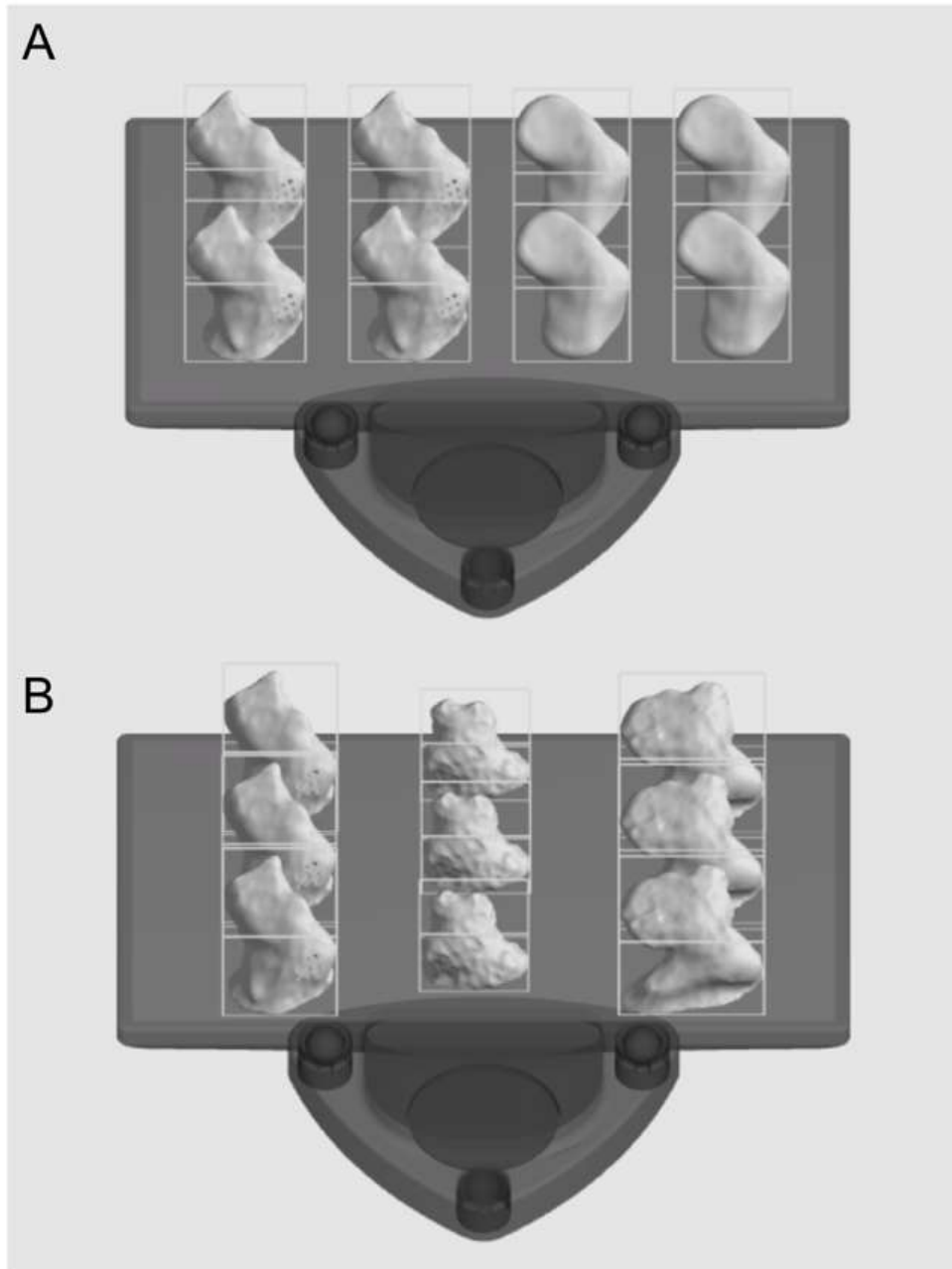


Figure C.6| Schematic of LAA occluders on print head. (a) Complex features, or smooth parts for the same patient can be printed on a single print. (b) LAA occluders for 3+ different patients can be fabricated on a single print.

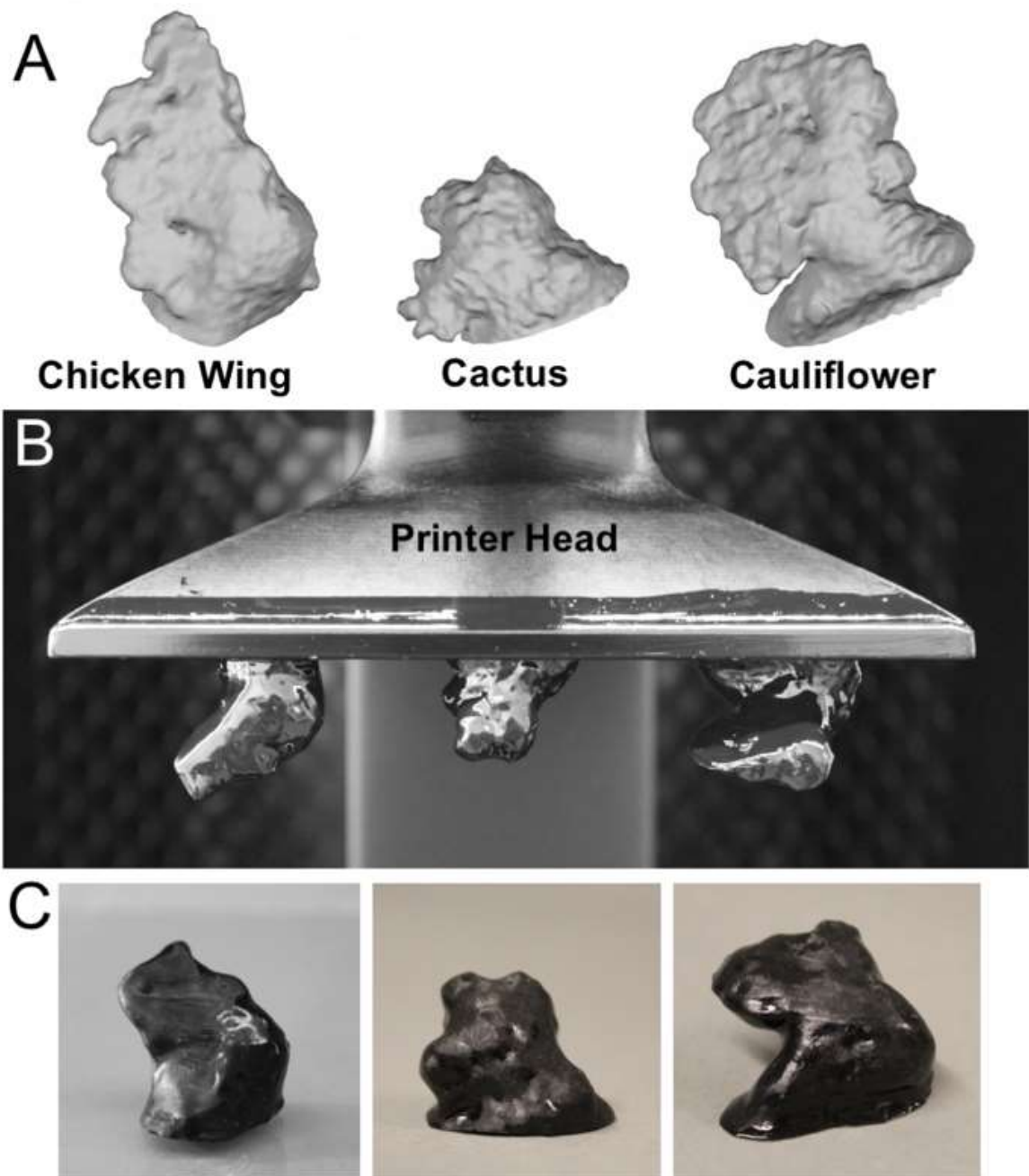


Figure C.7| Multiple patient-specific occluders can be printed simultaneously. (a) CAD renderings of CT segmented LAA for three typically encountered LAA morphologies, Chicken Wing (CW), Cactus, and Cauliflower. (b) 3D printed morphologies *green bodies*. (c) Fully cured LAA occluders for three patient morphologies.



Figure C.8| Pressure – volume test set-up. Occluders were attached through their plug onto the tip of a 30 gauge needle. They were then inflated with air up to 60 mL (size of syringe) while the volume input and pressure output was being recorded in labview VI. Each sample ($n = 6$) was tested five times and the 5th recording was used to determine the mean pressure and standard deviation of the samples.

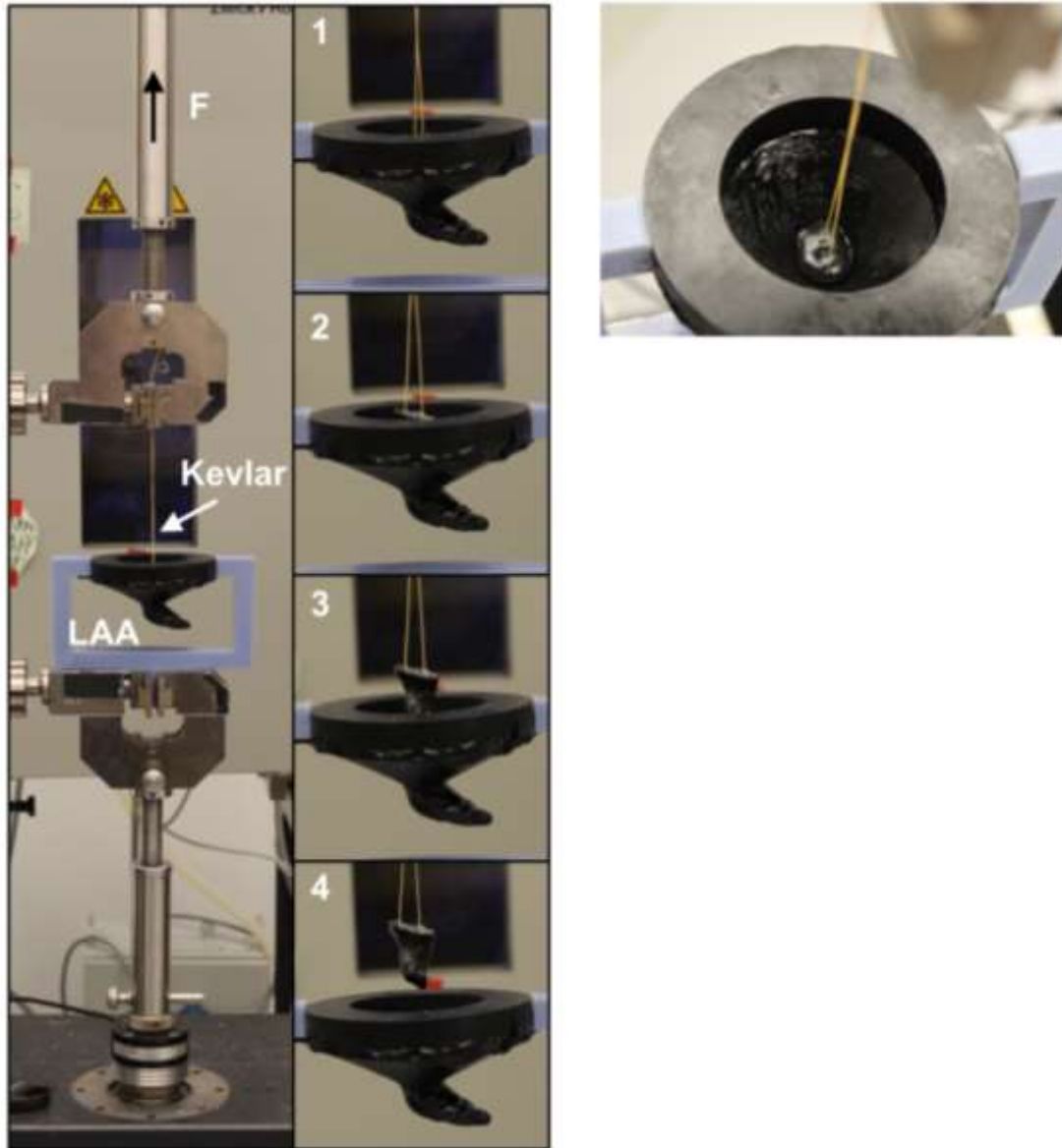


Figure C.9| Pull-out test. Kevlar thread (yellow) was looped through the ostial surface of the occluders and then attached to the upper crosshead of the tensile tester. The 3D printed LAA test-jig was attached to the bottom grip of the tensile tester. Occluders (which were prefilled with Ecoflex 00-30) were inserted into the LAA and then pulled out. (1-4) Images of the various stages of the test.

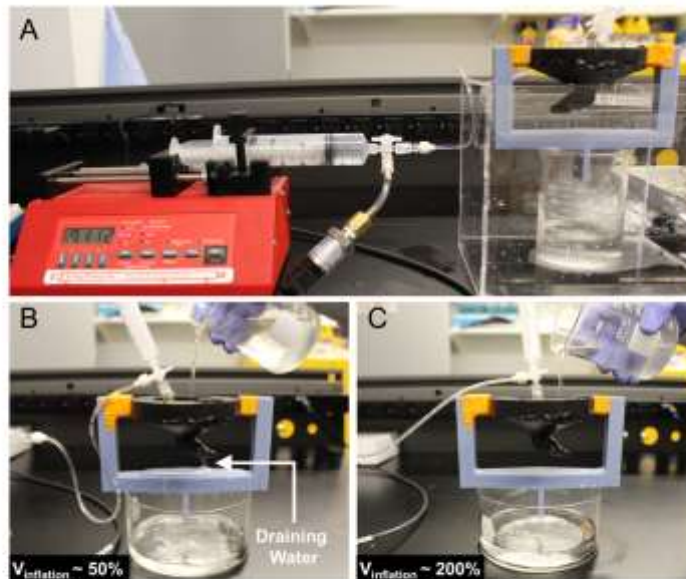


Figure C.10| Occlusion Volume Testing Setup. (a) A deflated P-S occluder was inserted into a 3D printed LAA and slowly infused with water. (b) The occlusion volume of the occluder was determined by pouring water into the LAA, where it drained around the inflating occluder and through a hole in the distal tip. (c) When the water stopped flowing through this hole, the P-S device was determined to be fully occluding the LAA.



Figure C.11| Embolism test set-up. Pumping water at physiological frequencies $f = 1\text{Hz}$. Measuring pressure within the idealized left atrium. Reservoir sits $\sim 15''$ below left atrium chamber.

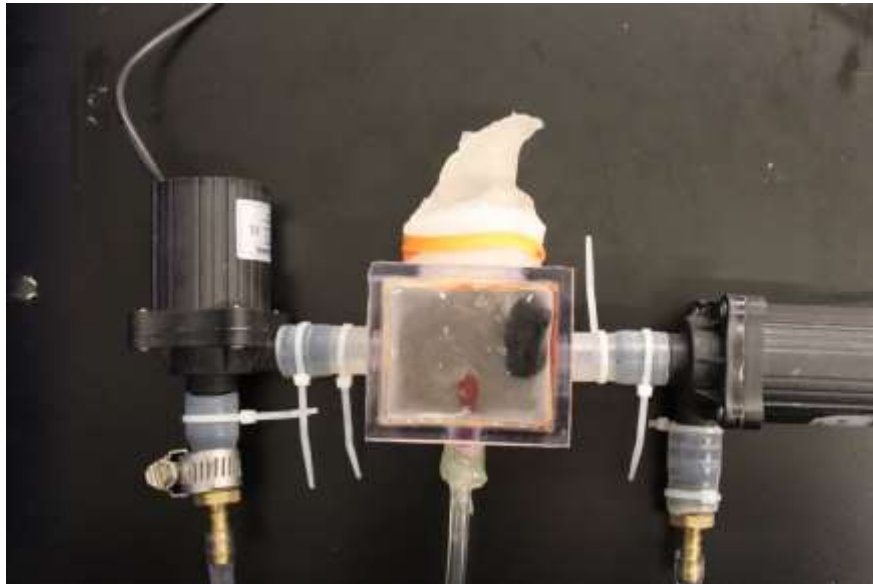


Figure C.12| P-S and spherical occluders embolized when they were underinflated, $V_{inflation} \sim 50\%$. In this image the P-S occluder is visible within the idealized left atrium of the flow set up. This demonstrates embolism of a device.

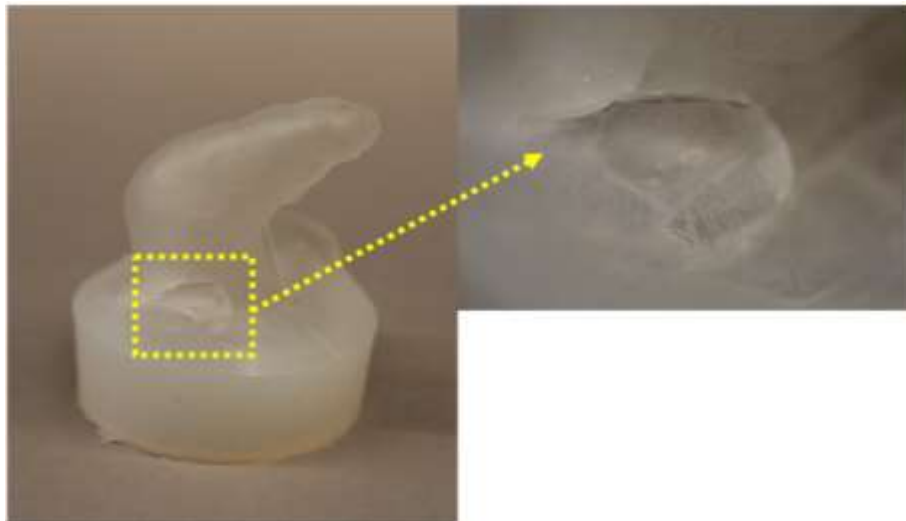


Figure C.13| Image of hole that was torn in the silicone phantom LAA by the $V_{inflation} \sim 200\%$ spherical occluder during the first 24 hours of testing.

REFERENCES

- 1 H. Zhao, Y. Li, A. Elsamadisi, R. Shepherd, *Extreme Mechanics Letters* **2015**, 3, 89.
- 2 T. J. Wallin, J. H. Pikul, S. Bodkhe, B. N. Peele, B. C. Mac Murray, D. Therriault, B. W. McEnerney, R. P. Dillon, E. P. Giannelis, R. F. Shepherd, *J. Mater. Chem. B* **2017**, 5, 6249.
- 3 S. S. Robinson, K. W. O'Brien, H. Zhao, B. N. Peele, C. M. Larson, B. C. Mac Murray, I. M. van Meerbeek, S. N. Dunham, R. F. Shepherd, *Extreme Mechanics Letters* **2015**, 5, 47.
- 4 B. C. Mac Murray, X. An, S. S. Robinson, I. M. van Meerbeek, K. W. O'Brien, H. Zhao, R. F. Shepherd, *Advanced Materials* **2015**, 27, 6334.
- 5 R. J. Morrison, S. J. Hollister, M. F. Niedner, M. G. Mahani, A. H. Park, D. K. Mehta, R. G. Ohye, G. E. Green, *Sci. Transl. Med.* **2015**, 7, DOI 10.1126/scitranslmed.3010825.
- 6 A. Díaz Lantada, R. Del Valle-Fernández, P. Lafont Morgado, J. Muñoz-García, J. L. Muños Sans, J. M. Munoz-Guijosa, J. Echávarri Otero, *Ann Biomed Eng* **2009**, 38, 280.
- 7 S. H. Sündermann, M. Gessat, N. Cesarovic, T. Frauenfelder, P. Biaggi, D. Bettex, V. Falk, S. Jacobs, *Interactive CardioVascular and Thoracic Surgery* **2013**, 16, 417.
- 8 P. S. D'Urso, D. J. Effeney, W. J. Earwaker, T. M. Barker, M. J. Redmond, R. G. Thompson, F. H. Tomlinson, *British Journal of Plastic Surgery* **2000**, 53, 200.
- 9 J. Brie, T. Chartier, C. Chaput, C. Delage, B. Pradeau, F. Caire, M.-P. Boncoeur, J.-J. Moreau, *Journal of Cranio-Maxillofacial Surgery* **2013**, 41, 403.
- 10 N. Xu, F. Wei, X. Liu, L. Jiang, H. Cai, Z. Li, M. Yu, F. Wu, Z. Liu, *SPINE* **2016**, 41, E50.
- 11 R. Schwarzkopf, M. Brodsky, G. A. Garcia, A. H. Gomoll, *Orthopaedic Journal of Sports Medicine* **2015**, 3, 232596711559037.

- 12 Y. Mao, C. Xu, J. Xu, H. Li, F. Liu, D. Yu, Z. Zhu, *International Orthopaedics (SICOT)* **2015**, *39*, 2023.
- 13 R. Akhtar, M. J. Sherratt, J. K. Cruickshank, B. Derby, *Materials Today* **2011**, *14*, 96.
- 14 P. Su, K. P. McCarthy, S. Y. Ho, *Heart* **2008**, *94*, 1166.
- 15 P. A. Wolf MD, R. D. Abbott, W. B. Kannel MD, *Stroke* **1991**, *22*, 983.
- 16 J. L. Blackshear MD, J. A. Odell FRCS(Ed), *Ann Thorac Surg* **1996**, *61*, 755.
- 17 S. C. Landefeld MD, R. J. Beyth MD, *The American Journal of Medicine* **1993**, *95*, 315.
- 18 C.-M. Yu, A. A. Khattab, S. C. Bertog, A. P. W. Lee, J. S. W. Kwong, H. Sievert, B. Meier, *Nat Rev Cardiol* **2013**, *10*, 707.
- 19 J. D. Moss, *Curr Cardiol Rep* **2014**, *16*, 448.
- 20 B. Kong, Y. Liu, H. Huang, H. Jiang, C. Huang, *J Thorac Dis* **2015**, *7*, 199.
- 21 C.-H. L. MD, J. B. K. M. PhD, S.-H. J. M. PhD, S. J. C. M. PhD, C. H. C. M. PhD, J. W. L. M. PhD, *Ann Thorac Surg* **2014**, *97*, 124.
- 22 E. S. Katz, T. Tsiamtsiouris, R. M. Applebaum, A. Schwartzbard, P. A. Tunick, I. Kronzon, *JACC* **2000**, *36*, 468.
- 23 A. S. Kanderian, A. M. Gillinov, G. B. Pettersson, E. Blackstone, A. L. Klein, *JACC* **2008**, *52*, 924.
- 24 J. O'Brien, D. Al-hassan, J. Ng, M. Joshi, C. Hague, S. Chakrabarti, J. Leipsic, *Int J Cardiovasc Imaging* **2014**, *30*, 819.
- 25 J. F. Viles-Gonzalez MD, S. Kar MD, P. Douglas MD, S. Dukkupati MD, T. Feldman MD, R. Horton MD, D. Holmes MD, V. Y. Reddy MD, *JACC* **2012**, *59*, 923.
- 26 S. S. Robinson, S. Alaie, H. Sidoti, J. Auge, L. Baskaran, K. Avilés-Fernández, S. D. Hollenberg, R. F. Shepherd, J. K. Min, S. N. Dunham, B. Mosadegh, *Nature Biomedical Engineering* **2018**, *1*.
- 27 D. B. Kolesky, K. A. Homan, **2016**.
- 28 B. Mosadegh, G. Xiong, S. Dunham, J. K. Min, *Biomed Mater* **2015**, *10*, 034002.

- 29 S. Anwar MD, G. K. Singh MD, J. Varughese, H. Nguyen MD, J. J. Billadello MD, E. F. Sheybani MD, P. K. Woodard MD, P. Manning MD, P. Eghtesady MD, *JACC: Cardiovascular Imaging* **2016**, 1.
- 30 J. Odent, T. J. Wallin, W. Pan, K. Kruemplestaedter, R. F. Shepherd, E. P. Giannelis, *Advanced Functional Materials* **2017**, 27, 1701807.
- 31 D. K. Patel, A. H. Sakhaei, M. Layani, B. Zhang, Q. Ge, S. Magdassi, *Advanced Materials* **2017**, 29, 1606000.
- 32 R. G. Carroll, *Elsevier's Integrated Physiology*, Mosby, Philadelphia, USA **2007**, pp. 65–75.
- 33 A. Akinapelli, O. Bansal, J. P. Chen, A. Pflugfelder, N. Gordon, K. Stein, B. Huijbregtse, D. Hou, *Current Cardiology Reviews* **2015**, 11, 334.
- 34 K. C. Koskinas, Y. S. Chatzizisis, A. P. Antoniadis, G. D. Giannoglou, Role of Endothelial Shear Stress in Stent Restenosis and Thrombosis, *J. Am. Coll. Cardiol.* 2012, 59, 1337.
- 35 M. Vukicevic, B. Mosadegh, J. K. Min MD, S. H. Little MD, *JACC: Cardiovascular Imaging* **2017**, 10, 171.
- 36 L. Lao, S. S. Robinson, B. Peele, H. Zhao, B. C. Mac Murray, J. K. Min, B. Mosadegh, S. Dunham, R. F. Shepherd, *Adv. Eng. Mater.* **2016**, 19, 1600591.
- 37 A. A. Giannopoulos MD, D. Mitsouras, S.-J. Yoo, P. P. Liu, Y. S. Chatzizisis, F. J. Rybicki, *Nat Rev Cardiol* **2016**, 13, 701.
- 38 J. Tu, K. Inthavong, K. K. L. Wong, *Computational Hemodynamics – Theory, Modelling and Applications*, Springer, **2015**.